FAILURE OF LIQUID STORAGE TANKS DUE TO EARTHQUAKE EXCITATION

Thesis by

Choon-Foo Shih

In Partial Fulfillment of the Requirements

for the Degree of

Doctor of Philosophy

California Institute of Technology

Pasadena, California

1981

(Submitted May 18, 1981)

ACKNOWLEDGEMENT

I would like to thank the members of the Caltech Faculty who have contributed to my education. In particular, I would like to express my sincere thanks and appreciation to Professor Charles D. Babcock for his guidance, encouragement and friendship during the course of this investigation. I also greatly appreciate the support and encouragement of Professor George W. Housner.

I am grateful to Dr. Medhat Haroun who developed the basic analysis that was applied in this study. The assistance of Mr. Raul Relles in maintaining the instrumentation system is greatly appreciated. I am also indebted to the members of the GALCIT technical staff for their assistance in conducting this work. Thanks are due to Marta Nyiri for her patience shown in typing this thesis, and to Betty Wood for preparing the figures.

This work was supported by the National Science Foundation under grant numbers PFR-7723687, PFR-7900712 and PFR-8013668. This support is gratefully acknowledged.

Finally, I wish to dedicate this thesis to my parents, whose love and concern have sustained me throughout my life.

ABSTRACT

Above ground liquid storage tanks have suffered serious damage during earthquakes. The damage of tanks can vary from local yielding or buckling of the tank wall, to loss of contents, or to collapse which leads to an unrepairable tank. Considerable work has been carried out on this problem with varying degree of success. However, the results are largely directed toward response rather than failure prediction. The information on failure mechanisms is very limited. The present work consists of scale model testing, correlation with existing analysis and failure prediction with laboratory verification. The scale model testing incorporates dynamic similarity of the fluid/structure interaction problem. The model study shows that small plastic models can be useful in studying the dynamics and buckling of liquid-filled tanks under ground excitation even though the model does not display complete similitude. The buckling criterion proposed in this study is based upon static considerations and the complex stress field in the shell wall is supplanted by a simple field for which analytical/ experimental results are available. Harmonic buckling tests demonstrate that the static buckling criterion is satisfactory even though the prebuckling stress field is time dependent. The harmonic buckling tests, when correlated with the stresses from a response analysis, also indicate that the buckling is largely dependent upon the n=1 response. Transient buckling tests are also carried out and the results show that the linear

analysis together with the static buckling criterion gives a good prediction of the failure of a full fluid-filled tank. The test parameters in these buckling tests include water depth, title angle, thickness of tank wall, top end condition, ground excitation pattern, etc. In addition, buckling tests of unanchored tanks are conducted to study the influence of changing the anchorage of the tank base. An analytical model is suggested to predict the response of an unanchored tank due to overturning moment. The current design criterion of an unanchored tank is also assessed in this study. The results of this investigation, in addition to those carried out previously, provide a better understanding of the forced vibration problem, failure criterion and appropriate design procedure for a liquid storage tank.

TABLE OF CONTENTS

NOMENCLATURE

a	Radius of the contact area between bottom plate and ground
$\underset{\sim}{A}, \underset{\sim}{B}, \underset{\sim}{C}$	Submatrices of mass matrix
C_{vn}	Virtual mass coefficient
d_b	Critical buckling water depth
d_c	Collapse water depth
D	Water Depth as shown in figures 4.1 and 4.10
E	Young's Modulus
$\underset{\sim}{E}, \underset{\sim}{F}$	Submatrices of stiffness matrix
F	Total axial force
g	Gravitational acceleration
$\underset{\sim}{G}, \underset{\sim}{H}$	Submatrices of stiffness matrix
h	Tank height
H	Water depth as defined in figures 4.1 and A.1
$\underset{\sim}{I}$	Submatrix of stiffness matrix
I_n	Modified Bessel function of order n
i,j	Subscripts
J_i	Bessel function of the first kind of i^{th} order
k_i	Coefficients in expressions for the displacement functions
ℓ	Subscript index for liquid
L	Tank length
L_s	Length scale factor
m	Axial mode number

m_{vn}	Virtual mass of the fluid inside the tank
M	Overturning moment
n	Number of circumferential waves
N	Number of displacement functions considered
N_c	Maximum Axial compressive force
N_t	Maximum Axial tensile force
N_x, N_z	Membrane resultant axial stresses
N_θ	Membrane resultant hoop stress
$N_{z\theta}$	Membrane resultant shearing stress
p	Internal pressure
$\bar{p}$	Internal pressure parameter
r	Cylindrical coordinate in radius direction
R	Radius of cylindrical tank
$R_{N\theta}$	Ratio of resultant hoop stress
s	Subscript index for shell wall
t	Time
t_b	Thickness of bottom plate
t_s	Thickness of shell wall
T	Total kinetic energy
T_e	Earthquake duration or typical period
T_ℓ	Kinetic energy of the fluid inside the tank
$T_{\ell s}$	Liquid sloshing period
T_s	Kinetic energy of the cylindrical tank wall
T_t	Tank vibration period
u,v,w	Displacements in axial, circumferential and radial directions, respectively

$\bar{U}_i, \bar{V}_i, \bar{W}_i$	Time dependent coordinates in the expression of u-, v- and w- displacements
$\underline{\bar{U}}, \underline{\bar{V}}, \underline{\bar{W}}$	Submatrices of displacement matrix
W	Total weight of fluid
W_d	Uplifting width
W_f	Weight of the fluid acting on the contact area of bottom plate
W_s	Downward shear force acting on the boundary of bottom plate
W_u	Dead load of the liquid acting on the uplifting area of bottom plate
V	Potential Energy
V_r, V_θ, V_z	Velocity components of the fluid in radial, circumferential and vertical directions, respectively
x, y, z	Cartesian Coordinates
$\ddot{x}_g, \ddot{X}_g$	Base Acceleration
α	Inclined angle
α_{ni}	Roots of $J_n'(\alpha_{ni})$
β	Angle for the compressive boundary of tank bottom
γ_{12}	Middle surface shear strain
γ_{xy}	Shear strain
δ	Uplifting distance
Δ	Natural frequency parameter
$\varepsilon_1, \varepsilon_2$	Middle surface strain
$\varepsilon_x, \varepsilon_y$	Strain
ζ	Structural damping ratio

η	Free surface displacement
$\kappa_1, \kappa_2, \kappa_{12}$	Changes of curvature and twist
λ_i	Coefficients in expressions for the displacement functions
μ	Viscosity
ν	Poisson's ratio
ξ_n	Roots of $J_1'(\xi_n)$
ρ_ℓ	Liquid density
ρ_s	Shell wall density
σ	Axial stress
σ_c	Axial compressive stress in the tank wall
σ_{cr}	Classical critical buckling stress
τ	Shear stress, due to the viscous fluid, acting on the tank wall
ϕ_i	Displacement functions corresponding to modal shapes of a cantilever beam
Φ	Velocity potential function for liquid
ψ_i	The first derivative of ϕ_i
ω	Natural frequency of tank wall
ω_1	Fundamental natural frequency of tank wall
ω_n	Resonant frequencies of the liquid sloshing modes

CHAPTER 1 INTRODUCTION

1.1 MOTIVATION

Above ground liquid storage tanks have suffered serious damage during earthquakes [1.1,1.2]. Water and petroleum tanks have suffered the most damage, with other fluid tanks (such as milk) being damaged less often due to their smaller size. The damage to tanks can vary from local yielding or buckling of the tank walls, to loss of contents, or to collapse which leads to an unrepairable tank. In general, the earthquake damage to cylindrical liquid storage tanks can be categorized as follows: (1) shell buckling near the bottom of the tank, (2) buckling at the top of the tank walls, (3) damage to roofs and accessories and (4) damage to connecting piping. In a few tanks of critical proportions, the buckling was followed by the collapse of the tank [1.3]. Two different types of shell buckling modes can be observed near the bottom of the tank. One is the axisymmetric outward budge of the shell close to ground level. This may extend almost all the way around the circumference as shown in figure 1.1. This kind of buckling is a plastic failure type mode [1.4]. The other buckling mode near the bottom of the tank is the typical elastic buckling mode, diamond shape, which can be observed in the damage of wine storage tanks during the Mt. Diablo earthquake of 1980 (figure 1.2).

Buckling is not confined to the bottom end of the tank. Figure 1.3 shows the buckling which occurred on the top end of the tank. This kind of buckling is thought to be the result of negative pressure acting on the tank wall. A large distorsion on the roof of tank can be seen in figure 1.4. It is believed due to the sloshing caused by the earthquake excitation. In addition, the uplifting phenomena can be presumed from the pull up distance of anchor bolts as shown in figure 1.5.

1.2 RESEARCH BACKGROUND

The problem of a liquid storage tank under earthquake excitation has been studied by many investigators. The earlier study of dynamic effects in cylindrical liquid storage tanks considered the tank to be rigid, and focused on dynamic response of the contained liquid. It included the linear [1.5-1.11] and nonlinear [1.12,1.13,1.14] sloshing behavior of the liquid. In ref. 1.8, Housner separated the hydrodynamic pressure of the contained liquid into two parts; one is the impulsive pressure caused by the inertial reaction of the contained liquid and the other is the convective pressure generated by the sloshing of the contained liquid. The impulsive effect can be modeled by attaching a rigid mass to the container and the convective effect can be modeled by a single degree of freedom oscillator. This so called Housner's model has been widely used for aseismic design of liquid storage tanks. Recently it has been observed that the seismic response

of some flexible tanks is substantially greater than that of rigid tanks. Circular cylindrical shells, with or without contained liquid, exhibit complex vibration modes which may have several waves along the length and/or around the circumference [1.15,1.16]. Much of this knowledge has come from investigations performed for development of design procedures for liquid propellant response in aerospace launch vehicles [1.17-1.21]. A comprehensive review of the theoretical and experimental investigations of the dynamic behavior of fuel tanks for space vehicles can be found in ref. 1.22.

The study of the seismic response for ground-supported tanks evolved slowly. Progress was made largely through studying tanks damaged by the 1964 Alaska and the 1971 San Fernando earthquakes. Considerable work has been carried out on this problem with varying degrees of success. Coupled liquid sloshing and tank vibration solutions have been formulated [1.23-1.28]. However, they have not been extended to predict buckling. Some experimental investigations [1.29-1.31] have also been reported for cylindrical tanks subject to horizontal ground motion but the results thus far have shed little light on the buckling criteria. Both theoretical and experimental results have shown that the flexibility of the thin shell wall plays a significant role in the dynamic response of a tank under ground excitation. The experimental work, along with previous work on the fluid sloshing problem, has some relevance to the present application but are largely

directed towards dynamic response (surface motion, resonant frequencies, stress, deflection, etc.) rather than failure analysis. The amount of experimental information on failure mechanisms is very limited.

1.3 OBJECTIVES AND SCOPE

The purpose of this study is to gain a better understanding of the forced vibration, failure criterion and appropriate design procedure for liquid storage tanks under seismic excitation. It is felt that this can best be done using scale model testing (laboratory size) coupled with simplified analysis procedures which display only the important parameters of the problem. By using laboratory size models, complete dynamic characterization of the structure and fluid/structure combination can be carried out. This will allow identification of important response and failure modes as well as the significance of tank parameters on these modes.

The present work consists of scale model testing, correlation with existing analysis and failure prediction with laboratory verification. The scale model testing will incorporate dynamic similarity of fluid/structure interaction problem. The adequacy of the scale modeling used in the experimental work is discussed in chapter 3. The buckling criterion proposed in this study is based upon static consideration and the complex stress field in the shell wall is supplanted by a simple field for which analytical/experi-

mental results are available. The adequacy of this step is discussed in section 4.1. A pilot investigation on the static buckling criterion of a circular cylindrical shell under axial compression is also carried out in chapter 2 to provide comparable data as a basis for obtaining the tank buckling criteria. The use of a static buckling criterion with a time dependent prebuckling stress field is assessed through harmonic buckling tests in section 4.3.3. Transient buckling tests, section 4.3.4, are also carried out to assess the adequacy of the failure criteria established by the harmonic tests. The test parameters in these buckling tests include water depth, tilt angle, thickness of tank wall, top end condition, ground excitation pattern, etc. In addition, the buckling tests of unanchored tanks are discussed in chapter 5 to study the influence of changing the anchorage of tank base . An analytical model is suggested in appendix D to predict the response of an unanchored tank due to overturning moment. The standard design criteria on an unanchored tank [1.32] are also assessed in this study.

REFERENCES - CHAPTER 1

1.1 Hanson, R.D., "Behavior of Liquid-Storage Tanks", The Great Alaska Earthquake of 1964, Engineering, National Academy of Sciences, Washington, D.C., 1973.

1.2 Jennings, P.C., "Damage of Storage Tanks, Engineering Features of the San Fernando Earthquake, February 9, 1971", Engineering Research Laboratory, California Institute of Technology, June, 1971.

1.3 Rinne, J.E., "Oil Storage Tanks", The Prince William Sound Alaska, Earthquake of 2964, and Aftershocks, Vol.II, Part A, ESSA, U.S. Coast and Geodetic Survey, Washington: Government Printing Office, 1967, pp. 245-252.

1.4 Sobel, L.H. and Newman, S.Z., "Plastic Buckling of Cylindrical Shells under Axial Compression", Transactions of ASME, Journal of Pressure Vessel Technology, Vol. 102, Feb., 1980, pp. 40-44.

1.5 Hoskins, L.M. and Jacobsen, L.S., "Water Pressure in a Tank Caused by a Simulated Earthquake", Bulletin Seism. Soc. America, Vol. 24, 1934, pp. 1-32.

1.6 Jacobsen, L.S., "Impulsive Hydrodynamics of Fluid Inside a Cylindrical Tank and of a Fluid Surrounding a Cylindrical Pier", Bulletin Seism. Soc. America, Vol. 39, 1949, pp. 189-204.

1.7 Jacobsen, L.S. and Ayre, R.S., "Hydrodynamic Experiments with Rigid Cylindrical Tanks Subjected to Transient Motions", Bulletin Seism. Soc. America, Vol. 49, 1951, pp. 313-346.

1.8 Housner, G.W., "Dynamic Pressures on Accelerated Fluid Containers", Bulletin Seism. Soc. America, Vol. 47, No.1, 1957, pp. 15-35.

1.9 Housner, G.W., "The Dynamic Behavior of Water Tanks", Bulletin Seism. Soc. America, Vol. 53, No.1, 1963, pp.381-387.

1.10 Kachigan, K., "Forced Oscillations of a Fluid in a Cylindrical Tank", ZU-7-046 (Contact AF 04 (6450-4), Convair Astronautics, Oct. 1955.

1.11 Bauer, H.F., "Theory of the Fluid Oscillations in a Circular Cylindrical Ring Tank Partially Filled with Liquid", NASA TN D-557, Dec. 1960.

1.12 Hutton, R.E., "An Investigation of a Resonant, Nonlinear, Nonplanar Free Surface Oscillation of a Fluid", NASA TN D-1870, May, 1963.

1.13 Weiss, H.J. and Rogge, T.R.,"A Nonlinear Analysis for Sloshing Forces and Moments on a Cylindrical Tank", NASA CR-221, 1965.

1.14 Abramson, H.N., Chu, W.H. and Kana, D.D., "Some Studies of Nonlinear Lateral Sloshing in Rigid Containers", Journal Applied Mechanics, Dec. 1966.

1.15 Lindholm, U.S., Kana, D.D. and Abramson, H.N., "Bending Vibrations of a Circular Cylindrical Shell Containing an Internal Liquid with a Free Surface", AIAA J., Vol.1, No.9, Sept. 1963, pp. 2092-2099.

1.16 Lindholm, U.S., Kana, D.D. and Abramson, H.N.,"Breathing Vibrations of a Circular Cylindrical Shell with an Internal Liquid", J. Aerospace Sci., Vol. 29, No.9, Sept. 1962, pp.1052-1059.

1.17 Miles, J.W., "On the Sloshing of Liquid in a Flexible Tank", J. App. Mech., June 1958, pp. 277-283.

1.18 Mixon, J.S. and Herr, R.W., "An Investigation of the Vibration Characteristics of Pressurized Thin-Walled Circular Cylindrical Shells Partly Filled with Liquid", NASA TR R-145, 1962.

1.19 Kana, D.D., Lindholm, U.S. and Abramson, H.N., "An Experimental Study of Liquid Instability in a Vibrating Elastic Tank", J. of Spacecraft, Vol.3, No.8, Aug. 1966, pp. 1183-1188.

1.20 Chu, W.H. and Kana, D.D., "A Theory for Nonlinear Transverse Vibrations of a Partially Filled Elastic Tank", Final Report, Part I, Project 02-1748, Southwest Research Institute, March 1966.

1.21 Bauer, H.F., Hsu, T.M. and Wang, J.J., "Liquid Sloshing in Elastic Containers", NASA CR-882, Sept. 1967.

1.22 Abramson, H.N., "The Dynamic Behavior of Liquids in Moving Containers", NASA SP-106, 1966.

1.23 Edwards, N.W., "A Procedure for Dynamic Analysis of Thin Walled Cylindrical Liquid Storage Tanks Subjected to Lateral Ground Motions", Ph.D. Dissertation, Univ. of Michigan, Ann Arbor, Michigan, 1969.

1.24 Hsiung, H.H. and Weingarten, V.I., "Dynamic Analysis of Hydroelastic Systems Using the Finite Element Method", Department of Civil Engineering, University of Southern California, Report USCCE 013, November 1973.

1.25 Yang, J.Y., "Dynamic Behavior of Fluid-Tank Systems", Ph.D. Dissertation, Rice University, Houston, Texas, March 1976.

1.26 Mouzakis, T., "Response of Partially Filled Elastic Cylindrical Storage Tanks Subjected to Arbitrary Lateral Base Excitation", Ph.D. Dissertation, Massachusetts University, Amherst, July 1976.

1.27 Balendra, T. and Nash, W.A., "Earthquake Analysis of a Cylindrical Liquid Storage Tank with a Dome by the Finite Element Method", Department of Civil Engineering, University of Massachusetts, Amherst, Massachusetts, May 1978.

1.28 Haroun, M.A., "Dynamic Analysis of Liquid Storage Tanks", Ph.D. Dissertation, California Institute of Technology, Pasadena, California, December 1979.

1.29 Clough, D.P., "Experimental Evaluation of Seismic Design Methods for Broad Cylindrical Tanks", University of California, Berkeley, Earthquake Engineering Research Center Report No. UCB/EERC-77/10, May 1977.

1.30 Niwa, A., "Seismic Behavior of Tall Liquid Storage Tanks", University of California, Berkeley, Earthquake Engineering Research Center Report No. UCB/EERC-78/04, February 1978.

1.31 Kana, D.D. "Seismic Response of Flexible Cylindrical Liquid Storage Tanks", Nuclear Engineering and Design, Vol.52, 1979, pp. 185-199.

1.32 Wozniak, R.S. and Mitchell, W.W., "Basis of Seismic Design Provisions for Welded Steel Oil Storage Tanks, Proposed Appendix P to API Standard 650", API Convention, Toronto, Canada, May 1978.

CHAPTER 2 BUCKLING CRITERIA OF A CYLINDRICAL SHELL

2.1 INTRODUCTION

The instability of cylindrical shells under axial compression has been studied both theoretically and experimentally by many investigators. Intense interest was initially generated by serious disagreement between experimental data and the results predicted by small deflection theory of buckling [2.1]. Nonlinear postbuckling theory had been used to obtain the minimum load the cylinder can support in the buckled state [2.2]. This concept did not work since the negative minimum postbuckling loads were possible. Indeed, the geometric initial imperfection of the cylinder is the main degrading factor. It was found that the load carrying capacity of cylindrical shells was extremely sensitive to initial imperfections of the order of a fraction of the wall thickness [2.3]. An excellent survey by Hutchinson and Koiter [2.4] lists 215 references on the subject of postbuckling and the influence of initial imperfections. The experiments in shell buckling were reviewed by Babcock [2.5] to discuss the specimen fabrication, initial imperfections, mounting and loading, and some special techniques. In addition, the influences of the nonuniformity of loading [2.6] and the testing conditions [2.7] have also been considered in seeking an explanation of the discrepancy between the analytical and the experimental capacities. Since the results for the circular

cylindrical shell under axial compression are quite scattered [2.8], it is felt that a pilot buckling test of the circular cylindrical shell will be necessary. This test will yield comparable data as a basis for obtaining the tank buckling criteria and provide a measure of the quality of the cylinders to be used in subsequent tests.

2.2 BUCKLING CRITERIA OF A CYLINDRICAL SHELL UNDER UNIFORM AXIAL COMPRESSION

If a cylindrical shell is uniformly compressed in the axial direction, the linearized buckling theory predicts that the critical buckling stress, σ_{cr}, is

$$\sigma_{cr}=\frac{1}{[3(1-\nu^2)]^{1/2}}\cdot\frac{E}{(R/t_s)} \qquad (2.1)$$

Experiments indicate that the measured critical value is usually on the order of one-third of that predicted by equation (2.1) for unpressurized shell and is larger for pressurized shell. It is this part of the experimental buckling criteria that will be addressed in this section.

The test tanks were constructed of Mylar A sheet. This material has a yield stain of approximately 1 % and a Young's modulus of 735000 psi with a $\pm$ 9% variation for all thickness [2.8]. The Poisson's ratio of this material is about 0.3. The advantages of using Mylar are that inexpensive specimens can be constructed and that one tank can be buckled

many times without any noticeable degradation of the shell quality. One disadvantage of Mylar is its anisotropic material properties. There can be as much as $\pm$ 15 % variation in the tensile modulus depending on the orientation of the specimen with the sheet axis [2,9]. The advantages outweight this deterrent to its use.

The test tanks were made by rolling the Mylar sheet around a mandrel and using a lap seam bounded with an epoxy. The cylinder was fixed on both the bottom and the top using a low melting temperature alloy (Cerrolow) in a circular groove in the end plates. The dimensions of test tanks are as follows; R= 4.0 in., t_s = 0.005 in., and L= 15 in., 18 in., and 19.2 in. .

The experimental setup for the uniform axial compression tests is shown in figure 2.1. The axial load is applied on the top plate of the tank by a loading screw. A load cell is used to measure the total axial force acting on the top plate. The load cell was calibrated using a 3000 pound Riche Brothers testing machine. Pressurization of the cylinder was accomplished with compressed air through a port in the top plate. A pressure gage was used to monitor the air pressure inside the cylinder.

For each fixed internal pressure, the axial load is increased gradually until the buckling occurs. At buckling there is an audible snap and a decrease in the dial gage of the load cell. The buckles will disappear as the cylinder is

being unloaded. The pressure parameter,

$$\bar{p} = \frac{pR^2}{Et_s^2} \qquad (2.2)$$

was varied from 0.0 to about 2.5. Figures 2.2a and 2.2b show the experimental buckling patterns of the unpressurized and the pressurized cylinders. It may be noted that the axial wave length of the buckling pattern for the unpressurized cylinder is much longer than that for the pressurized cylinder.

The experimental results are shown in figure 2.3 for three different test tanks. It indicates that the buckling strength of the cylinders increases as the internal pressure is increased. This is quite different from the theoretical prediction based on the perfect shell assumption and the classical buckling analysis. This behavior can be explained by considering the influence of initial imperfection of the shell wall and applying the nonlinear buckling analysis [2.10]. The discrepancy of the results between each cylinder, as shown in figure 2.3, is most likely due to the variations of the imperfection.

2.3 NONUNIFORMITY EFFECT ON THE BUCKLING STRENGTH OF A CIRCULAR CYLINDRICAL SHELL

Since the stress distributions of a liquid storage tank under earthquake excitation are not uniform both along the vertical axis and around the circumference, it is felt that

a better understanding of the "nonuniformity effect" is necessary. The static buckling criterion for nonuniformly loaded shell structure is not a well developed subject area. The classical problem in this area is the cylindrical shell under uniform axial load and pure bending. Theoretically these problems have exactly the same maximum stress at buckling [2.11]. Experimentally they differ by a factor varying from 1.0 to about 1.6 with both values considerable below the theoretical results [2.8]. The reason for this is commonly thought to be the influence of initial imperfection. Imperfections on the tensile side of the shell under bending will have no influence on the buckling moment but those on the compressive side will be determined.

It is interesting to study the maximum allowable stress of a cylinder under different varying stress fields along the axial direction but having a uniform stress around the circumferential direction. The numerical program BØSØR4 [2.11] can be applied to predict this maximum allowable stress. Three different cases have been studied and the results are shown in figure 2.4. The first one is a uniform loading case and the maximum allowable stress is the classical buckling stress σ_{cr}. The second case is a linear axial loading case and the maximum allowable stress is 1.18 times the classical buckling stress. The third stress distribution is exactly the same as the membrane axial stress, at $\theta = 0$, in the shell wall of the tank which is subjected to a ground excitation

(see Eq. 4.3a). In this case, the result indicates that the maximum allowable stress is 1.24 times the classical buckling stress. The comparison between these different axial loading cases demonstrates that due to the varying stress field the maximum allowable stress is greater than that which would be allowable for a shell with stress applied uniformly. However, the increase in maximum allowable stress is not large.

2.4 CONCLUSIONS

It is seen that there are three effects which must be taken into account when establishing a buckling criterion. Two of them tend to increase the maximum allowable stress and one has a decreasing effect. (1) Nonuniformity effect for a perfect shell. The results shown in figure 2.4 indicate that the non-uniform axial loading will increase the maximum allowable stress (buckling failure assumed) for a perfect shell. (2) Nonuniformity effect for an imperfect shell. The imperfections in the shell are less influential when the stresses are not uniformly distributed over the whole area of the shell. This has been shown in the experimental results of a cylinder under uniform axial load and pure bending. (3) Knockdown factor due to initial imperfection of shell. Experiments indicate that the actual buckling stress of a cylindrical shell under uniform loading is always less than the theoretical results for a perfect shell. This difference depends on the magnitude

and shape of the initial geometric imperfections of the shell. The ratio of actual buckling stress to the calculated critical stress is known as the "knockdown" factor. This "knockdown" factor, k_d, has been widely applied to the seismic design of storage tanks. The value assumed in ref. 2.13 is given by $k_d = 0.21$ or $\sigma_{cr} = 0.125\ Et_s/R$. More information on this "knockdown" factor can be found in ref. 2.14.

REFERENCES - CHAPTER 2

2.1 Donnell, L.H., "A New Theory for the Buckling of Thin Cylinders under Axial Compression and Bending", Transactions of the ASME, Vol. 56, November 1934, pp. 795-806.

2.2 von Karman, T. and Tsien, H.S., "The Buckling of Thin Cylindrical Shells under Axial Compression", Journal of the Aeronautical Science, Vol. 8, No.6, June 1941, pp. 303-312.

2.3 Koiter, W.T., "The Effect of Axisymmetric Imperfection on the Buckling of Cylindrical Shells under Axial Compression", Proc. K. Ned. Akad. Wet., Amsterdam Ser.B, Vol.6, 1963; also, Lockheed Missiles and Space Co. Rep. 6-90-63-86, Palo Alto, Cal., August 1963.

2.4 Hutchinson, J.W. and Koiter, W.T., "Postbuckling Theory", Apply Mech. Rev., No. 23, 1970, pp. 1353-1366.

2.5 Babcock, C.D., "Experiments in Shell Buckling", Thin Shell Structures, Fung, Y.C. and Sechler, E.E., eds., pp. 345-369, Prentice Hall, 1974.

2.6 Dow, M.B. and Peterson, J.P., "Bending and Compression Tests of Pressurized Ring-Stiffened Cylinders", NASA TN D-360, April 1960.

2.7 Babcock, C.D., "The Influence of the Testing Machine on the Buckling of Cylindrical Shells under Axial Compression", Intern. J. Solids Structures 3, 1967, pp. 809-817.

2.8 Weingarten, V.I., Morgan, E.J. and Seide P., "Final Report on Development of Design Criteria for Elastic Stability of Thin Shell Structures", STL/TR-60-0000-19425, Space Technology Laboratories, Inc., Los Angeles, California, Dec. 1960.

2.9 Ishai, O., Weller, T. and Singer, J., "Anisotropy of Mylar A Sheets", Journal of Materials, Vol. 3, No.2, 1968.

2.10 Hutchinson, J., "Axial Buckling of Pressurized Imperfect Cylindrical Shells", AIAA Journal, Vol.3, No.8, August 1965, pp. 1461-1466.

2.11 Seide, P., and Weingarten, V.I., "On the Bending of Circular Cylindrical Shells under Pure Bending", Journal of Applied Mechanics, Vol. 28, No.1, March 1961, pp.112-116.

2.12 Bushnell D., "Stress, Stability and Vibration of Complex Branched Shells of Revolution: Analysis and User's Manual for BØSØR4", LMSC-D243605, Lockheed Missiles and Space Company, Inc., Sunnyvale, California, March 1972.

2.13 Wozniak, R.S., and Mitchell, W.W., "Basis of Seismic Design Provisions for Welded Steel Oil Storage Tanks, Proposed Appendix P to API Standard 650", API Convention, Toronto, Canada, May 1978.

2.14 Miller, C.D., "Buckling of Axially Compressed Cylinders", Journal of the Structural Division, ASCE, Vol. 103, No. ST3, March 177, pp.695-721.

CHAPTER 3 SCALE TANK MODEL

3.1 INTRODUCTION

When investigating structural systems there are two classes that may be distinguished. The first is that for which an explicit formulation of the response function is available and the structural response can be computed directly. On the other hand, if the structures are too complicated to determine a solution of the response function then the response of these structures may be found by conducting an experiment. Most civil structures are of such dimensions that it is impossible to carry out full scale experiments and laboratory models must be used. The experimental models are small relative to the prototype and cost less to build. The problem of liquid storage tanks under earthquake excitation is one of the second type of structural systems. The complexities of this problem include: a thin shell structure, multiple dynamic response modes - axial and circumferential modes of shell and the sloshing modes of the fluid, geometric initial imperfections, end conditions, nonlinear sloshing behavior and shell vibration, buckling criteria, etc.

The method of dimensional analysis provides a unifying tool to design an appropriate scale model to simulate the prototype structure, failure properties, and system variables. The methods of dimensional analysis are based on the principle of dimensional homogeneity, i.e., an equation expressing a

physical relationship between quantities must be dimensionally homogeneous. The former methods were probably started by Lord Rayleigh [3.1] and improved upon by Buckingham [3.2] with a broad generalization known as the "π-theorem". In general terms, the Buckingham Pi Theorem states that the number of dimensionless and independent quantities required to express a relationship among the variables in any phenomenon is equal to the number of quantities involved, minus the number of dimensions in which those quantities may be measured. The details of the dimensional analysis and some of its appications can be found in any textbook on dimensional analysis and similitude [3.3, 3.4, 3.5]. This chapter will present a general similitude analysis for seismic excitation and response of an elastic cylindrical tank containing a liquid with a free surface. The adequacy of the scale modeling used in the experimental work is discussed.

3.2 SCALING

Scale model dynamic response tests on fluid filled tanks have been carried out previously [3.6, 3.7, 3.8] and the appropriate scaling laws discussed. The primary objective of these tests was response (stress, deflection, surface motion, etc.) not buckling. It appears appropriate to review the scaling since the buckling of shells involves both extension and bending effects not considered in some of those previous studies.

The nondimensional relation between response quantities and experimental parameters is derived formally using the Buckingham "π-Theorem". If the radius, R, liquid density, ρ_ℓ, and the acceleration of gravity, g, are chosen as the basic parameters, this relation may be written as follows

$$\left\{T_t\sqrt{\frac{g}{R}},\ \frac{\sigma}{\rho_\ell gR},\ \frac{w}{R},\ T_{\ell s}\sqrt{\frac{g}{R}},\ \frac{\eta}{R},\ \frac{P}{\rho_\ell gR}\right\} \tag{3.1}$$

$$= F\left\{\frac{h}{R},\ \frac{t_s}{R},\ \frac{H}{R},\ \frac{E}{\rho_\ell Rg},\ \frac{\ddot{x}_g}{g},\ T_e\sqrt{\frac{g}{R}},\ \zeta,\ \nu,\ \frac{\mu}{\rho_\ell g^{1/2}R^{3/2}},\ \frac{\rho_s}{\rho_\ell}\right\}$$

where

E = Young's modulus ($\underline{M}\underline{L}^{-1}\underline{T}^{-2}$)

g = acceleration of gravity ($\underline{L}\underline{T}^{-2}$)

h = tank height ($\underline{L}$)

H = liquid height ($\underline{L}$)

P = pressure ($\underline{M}\underline{L}^{-1}\underline{T}^{-2}$)

R = tank radius ($\underline{L}$)

t_s = tank thickness ($\underline{L}$)

T_e = earthquake duration or typical period ($\underline{T}$)

$T_{\ell s}$ = liquid sloshing period ($\underline{T}$)

T_t = tank vibration period ($\underline{T}$)

w = tank wall displacement ($\underline{L}$)

$\ddot{x}_g$ = base acceleration ($\underline{L}\underline{T}^{-2}$)

ζ = structural damping ratio (nondimensional)

η = sloshing dipslacement of liquid surface ($\underline{L}$)

μ = viscosity ($\underline{M}\underline{L}^{-1}\underline{T}^{-1}$)

ν = Poisson's ratio (nondimensional)

ρ_ℓ = liquid density ($\underline{ML}^{-3}$)

ρ_s = tank density ($\underline{ML}^{-3}$)

σ = tank stress ($\underline{ML}^{-1}\underline{T}^{-2}$)

$\underline{L}$ = dimension of Length

$\underline{M}$ = dimension of Mass

$\underline{T}$ = dimension of Time

The nondimensional quantities can be combined to produce other quantities that may be more appropriate in some instances. If the parameters are the same in both scale model and prototype then the response of the prototype can be predicted from the observed results of the scale model test. Unfortunately it is extremely difficult (if not impossible) to have complete similitude between model and prototype and it is necessary to justify the inconsistencies.

To begin the discussion it will be assumed that the geometry of the tank is preserved in the scaling. Therefore

$$\left(\frac{h}{R}\right)_m = \left(\frac{h}{R}\right)_p, \quad \left(\frac{t_s}{R}\right)_m = \left(\frac{t_s}{R}\right)_p, \quad \left(\frac{H}{R}\right)_m = \left(\frac{H}{R}\right)_p$$

The length scale factor L_s is then

$$\frac{R_p}{R_m} = L_s$$

If the model is tested in a "1g" field and the fluid used in the model is the same as in the prototype

$$g_m = g_p, \quad \rho_{\ell m} = \rho_{\ell p} \text{ and } \mu_m = \mu_p$$

The fourth quantity in the right hand side of equation (3.1) then requires

$$\left(\frac{E}{\rho_\ell Rg}\right)_m = \left(\frac{E}{\rho_\ell Rg}\right)_p$$

it implies

$$E_p/E_m = R_p/R_m = L_s$$

If the scale factor is to be large (so that a small model can be used), the material for the model must have a low modulus. This is one of the reasons for the use of a plastic (Mylar) model.

The next four quantities on the right hand side of equation (3.1) show that

a) the excitation level for model and prototype should be the same.

b) the time scale of the seismic excitation should be scaled by $\sqrt{L_s}$

c) the structural damping should be the same

d) Poisson's ratio should be the same.

Except for the usual difficulty with structural damping, the scaling of these four factors can be accomplished. More difficulty is encountered with the next two.

The next quantity is a disguised Reynold's number, R_e. If a velocity, $\bar{u}$, is formed from $\bar{u} \sim \eta/T_{\ell s}$

$$\left[\frac{\mu}{\rho_\ell g^{1/2} R^{3/2}}\right]_{p/m} = \left[\frac{\mu}{\rho_\ell g^{1/2} R^{3/2}} \frac{R}{\eta} \frac{T_{\ell s} g^{1/2}}{R^{1/2}}\right]_{p/m} =$$

$$= \left[\frac{\mu}{\rho_\ell \bar{u} R}\right]_{p/m} = \left[\frac{1}{R_e}\right]_{p/m}$$

then the nature of this term is clear. Since the same fluid is used in model and prototype, the Reynold's number is off by $(L_s)^{3/2}$. This lack of similitude is not important for the problem at hand. An order of magnitude estimate of the viscous effect can be made by looking at the wall shear stress τ. Assuming the free surface motion, near the tank wall, is

$$\eta(t) = \eta_0 \sin\omega_n t$$

where η_0 is the maximum free surface displacement

ω_n is the sloshing frequency of the liquid

Then the velocity of the free surface motion $\bar{u}(t)$ will be

$$\bar{u}(t) = \eta_0 \omega_n \cos\omega_n t$$

Therefore, the shear stress τ can be expressed as follows.

$$\tau = 2\mu\varepsilon = 2\mu \frac{\partial \bar{u}}{\partial x} \sim \frac{2\mu\eta_0\omega_n}{\sqrt{\mu/(\rho_\ell \omega_n)}} = 2\rho_\ell \eta_0 \sqrt{\mu/\rho_\ell}\, \omega_n^{3/2}$$

where ε is the shear strain and $\sqrt{\mu/(\rho_\ell \omega_n)}$ has the same dimension as the boundary layer length. In the range of interest the shear stress τ is proportional to $\sqrt{\mu}$ (or $1/\sqrt{R_e}$)

and for one of the full scale tanks considered in this study (R = 102 in., H = 404 in.)

$$\frac{\tau}{\rho_\ell g \eta_0} \sim \frac{2\sqrt{\mu}\omega_n^{3/2}}{g\sqrt{\rho_\ell}} = 0.00096$$

This implies that the shear stress at the wall is much less than the change in the hydrostatic pressure $\rho g \eta_0$ due to the sloshing of liquid. This pressure is in turn smaller than the pressure resulting from the excitation. Scaling down to the model reduces the Reynolds number but the viscous effects are still unimportant.

The last term on the right hand side of equation (3.1) will not be equal in the model and prototype. The question that must be answered is how does this lack of similitude effect the response parameters in the left hand side of equation (3.1).

The first response parameter on the left hand side of equation (3.1) represents the nondimensional period of the tank vibration. This can be converted as follows

$$\left[T_t\sqrt{\frac{g}{R}}\right]_{p/m} = \left[T_t\sqrt{\frac{g}{R}\frac{E}{\rho_\ell Rg}}\right]_{p/m} = \left[T_t\sqrt{\frac{E}{\rho_\ell}}\frac{1}{R}\right]_{p/m}$$

The period of a full tank with simply support boundary condition at top and bottom has been calculated in ref. 3.9. This one term approximation for the lowest axial mode (m=1) is as follows:

$$T_t\sqrt{\frac{E}{\rho_\ell}}\frac{1}{R} = \left\{ \frac{\left[\frac{\rho_s}{\rho_\ell} + \frac{R}{t_s}\frac{I_n(\lambda_o)}{\lambda_o I'_n(\lambda_o)}\right]4\pi^2(1-\nu^2)}{\frac{(1-\nu^2)\lambda_o^4}{(n^2+\lambda_o^2)^2} + \frac{t_s^2}{12R^2}(n^2+\lambda_o^2)^2 + \frac{1-\nu^2}{2}n^2\left(\frac{\rho_\ell gR}{E}\right)\left(\frac{h}{t_s}\right)} \right\}^{1/2} \quad (3.2)$$

where

I_n = modified Bessel function of order n

λ_o = $\pi R/h$

n = circumferential wave number

From equation (3.2), the ratio of the tank vibration period of the prototype to that of the scale model can be expressed

$$\left[T_t\sqrt{\frac{E}{\rho_\ell}}\frac{1}{R}\right]_{p/m} = \left[\frac{\rho_s}{\rho_\ell} + \frac{R}{t_s}\frac{I_n(\lambda_o)}{\lambda_o I'_n(\lambda_o)}\right]^{1/2}_{p/m} \quad (3.3)$$

If $\frac{\rho_s}{\rho_\ell} << \frac{R}{t_s}\frac{I_n(\lambda_o)}{\lambda_o I'_n(\lambda_o)}$ then the density ratio dismatch between the model and prototype is not important in the frequency term. This is demonstrated in Table 3.1 where the ratio of tank natural period is listed for a tank used in the experimental work. The results indicate that the difference is less than 3% up to n= 10.

The next two terms on the left hand side of equation (3.1) are the normalized stress and the normalized tank wall displacement. The influence of mismatched tank density on these

two terms will be small since this effect on the natural period of tank is small.

The sloshing period and the free surface displacement of a fluid in a flexible tank are almost identical to those of a rigid tank [3.10]. Ref. 3.11 also shows that the pressure acting on the tank wall is independent of the tank density. These results point out that the mismatch of the tank density does not have a great influence on the last three terms on the left hand side of equation (3.1).

TABLE 3.1

EFFECT OF SHELL MASS ON NATURAL FREQUENCY

R/t = 833	R/h = 0.234 H/h = 1.0
Equ. (3.3)	Circumferential Wave Number, n
1.006	2
1.012	4
1.014	6
1.021	8
1.025	10

3.3 SUMMARY

Most prototype tanks are fabricated from steel which has an elastic modulus of about 30×10^6 psi and Poisson's ratio of about 0.3. Consideration of laboratory size models

and inexpensive cost of specimens led to the selection of Mylar A sheet as the test tank material. This material has modulus of about 7.3×10^5 psi and Poisson's ratio of about 0.3 (ref. 3.12). Therefore, the length scale factor $L_s = E_p/Em \simeq 41$; i.e., all geometric dimensions of the model must be 1/41 the corresponding prototype dimension. The terms on the right hand side of equation (3.1) are nondimensional system parameters. The scaling requirements for these system parameters are summarized as follows.

(1) All the geometry of the tank should be scaled by $L_s = 41$.

(2) The model is tested in a "1g" field and the fluid in the model is the same as in the prototype.

(3) The structural damping and the Poisson's ratio should be the same.

(4) The excitation level for model and prototype should be the same.

(5) The time scale of seismic excitation should be scaled by factor $\sqrt{L_s} = 6.4$.

(6) The viscosity should be scaled by factor $L_s^{3/2} = 262$.

(7) The tank density should be the same.

Although the requirements on the viscosity and the tank density are not satisfied, no significant effect on the results is anticipated. The terms on the left hand side of equation (3.1) are normalized response functions. The predicted relation for prototype response can also be summarized as follows.

(1) The prototype tank vibration period and the liquid sloshing period should be $\sqrt{L_s}$(=6.4) times the observed periods of the model respectively.

(2) The pressure and the tank stress should be L_s(=41) times the measured values in the model respectively.

(3) The sloshing displacement of free surface and tank wall displacement should be L_s(=41) times the observed values in the model respectively.

3.4 CONCLUSIONS

Brief discussion of dimensional analysis points out the fact that it is difficult to model all behavior in one subscale model. To design a successful subscale model, the physical phenomenon must be understood and isolated so that it is correctly modeled. For instance, the importance of tank flexibility on tank stresses may be studied from two standpoints. First, the static stiffness of the tank may be modeled as in ref. 3.8. Second, to include the "dynamic" stiffness, both the fluid (sloshing) frequencies and the tank frequencies should be modeled. This model study has shown that small plastic models can be useful in studying the dynamic response and buckling of liquid filled tanks under base excitation even though the model does not display complete similitude.

REFERENCES - CHAPTER 3

3.1 Lord Rayleigh, "Stability of Flow of Fluids and Investigations in Capillarity", Phil. Mag., Vol.34, No.59, 1892.

3.2 Buckingham, E., "Model Experiments and the Forms of Empirical Equations", Trans. ASME, Vol.37, 1915, pp. 263.

3.3 Murphy, G., Similitude in Engineering, The Ronald Press Co., New York, 1950.

3.4 Bridgman, P.W., Dimensional Analysis, Yale University Press, 1931.

3.5 Duncan, W.J., Physical Similarity and Dimensional Analysis, Edward Arnold & Co., 1955.

3.6 Kana, D.D., and Dodge, F.T., "Design Support Modeling of Liquid Slosh in Storage Tanks Subject to Seismic Excitation", ASCE Specialty Conference on Structural Design of Nuclear Plant Facilities, Dec. 1975.

3.7 Kana, D.D., "Seismic Response of Flexible Cylindrical Liquid Storage Tanks", Nuclear Engineering and Design, Vol. 52, 1979, pp. 185-199.

3.8 Clough, D.P., "Experimental Evaluation of Seismic Design Methods for Broad Cylindrical Tanks", University of California, Berkeley, Earthquake Engineering Research Center Report No. UCB/EERC-77/10, May 1977.

3.9 Mixson, J.S. and Herr, R.W., "An Investigation of the Vibration Characteristics of Pressurized Thin-Walled Circular Cylinders Partly Filled with Liquid", NASA TR R-145, 1962.

3.10 Haroun, M.A., "Dynamic Analysis of Liquid Storage Tanks", Ph.D. Dissertation, California Institute of Technology, Pasadena, California, December 1979.

3.11 Yang, J.Y., "Dynamic Behavior of Fluid-Tank Systems", PhD Dissertation, Rice University, Houston, Texas, March 1976.

3.12 Weingarten, V.I., Morgan, E.J. and Seide, P., "Final Report on Development of Design Criteria for Elastic Stability of Thin Shell Structures", SIL/TR-60-0000-19425, Space Technology Laboratories, Inc., Los Angeles California, Dec. 1960.

CHAPTER 4 BUCKLING TESTS OF ANCHORED TANKS UNDER EARTHQUAKE EXCITATION

The first part of the experimental program is appropriate to the full size tanks supported so as to prevent an occurrence such as uplifting. This study will not address the problem of foundation/structure interaction. This chapter describes an experimental program, which includes static and dynamic (harmonic and transient) buckling tests for the anchored tank models subjected to simulated earthquake loading. Resonance tests are also conducted and compared with the analytical results from the energy method.

4.1 STATIC BUCKLING TEST

4.1.1 INTRODUCTION

The problem of predicting the critical buckling stresses of a cylindrical tank is complicated by two factors. The first is that the stress distribution in the tank wall prior to buckling is fairly complicated and closed form buckling solutions are not available. The second difficulty is that the buckling analysis will predict the buckling condition of the perfect tank structure. The actual buckling stress will be less than this, the difference depending upon the magnitude and shape of the initial geometric inperfections of the tank wall [4.1, 4.2]. The ratio of actual critical

stress to calculated critical stress is known as the "knock-down" factor. This knockdown factor is found from buckling tests for the shell/load combination of interest. Unfortunately, test data exist only for simple geometry and simple loading conditions [4.3, 4.4]. For complicated loads the usual procedure is to use the results for simple conditions that somehow represent the more complex actual condition. It is this part of the failure prediction that will be addressed in this section.

In order to experimentally examine the buckling criterion for a tank, the appropriate pressure distribution must be simulated in the laboratory. This can be accomplished by shaking a fluid filled model tank, but the experiment is complicated. A more desirable method for isolating the buckling problem is to simulate statically the pressure distribution. This cannot be done exactly but the stresses resulting in a partially filled inclined tank is a satisfactory approximation as will be subsequently shown.

4.1.2 APPROACH

The pressure acting on the wall of a fluid filled tank excited by ground acceleration $\ddot{x}_g(t)$ can be calculated using a hierarchy of simplifying assumptions. The assumptions of an inviscid, incompressible fluid, a linearized free surface boundary condition and a rigid tank lead to the following pressure distribution acting on the tank wall (see Appendix A)

$$P(R,\theta,z,t) = -\rho_\ell \ddot{x}_g(t) R\cos\theta \left\{1 - \sum_{n=1}^{\infty} \frac{2}{(\xi_n^2-1)} \frac{\cosh[\xi_n(z+H)/R]}{\cosh(\xi_n H/R)}\right\} -$$

$$\rho_\ell R\cos\theta \sum_{n=1}^{\infty} \frac{2}{(\xi_n^2-1)} \frac{\cosh[\xi_n(z+H)/R]}{\cosh(\xi_n H/R)} \int_0^t \omega_n \ddot{x}_g(\tau)\sin\omega_n(t-\tau)d\tau \tag{4.1}$$

where $\xi_{n's}$ are the roots of $J_1'(\xi_n)=0$, $\omega_{n's}$ are the frequencies of the sloshing modes of free surface liquid given by

$$\omega_n^2 = \frac{g\xi_n}{R} \tanh\left(\frac{\xi_n H}{R}\right) \tag{4.2}$$

The loading condition and nomenclature are shown in fig.4.1.

The first term in equation (4.1) is the so called impulsive pressure and the second term, which represents the pressure resulting from fluid sloshing, is the convective term. These two contributions are fairly well separated in time due to the long periods of sloshing as compared to the ground acceleration periods expected in a region of strong motion. Only the impulsive term will be considered in this section.

The stress distribution in the tank wall can now be calculated using the impulsive term only. This task is further simplified by using membrane theory which provides a good approximation to the actual stresses at some distance from the wall/bottom intersection. These stresses can be expressed as follows

$$N_z = \rho_\ell \ddot{x}_g(t)\cos\theta\left[\frac{z^2}{2} - \sum_{n=1}^{\infty} \frac{2}{\xi_n^2-1} \frac{R}{\xi_n} \frac{\frac{R}{\xi_n}\left[\cosh\frac{\xi_n(z+H)}{R} - \cosh\frac{\xi_n H}{R}\right]}{\cosh(\xi_n H/R)} - \frac{z\sinh\frac{\xi_n H}{R}}{\cosh(\xi_n H/R)}\right\} \tag{4.3a}$$

$$N_\theta = -\rho_\ell g R z - \rho_\ell \ddot{x}_g(t) R^2 \cos\theta \{1 - \sum_{n=1}^{\infty} \frac{2}{\xi_n^2 - 1} \frac{\cosh(\xi_n(z+H)/R)}{\cosh(\xi_n H/R)}\} \quad (4.3.b)$$

$$N_{z\theta} = -\rho_\ell \ddot{x}_g(t) R \sin\theta \{z - \sum_{n=1}^{\infty} \frac{2}{\xi_n^2 - 1} \frac{R}{\xi_n} \frac{\sinh(\xi_n(z+H)/R) - \sinh(\xi_n H/R)}{\cosh(\xi_n H/R)}\} \quad (4.3.c)$$

The stresses for the inclined tank problem (fig. 4.1) can also be calculated using membrane theory [4.5]. These results are as follows

$$N_z = \frac{1}{2}\rho_\ell g \sin\alpha \{(z^2 + \frac{R^2 \tan^2\alpha}{4})\cos\theta + 2Rz\tan\alpha\cos 2\theta + \frac{3R^2\tan^2\alpha}{4}\cos 3\theta\} \quad (4.4.a)$$

$$N_\theta = -\rho_\ell g R(z\cos\alpha + R\sin\alpha\cos\theta) \quad (4.4.b)$$

$$N_{z\theta} = \rho_\ell g R \sin\alpha \sin\theta (R\tan\alpha\cos\theta + z) \quad (4.4.c)$$

In order to compare these two stress distributions, $\ddot{x}_g(t)$ is chosen such that N_z at $\theta=\pi$, $z=-H$ is the same in both cases. The comparisons as a function of θ are shown in fig.4.2 for three different inclined angles. The comparison gets worse as the tilt angle α increases but the important compressive region is reasonably simulated up to $\alpha=40^o$. The axial variation of N_z at $\theta=\pi$ is indistinguishable for the two cases. A typical variation is shown in fig.4.3. The comparison of the resultant hoop stress N_θ at $\theta=\pi$, $z= -H$, at the chosen $\ddot{x}_g(t)$, is also shown in table 4.1 for three different inclined angles.

TABLE 4.1 Comparison of N_θ at $\theta=\pi$, z= -H			
α	30^o	40^o	50^o
R_{N_θ}	1.018	1.044	1.100

where

$$R_{N_\theta} = \frac{\text{Hoop Stress in Impulsive Pressure Case}}{\text{Hoop Stress in Inclined Tank Case}}$$

The stress comparisons while not exact are sufficiently close that the experimental simulation to be used to test the buckling criterion seems reasonable.

The next problem to be addressed is the knockdown factor appropriate for the model structures. Since the proposed procedure for predicting the buckling of the inclined cylinder uses the result of a uniformly loaded cylinder, this problem can be circumvented. This is done by testing the same cylinder under the two loading conditions (uniform internal pressure and axial load/inclined tank load). Since the tank has the same imperfection for both tests the effect of imperfection is automatically incorporated into the comparison of the two results.

4.1.3 EXPERIMENT

The model tanks were constructed of 5 mil Mylar with a lap bonded seam. The ends were plotted into aluminum end plates. The uniform load tests were conducted using internal pressure (air) and a centrally located axial load applied to the upper end plate. The details have been described in

chapter 2. The inclined tank tests were conducted by tipping the bottom plate to a desired angle (α) and slowly filling the tank with water until buckling occurred. The buckling was followed by the collapse of the tank. Two wires were used to hang up the top plate of the tank after buckling occurred so that the same tank can be tested many times. The buckling pattern is the typical elastic buckling shape -diamond shape (fig.4.4). It is interested to note that the long wavelength type deformation (axisymmetric mode shape) could be felt, by touching the tank wall near the bottom, prior to the buckling occurred. As the load was increased the shell snapped into a diamond shaped buckling pattern. The ring shaped deformation can be observed more clearly in ref. 4.6.

4.1.4 RESULTS

The uniform loading results for two models tested and the dimensions of these models are shown in figure 4.5. The increase of critical stress with increasing internal pressure is typical for this type of testing although analytical results for perfect shell do not show this trend [4.7]. The prediction of the critical condition for the inclined test was done by first calculating the stresses at the toe of the tank ($z=-H$, $\theta=\pi$). Assuming this stress is uniformly distributed around the tank and along its length, the critical condition can be found. This result, as well as the results of the inclined tank test are shown in fig. 4.6 as a function of inclined angle α. It should be pointed out that the axial stress due to the bending

moment generated by the top aluminum plate (its weight is approximate 2.8 lb) has been included in all the predicted results. The ordinant of this figure is the depth to which the tank must be filled to cause buckling. The prediction from the uniform loading result is much lower than the experimental results. The critical condition of a perfect shell can be predicted using the classical buckling criterion instead of the uniform loading result. This result is also shown in figure 4.6 and it indicates that this assumption (perfect cylinder) still gives a conservative prediction.

Furthermore if we take the axial nonuniform stress distribution into consideration and assume it is uniform around the circumference, the predicted result can be plotted as a dashed line in figure 4.6. This result is based on the assumption that the maximum allowable stress in the tank wall is 1.24 times the classical buckling stress as discussed in section 2.3. The results show that the predicted result based on the assumption of a perfect cylinder and the consideration of the nonuniformity effect gives a good agreement with the experimental results.

Since $\ddot{x}_g(t)$ is chosen such that N_z at $\theta=\pi$, $z=-H$ is the same in both the impulsive case and the inclined test, the critical ground acceleration of a tank with a fixed water depth can be correlated to the corresponding critical inclined angle of the same tank through equations (4.3a) and (4.4a). Thus, the results in figure 4.6 can be replotted as shown in figure 4.7, indicating the required ground acceleration to

cause buckling for different water depths in the tank. The membrane stresses calculated from the membrane theory have been used to determine the stresses developed in both cases.

In order to determine the effect of the bending stresses in the inclined tests, the computer program BØSØR4 [4.8] has been applied to calculate the bending stresses as well as the membrane stresses for the inclined test. One of the results is shown in figure 4.8. It indicates that the membrane stresses calculated both from membrane theory and BØSØR4 numerical program are almost the same and the bending stress is significant only in a very small boundary layer near the wall/bottom interaction as shown in figure 4.8. The effect of the prebuckling bending stress in the boundary layer has been the subject of much research [4.9]. It was found that the effect for the clamped boundary condition was approximately 7%. However, this reduction in critical stress from the classical buckling stress is so small that it is never a predominant consideration. Other effects such as initial imperfections are so dominate that the details of boundary conditions rarely become important. For the case at hand it is believed that the same situation prevails.

4.1.5 CONCLUSION

Comparison of the results shows that the commonly used buckling criterion for the problem is somewhat conservative. The prediction, based on the perfect tank assumption and the consideration of the nonuniformity effect, gives

good agreement with the experimental results. This no doubt results from the localized natural of buckling in the inclined tank problem as opposed to the global buckling of the uniformly loading case. A similar situation exists when comparing pure bending and axial compression buckling. The difference in these cases is thought to result since the nonuniform loading case may not involve the most imperfect part of the shell.

4.2 FREE VIBRATION OF FLUID FILLED CYLINDRICAL TANKS

4.2.1 INTRODUCTION

Knowing the natural frequencies and the associated mode shapes is the first step to analyze the forced vibration problem. The dynamic characteristics of fluid filled tank have been studied by many investigators [4.10-4.18]. Among these analytical techniques, the energy method seems to be the most practical and simplest technique to derive the dynamic characteristics of the fluid filled tanks. This method has been applied in refs. 4.10-4.12, but the hydrostatic prestress effect is neglected in the derivation of the strain energy and no experimental results are available to compare with this analytical method. This section deals with the free vibration problem of a liquid filled tank which has a fixed bottom and free top. The axial mode shape function of this cylinder is assumed to be the linear combination of the cantilever beam modes. In addition, the nonlinear term in

the strain-displacement relation is used to account for the hydrostatic prestress effect. The approximate virtual mass is applied to simplify the derivation of the kinetic energy of the liquid inside the tank. Experimental work is also carried out to compare with the analytical results.

4.2.2 SHELL VIBRATION

The natural modes of a circular cylindrical shell can be defined by two integers m (roughly the number of half-waves in axial direction) and n (the number of full waves in the circumferential direction). Typical wave patterns are illustrated in figure 4.9. For any given pair of (m,n), there exist three distinct vibration modes and associated frequencies. Among these three modes the radial transverse mode is predominant and corresponds to the lowest natural frequency [4.19]. The n=0 modes are sometimes referred to as breathing modes. The n=1 mode shape looks like the bending mode of the tank as a beam in which the cross section does not deform during vibration. For higher circumferencial modes the bending energy is predominant and insensitive to the number of axial waves. The axial mode shapes for a cylinder fixed at one end and free at the other end can be represented satisfactorily by the cantilever beam modes. A sketch of a cylinder with the coordinate system is shown in figure 4.10.

4.2.3 DEFLECTION FUNCTIONS

The expressions assumed for the displacements u,v and w are as follows

$$u = \cos n\theta \sum_{i=1}^{N} \bar{U}_i(t)\psi_i(x)$$

$$v = \sin n\theta \sum_{i=1}^{N} \bar{V}_i(t)\phi_i(x) \qquad (4.5)$$

$$w = \cos n\theta \sum_{i=1}^{N} \bar{W}_i(t)\phi_i(x)$$

where $\psi_i(x)$ and $\phi_i(x)$ are admissible functions which satisfy the geometric boundary condition of the shell, $\bar{U}_i(t)$, $\bar{V}_i(t)$ and $\bar{W}_i(t)$ are functions of time and N is the number of functions considered. The deflection function w is assumed to be the same form as that of a cantilever beam during flexural vibration and $\psi_{i's}$ are taken as the first derivative of $\phi_{i's}$. These functions are given [4.20] by

$$\phi_i(x) = \cosh(\lambda_i x) - \cos(\lambda_i x) - k_i[\sinh(\lambda_i x) - \sin(\lambda_i x)] \qquad (4.6)$$

$$\psi_i(x) = \sinh(\lambda_i x) + \sin(\lambda_i x) - k_i[\cosh(\lambda_i x) - \cos(\lambda_i x)]$$

where k_i is given by

$$k_i = [\cosh(\lambda_i L) + \cos(\lambda_i L)]/[\sinh(\lambda_i L) + \sin(\lambda_i L)] \qquad (4.7)$$

and L is the length of the tank, $\lambda_i L$ = 1.875, 4.694, 7.855, 10.137,..., etc., i= 1, 2, 3, ... corresponding to axial first mode, second mode, ..., etc.. These functions satisfy

the geometric boundary conditions at the bottom of the tank:

$$u= v= w= \frac{\partial w}{\partial x} = 0$$

4.2.4 POTENTIAL ENERGY AND KINETIC ENERGY

The potential energy of this fluid filled tank can be expressed in terms of the displacements and is given [see Appendix B] by

$$V= \frac{Et_s}{2(1-\nu^2)} \int_0^{2\pi} \int_0^L \Bigg[\left(\frac{\partial u}{\partial x}\right)^2 + \frac{1}{R^2} \left(\frac{\partial v}{\partial \theta} - w\right)^2 + \frac{2\nu}{R} \frac{\partial u}{\partial x}\left(\frac{\partial v}{\partial \theta} - w\right) + \frac{1-\nu}{2}\left(\frac{1}{R} \frac{\partial u}{\partial \theta} + \frac{\partial v}{\partial x}\right)^2 \Bigg] R \, dx \, d\theta + \frac{Et_s^3}{24(1-\nu^2)} \int_0^{2\pi} \int_0^L \Bigg[\left(\frac{\partial^2 w}{\partial x^2}\right) + \frac{1}{R^4}\left(\frac{\partial^2 w}{\partial \theta^2} + \frac{\partial v}{\partial \theta}\right)^2 + \frac{2\nu}{R^2} \frac{\partial^2 w}{\partial x^2}\left(\frac{\partial^2 w}{\partial \theta^2} + \frac{\partial v}{\partial \theta}\right) + \frac{2(1-\nu)}{R^2}\left(\frac{\partial^2 w}{\partial x \partial \theta} + \frac{\partial v}{\partial x}\right)^2 \Bigg] R dx d\theta + \rho_\ell g R \int_0^{2\pi} \int_0^D (D-x) \Bigg[\frac{1}{R} \frac{\partial v}{\partial \theta} - \frac{w}{R} + \frac{1}{2R^2}\left(\frac{\partial^2 u}{\partial \theta^2} + \frac{\partial^2 v}{\partial \theta^2} + \frac{\partial^2 w}{\partial \theta^2}\right) \Bigg] R \, dx \, d\theta \qquad (4.8)$$

The first, second, and third integral expressions in equation (4.8) represent the stretching energy of the middle-surface deformation, the bending energy of the finite-thickness shell wall and change of the strain energy due to hydrostatic prestress, respectively.

The kinetic energy of the cylindrical tank wall is given by

$$T_s = \frac{\rho_s t_s}{2} \int_0^{2\pi} \int_0^L (\dot{u}^2 + \dot{v}^2 + \dot{w}^2) R \, dx \, d\theta \qquad (4.9)$$

and the kinetic energy of the fluid can also be derived as shown in refs. 4.12 and 4.13. In this section the virtual mass of the fluid, per unit area of shell surface, is used to simplify the derivation of the kinetic energy of the fluid inside the tank. The kinetic energy of the fluid can be expressed in terms of the radial displacement of the shell [4.11]

$$T_\ell = \frac{m_{vn}}{2} \int_0^{2\pi} \int_0^D \dot{w}^2 R \, dx \, d\theta \tag{4.10}$$

The virtual mass of the fluid, m_{vn}, may be considered as the added mass on the tank wall to take into account the fluid in the tank. Assuming the virtual mass of the fluid for a tank fixed at bottom end and free on the top end is the same as that of a tank with simply supported bottom end and free top end, the virtual mass of the fluid can be expressed by

$$m_{vn} = C_{vn} \rho_\ell R \tag{4.11}$$

where C_{vn} is the virtual mass coefficient which can be given [4.10] by

$$C_{vn} = \frac{1}{n} \left\{ 1 - \sum_{i=1}^{\infty} \frac{6R^2 n \left[1 - \frac{2R}{\alpha_{ni} D} \tanh(\alpha_{ni} D/(2R)) \right]}{\alpha_{ni}^2 D^2 (\alpha_{ni}^2 - n^2)} \right\} -$$

$$\sum_{i=1}^{\infty} \frac{6R \tanh(\alpha_{ni} D/R)}{\alpha_{ni} D(\alpha_{ni}^2 - n^2)} \left[1 - \frac{R}{2\alpha_{ni} D \tanh(\alpha_{ni} D/R)} + \frac{R}{2\alpha_{ni} D \sinh(\alpha_{ni} D/R)} \right.$$

$$\left. - \frac{R \tanh(\alpha_{ni} D/(2R))}{2\alpha_{ni} D} \right]^2 \tag{4.12}$$

and α_{ni} are the roots of $J_n'(\alpha_{ni})$. J_n is the Bessel's function of order n. Equation (4.12) shows that C_{vn} depends on the water depth ratio, D/R, and the circumferential wave number, n, only. It has been plotted as shown in figure 4.11. The total kinetic energy is the sum of equations (4.9) and (4.10) and given by

$$T = \frac{\rho_s t_s}{z} \int_0^{2\pi} \int_0^{L} (\dot{u}^2+\dot{v}^2+\dot{w}^2) R \, dx \, d\theta + \frac{m_{vn}}{2} \int_0^{2\pi} \int_0^{D} \dot{w}^2 R \, dx \, d\theta \qquad (4.13)$$

4.2.5 FREQUENCY EQUATION

Substituting the displacement equations (4.5) into the equations (4.8) and (4.13), the potential energy and the kinetic energy can be expressed in terms of the displacement amplitudes $\bar{U}_i(t)$, $\bar{V}_i(t)$ and $\bar{W}_i(t)$. As $\bar{U}_i(t)$, $\bar{V}_i(t)$ and $\bar{W}_i(t)$ are independent variables, they may be taken as generalized coordinates and the Lagrange equation applied. The equation of motion can be derived from Lagrange equation

$$\begin{aligned}
\frac{d}{dt}\left[\frac{\partial T}{\partial \dot{\bar{U}}_i(t)}\right] + \frac{\partial V}{\partial \bar{U}_i(t)} &= 0 \\
\frac{d}{dt}\left[\frac{\partial T}{\partial \dot{\bar{V}}_i(t)}\right] + \frac{\partial V}{\partial \bar{V}_i(t)} &= 0 \qquad (4.14) \\
\frac{d}{dt}\left[\frac{\partial T}{\partial \dot{\bar{W}}_i(t)}\right] + \frac{\partial V}{\partial \bar{W}_i(t)} &= 0
\end{aligned}$$

Assuming the simple harmonic motion, $\ddot{\bar{U}}_i(t) = -\omega^2\bar{U}_i$, $\ddot{\bar{V}}_i(t) = -\omega^2\bar{V}_i(t)$, $\ddot{\bar{W}}(t) = -\omega^2\bar{W}(t)$, the results can be expressed as follows

$$\begin{bmatrix} \underset{\sim}{D}^2 - \omega^2\underset{\sim}{A} & \underset{\sim}{E} & \underset{\sim}{F} \\ \underset{\sim}{E} & \underset{\sim}{G} - \omega^2\underset{\sim}{B} & \underset{\sim}{H} \\ \underset{\sim}{F} & \underset{\sim}{H} & \underset{\sim}{I} - \omega^2\underset{\sim}{C} \end{bmatrix} \begin{Bmatrix} \underline{\bar{U}} \\ \underline{\bar{V}} \\ \underline{\bar{W}} \end{Bmatrix} = 0 \qquad (4.15)$$

where

$$\underline{\bar{U}} = \{\bar{U}_1, \bar{U}_2, \bar{U}_3, \ldots\}^T$$

$$\underline{\bar{V}} = \{\bar{V}_1, \bar{V}_2, \bar{V}_3, \ldots\}^T$$

$$\underline{\bar{W}} = \{\bar{W}_1, \bar{W}_2, \bar{W}_3, \ldots\}^T$$

and

$$A_{ij} = \frac{\rho_s t_s R}{2} \langle\psi_i\psi_j\rangle$$

$$B_{ij} = \frac{\rho_s t_s R}{2} \langle\phi_i\phi_j\rangle$$

$$C_{ij} = \frac{\rho_s t_s R}{2} \langle\phi_i\phi_j\rangle + \frac{C_{vn}\rho_\ell R^2}{2} \langle\langle\phi_i\phi_j\rangle\rangle$$

$$D_{ij} = \frac{Et_sR}{2(1-\nu^2)}\{\langle\psi_i'\psi_i'\rangle + \frac{1-\nu}{2}\frac{n^2}{R^2}\langle\psi_i\psi_j\rangle\} + \frac{\rho_\ell g}{2}\{n^2\langle\psi_i\psi_j\rangle_D\}$$

$$E_{ij} = \frac{Et_sR}{2(1-\nu^2)}\{\frac{\nu n}{R}\langle\psi_i'\phi_j\rangle - \frac{(1-\nu)n}{R}\langle\psi_i\phi_j'\rangle\}$$

$$F_{ij} = \frac{Et_sR}{2(1-\nu^2)}\{-\frac{\nu n}{R}\langle\psi_i'\phi_j\rangle\}$$

$$G_{ij} = \frac{Et_sR}{2(1-\nu^2)}\{\frac{n^2}{R^2}\langle\phi_i\phi_j\rangle + \frac{1-\nu}{2}\langle\phi_i'\phi_j'\rangle + \frac{t_s^2}{12R^2}[\frac{n^2}{R^2}\langle\phi_i\phi_j\rangle + 2(1-\nu)\langle\phi_i'\phi_j'\rangle]\} + \frac{\rho_\ell g}{2}\{n^2\langle\phi_i\phi_j\rangle_D\}$$

$$H_{ij} = \frac{Et_s R}{2(1-\nu^2)} \left\{ \frac{-n}{R^2} <\phi_i \phi_j> + \frac{t_s^2}{12R^2} \left[\frac{-n^2}{R^2} <\phi_i \phi_j> + \right.\right.$$

$$\left.\left. \nu n <\phi_i'' \phi_j> - 2(1-\nu) n <\phi_i' \phi_j'> \right] \right\}$$

$$I_{ij} = \frac{Et_s R}{2(1-\nu^2)} \left\{ \frac{1}{R^2} <\phi_i \phi_j> + \frac{t_s^2}{12R^2} \left[R^2 <\phi_i'' \phi_j''> + \frac{n^4}{R^2} <\phi_i \phi_j> - \right.\right.$$

$$\left.\left. 2\nu n^2 <\phi_i'' \phi_j> + 2(1-\nu) n^2 <\phi_i' \phi_j'> \right] \right\} + \frac{\rho_\ell g}{2} \{ n^2 <\phi_i \phi_j>_D \}$$

The symbols, $<A>$, $<A>_D$, $<<A>>$, A' and A'' are defined as follows:

$$<A> = \int_0^L A \, dx$$

$$<A>_D = \int_0^D (D-x) A \, dx$$

$$<<A>> = \int_0^D A \, dx$$

$$A' = \frac{dA}{dx} \quad \text{and} \quad A'' = \frac{d^2 A}{dx^2}$$

In order to get a nontrivial solution of $\bar{U}_i(t)$, $\bar{V}_i(t)$ and $\bar{W}_i(t)$, the determinant of the coefficients of $\bar{U}_i(t)$, $\bar{V}_i(t)$, $\bar{W}_i(t)$ should be equal to zero. This zero determinant is the so called frequency equation. The natural frequencies of this fluid filled tank, ω, can be obtained by solving this eigenvalue problem and the mode shapes of the system can be determined by the corresponding eigenvectors. The frequency equations for one term approximation (N=1) and two terms approximation (N=2) are shown in Appendix C.

4.2.6 EXPERIMENT

The experimental program is performed using a plastic model tank which is made of Mylar A sheet. The geometric dimensions and the material properties of the model tank are given as follows: L= 12.5 in., R= 4.0 in., t_s= 0.005 in., E= 735,000 psi, ν= 0.3, ρ_s= 0.05 lb/in^{-3}. The cylinder is fixed on the bottom plate and free on the top end. The cylinder is mounted on the table of a 30 lb shaker and filled with water to the desired level. The input forcing functions are generated by a sine function generator. The table motion is measured using an LVDT and the excitation frequency is checked by a counter. A fiber optic probe is used to measure the shell response. The vibration modes are determined by relocating the displacement probe at several locations, both around the circumferential direction and along the axial direction. The number of the circumferential waves can also be observed from the response at the top end of the tank wall during the resonant testing. A block diagram of the experimental set up is shown in figure 4.12.

4.2.7 RESULTS AND DISCUSSIONS

The theoretical prediction and the experimental results for the natural frequencies of the empty tank are shown in figure 4.13. The natural frequencies increase as the number

of axial half-waves increases. For a fixed axial wave number there is a minimum as the number of circumferential waves is increased. The lowest natural frequency of this model tank occurs with m = 1 and n = 5 as shown in figure 4.13. Arnold and Warburton [4.21] have pointed out that at the low circumferential wave numbers the bending energy is small and the stretching energy is large while at the higher circumferential wave numbers the relative contributions from these two types of strain energy are reversed. This interchange in the relative contributions of the bending energy and the stretching energy explains the decrease and subsequent increase in the natural frequencies as shown in figure 4.13. The results also indicate that the comparison between the theoretical prediction and experiment at the low circumferential modes is not as good as that at the higher circumferential modes.

The natural frequencies of a partially filled water tank are shown in figures 4.14, 4.15 and 4.16 for three different circumferential wave numbers, n = 4, 6, 8 (m = 1), respectively. These results indicate that the natural frequency decreases as the water depth is increased. This can be easily explained since the added mass on the shell wall, due to the virtual mass of the liquid, is increased as the water depth is increased. The comparison between the current analytical and the experimental results shows that the one term approxi-

mation (N=1; designated as curve I) is not satisfactory but the two term approximation (N=2; designated as cure II) gives very good agreement with the experimental results. The previous analytical result [4.11], which neglect the initial prestress effect are also shown in these figures and designated as curve III. The results show that this prestress effect is significant as the water depth is increased. It is also interesting to point out that this prestress effect is increased as the circumferential wave number is increased. This fact can be observed from the expression of the potential energy. The third integral expression in equation (4.8) indicates that the strain energy caused by the hydrostatic pressure is proportional to the square of the circumferential wave number. For the n=1 case Table 4.2 shows that the prestress effect is negligible.

TABLE 4.2 The Prestress Effect of n=1 Mode
L= 12.5 in., R= 4.0 in., t=0.005 in.

D/L	0	0.2	0.4	0.6	0.8	1.0
ω_0	560.3	549.5	328.5	137.1	69.67	42.06
ω_p	560.3	549.5	328.5	137.1	69.68	42.09

where ω_0 is the natural frequency derived from ref. 4.11 (no prestress effect) and ω_p is the natural frequency predicted from the one term approximation method. The axial mode

shapes are shown in figure 4.17 for three different water depth cases. The vertical axis represents the distance from the bottom of the tank normalized by the tank length. The horizontal axis represents the radial displacement which is normalized by the radial displacement at the top of the tank wall. The solid lines are based on the two terms approximation (N=2) in current analytical method. It indicates that the two terms approximation gives a very good prediction of the axial mode shapes. Figures 4.18 and 4.19 shown the experimental measurements on both the axial mode shapes and the circumferential mode shapes during the resonant testing.

4.2.8 CONCLUSIONS

The energy method is applied to predict the dynamic characteristics of a fluid filled tank system. The displacement forms are assumed to be the linear combination of the cantilever beam modes and the approximate virtual mass of the fluid is used for the derivation of the kinetic energy of the fluid. Experimental work is carried out to compare with this analytical method. The results indicate that the lowest natural frequency does not occur with the simplest mode pattern and the natural frequency of a partially filled water tank decreases as the water depth is increased. The prestress effect due to the hydrostatic pressure is also studied by including the non-linear terms in the strain-displacement relations. This prestress effect is important at the higher circumferential

wave pattern and the higher water depth cases. The one term approximation of this energy method is not satisfactory to predict the dynamic characteristics of this fluid filled tank system. The two term approximation (N=2) provides very good agreement, with the experimental results, both in natural frequencies and axial mode shapes. This method can also be applied to other boundary conditions [4.13] by properly selecting the assumed displacement shape functions and it is simple enough for the practical application. Knowing the dynamic characteristics of this fluid/structure system, the forced vibration problem of this system can be carried out by the classical method of spectral representation [4.22].

4.3 DYNAMIC BUCKLING TESTS OF SCALE MODEL TANKS

4.3.1 INTRODUCTION

The dynamic behavior of fluid filled tank under earthquake excitation has been studied by a number of investigators. These analyses [4.12, 4.15, 4.17, 4.22-4.24] and experiments [4.25-4.28] have dealt with the response of the fluid and structure either separately or interactively. From these studies have emerged a fairly good understanding of the linear dynamic response problem, a beginning on some of the nonlinear response problems and virtually no information on the adequacy

of any postulated failure criterion. Failure mechanisms proposed are yielding, elastic buckling and inelastic buckling. The usual buckling criterion proposed is static in nature and the complex stress field in the shell wall is supplanted by a simple field for which analytical/experimental results are available. The adequacy of this latter step was assessed in section 4.1 for elastic buckling. Through the harmonic buckling tests, this section attempts to assess the assumption that a static buckling criterion is satisfactory even though the prebuckling stress field is time dependent. The transient buckling tests are also carried out to assess the adequacy of the failure criteria established by the harmonic tests. Variation in critical buckling acceleration resulting from different kinds of simulated earthquakes is also examined. The experimental work to be described uses scale model tanks. The scaling law has been discussed in detail in chapter 3.

4.3.2 SCALE MODEL TANKS AND EXPERIMENTAL SET UP

As previously stated, the test tanks were constructed of plastic. This allows a large scale factor and also allows one model tank to be buckled many times since recovery is possible unless complete collapse of the model tank occurs. The material used is the same as that discussed in chapter 2. The cylinder was fixed on the bottom plate and the top end

was either free or fitted with a light weight (0.3 oz) plastic end plate in order to simulate a roof. The dimensions of the tanks are given in Table 4.3 as well as the dimensions of the full scale tanks (assumed to be steel). Several tank models were constructed corresponding to the dimensions of model I and II. These are designated Ia, Ib, etc.

TABLE 4.3

MATERIAL PROPERTIES AND TANK DIMENSIONS

		Model	Prototype
Modulus, $E(lb\text{-}in^{-2})$		7.35×10^5	30.0×10^6
Poisson's Ratio, ν		0.3	0.3
Radius, R(in/ft)		2.5	102/8.5
Height, L(in/ft)		10.7	436.7/36.4
Thickness, t_s(in)	I	0.002	0.082
	II	0.003	0.122
R/t_s	I	1250	1250
	II	833	833
L/R		4.28	4.28
Density, $\rho_s(lb/in^3)$		0.050	0.284
ρ_s/ρ_ℓ		1.39	7.87

The bottom end condition of the tank (essentially full clamped $u = v = w = \frac{\partial w}{\partial x} = 0$) is not that usually encounted in the field nor are the full scale tank dimensions necessarily realistic. The models for these studies were sized to fit the capabilities of the available shake table. It did not seem

necessary to attempt to duplicate an actual tank until the buckling phenomenon is understood somewhat better. The two top conditions (free and essentially rigid) were considered to be the two extremes of realistic designs.

The test tank was mounted on the shake table and the motion of this table was measured using an LVDT and an accelerometer. All buckling tests were carried out under both harmonic excitation and transient excitation. The harmonic tests carried out near the n=1 resonance of the tank showed considerable distorsion of the base excitation due to model/shake table coupling. The influence of this was judged to be significant only in the vicinity of that resonance. The block diagrams of the experimental set-up are shown in figure 4.12 for harmonic buckling tests and in figure 4.20 for the transient buckling tests.

4.3.3 HARMONIC BUCKLING TESTS

Before carrying out the buckling tests a model survey was conducted. The modes are categorized by their circumferential wave numbers, n, and the complexity of the mode shape in the axial direction, m. The natural frequencies for model IIb are shown in figure 4.21 for both the free end and the end with a plate attached. The analysis was carried out using the solution developed in ref. 4.24. For the free ended case the comparison is quite good except for the n=1 mode. The experimental result for this mode was inferred from the buckling test data since it was not detected during the

resonance testing. Part of the experiment/analysis disagreement for the n=1 mode is most likely due to the shake table flexibility in the rocking mode.

The results for the tank with a top plate do not compare as well with the analysis as the free ended case. The analysis is approximately 10% low. This difference may be due to the simple support boundary conditions assumed in the analysis. The actual boundary conditions depend on the stiffness of the roof which was judged to provide a support closer to clamped.

The buckling test was carried out by fixing the frequency of excitation and increasing the amplitude until buckling occurred. Tests were carried out in a range from 8 Hz to 40 Hz. The scaled frequencies correspond to 1.3 Hz to 6.3 Hz for the full size structure. The first sloshing mode of the models has a frequency below 2.7 Hz for all the conditions tested.

At low frequencies the buckling can be seen by eye. Since the stress field in the shell wall is cyclic, the buckles disappear and emerge during a period of the excitation. Buckling can also be detected by the noise generated by the vibrating fluid/structure. Below 8 Hz the buckles have enough time to reach quite large amplitudes and complete collapse of the tank results. This dictated the lower bound in frequency for the buckling tests. At frequencies above 25 Hz the buckling could not be observed by eye. Changes in noise level and displacement probe output were used as an indication of buckling. The buckling was also observed by photographing

the response (exposure time $\leq$ .004 sec) during the excitation. Examples of the buckling are shown in figs. 4.22 and 4.23. A dye has been added to the fluid.

Figure 4.22a shows the tank being oscillated at an amplitude below the buckling level. Figure 4.22b shows the buckling deformation. Considerable spray at the liquid surface is noticeable. It is also interesting to note that the buckling is not confined to the bottom of the tank. Figure 4.22c shows one type of buckling pattern which occurred on the top end of the tank. It is thought that this kind of buckling is due to the pressure inside the tank is lower than the hydrostatic pressure. It is equivalent to the buckling of a cylindrical shell under external pressure. A buckling example in more detail is shown in figure 4.23.

The buckling results for model I with free top condition are shown in figure 4.24 for three different water levels. These results are for model Ib. Very similar results were obtained with model Ia. The dashed horizontal lines give the buckling criterion as calculated using the procedure given in section 4.1. In this criterion, buckling is assumed to occur when the axial membrane stresses at the bottom of the tank wall reaches the classical value

$$\sigma_{cr} = \frac{1}{\sqrt{3(1-\nu^2)}} \frac{Et_s}{R} \qquad (4.16)$$

The stress is calculated using membrane theory and the pressure is that found using only the impulsive term of the pressure

calculation and the assumption of a rigid tank. At low values of frequency this quasi-static/quasi-rigid criterion is fairly satisfactory. As the frequency approaches that of the n=1 fundamental mode it is clear that the flexibility of the tank plays an important role in amplifying the stress in the tank wall. Similar results for model IIb are shown in fig. 4.25. In this test series the influence of the roof was examined. At low frequency the roof appears to increase the buckling strength of the tank.

The data for the free end case are shown in fig. 4.26 for both model I and II. The frequency for the experimental data has been normalized using the n=1 frequency inferred from the data presented in figs. 4.24 and 4.25. The analysis shown in the figure is that of ref. 4.24 modified for harmonic excitation. This linear analysis (2% damping assumed) includes the fluid/structure interaction but the slosh modes have been suppressed (the free surface displacement is zero). The first slosh mode for n=1 is near $\omega/\omega_1 = .07$. The base acceleration for both the experiment and analysis has been normalized by the acceleration necessary to cause buckling (using equation 4.16) in the limit as ω approaches zero. It should be emphasized that the frequency used to normalize the experimental results is not the same as that used for the analysis (see fig. 4.21).

The favorable comparison of the analysis and experiment indicates that the buckling is predominately influenced by the response in the n=1 mode. This response is numerically

the same for model I and II when normalized by the n=1 frequency and when only the membrane stress is considered. The shell boundary layer developed at the tank base is ignored in this calculation.

The n=1 frequency is not the lowest shell frequency as can be seen from fig. 4.21. For model IIb there are five modes (n=2→6) with lower frequencies. The lowest one (n=3) is at $\omega/\omega_1 = .47$. The buckling data show some scatter which may result from the influence of these modes (model IIb near $\omega/\omega_1 = .50$) but the influence does not appear strong. The experimental results for low frequencies are quite a bit higher than the analysis. At these frequencies considerable surface motion occurs and liquid is ejected from the tank. These nonlinear effects have not been studied in detail.

4.3.4 TRANSIENT BUCKLING TESTS

The transient base excitation was produced by a noise generator. This noise generator can produce a continuous analog waveform of approximately Gaussian random noise. The power spectrum of this Gaussian output is approximately rectangular. The bandwidth (at -3 dB point) of this Gaussian noise is selectable from 0.0015 Hz to 50 kHz. In this experimental program only 15 Hz and 50 Hz were chosen to be the bandwidth of the base excitation. The duration of the random noise pattern can also be chosen from the sequence length settings. Two noise patterns were used as the base

excitations during the transient buckling tests. The first noise pattern has 1.67 second durations and its bandwidth is 15 Hz (designated A-type noise pattern). The second one has 1.02 second durations and its bandwidth is 50 Hz (designated B-type noise pattern). These two noise patterns were recorded directly from the output of noise generator as shown in figures 4.27a and 4.28a. The true base accelerations of the water tanks, generated by these noise patterns, were read from an accelerometer mounted on the shake table as shown in figures 4.27b and 4.28b.

The two base acceleration histories were recorded by a tape recorder. The analog signals were converted into digital data using an A/D conventor. These digital data were used as the input data in the theoretical analyses. These digital acceleration histories are shown in figures 4.27c and 4.28c. The Fourier amplitude spectrum of these base accelerations is also calculated and plotted using a Digital Signal Processor and the results are shown in figures 4.27d and 4.28d. The vertical axis represents the Fourier amplitude which is normalized by the maximum Fourier amplitude and the horizontal axis represents the frequency in Hz. The predominant frequency domain of A-type excitation is from 1.5 Hz to 16 Hz (the corresponding period is from 0.38 sec. to 4.0 sec. for the full scale case) and its peak is at 3.0 Hz as shown in figure 4.27d. Similarly, figure 4.28d indicates that the B-type base acceleration has a frequency domain from 1.0 Hz to 57 Hz

(the corresponding period is from 0.11 sec. to 6.1 sec. for the full scale case) and the peak is at 3.6 Hz. The comparisons of the power spectrum density [4.29] and the frequency domain of the Fourier amplitude [4.30] indicate that both base excitations give a reasonable simulation to the real earthquake excitation. In addition, these two base excitations are similar to the C-type artifical earthquake motion discussed in ref. 4.31 This type of simulated ground motion is expected in the epicentral region of a Magnitude 5.5 to 6 shock, such as occurred in San Francisco in 1957. In highly seismic regions such shocks could occur several times in the life of a structure. The acceleration history of the B-type base excitation is close to the strong motion part of the C-1 type artificial earthquake in ref. 4.31.

The buckling tests were carried out by fixing the noise pattern and increasing its magnitude until buckling occurred. The output signals from the noise generator were controlled by a GATE signal which remains open throughout one complete sequence. Each noise pattern can also be repeated exactly as it occurred at an earlier time. The buckling can be seen by eye.

The test results for model Ic and IIc subjected to A-type base excitation are shown in figures 4.29 and 4.30, respectively. The ordinate of these figures represents the magnitude of the maximum acceleration in A-type base excitation which will cause the tank to buckle and the abscissa

represents the water depth of the tank. The true base acceleration patterns generated by the A-type noise pattern are almost identical for different water levels. This can be observed in figures 4.31 and 4.32, which also show the base accelerations with the maximum amplitude just below and above the critical buckling magnitude. It is interesting to note that figure 4.32 indicates that the base acceleration is altered when the buckling occurs.

The theoretical prediction, in figures 4.29 and 4.30, are based on the linear analysis [4.24]. Buckling is assumed to occur when the maximum axial membrane stress reaches the classical buckling stress (see equation 4.16). The free surface displacement is assumed to be zero in this linear analysis. The time histories of the predicted axial membrane stress are also shown in figures 4.27e and 4.28e. The comparison between the predicted and experimental results (figures 4.29 and 4.30) shows that the linear analysis gives a good prediction only when the tank is close to being full. For a tank with less water (say D/L = 0.7), large surface displacement can be observed during the transient ground acceleration period and it is thought to be the reason which cause the large discrepancy between the predicted and experimental results for the lower water depth cases. The experimental results indicate that the tank with a simulated roof requires a larger ground acceleration to cause buckling than that for a tank without a roof. The buckling for the tank

without roof occurs near $\theta=30^{o}$, on the bottom of tank wall, which is different from that of the tank with a roof (buckle at $\theta=0^{o}$). The buckling mode shape, on the bottom of tank wall, is the typical elastic diamond shape. As the water depth is increased, the buckling mode displacements becomes smaller and more water is expelled out of the tank without a roof. All the maximum free surface displacements due to the A-type critical excitation are higher than the top end of the shell wall.

Similar results are shown in figures 4.33, 4.34, 4.35 and 4.36 for the model tanks subjected to the B-type base excitation. Figure 4.33 shows the maximum free surface displacement of the liquid at the critical base excitation vs. the depth of the liquid inside tank. The comparisons of the maximum critical acceleration between the predicted and the experimental results for the model tanks under B-type base excitation are shown in figures 4.34 and 4.35. Figure 4.34 indicates that the linear analysis gives a reasonable prediction even in the lower water depth cases. This implies that the sloshing behavior does not play a significant role in the buckling. This can be explained by looking at the base excitation time history. The maximum acceleration of this base excitation occurs at the very beginning of the excitation period. The fluid sloshing amplitude has not grown to combine with the inertial effect at this early time. This was verified by the experimental observation that the buckling occurs at

the very beginning of the excitation period.

Figure 4.35 does not give the same results as figure 4.34 does. This kind of results are also thought due to the sloshing effect. It can be presumed that the sloshing effect in the model tank I(figure 4.34) is not as significant as that in the model tank II(figure 4.35) since the required critical base excitation is smaller in the first case and the sloshing effect is proportional to the magnitude of the base excitation. In the second case the maximum axial stress is generated by the inertial acceleration and in addition by the sloshing effect as well. This peak stress occurs at some instant of time after the time at which the maximum stress is observed in the first case. In figure 4.35 the experimental points for a tank with a simulated roof are not available at the low water level cases. This is due to the limitation on the shake table capability. Figure 4.36 shows the base accelerations with different water levels for both buckling and non-buckling cases. Due to coupling with the shake table, the base acceleration history changes slightly as the water depth is increased. It is believed that this small change does not have significant effect on the results predicted from linear theory. All test results also indicate that the roof increases the buckling strength of the tanks.

4.3.5 CONCLUSIONS

The harmonic buckling tests, when correlated with the stresses from a response analysis, indicate that the buckling is largely dependent upon the n=1 response. The higher order shell modes with lower frequencies seem to have only a secondary role. The experimental n=1 frequency is lower than that calculated, probably resulting from rocking flexibility. The buckling on the top end of the tank wall is equivalent to the buckling of the tank under external pressure. The buckling criterion used is that of the classical analysis of a statically loaded shell under uniform axial compression. No "knockdown" factor is used to account for imperfection. It is thought that the imperfection effect is insignificant because of the localized nature of buckling and the internal pressure effect due to the liquid inside the tank.

The transient buckling tests indicate that the linear analysis gives a good prediction when the water depth is close to being full. Large free surface displacement of the liquid can be observed, particularly when the water depth is low, during the transient tests. The discrepancy between the predicted and experimental results is most likely due to the sloshing effect. This sloshing effect depends upon both the magnitude and the time history pattern of the base excitation and it has not been studied in detail to date. The experimental results indicate that the sloshing effect is important in the A-type base excitation case. It is interesting to

point out that the ground acceleration pattern for the San Fernando Earthquake in 1971 [4.32] is very similar to the A-type excitation pattern; the peak acceleration occurs near the end of the strong excitation period. The experimental results also indicate that the tank with roof requires higher acceleration to cause the buckling than that in a tank without roof.

REFERENCES - CHAPTER 4

4.1 Arbocz, J., "The Effect of Initial Imperfections on Shell Stability", Thin-Shell Structures, Fung, Y.C., and Sechler E.E., eds., pp. 205-246, Prentice Hall, 1974.

4.2 Babcock, C.D. and Sechler, E.E., "The Effect of Initial Imperfections on the Buckling Stress of Cylindrical Shells", NASA TN D-20005, 1963.

4.3 NASA Space Vehicle Design Criteria, "Buckling of Thin-Walled Circular cylinders", NASA SP-8007, 1965.

4.4 Miller, C.D., "Buckling of Axial Compressed Cylinders", Journal of the Structural Division, Proceedings of the ASCE, Vol. 103, No ST3, March 1977, pp. 695-721.

4.5 Flügge, W., Stresses in Shells, Second Edition, Springer-Verlag, 1973, pp. 114-115.

4.6 Veronda, D.R. and Weingarten, V.I., "Stability of Hyperboloidal Shells: An Experimental and Analytical Investigation", University of Southern California, USCCE 009, March 1973.

4.7 Flügge, W., "Die Stabilität der Kreiszylinderschale", Ing.-Archiv, Bd.III, Heft 5, Dec. 1932, pp.463-506.

4.8 Bushnell D., "Stress, Stability and Vibration of Complex Branched Shells of Revolution: Analysis and User's Manual for BØSØR4", LMSC-D243605, Lockheed Missiles and Space Company, Inc., Sunnyvale, California, March 1972.

4.9 Almroth, B.O., "Influence of Edge Conditions on the Stability of Axially Compressed Cylindrical Shells", NASA CR-161, 1965.

4.10 Baron, M.L. and Skalak, R., "Free Vibration of Fluid-Filled Cylindrical Shells", Journal of the Eng. Mech. Division, ASCE, Vol. 88, No. EM3, June 1962, PP 17-43.

4.11 Arya, A.S., Thakkar S.K. and Goyal A., "Vibration Analysis of Thin Cylindrical Containers", Journal of the Eng. Mech. Division, ASCE, Vol, 97, No. EM2, April 1971, PP 317-331.

4.12 Young, J.Y., "Dynamic Behavior of Fluid-Tank Systems", Ph.D. Dissertation, Rice University, Houston, Texas, March 1976.

4.13 Mixson, J.S. and Herr, R.W., "An Investigation of the Vibration Characteristics of Pressurized Thin-Walled Circular Cylinders Partly Filled with Liquid", NASA TR R-145, 1962.

4.14 Abramson, H.N., "The Dynamic Behavior of Liquids in Moving Containers", NASA SP-106, 1966, PP 303-350.

4.15 Edward, N.W., "A Procedure for Dynamic Analysis of Thin Wall Cylindrical Liquid Storage Tanks Subjected to Lateral Ground Motion", Ph.D. Dissertation, University of Michigan, Ann Arbor, Michigan, 1969.

4.16 Wu, C.I., Mouzakis, T., Nash, W.A. and Colonell, J.M., "Natural Frequencies of Cylindrical Liquid Storage Containers", NSF-RA-E-75-134, June 1975.

4.17 Nash, W.A., Balendra, T., Shaaban, S.and Mouzakis, T., "Finite Element Analysis of Seismic Response of Cylindrical Tanks", ASCE, Convention and Exposition, Chicago Oct. 1978.

4.18 Haroun, M.A. and Housner G.W., "Free Lateral Vibrations of Liquid Storage Tanks", 3rd Eng. Mech. Division Specialty Conference, ASCE, Austin, Texas, Sep. 1979, PP. 466-470.

4.19 Kraus, H., Thin Elastic Shells , Wiley, New York, 1972, PP.310-313.

4.20 Young, D. and Felgar, R.P., "Table of Characteristic Function Representing Normal Modes of Vibration of a Beam", Texas University, Engineering Research Series No.44, July 1949.

4.21 Arnold, R.N. and Warburton, G.B., "Flexural Vibrations of the Walls of Thin Cylindrical Shells Having Freely Supported Ends", Proc. Royal Soc. Lond., 197A, 1949, PP.238-256.

4.22 Mouzakis, T., "Response of Partially Filled Elastic Cylindrical Storage Tank Subjected to Arbitrary Lateral Base Excitation", Ph.D. Dissertation, Massachusetts University, Amherst, July 1976.

4.23 Housner, G.W.,"The Dynamic Behavior of Water Tanks", Bulletin Seism. Soc. America, Vol.53, No.1, 1963, PP.381-387.

4.24 Haroun, M.A., "Dynamic Analysis of Liquid Storage Tanks", Ph.D. Dissertation, California Institute of Technology, Pasadena, California, December 1979.

4.25 Clough, D.P., "Experimental Evaluation of Seismic Design Methods for Broad Cylindrical Tanks", University of California, Berkeley, Earthquake Engineering Research Center Report No. UCB/EERC-77/10, May 1977.

4.26 Niwa, A., "Seismic Behavior of Tall Liquid Storage Tanks", University of California, Berkeley, Earthquake Engineering Research Center Report No. UCB/EERC-78/04, February 1978.

4.27 Kana, D.D., "Seismic Response of Flexible Cylindrical Liquid Storage Tanks", Nuclear Engineering and Design, Vol. 52, 1979, PP.185-199.

4.28 Clough, R.W. and Niwa, A., "Static Tilt Tests of a Tall Cylindrical Liquid Storage Tank", University of Calif. Berkeley, Earthquake Engineering Research Center Report No. UCB/EERC-79/06, February 1979.

4.29 Housner, G.W. and Jennings, P.C., "Generation of Artificial Earthquakes", Journal of the Engineering Mechanics Division, ASCE, Vol. 90, No. EM1, February 1964, pp. 113-150.

4.30 Hudson, D.E., "Analyses of Strong Motion Earthquake Accelerograms", Earthquake Engineering Research Lab., California Institute of Technology, Report No. EERL 72-80, Pasadena, California, August 1972.

4.31 Jennings, P.C., Housner, G.W. and Isai, N.C., "Simulated Earthquake Motions", Earthquake Engineering Research Laboratory, California Institute of Technology, Pasadena, California, April 1968.

4.32 Hudson, D.E. "Strong-Motion Instrumental Data on the San Fernando Earthquake of Feb. 9, 1971", Earthquake Engineering Research Laboratory, California Institute of Technology, September 1971.

CHAPTER 5 BUCKLING TESTS OF UNANCHORED TANKS UNDER EARTHQUAKE EXCITATION

In previous studies it has been assumed that the liquid storage tank is attached to its foundation. This kind of bottom end condition is not that usually encountered in the field. Field observations after strong earthquakes indicate that tanks lift off from their foundations. It may be noted that this effect is nonlinear. The adequacy of design procedures may be questioned in that the uplifting effect is not accounted for. This chapter describes the experimental buckling tests for unanchored tanks subjected to static and dynamic loading. The observed results are compared with that of an anchored tank as well as the standard design criteria. An analytic model is also developed which predicts tank maximum stress due to overturning moment.

5.1 INTRODUCTION

The behavior of the liquid storage tanks under earthquake excitation has been studied by many investigators, but most of these studies focused on the response of an anchored tank. The problem of the unanchored tank subjected to seismic loading is complicated and difficult to analyze and only a few scale model tests have been carried out thus far [5.1, 5.2, 5.3]. These studies have shown that the unanchored tank develops greater axial stresses than that an anchored tank, but the tank failure mechanism has not been studied.

The buckling behavior of the anchored tanks has been previously studied in chapter 4. The current chapter describes an experimental program which includes static and dynamic buckling tests of an unanchored tank under simulated earthquake loading. The experimental tank models are constructed of plastic. The static buckling tests are performed by putting a tank on an inclined, transparent, rigid plate and filling the tank with water until buckling and collapse of the tank occur. The dynamic buckling test is accomplished by shaking a fluid filled tank model partially fixed on a shake table. The nonlinear buckling behavior and the uplifting effect are studied. The test parameters include water depth, tilt angle, bottom plate thickness, bottom ring size, top end condition and dynamic excitation patterns. The buckling criterion is based on the classical buckling criterion. The adequacy of this assumption has been assessed in chapter 4.

5.2 EXPERIMENTAL SPECIMENS

As previously stated, the test tanks were made of Mylar A sheet. The test tanks were made by rolling the Mylar A sheet around a mandrel and using a lap seam bonded with a double sided tape. The cylinder was fixed on a circular plastic plate, (Mylar A), with or without a reinforcing ring on the bottom end by using an epoxy. The top end was either free or fitted with a plastic plate to simulate a roof. The dimensions of the test tanks with their corresponding dimensions of the full scale tank are given in Table 5.1 (assumed to be steel). Several

tank models were constructed corresponding to the dimensions of model I, II and III. The classification of these test models are listed in Table 5.1. Figure 5.1 shows the sizes of the bottom reinforcing rings which are made of Lucite.

TABLE 5.1

MATERIAL PROPERTIES AND TANK DIMESIONS

		Model	Prototype
Modulus, $E(N\text{-}m^{-2})$		5.07×10^{9}	20.8×10^{10}
Poisson's Ratio, ν		0.3	0.3
Radius, R (cm)		6.35	260
Length, L (cm)		26.67	1094
Thickness of Shell Wall t_s (cm)	I	0.0051	0.2091
	II	0.0076	0.3116
	III	0.0127	0.5210
Thickness of Bottom Plate t_b (cm)	a	0.0051	0.2091
	b	0.0076	0.3116
	c	0.0127	0.5210
	d	0.0153	0.6277
Density, ρ_s (kg/m^3)		1.39×10^{3}	7.87×10^{3}

The classification of tank models:

Tank # Ia0 means: t_s =0.0051 cm; t_b =0.0051 cm; No Ring

IIb1 means: t_s =0.0076 cm; t_b =0.0076 cm; Ring #1

#IIIc2 means: t_s = 0.0127 cm, t_b = 0.0127 cm; Ring #2

5.3 STATIC BUCKLING TEST

The static buckling test was performed by putting a tank on an inclined, transparent, rigid plate and filling the tank with water slowly until the buckling and collapse of the tank occurred. The loading condition and nomenclature for the static buckling test are shown in figure 5.2. Figure 5.3 shows a buckling experiment which indicates that the buckling can be observed at one side ($\theta=\pi$) of the inclined, unanchored, tank and the uplifting occurs at the other side ($\theta= 0^{o}$) of the tank. An optic device displacement pickup was used to measure the radial displacements at the buckling area of the tank wall. A typical result is shown in figure 5.4. It shows the relative radial displacements at two different measured locations vs. the water depth. These two measured locations are roughly indicated in figure 5.4 . One is near the center of the buckling deformation shape (curve A) and the other one is near the edge of the buckling deformation shape (curve B). It should be pointed out that this radial displacement was defined to be zero at the initial water depth. The results indicate that the distance between the tank wall and the displacement pickup decreases as the water depth is increased but does not exceed the critical buckling water depth, d_b. This outward radial displacement is believed to be the result of hydrostatic hoop stress and rotation of the fluid filled tank. When the water depth reaches the critical buckling point the buckling deformations start to appear (diamond shape). At this moment

the radial displacement becomes inward as shown in figure 5.4. If the water depth is increased the buckling deformation gets larger and larger. Finally the whole fluid filled tank collapses at a certain water depth which is defined as the collapse water depth, d_c. This kind of buckling behavior of an unanchored tank is quite different from that of an anchored tank. For the anchored tank the shell wall snaps into a diamond shaped buckling pattern and the collapse of the tank follows at the same water depth. It is interesting to note that this behavior is similar to that of a column with initial curvature under axial compressive loading [5.4]. The critical buckling water depth (d_b) and the collapse water depth (d_c) are compared in figure 5.5 for different inclined angles. It indicates that the difference between d_b and d_c is quite large for an unanchored tank without a reinforcing bottom ring.

The bottom uplifting areas of the tank are observed by photographing the response during the tilt test. These pictures (fig. 5.6) were taken from below the bottom of the tank. A dye was used to distinguish the uplifted area and the contact area between the bottom plate and the rigid transparent plate. The results indicate that the shape of contact area is very close to a circle. The diameter of this circle becomes smaller as the water depth is increased. Both the uplifting distance δ and the uplifting width W_d are measured by using a feeler gage. The results of a typical test are shown in fig. 5.7 for three different inclined angles.

The figure indicates that there is correlation between the uplifting distance, δ, and the uplifting width, W_d. If we define $\phi = \tan^{-1}(\delta/W_d)$ then the range of ϕ is about $6^o \sim 7^o$.

The collapse water depths vs. the inclined angles are shown in figures 5.8a, 5.8b and 5.8c for R/t_s= 1250, 833 and 500, respectively. The results indicate that the bottom reinforcing ring does have an effect as far as the buckling strength of the unanchored tank is concerned, but it does not seem significant. The predicted result based on membrane theory results is also shown in figure 5.8a for the comparison. The membrane theory was applied to calculate the axial membrane stress and the buckling was assumed to occur when the maximum axial stress reaches the classical buckling stress (equation 4.16). The ratio of the experimental collapse water depth of an unanchored tank to the predicted buckling water depth of an anchored tank, where the collapse water depth and the buckling water depth are believed to be identical, is about 1/2 for R/t_s=1250 (figure 5.8a). This means that the unanchored tank develops much greater axial stresses (at least 4 times) than that an anchored tank since the axial membrane stress of an anchored tank is proportional to the square of the water depth (equation 4.4a). Figure 5.9 shows the comparison of the collapse water depth for three different R/t_s ratio. It may be noted that the collapse water depths of tank # IIIc2 (R/t_s= 500) and tank # IIb2 (R/t_s= 833) are about 1.65 and 1.33 times those of tank # Ia2 (R/t_s= 1250).

Fig. 5.10a shows the collapse water depths of two tanks which have the same dimensions and bottom reinforcing ring but with different bottom plate thickness (mylar A). This figure demonstrates that the change of the stiffness of bottom plate does not have a great effect on the collapse water depth. However, if we use the lucite plate (t_b= 1/16 inch) instead of Mylar A sheet (t_b= 0.002 inch) as the bottom plate then the effect on the collapse water depth can be observed from the curve L in figure 5.8a. The results indicate that the collapse water depth increases dramatically as the stiffness of the bottom plate becomes much greater than the stiffness of the thin shell wall. Fig. 5.10b shows the collapse water depth on three different locations of a tank where the original location of seam side is defined to be $\theta = 270^{o}$. The results indicate that the initial imperfection effect of this tank model is small and negligible.

5.4 DYNAMIC BUCKLING TEST

The dynamic buckling tests were carried out by shaking the fluid filled tank model partially fixed (by double-sided tape) on the shake table. The adhesive area of the bottom plate is 1 inch square as shown in figure 5.11. The experimental set up and procedures are the same as those in section 4.3 except the tank is unanchored in this section. Both harmonic buckling tests and transient buckling tests are carried out and the results are compared with that of an anchored tank.

5.4.1 HARMONIC BUCKLING TEST

The buckling deformation of an unanchored tank can be observed by photographing the response during the harmonic excitation. Examples of buckling are shown in figures 5.12 and 5.13. A dye has been added to the fluid to facilitate the observation. When the excitation amplitude reaches the buckling level, a small dent appears first (figure 5.12c). If the excitation amplitude is increased above the buckling level, the small dent becomes large and the number of the diamond-shaped deformations is increased (figure 5.12d). It is also interesting to note that the buckling is not confined to the bottom end of the tank. Figures 5.12a and 5.12b show two different kinds of buckling patterns which occur on the top end of the tank wall. The observations indicate that the buckling on the top end of the tank wall always appears near the top of the liquid inside the tank. Figure 5.13a shows the detail of the bottom end of the tank when it is sitting at rest on the shake table. Figures 5.12b and 5.13b show that the uplifting appears on one side of the tank without any buckling. On the other hand, figures 5.12c and 5.13c show the opposite phenomena; i.e., there is buckling on the bottom end of the tank but no uplifting. It should be pointed out that both the excitation frequency (8 Hz) and the excitation amplitude (0.2 g) in the set-up shown in figure 5.13b are the same as those in figure 5.13c. These two pictures are presumed to be taken approximately at two opposite peak

acceleration instants. These two pictures are equivalent to the pictures, on both side of the tank, taken at the same instant when it is near the peak acceleration. The observations indicate that the compressive stress was generated on one side of the tank to cause buckling while the tensile stress was developed on the other side of the tank to lift off part of the bottom plate of the tank.

The buckling results for model IIb2-1 with a simulated roof are shown in figure 5.14 for three different water levels. the results of an anchored tank under harmonic excitation are also shown in the figure for comparison. This figure indicates that the buckling strength of the unanchored tank was reduced substantially in the low frequency range. At higher excitation frequency (for instance $\omega \geq$ 14 Hz in figure 5.14) the buckling on the top end of tank wall appears first before the buckling on the bottom end of tank wall can be observed. Near some particular frequencies (e.g. ω = 16 Hz, 17 Hz in figure 5,14) the buckling deformation on the bottom end of tank wall will disappear then appear again as the excitation amplitude is increased above the level of the first required buckling acceleration. Similar results for model Ia1 with the same simulated roof are shown in figure 5.15. It also shows that much greater stress was developed in an unanchored tank than in an anchored tank as the excitation frequency is decreased.

It is interesting to look at the response of the model tank subjected to the very low frequency excitation. Figure 5,16 shows that the required buckling acceleration (tank #

IIb2-2) vs. the excitation frequency which approaches the first sloshing frequency of the fluid. Since figures 5.14 and 5.15 indicates that the tank appears to be approaching some rocking mode as the excitation frequency is decreased, the results in figure 5.16 suggest that this rocking mode of the tank is close to the first sloshing mode of the liquid. The nonlinear sloshing behavior can be observed as the excitation frequency approaches the natural frequency of the first slosh mode, A swirling of the fluid inside the tank can make the tank buckle all around the bottom end of tank wall. The nonlinear, nonplanar free oscillations of a fluid in a fixed base rigid tank, subjected to lateral harmonic vibration at a frequency in the neighbourhood of the lowest resonant frequency of the fluid is studied in details in ref. 5.5.

5.4.2 TRANSIENT BUCKLING TEST

The experimental set up and procedures of an unanchored tank subjected to a transient loading are the same as those in section 4.3.4. The testing results for different model tanks subjected to the A-type and the B-type noise patterns are shown in figures 5.17 and 5.18. The ordinate of these figures represents the maximum magnitude of the base acceleration which is just high enough to cause tank buckle and the abscissa represents the depth of liquid inside tank. The results for anchored tank are also shown in these figures. The

comparison between the results of anchored tank and unanchored tank indicates that the former one has a higher buckling strength than that in the latter one. This difference depends on the testing parameters (e.g. water depth, bottom reinforcing ring, etc.). The ratio of buckling strength is approximately from 3 to 6 as shown in the figures. Although the base accelerations of an unanchored tank (figures 5,19, 5.20) are not exactly the same as those of an anchored tank (figures 4.31 4.36), this effect is believed to be insignificant. The results also indicate that the bottom reinforcing ring slightly increases the buckling strength of unanchored tank, but it is not significant if it is compared to the effect of changing the anchorage of tank base.

5.5 CONCLUSIONS

The static buckling test of an unanchored fluid tank gives a clear picture of the nonlinear buckling behavior and the uplifting phenomena. The buckling deformation starts from a small dent and proceeds to total collapse as the loading is being increased above the buckling level. The similar behavior (except totally collapse) is also observed in the dynamic buckling test. This kind of buckling behavior of an unanchored tank is quite different from that of an anchored tank. The experimental observation also shows that the shape of the contact area between bottom plate of the tank and ground is close to being a circle. The diameter of this circular contact area decreases as the loading is increased. It should be

pointed out that there exists some kind correlation between the uplifting distance and the uplifting width which is related to the diameter of the contact area. The static buckling test results show that the previous rigid base assumption much underestimates the stresses developed in the tank wall of an unanchored tank. It is also interesting to compare the present design procedures with the experimental results. Table 5.2 gives a comparison of the axial stresses in the tank wall of an unanchored tank from different references and a suggested analytic model which is discussed in detail in Appendix D. The design predictions are based on the analytical model suggested in reference 5.6 and the experimental data are from ref. 5.3. Table 5.2 indicates that the present design procedure also underestimates the stresses developed in an unanchored tank. The current suggested analytical model (see Appendix D) predicts much better results, but it is based on the experimental results of knowing the arc length of the uplifting tank base.

The harmonic buckling tests indicate that the buckling of an unanchored tank is most likely dependent upon the response of the rocking mode of the tank. The natural frequency of this rocking mode is close to the first sloshing frequency of the liquid inside the tank. This is quite different from that of an anchored tank which the natural frequency of the n=1 shell mode is much higher than the first sloshing frequency of the liquid and the buckling is predominantly dependent upon the n=1 response. The swirling behavior and large free surface displacement of the liquid, generated as the excitation frequency in the neighborhood of

the first sloshing frequency, can make tank buckle all around the bottom end of the tank wall. This suggests the possiblity of the elephant foot bulge which is particularly observed in earthquake damage. The transient buckling tests are also carried out and the results indicate that the unanchored tank develops much greater stresses than that in an anchored tank. The differences depend on the testing parameters which include water depth, bottom ring, roof, base excitation pattern, etc.. The bottom reinforcing ring has an effect on the buckling strength, but it is small compared to the effect of changing the anchorage of tank base. The linear analysis [5.7] seems good for an anchored, full-filled, tank, but it is not applicable to predict the response of an unanchored tank.

TABLE 5.2

R= 46.5 in., t_s= 0.09 in., L= 15 ft.

Comparison of Design Predictions/Experimental Results

water depth D(in)	inclined angle $\alpha(^0)$	axial stress σ(Psi) ref. 5.6	ref. 5.3	Appendix D
156	4.2	900	357	1602
156	5.6	2000	476	2383
156	6.5	2550	554	2884
156	8.5	4200	881	4004
156	6.0	2279	504	2606
126	6.0	1098	333	1585
84	6.0	502	148	572

REFERENCES - CHAPTER 5

5.1 Clough, D.P., "Experimental Evaluation of Seismic Design Methods for Broad Cylindrical Tanks", University of California, Berkeley, Earthquake Engineering Research Center Report No. UCB/EERC-77/10, May 1977.

5.2 Niwa, A., "Seismic Behavior of Tall Liquid Storage Tanks", University of California, Berkeley, Earthquake Engineering Research Center Report No. UCB/EERC-78/04, February 1978.

5.3 Clough, R.W. and Niwa, A., "Static Tilt Tests of a Tall Cylindrical Liquid Storage Tank", University of California, Berkeley, Earthquake Engineering Research Center Report No. UCB/EERC-79/06, February 1979.

5.4 Housner, G.W. and Vreeland, T., "The Analysis of Stress and Deformation", Division of Engineering and Applied Science, California Institute of Technology, pp. 166-168.

5.5 Hutton, R.E., "An Investigation of Resonant, Nonlinear, Nonplanar Free Surface Oscillations of a Fluid", NASA TN D-1870, May 1963.

5.6 Wozniak, R.S. and Mitchell, W.W., "Basis of Seismic Design Provisions for Welded Steel Oil Storage Tanks; Proposed Appendix P to API Standard 650", API Convention, Toronto, May 1978.

5.7 Haroun, M.A., "Dynamic Analysis of Liquid Storage Tanks", Ph.D. Dissertation, California Institute of Technology, Pasadena, California, December 1979.

APPENDIX A: THE HYDRODYNAMIC BEHAVIOR OF RIGID TANKS

A.1 SYSTEM AND ASSUMPTIONS

The system considered is shown in fig. A.1. It is a rigid circular cylinder of radius, R, fixed to a rigid base. The tank is filled with a fluid of density ρ_ℓ to a level H. The fluid-tank system is presumed to be subjected to a small horizontal ground motion $x_g(t)$ directed along the x-axis. The system coordinates are also shown in fig. A.1. The r, θ, and z denote the radial, circumferential and vertical coordinates, respectively. In a consideration of the different factors affecting the motion of the liquid, the following conventional assumptions are made:

1. The fluid is homogeneous, inviscid and incompressible.
2. The flow field is irrotational.
3. There are no sources, sinks or cavities anywhere in the flow field.
4. The free surface boundary conditions for the liquid are linearized.

A.2 GOVERNING EQUATION AND BOUNDARY CONDITIONS

For the irrotational flow of an incompressible inviscid liquid, the velocity potential, $\Phi(r,\theta,z,t)$, satisfies the Laplace equation, i.e.,

$$\nabla^2\Phi = \frac{\partial^2\Phi}{\partial r^2} + \frac{1}{r}\frac{\partial\Phi}{\partial r} + \frac{1}{r^2}\frac{\partial^2\Phi}{\partial\theta^2} + \frac{\partial^2\Phi}{\partial z^2} = 0 \qquad (A.1)$$

in the region occupied by the fluid. The velocity components of the fluid in the radial, circumferential and vertical directions are given by

$$\begin{aligned} V_r &= -\frac{\partial\Phi}{\partial r} \\ V_\theta &= -\frac{1}{r}\frac{\partial\Phi}{\partial\theta} \\ V_z &= -\frac{\partial\Phi}{\partial z} \end{aligned} \qquad (A.2)$$

In addition to being a harmonic function, Φ must satisfy the proper boundary conditions which can be expressed as follows:

(a) At the bottom of rigid tank, the liquid velocity in the vertical direction is zero

$$\frac{\partial\Phi}{\partial z}(r, \theta, -H, t) = 0 \qquad (A.3)$$

(b) The radial velocity component of the liquid at r=R must be equal to the corresponding component of the ground motion. This boundary condition can be approximately given by

$$\frac{\partial\Phi}{\partial r}(R, \theta, z, t) = \dot{x}_g(t)\cos\theta \qquad (A.4)$$

(c) At the liquid free surface, $z = \eta(r,\theta,t)$, two boundary conditions must be imposed. The first one is called the kinematic condition which states that a fluid particle on the free surface will always remain on the free surface. The other one is the dynamic condition which specifies that the pressure on the free surface is zero. By considering small free surface response, these two boundary conditions at the free surface

can be expressed respectively by

$$\frac{\partial \Phi(r,\theta,0,t)}{\partial z} = \frac{\partial \eta(r,\theta,t)}{\partial t} \tag{A.5a}$$

$$\frac{\partial \Phi(r,\theta,0,t)}{\partial t} + g\eta(r,\theta,t) = 0 \tag{A.5b}$$

in which the second-order terms are neglected. The Bernoulli equation has been used to formulate (A.5b). Where $\eta(r,\theta,t)$ is the free surface displacement of liquid and g is the gravity acceleration. Equation (A.5a) and (A.5b) can be combined to yield the following equation which involves only the velocity potential

$$\frac{\partial^2 \Phi(r,\theta,0,t)}{\partial t^2} + g\frac{\partial \Phi(r,\theta,0,t)}{\partial z} = 0 \tag{A.5}$$

A.3 DERIVATION OF VELOCITY POTENTIAL

The velocity potential, Φ, can be derived by solving the partial differential equation (A.1) with the corresponding boundary conditions (A.3)-(A.5). By using the method of separation of variables

$$\Phi = \bar{R}(r)\ \bar{\Theta}(\theta)\ \bar{Z}(z)\ \bar{T}(t) \tag{A.6}$$

The governing equation (A.1) becomes

$$\frac{1}{\bar{R}}\frac{d^2\bar{R}}{dr^2} + \frac{1}{r\bar{R}}\frac{d\bar{R}}{dr} + \frac{1}{r^2\bar{\Theta}}\frac{d^2\bar{\Theta}}{d\theta^2} + \frac{1}{\bar{Z}}\frac{d^2\bar{Z}}{dz} = 0 \tag{A.7}$$

Let

$$\frac{1}{\bar{Z}}\frac{d^2\bar{Z}}{dz^2} = k \quad \text{and} \quad \frac{d^2\bar{\theta}}{d\theta^2}\frac{1}{\bar{\theta}} = -m^2 \tag{A.8}$$

then $\bar{Z}(z)$ and $\bar{\theta}(\theta)$ can be found as follows

$$\bar{Z}(z) = \begin{cases} C_1 \sinh(kz) + C_2 \cosh(kz), & k\neq 0 \\ C_3 Z + C_4 , & k=0 \end{cases} \tag{A.9}$$

$$\bar{\theta}(\theta) = C_5 \cos(m\theta) + C_6 \sin(m\theta) \tag{A.10}$$

Substituting equation (A.8), equation (A.7) becomes

$$r^2\frac{d^2\bar{R}}{dr^2} + r\frac{d\bar{R}}{dr} + (k^2r^2-m^2)\bar{R} = 0 \tag{A.11}$$

therefore, $\bar{R}(r)$ can be expressed by

$$\bar{R}(r) = \begin{cases} C_7 J_m(kr) + C_8 Y_m(kr), & k\neq 0 \\ C_9 r^m + C_{10} r^{-m} , & k=0 \end{cases} \tag{A.12}$$

where J_m, Y_m are the Bessel function of the first and the second kind of order m, respectively; and C_n, n= 1,2,...,10, are constants. Since the solution is bounded at r=0, but $Y_m(0)$ and r^{-m} are singular at r=0, hence $C_8=C_{10}= 0$. From equations (A.9), (A.10) and (A.12), the velocity potential can be expressed by

$$\begin{aligned} \Phi(r,\theta,z,t) = {} & C_9 r^m [C_5\cos(m\theta) + C_6\sin(m\theta)](C_3 Z+C_4)\bar{T}(t) + \\ & C_7 J_m(kr)[C_1\sinh(kz) + C_2\cosh(kz)][C_5\cos(m\theta)+ \\ & + C_6\sin(m\theta)]\bar{T}(t) \end{aligned} \tag{A.13}$$

Substituting equation (A.13) into the boundary condition (A.4), the following equation can be found

$$\{C_9 m R^{m-1}(C_3 Z+C_4) + C_7 k J'_m(kR)[C_1 \sinh(kz) + C_2 \cosh(kz)]\}.$$

$$[C_5 \cos(m\theta) + C_6 \sin(m\theta)]\bar{T}(t) = \dot{x}_g(t)\cos\theta \qquad (A.14)$$

Which implies that m=1, $C_6=0$, $C_3=0$, $J'_m(kR)=0$ and $C_4 C_5 C_9 \bar{T}(t) = \dot{x}_g(t)$. The velocity potential, Φ, can be rewritten as follows

$$\Phi(r,\theta,z,t) = \dot{x}_g(t) r\cos\theta + \sum_{n=1}^{\infty} C_n(t) J_1\left(\frac{\xi_n r}{R}\right)\cos\theta$$

$$\left[C_{n1}\sinh\left(\frac{\xi_n z}{R}\right) + C_{n2}\cosh\left(\frac{\xi_n z}{R}\right)\right] \qquad (A.15)$$

where ξ_n such that $J'_1(\xi_n) = 0$; C_{n1}, C_{n2} are constants and $C_n(t)$ is function of time, t, only. Applying the boundary condition (A.3), we can find the C_{n1} in term of C_{n2},

$$C_{n1} = C_{n2} \tanh\left(\frac{\xi_n H}{R}\right) \qquad (A.16)$$

The velocity potential can be further organized as follows

$$\Phi(r,\theta,z,t) = \dot{x}_g(t) r\cos\theta + \sum_{n=1}^{\infty} \beta_n(t) J_1\left(\frac{\xi_n r}{R}\right)\cos\theta \frac{\cosh\left(\frac{\xi_n (H+z)}{R}\right)}{\cosh\left(\frac{\xi_n H}{R}\right)} \qquad (A.17)$$

where $\beta_n(t)$ can be determined by the boundary condition (A.5); substituting equation (A.17) into equation (A.5) will give, to linear order in the inertial frame of reference, the following equation

$$\ddot{x}_g(t)r\cos\theta + \sum_{n=1}^{\infty} \ddot{\beta}_n(t) J_1\left(\frac{\xi_n r}{R}\right)\cos\theta + \sum_{n=1}^{\infty} g\beta_n(t) J_1\left(\frac{\xi_n r}{R}\right)\cos\theta$$

$$\frac{\xi_n}{R} \tanh\left(\frac{\xi_n H}{R}\right) = 0 \qquad (A.18)$$

Taking the Laplace transform of equation (A.18) with the zero initial conditions results in

$$s^3 x_g(s) r\cos\theta + \sum_{n=1}^{\infty} \beta_n(s) J_1\left(\frac{\xi_n r}{R}\right)(s^2 + \omega_n^2)\cos\theta = 0 \qquad (A.19)$$

where

$$\omega_n^2 = \frac{g\xi_n}{R} \tanh\left(\frac{\xi_n H}{R}\right) \qquad (A.20)$$

Applying the orthogonality properties of the Bessel's function, equation (A.19) will give

$$\beta_n(s) = - \frac{s^3 x_g(s)}{s^2 + w_n^2} \frac{2R}{(\xi_n^2-1)\ J_1(\xi_n)} \qquad (A.21)$$

Therefore,

$$\Phi(s) = s x_g(s) r\cos\theta - \sum_{n=1}^{\infty} \frac{s^3 x_g(s)\cos\theta}{s^2 + \omega_n^2} \frac{2R J_1\left(\frac{\xi_n r}{R}\right)}{(\xi_n^2-1) J_1(\xi_n)} \cdot$$

$$\frac{\cosh\left(\frac{\xi_n}{R}(z+H)\right)}{\cosh\left(\frac{\xi_n H}{R}\right)} \qquad (A.22a)$$

i.e.

$$\Phi(t)= \dot{x}_g(t)r\cos\theta - \sum_{n=1}^{\infty} \frac{2R\cos\theta J_1(\frac{\xi_n r}{R})}{(\xi_n^2-1)J_1(\xi_n)} \frac{\cosh(\frac{\xi_n(z+H)}{R})}{\cosh(\frac{\xi_n H}{R})} \int_0^t \ddot{x}_g(\tau).$$

$$\cos\omega_n(t-\tau)d\tau \qquad (A.22)$$

where ω_n is defined in equation (A.20)

A.4 HYDRODYNAMIC PRESSURE AND FREE SURFACE DISPLACEMENT

Both the pressure distribution, $p(r,\theta,z,t)$, and the free surface displacement, $\eta(r,\theta,t)$, can be determined from the Bernoulli equation and are given, respectively, by

$$P(r,\theta,z,t) = -\rho_\ell \frac{\partial\Phi}{\partial t} - \rho_\ell gz \qquad (A.23)$$

$$\eta(r,\theta,t) = -\frac{1}{g}\frac{\partial\Phi(r,\theta,0,t)}{\partial t} \qquad (A.24)$$

where the nonlinear term $\nabla\Phi\cdot\nabla\Phi$ is neglected as being quadratically small. It should be noted that the pressure $p(r,\theta,z,t)$ in equation (A.23) is the sum of the hydrostatic pressure $P_s = -\rho_\ell gz$ and the hydrodynamic pressure $P_d = -\rho_\ell\frac{\partial\Phi}{\partial t}$. Therefore, from equation (A.22), the hydrodynamic pressure can be expressed as follows.

$$P_d(r,\theta,z,t) = -\rho_\ell \ddot{x}_g(t)\cos\theta \left\{ r - \sum_{n=1}^{\infty} \frac{2RJ_1(\frac{\xi_n r}{R})}{(\xi_n^2-1)J_1(\xi_n)} \frac{\cosh(\frac{\xi_n(z+H)}{R})}{\cosh(\frac{\xi_n H}{R})} \right\}$$

$$+ \rho_\ell \sum_{n=1}^{\infty} \frac{2R\cos\theta J_1(\frac{\xi_n r}{R})\cosh(\frac{\xi_n(H+z)}{R})}{(\xi_n^2-1)\ J_1(\xi_n)\ \cosh(\frac{\xi_n H}{R})} \int_0^t \omega_n \ddot{x}_g(\tau)\sin\omega_n(t-\tau)d\tau \qquad (A.25)$$

This hydrodynamic pressure, P_d, can be separated into two parts. The first part is called the impulsive pressure, P_I, which is proportional to the ground acceleration. It can be observed in equation (A.25) and is given by

$$P_I(r,\theta,z,t) = -\rho_\ell \ddot{x}_g(t)\cos\theta \left\{ r - \sum_{n=1}^{\infty} \frac{2RJ_1(\frac{\xi_n r}{R})\cosh(\frac{\xi_n(z+H)}{R})}{(\xi_n^2-1)J_1(\xi_n)\cosh(\frac{\xi_n H}{R})} \right\} \qquad (A.26)$$

The other part is called the convective pressure, P_c, which is caused by the sloshing of the liquid (ω_n). It can also be given from the second part of equation (A.25) and expressed by

$$P_c(r,\theta,z,t) = \rho_\ell \sum_{n=1}^{\infty} \frac{2R\cos\theta J_1(\frac{\xi_n r}{R})\cosh(\frac{\xi_n(H+z)}{R})}{(\xi_n^2-1)J_1(\xi_n)\cosh(\frac{\xi_n H}{R})} \int_0^t \omega_n \ddot{x}_g(\tau) \cdot$$

$$\cdot \sin\omega_n(t-\tau)d\tau \qquad (A.27)$$

The surface displacement can be found from equation (A.22) and (A.24) and is given by

$$\eta(r,\theta,t) = \frac{-\ddot{x}_g(t)\cos\theta}{g}\left[r - \sum_{n=1}^{\infty} \frac{2RJ_1(\frac{\xi_n r}{R})}{(\xi_n^2-1)J_1(\xi_n)}\right] -$$

$$\frac{\cos\theta}{g}\sum_{n=1}^{\infty} \frac{2RJ_1(\frac{\xi_n r}{R})}{(\xi_n-1)J_1(\xi_n)} \int_0^t \omega_n \ddot{x}_g(\tau)\sin\omega_n(t-\tau)d\tau \qquad (A.28)$$

The maximum surface displacement, η_m, occurs at r=R and $\theta=0^o$, then

$$\eta_m = \frac{-1}{g}\sum_{n=1}^{\infty} \frac{2R}{(\xi_n^2-1)} \int_0^t \omega_n \ddot{x}_g(\tau)\sin\omega_n(t-\tau)d\tau \qquad (A.29)$$

It should be noted that the relation

$$1 - \sum_{n=1}^{\infty} \frac{2}{\xi_n^2-1} = 0 \qquad (A.30)$$

has been used to derive equation (A.30). The integral is the well known Duhamel's integral which represents the pseudo-acceleration of a single-degree-of-freedom system having a circular natural frequency ω_n and subjected to the prescribed ground acceleration $\ddot{x}_g(t)$.

APPENDIX B POTENTIAL ENERGY OF A CIRCULAR CYLINDER PARTIALLY FILLED WITH LIQUID

The potential energy of a circular cylindrical fluid-filled tank (figure 4.10) can be formulated and given [4.13] by

$$V = \int_{-t_{s/2}}^{t_{s/2}} \int_{0}^{2\pi} \int_{0}^{L} \frac{1}{2}(\sigma_{x,s}\varepsilon_x + \sigma_{y,s}\varepsilon_y + \tau_{xy,s}\gamma_{xy})R\,dx\,d\theta\,dz$$

$$+\int_{-t_{s/2}}^{t_{s/2}} \int_{0}^{2\pi} \int_{0}^{L} (\sigma_{x,f}\varepsilon_x + \sigma_{y,f}\varepsilon_y + \tau_{xy,f}\gamma_{xy})R\,dx\,d\theta\,dz \qquad (B.1)$$

The shell elastic stresses can be expressed in terms of stains

$$\sigma_{x,s} = \frac{E}{1-\nu^2}(\varepsilon_x + \nu\varepsilon_y)$$

$$\sigma_{y,s} = \frac{E}{1-\nu^2}(\varepsilon_y + \nu\varepsilon_x) \qquad (B.2)$$

$$\tau_{xy,s} = \frac{E}{2(1+\nu)}\gamma_{xy}$$

The strains ε_x, ε_y and γ_{xy} in the element at a distance z from the middle surface of the shell are related to the middle-surface stains ε_1, ε_2 and γ_{12} and to the changes of curvature and twist κ_1, κ_2 and κ_{12} by the expression

$$\varepsilon_x = \varepsilon_1 - z\kappa_1$$

$$\varepsilon_y = \varepsilon_2 - z\kappa_2$$

$$\gamma_{xy} = \gamma_{12} - 2z\kappa_{12}$$

With the assumption that the stresses due to the hydrostatic pressure, $\sigma_{x,f}$, $\sigma_{y,f}$, and $\tau_{xy,f}$, are constant across the thickness of the shell, the equation (B.1) can be reduced to be

$$V = \frac{Et_s}{2(1-\nu^2)} \int_0^{2\pi} \int_0^{L} (\varepsilon_1^2 + \varepsilon_2^2 + 2\nu\varepsilon_1\varepsilon_2 + \frac{1-\nu}{2}\gamma^2)\, R\, dx\, d\theta$$
$$+ \frac{Et_3^3}{24(1-\nu^2)} \int_0^{2\pi} \int_0^{L} [\kappa_1^2 + \kappa_2^2 + 2\nu\kappa_1\kappa_2 + 2(1-\nu)\kappa_{12}^2]\, R\, dx\, d\theta \qquad (B.4)$$
$$+ t_s \int_0^{2\pi} \int_0^{L} (\sigma_{x,f}\varepsilon_1 + \sigma_{y,f}\varepsilon_2 + \tau_{xy,f}\gamma_{12})\, R\, dx\, d\theta$$

The first term of equation (B.4) represents the stretching energy of the middle-surface deformation, the second term represents the bending energy of the shell wall and the third term is the strain energy caused by the hydrostatic pressure. The middle surface strains and the changes of curvature and twist can be expressed in terms of the displacements, u,v, and w, as follows

$$\varepsilon_1 = \frac{\partial u}{\partial x} + \frac{1}{2}\left[\left(\frac{\partial u}{\partial x}\right)^2 + \left(\frac{\partial v}{\partial x}\right)^2 + \left(\frac{\partial w}{\partial x}\right)^2 \right]$$

$$\varepsilon_2 = \frac{1}{R}\frac{\partial v}{\partial \theta} - \frac{w}{R} + \frac{1}{2R^2}\left[\left(\frac{\partial u}{\partial \theta}\right)^2 + \left(\frac{\partial v}{\partial \theta}\right)^2 + \left(\frac{\partial w}{\partial \theta}\right)^2 \right] \qquad (B.5)$$

$$\gamma_{12} = \frac{1}{R}\frac{\partial u}{\partial \theta} + \frac{\partial v}{\partial x} + \frac{1}{R}\left[\frac{\partial w}{\partial x}\frac{\partial w}{\partial \theta} + \frac{\partial v}{\partial x}\frac{\partial w}{\partial \theta} + \frac{\partial u}{\partial x}\frac{\partial w}{\partial \theta} \right]$$

$$\kappa_1 = \frac{\partial^2 w}{\partial x^2}$$

$$\kappa_2 = \frac{1}{R^2}\left(\frac{\partial^2 w}{\partial \theta^2} + \frac{\partial v}{\partial \theta}\right) \qquad (B.6)$$

$$\kappa_{12} = \frac{1}{R}\frac{\partial}{\partial x}\left(\frac{\partial w}{\partial \theta} + v\right)$$

The stresses due to hydrostatic pressure are given by

$$\sigma_{x,f} = \tau_{xy,f} = 0 , \qquad \text{for } 0 < x < L$$

$$\sigma_{y,f} = \frac{\rho_\ell R}{t_s}(D - x), \qquad \text{for } 0 < x < D \qquad (B.7)$$

$$\sigma_{y,f} = 0 , \qquad \text{for } D < x < L$$

Substituting equations (B.5), (B.6), and (B.7) into equation (B.4), the potential energy will be expressed in terms of the displacements u,v and w as follows

$$V = \frac{Et_s}{2(1-\nu^2)} \int_0^{2\pi}\int_0^{L} \left[\left(\frac{\partial u}{\partial x}\right)^2 + \frac{1}{R^2}\left(\frac{\partial v}{\partial \theta} - w\right)^2 + \frac{2\nu}{R}\frac{\partial u}{\partial x}\left(\frac{\partial v}{\partial \theta} - w\right) + \frac{1-\nu}{2}\left(\frac{1}{R}\frac{\partial u}{\partial \theta} + \frac{\partial v}{\partial x}\right)^2\right] R\, dx\, d\theta + \frac{Et_s^3}{24(1-\nu^2)} \int_0^{2\pi}\int_0^{L} \left[\left(\frac{\partial^2 w}{\partial x^2}\right)^2 + \frac{1}{R^4}\left(\frac{\partial^2 w}{\partial \theta^2} + \frac{\partial v}{\partial \theta}\right)^2 + \frac{2\nu}{R^2}\frac{\partial^2 w}{\partial x^2}\left(\frac{\partial^2 w}{\partial \theta^2} + \frac{\partial v}{\partial \theta}\right) + \frac{2(1-\nu)}{R^2}\left(\frac{\partial^2 w}{\partial x \partial \theta} + \frac{\partial v}{\partial x}\right)^2\right] R\, dx\, d\theta + \rho_\ell g R \int_0^{2\pi}\int_0^{D} (D-x)\left[\frac{1}{R}\frac{\partial v}{\partial \theta} - \frac{w}{R} + \frac{1}{2R^2}\left(\frac{\partial u}{\partial \theta}\right)^2 +$$

$$\frac{1}{2R^2}\left(\frac{\partial v}{\partial \theta}\right)^2 + \frac{1}{2R^2}\left(\frac{\partial w}{\partial \theta}\right)^2 R\, dx\, d\theta \qquad (B.8)$$

It should be noted that the second-order terms of equation (B.5) are neglected in the evaluation of the first integral of equation (B.4) since they are small compared with the first-order terms, but they are the main contributions of the third integral of the equation (B.4) because the integration from 0 to 2π on the first-order terms will be equal to zero. Making the simplifying assumptions associated with Donnell shell theory, the expression (B.8) can be rewritten as

$$V = \frac{Et_s}{2(1-\nu^2)}\int_0^{2\pi}\int_0^{L}\left[\left(\frac{\partial u}{\partial x}\right)^2 + \frac{1}{R^2}\left(\frac{\partial v}{\partial \theta} - w\right)^2 + \frac{2\nu}{R}\frac{\partial u}{\partial x}\left(\frac{\partial v}{\partial \theta} - w\right) + \frac{1-\nu}{2}\left(\frac{1}{R}\frac{\partial u}{\partial \theta} + \frac{\partial v}{\partial x}\right)^2\right] R\, dx\, d\theta + \frac{Et_s^3}{24(1-\nu^2)}\int_0^{2\pi}\int_0^{L}\left[\left(\frac{\partial^2 w}{\partial x^2}\right)^2 + \frac{1}{R^4}\left(\frac{\partial^2 w}{\partial \theta^2}\right)^2 + \frac{2\nu}{R^2}\frac{\partial^2 w}{\partial x^2}\frac{\partial^2 w}{\partial \theta^2} + \frac{2(1-\nu)}{R^2}\left(\frac{\partial^2 w}{\partial x \partial \theta}\right)^2\right] R\, dx\, d\theta + \rho_\ell g R\int_0^{2\pi}\int_0^{D}(D-x)\left[\frac{1}{R}\frac{\partial v}{\partial \theta} - \frac{w}{R} + \frac{1}{2R^2}\left(\frac{\partial w}{\partial \theta}\right)^2\right] R\, dx\, d\theta \qquad (B.9)$$

APPENDIX C FREQUENCY EQUATIONS

(a) ONE TERM APPROXIMATION (N = 1)

If N = 1, only the first term of the series in equation (4.5) is retained and the displacement expressions are as follows

$$U = \bar{U}_1(t)\cos n\theta[\sinh(\lambda_1 x)+\sin(\lambda_1 x) - k_1(\cosh(\lambda_1 x)-\cos(\lambda_1 x)]$$

$$V = \bar{V}_1(t)\sin n\theta[\cosh(\lambda_1 x)-\cos(\lambda_1 x) - k_1(\sinh(\lambda_1 x)-\sin(\lambda_1 x)] \quad (C.1)$$

$$W = \bar{W}_1(t)\cos n\theta[\cosh(\lambda_1 x)-\cos(\lambda_1 x) - k_1(\sinh(\lambda_1 x)-\sin(\lambda_1 x)]$$

where $\lambda_1 L = 1.875$ and $k_1 = 1.348$, and the frequency determinant can be given by

$$\begin{vmatrix}
\langle\psi_1'\psi_1'\rangle+\frac{1-\nu}{2}\frac{n^2}{R^2}\langle\psi_1\psi_1\rangle & \frac{\nu n}{R}\langle\psi_1'\phi_1\rangle-\frac{(1-\nu)n}{2R}\langle\psi_1\phi_1'\rangle & \frac{-\nu}{R}\langle\psi_1'\phi_1\rangle \\
+Q\langle\psi_1\psi_1\rangle_D-\Delta\langle\psi_1\psi_1\rangle & & \\
\frac{\nu n}{R}\langle\phi_1\psi_1'\rangle-\frac{(1-\nu)n}{2R}\langle\psi_1\phi_1'\rangle & \frac{n^2}{R^2}\langle\phi_1\phi_1\rangle+\frac{1-\nu}{2}\langle\phi_1'\phi_1'\rangle+K\cdot & \frac{-n}{R^2}(1+n^2K)\langle\phi_1\phi_1\rangle+ \\
 & [\frac{n^2}{R^2}\langle\phi_1\phi_1\rangle+2(1-\nu)\langle\phi_1'\phi_1'\rangle] & \nu Kn\langle\phi_1''\phi_1\rangle- \\
 & +Q\langle\phi_1\phi_1\rangle_D-\Delta\langle\phi_1\phi_1\rangle & 2(1-\nu)n\langle\phi_1'\phi_1'\rangle \\
\frac{-\nu}{R}\langle\psi_1'\phi_1\rangle & \frac{-n}{R^2}(1+n^2K)\langle\phi_1\phi_1\rangle+\nu Kn\langle & \frac{1}{R^2}(1+n^4K)\langle\phi_1\phi_1\rangle+R^2K \\
 & \phi_1''\phi_1\rangle-2(1-\nu)n\langle\phi_1'\phi_1'\rangle & \langle\phi_1''\phi_1''\rangle-2\nu Kn^2\langle\phi_1''\phi_1\rangle \\
 & & +4(1-\nu^2)K\langle\phi_1'\phi_1'\rangle+Q \\
 & & \langle\phi_1\phi_1\rangle_D-\Delta\langle\phi_1\phi_1\rangle-\Delta\frac{C_{vn}\rho_\ell R}{\rho_s t_s}\langle\langle\phi_1\phi_1\rangle\rangle
\end{vmatrix} = 0 \quad (C.2)$$

where

$$Q = \frac{\rho_\ell g(1-\nu^2)n^2}{Et_sR} \quad ; \quad K = \frac{t_s^2}{12R^2}$$

(b) TWO TERM APPROXIMATION (N=2)

If N=2, only two terms of the series in the deflection functions are retained and the displacements are given by

$$U = \bar{U}_1(t)\cos n\theta[\sinh(\lambda_1 x)+\sin(\lambda_1 x) - k_1(\cosh(\lambda_1 x)-\cos(\lambda_1 x)] +$$
$$\bar{U}_2(t)\cos n\theta[\sinh(\lambda_2 x)+\sin(\lambda_2 x) - k_2(\cosh(\lambda_2 x)-\cos(\lambda_2 x)]$$

$$V = \bar{V}_1(t)\cos n\theta[\cosh(\lambda_1 x)-\cos(\lambda_1 x) - k_1(\sinh(\lambda_1 x)-\sin(\lambda_1 x))]+$$
$$\bar{V}_2(t)\cos n\theta[\cosh(\lambda_2 x)-\cos(\lambda_2 x) - k_2(\sinh(\lambda_2 x)-\sin(\lambda_2 x)]$$

$$W = \bar{W}_1(t)\cos n\theta[\cosh(\lambda_1 x)-\cos(\lambda_1 x) - k_1(\sinh(\lambda_1 x)-\sin(\lambda_1 x))]+$$
$$\bar{W}_2(t)\cos n\theta[\cosh(\lambda_2 x)-\cos(\lambda_2 x) - k_2(\sinh(\lambda_2 x)-\sin(\lambda_2 x))]$$

where $\lambda_1 L = 1.875$, $\lambda_2 L = 4.694$; $k_1 = 1.348$, $k_2 = 1.018$. The frequency equation of the two term approximation can be expressed as follows

$$[E] = \Delta[F] \qquad (C.4)$$

where $\Delta = \frac{(1-\nu^2)\rho_s\omega^2}{E}$ and [E], [F] are 6x6 matrices, the elements of [E] and [F] are given by

$$E_{11} = \langle\psi_1'\psi_1'\rangle + \frac{1-\nu}{2}\frac{n^2}{R^2}\langle\psi_1\psi_2\rangle + \frac{\rho_\ell g(1-\nu^2)n^2}{Et_sR}\langle\psi_1\psi_1\rangle_D$$

$$E_{12} = E_{21} = \frac{\nu n}{R}\langle\psi_1'\phi_1'\rangle - \frac{(1-\nu)n}{2R}\langle\phi_1'\psi_1\rangle$$

$$E_{13} = E_{31} = -\frac{\nu}{R}\langle\psi_1'\phi_1\rangle$$

$$E_{14} = E_{41} = \langle\psi_1'\psi_2'\rangle + \frac{1-\nu}{2}\frac{n^2}{R^2}\langle\psi_1\psi_1\rangle + \frac{\rho_\ell g(1-\nu^2)}{Et_sR}\langle\psi_1\psi_2\rangle_D$$

$$E_{15} = E_{51} = \frac{\nu n}{R}\langle\psi_1'\phi_2\rangle - \frac{(1-\nu)n}{2R}\langle\psi_1\phi_2'\rangle$$

$$E_{16} = E_{61} = -\frac{\nu}{R}\langle\psi_1'\phi_2\rangle$$

$$E_{22} = \frac{n^2}{R^2}\langle\phi_1\phi_1\rangle + \frac{1-\nu}{2}\langle\phi_1'\phi_1'\rangle + \frac{t_s^2}{12R^2}\left[\frac{n^2}{R^2}\langle\phi_1\phi_1\rangle + 2(1-\nu)\langle\phi_1'\phi_1'\rangle\right] + \frac{\rho_\ell g(1-\nu^2)n^2}{Et_sR}\langle\phi_1\phi_1\rangle_D$$

$$E_{23} = E_{32} = \frac{-n}{R}\langle\phi_1\phi_1\rangle + \frac{t_s^2}{12R^2}\left[\frac{-n^2}{R^2}\langle\phi_1\phi_1\rangle + \nu n\langle\phi_1''\phi_1\rangle - 2(1-\nu)n\langle\phi_1'\phi_1'\rangle\right]$$

$$E_{24} = E_{42} = \frac{\nu n}{R}\langle\psi_2'\phi_1\rangle - \frac{(1-\nu)n}{2R}\langle\psi_2\phi_1'\rangle$$

$$E_{25} = E_{52} = \frac{n^2}{R^2}\langle\phi_1\phi_2\rangle + \frac{1-\nu}{2}\langle\phi_1'\phi_2'\rangle + \frac{t_s^2}{12R^2}\left[\frac{n^2}{R^2}\langle\phi_1\phi_2\rangle + 2(1-\nu)\langle\phi_1'\phi_2'\rangle\right] + \frac{\rho_\ell g(1-\nu^2)n^2}{Et_sR}\langle\phi_1\phi_2\rangle_D$$

$$E_{26} = E_{62} = \frac{-n}{R^2}\langle\phi_1\phi_2\rangle + \frac{t_s^2}{12R^2}\left[\frac{-n}{R^2}\langle\phi_1\phi_2\rangle + \nu n\langle\phi_1''\phi_2\rangle - 2(1-\nu)n\langle\phi_1'\phi_2'\rangle\right]$$

$$E_{33} = \frac{1}{R^2}\langle\phi_1\phi_1\rangle + \frac{t_s^2}{12R^2}\left[R^2\langle\phi_1''\phi_1''\rangle + \frac{n^4}{R^2}\langle\phi_1\phi_1\rangle - 2\nu n^2\langle\phi_1''\phi_1\rangle + 2(1-\nu)n^2\langle\phi_1'\phi_1'\rangle\right] + \frac{\rho_\ell g(1-\nu^2)n^2}{Et_sR}\langle\phi_1\phi_1\rangle_D$$

$$E_{34} = E_{43} = \frac{-\nu}{R}\langle\psi_2'\phi_2\rangle$$

$$E_{35} = E_{53} = \frac{-n}{R^2}\langle\phi_2\phi_1\rangle + \frac{t_s^2}{12R^2}\left[\frac{-n^2}{R^2}\langle\phi_2\phi_1\rangle + \nu n\langle\phi_2''\phi_1\rangle - 2(1-\nu)n\langle\phi_1'\phi_2'\rangle\right]$$

$$E_{36}=E_{63}=\frac{1}{R^2}\langle\phi_1\phi_2\rangle+\frac{t_s^2}{12R^2}\left[R^2\langle\phi_1''\phi_2''\rangle+\frac{n^4}{R^2}\langle\phi_1\phi_2\rangle-2\nu n^2\langle\phi_2''\phi_1\rangle+2(1-\nu)n^2\langle\phi_2'\phi_1'\rangle\right]+\frac{\rho_\ell g(1-\nu^2)n^2}{Et_sR}\langle\phi_2\phi_1\rangle_D$$

$$E_{44}=\langle\psi_2'\psi_2'\rangle+\frac{1-\nu}{2}\frac{n^2}{R^2}\langle\psi_2\psi_2\rangle+\frac{\rho_\ell g(1-\nu^2)n^2}{Et_sR}\langle\psi_2\psi_2\rangle_D$$

$$E_{45}=E_{54}=\frac{\nu n}{R}\langle\psi_2'\psi_2\rangle-\frac{(1-\nu)n}{2R}\langle\psi_2\phi_2'\rangle$$

$$E_{46}=E_{64}=\frac{-\nu}{R}\langle\psi_2'\phi_2\rangle$$

$$E_{55}=\frac{n^2}{R^2}\langle\phi_2\phi_2\rangle+\frac{1-\nu}{2}\langle\phi_2'\phi_2'\rangle+\frac{t_s^2}{12R^2}\left[\frac{n^2}{R^2}\langle\phi_2\phi_2\rangle+2(1-\nu)\langle\phi_2'\phi_2'\rangle\right]+\frac{\rho_\ell g(1-\nu^2)n^2}{Et_sR}\langle\phi_2\phi_2\rangle_D$$

$$E_{56}=E_{65}=\frac{-n}{R}\langle\phi_2\phi_2\rangle+\frac{t_s^2}{12R^2}\left[\frac{-n}{R^2}\langle\phi_2\phi_2\rangle+\nu n\langle\phi_2''\phi_2\rangle-2(1-\nu)n\langle\phi_2'\phi_2'\rangle\right]$$

$$E_{66}=\frac{1}{R^2}\langle\phi_2\phi_2\rangle+\frac{t_s^2}{12R^2}\left[R^2\langle\phi_2''\phi_2''\rangle+\frac{n^4}{R^2}\langle\phi_2\phi_2\rangle-2\nu n^2\langle\phi_2''\phi_2\rangle+2(1-\nu)n^2\langle\phi_2'\phi_2'\rangle\right]+\frac{\rho_\ell g(1-\nu^2)n^2}{Et_sR}\langle\phi_2\phi_2\rangle_D$$

$$F_{11}=\langle\psi_1\psi_1\rangle$$

$$F_{12}=F_{21}=\langle\psi_1\psi_2\rangle$$

$$F_{22}=\langle\psi_2\psi_2\rangle$$

$$F_{33}=\langle\phi_1\phi_1\rangle$$

$$F_{34}=F_{43}=\langle\phi_1\phi_2\rangle$$

$$F_{44} = \langle\phi_2\phi_2\rangle$$

$$F_{55} = \langle\phi_1\phi_1\rangle + \frac{C_{vn}\rho_\ell R}{\rho_s t_s}\langle\langle\phi_1\phi_1\rangle\rangle$$

$$F_{56} = F_{65} = \langle\phi_1\phi_2\rangle + \frac{C_{vn}\rho_\ell R}{\rho_s t_s}\langle\langle\phi_1\phi_2\rangle\rangle$$

$$F_{66} = \langle\phi_2\phi_2\rangle + \frac{C_{vn}\rho_\ell R}{\rho_s t_s}\langle\langle\phi_2\phi_2\rangle\rangle$$

$$F_{ij} = 0, \text{ otherwise}$$

The symbols, $\langle A\rangle$, $\langle A\rangle_D$, $\langle\langle A\rangle\rangle$, A' and A'' are defined as follows:

$$\langle A\rangle = \int_0^L A\, dx$$

$$\langle A\rangle_D = \int_0^D (D-x)A\, dx$$

$$\langle\langle A\rangle\rangle = \int_0^D A\, dx$$

$$A' = \frac{dA}{dx} \quad \text{and} \quad A'' = \frac{d^2A}{dx^2}$$

APPENDIX D - RESPONSE OF AN UNANCHORED TANK SUBJECTED TO OVERTURNING MOMENT

The formulas for maximum longitudinal compressive force in the shell of an unanchored tank are recommended in reference 5.6, but the application of these formulas is questionable. This can be observed from the comparison of the stress listed in table 5.2. The experimental results [5.3] indicate that the stresses predicted from ref. 5.6 are too much underestimated in this specific tank. In this appendix, an analytic model for predicting the maximum axial stress in the shell wall of an unanchored tank is developed. The results are also compared with the experimental data as shown in table 5.2. It shows that the current analytic model predicts better results on the maximum axial stress of an unanchored tank.

Figure D.1 shows the loading conditions and the nomenclatures of an unanchored fluid -filled tank, assumed to be rigid, subjected to a lateral acceleration. The experimental observations (fig. 5.6) indicate that a crescent-shaped portion of the tank bottom is lifted off the foundation. We can assume that the contact area between the bottom plate of the tank and the foundation is a circle, of radius a, as shown in figure D.2. When the tank bottom is partially lifted off the foundation, the different types of loading on the bottom plate of the unanchored tank can be described as follows:

1) The dead load of the liquid, $W = \rho_\ell g\pi R^2$, acting on the top of this bottom plate.

2) Part of the liquid weight, $W_f = \rho_\ell g\pi a^2$, is transmitted to the foundation through the contact area of the bottom plate. It is equivalent to add a reacted force, W_f, on the bottom of the bottom plate.

3) The shear forces, generated by the stresses in the shell wall, acting on the boundary of the bottom plate. These shear forces can be separated into two parts. The first part is the downward shear force, generated by the compressive stresses in the shell wall of the tank (from $-\beta$ to β), whose peak is assumed at $\theta=0$. This downward shear force is also transmitted to the foundation and is balanced by a reaction force, W_s, since the compressive part of the boundary of the bottom plate is assumed to be in contact with the foundation. The other part is the upward shear force, generated by the tensile stresses in the shell wall of the tank, whose peak is assumed at $\theta = \pi/2$. The distribution of these shear forces is assumed to be linear as shown in figure D.3. It should be pointed out that the shear force is assumed to be zero at $\theta=\pi$. This assumption can be confirmed from the experimental results [5.3].

From the force equilibrium, we know that the dead load of the liquid acting on the uplifting area of the bottom plate, $W-W_f$, must equal the total upward shear force acting on the uplifting boundary of the bottom plate. The equation can be written as follows.

$$N_t R(\pi-\beta) = W(1 - \frac{a^2}{R^2}) \qquad (D.1)$$

The relation of a and β can be assumed as follows

$$a = R(1 - \beta/\pi) \qquad (D.2)$$

This assumption based on the experimental observation that the value of β increases and the radius of the contact area decreases as the water depth is increased (fig. 5.6). A rough observation on the value of β vs. the diameter of the contact area, a, is shown in figure D.4.

The shear forces acting on the boundary of the bottom plate can be related to the overturning moment, M, by the moment equilibrium. The moment equilibrium can be expressed by

$$M = 2\int_0^{\beta} N_c(1 - \theta/\beta)R\cos\theta R d\theta + 2\int_0^{\frac{\pi}{2}} N_t \frac{\theta}{\pi/2} R\cos\theta R d\theta +$$

$$2\int_{\frac{\pi}{2}}^{\pi-\beta} N_t \frac{(\pi-\beta-\theta)}{(\frac{\pi}{2}-\beta)} R\cos\theta R d\theta$$

$$= \frac{2R^2N_c(1-\cos\beta)}{\beta} + 4R^2N_t\left[\frac{(\frac{\pi}{2}-1)}{\pi} + \frac{\cos\beta+\beta-\frac{\pi}{2}}{(\pi-2\beta)}\right] \qquad (D.3)$$

Substituting equations (D.1) and (D.2) into equation (D.3), the maximum compressive stress, σ_c, can be expressed in terms of the overturning moment, M, and the angle for the compressive boundary, β, as follows

$$\sigma_c = \frac{N_c}{t_s} = \frac{W\beta}{Rt_s 2(1-\cos\beta)} \left\{ \frac{M}{WR} - \frac{4\beta(2-\frac{\beta}{\pi})}{\pi(\pi-\beta)} \left[\frac{(\frac{\pi}{2}-1)}{\pi} + \frac{\cos\beta+\beta-\frac{\pi}{2}}{\pi-2\beta} \right] \right\} \qquad (D.4)$$

For the static tilt test, the overturning moment can be written as

$$M = WD \sin\alpha/2 \qquad (D.5)$$

and the dead load of the liquid acting on the uplifting area of the bottom plate, W_u, can be approximately expressed by

$$W_u = (W - W_f) \cos\alpha \qquad (D.6)$$

Therefore, the maximum compressive stress can be rewritten by

$$\sigma_c = \frac{W\beta}{Rt_s 2(1-\cos\beta)} \left\{ \frac{D}{R} \frac{\sin\alpha}{2} - \frac{4\beta(2-\frac{\beta}{\pi})\cos\alpha}{\pi(\pi-\beta)} \left[\frac{(\frac{\pi}{2}-1)}{\pi} + \frac{\cos\beta+\beta-\frac{\pi}{2}}{\pi-2\beta} \right] \right\} \qquad (D.7)$$

In general, the value of β can be determined by satisfying the condition that the moment at the circumference of the contact circle must equal zero. In order to avoid solving this complicated problem, the experimental value of β [5.3] is used to check the validity of equations (D.4) and (D.7). The results based on equation (D.7) are listed in table 5.2 for comparison,

where the value of β is assumed to be 28^{o}. The results indicate that equation (D.7), based on an experimental approximation for β, gives a better prediction for the maximum axial stress in the shell wall of an unanchored fluid-filled tank. Furthermore, equation (D.7) can also be applied to predict the critical water depth of an inclined unanchored tank. The results, based on the assumption that the buckling occurs when the maximum axial stresses at the bottom of the tank wall reach the classical buckling stress, are shown in figures D.5a, D.5b and D.5c for three different tank dimensions (β is assumed to be 30^{o}). The comparisons indicate that the current analytic model gives a resonable prediction once the angle for the compressive boundary is properly found.

(a)

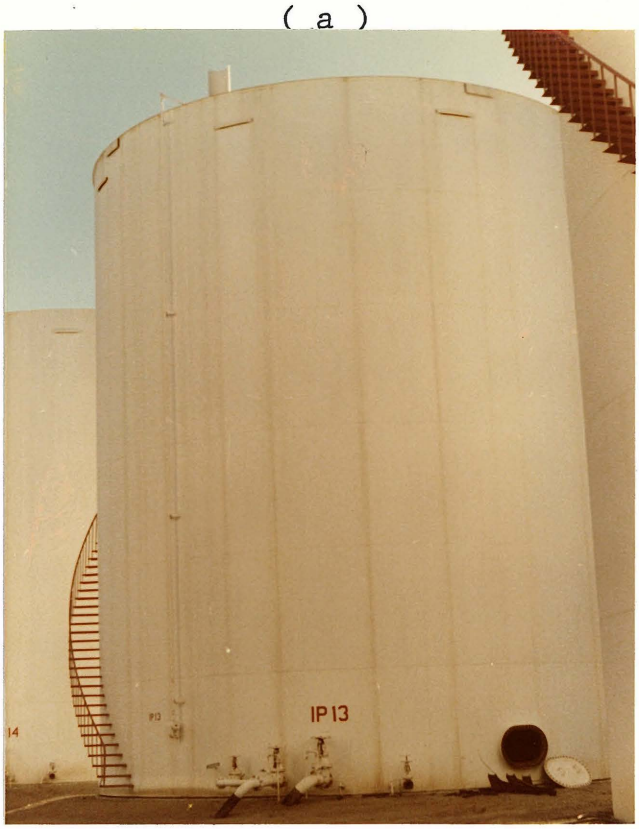

(b)

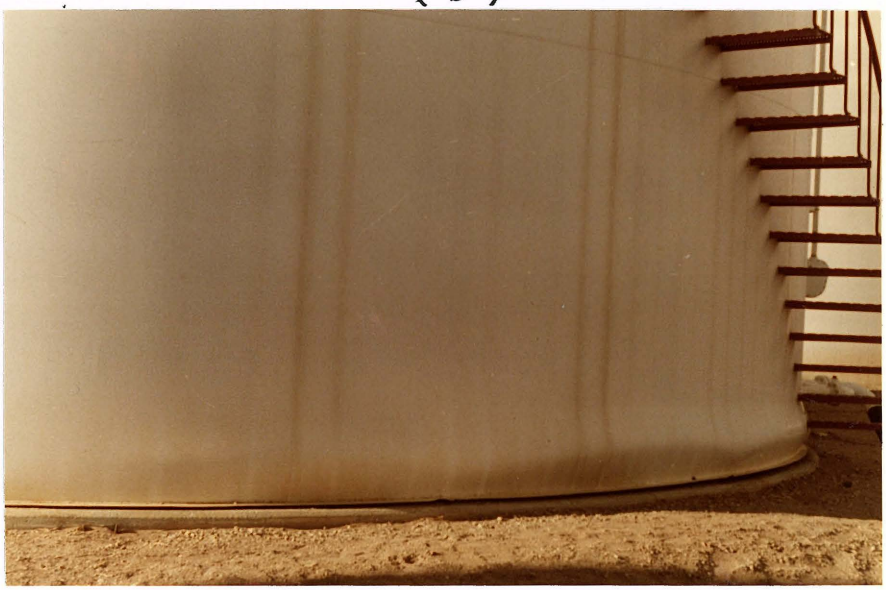

Fig. 1.1 ELEPHANT-FOOT TYPE BULGE

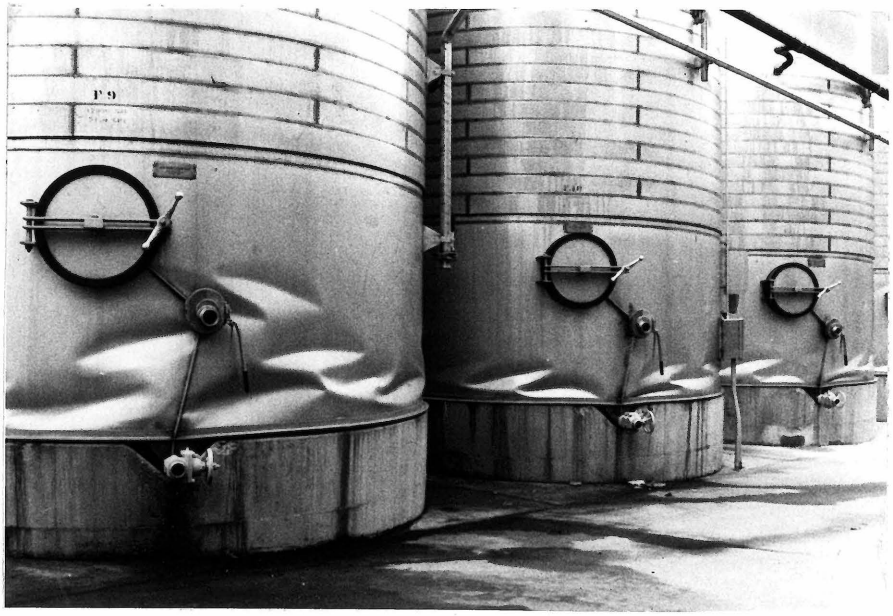

Fig. 1.2 DIAMOND-SHAPED BUCKLING (COURTESY OF DAVID BUSHNELL)

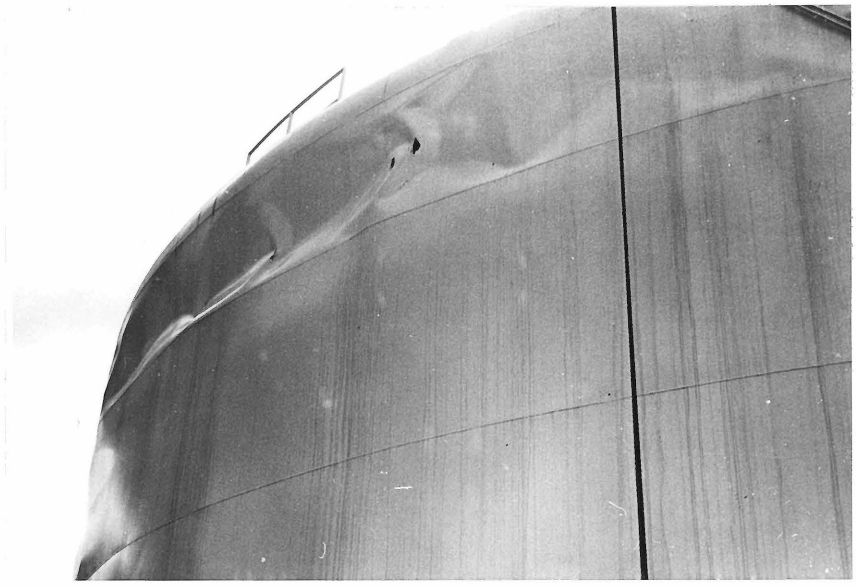

Fig. 1.3 BUCKLE AT TOP END OF TANK WALL (COURTESY OF PAUL C. JENNINGS)

Fig. 1.4 DAMAGE ON ROOF OF TANK

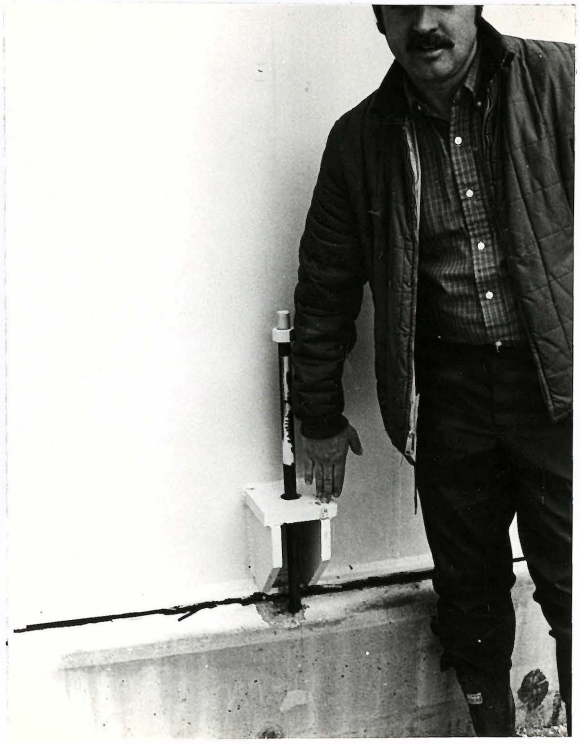

Fig. 1.5 UPLIFTING OF ANCHOR BOLT (COURTESY OF PAUL C. JENNINGS

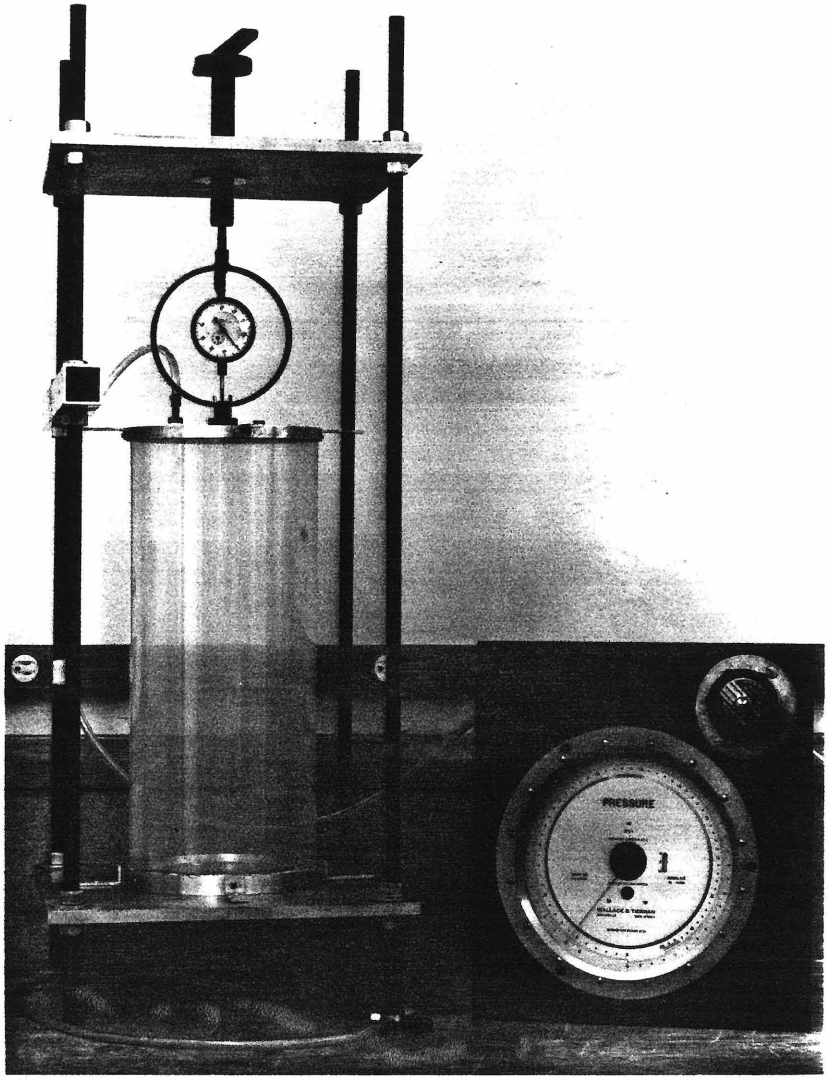

FIG. 2.1 EXPERIMENTAL SETUP FOR AXIAL COMPRESSIVE BUCKLING TEST

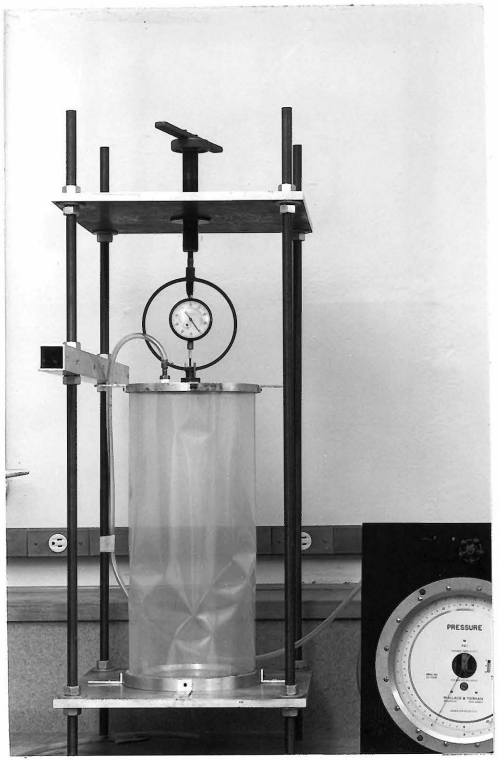

FIG. 2.2a BUCKLING PATTERN FOR AN UNPRESSURIZED CYLINDER

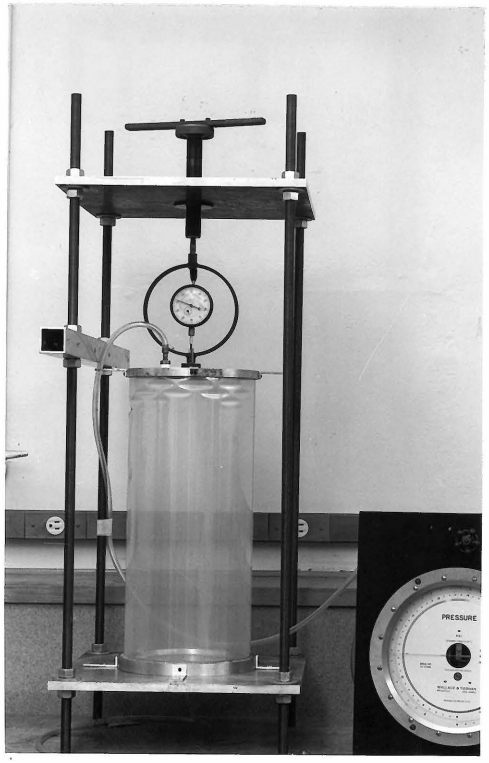

FIG. 2.2 b BUCKLING PATTERN FOR A PRESSURIZED CYLINDER

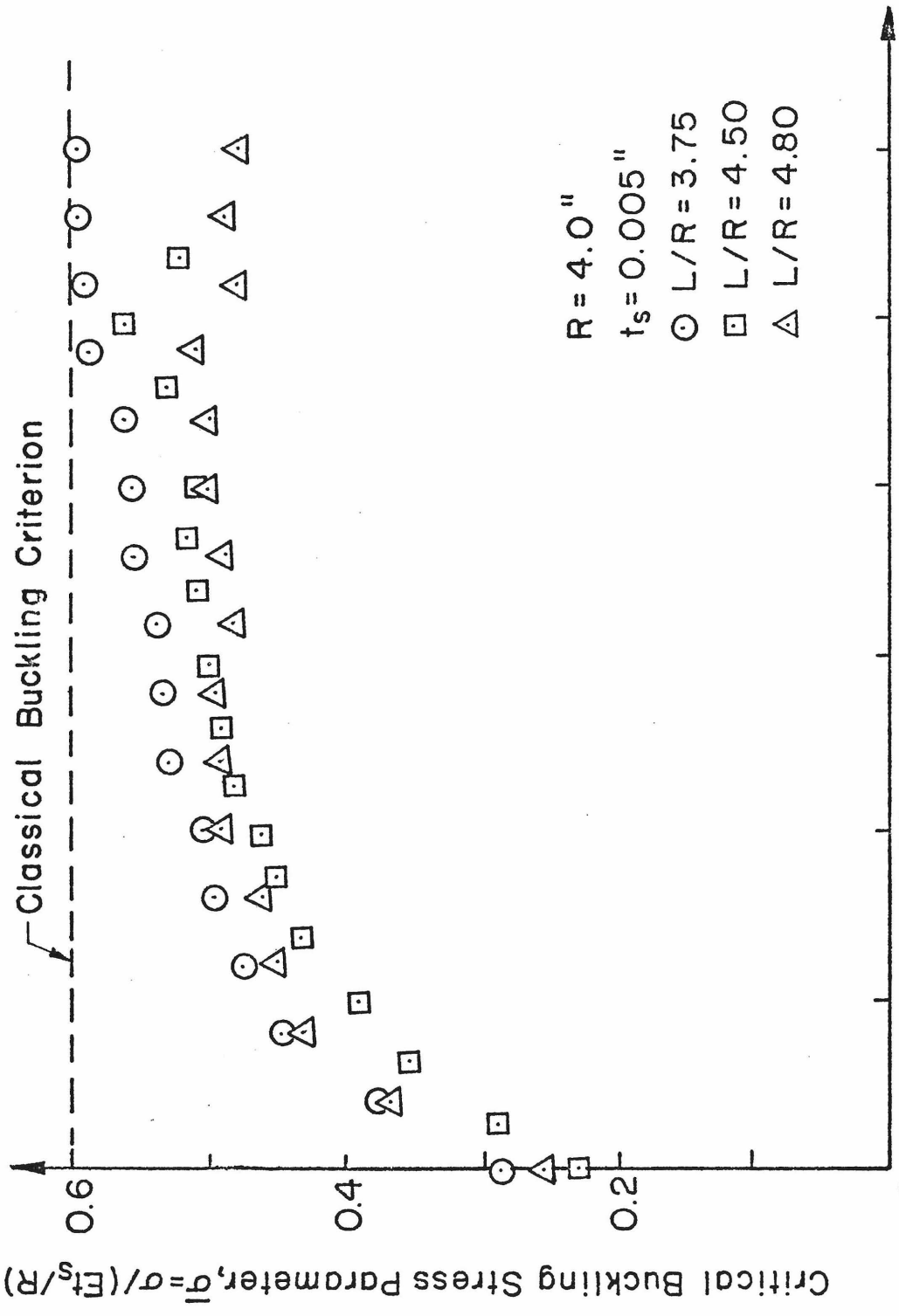

FIG. 2.3 CRITICAL BUCKLING STRESS VS. INTERNAL PRESSURE

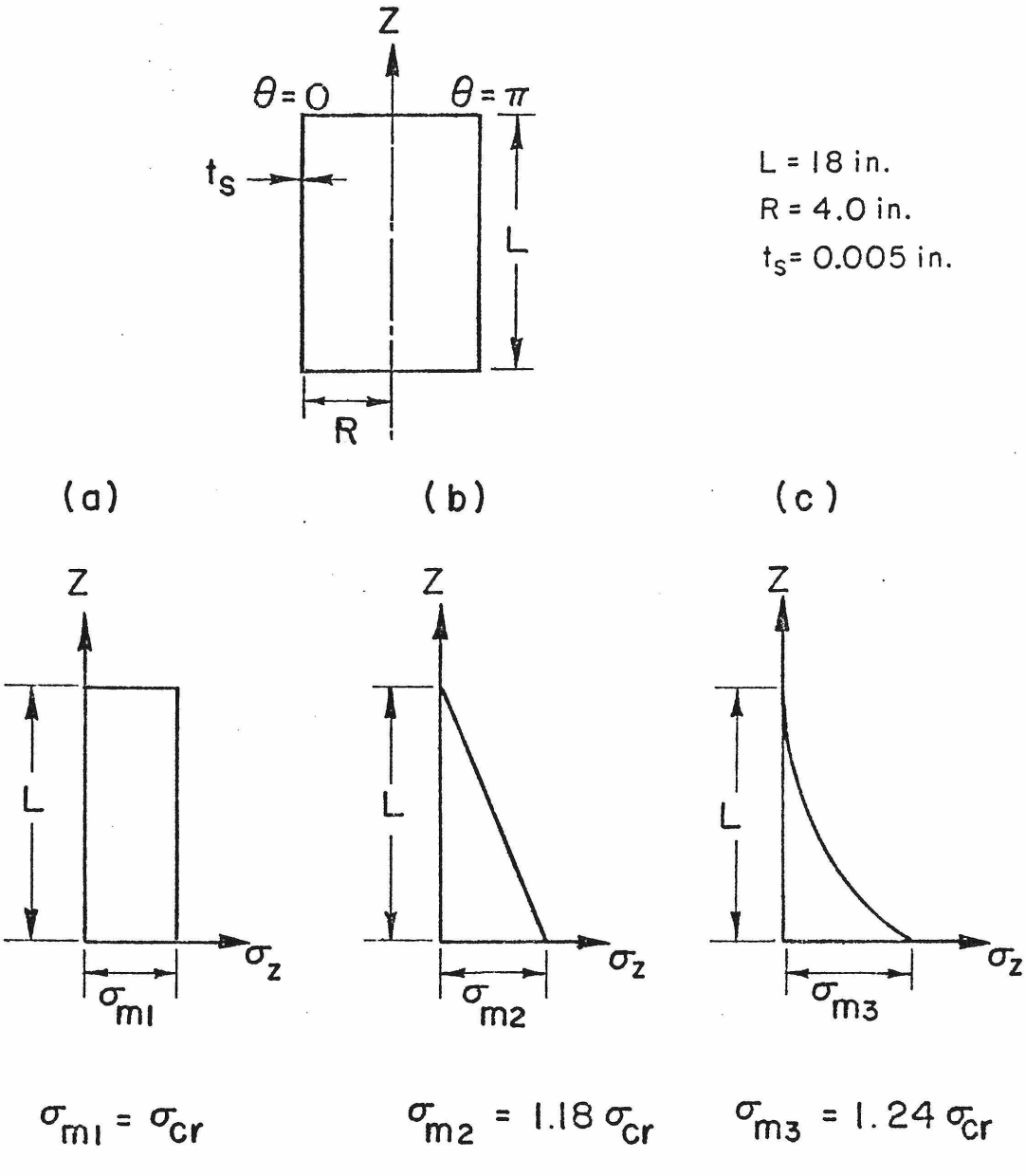

FIG. 2.4 AXIAL COMPRESSIVE STRESS DISTRIBUTION AND MAXIMUM ALLOWABLE STRESS

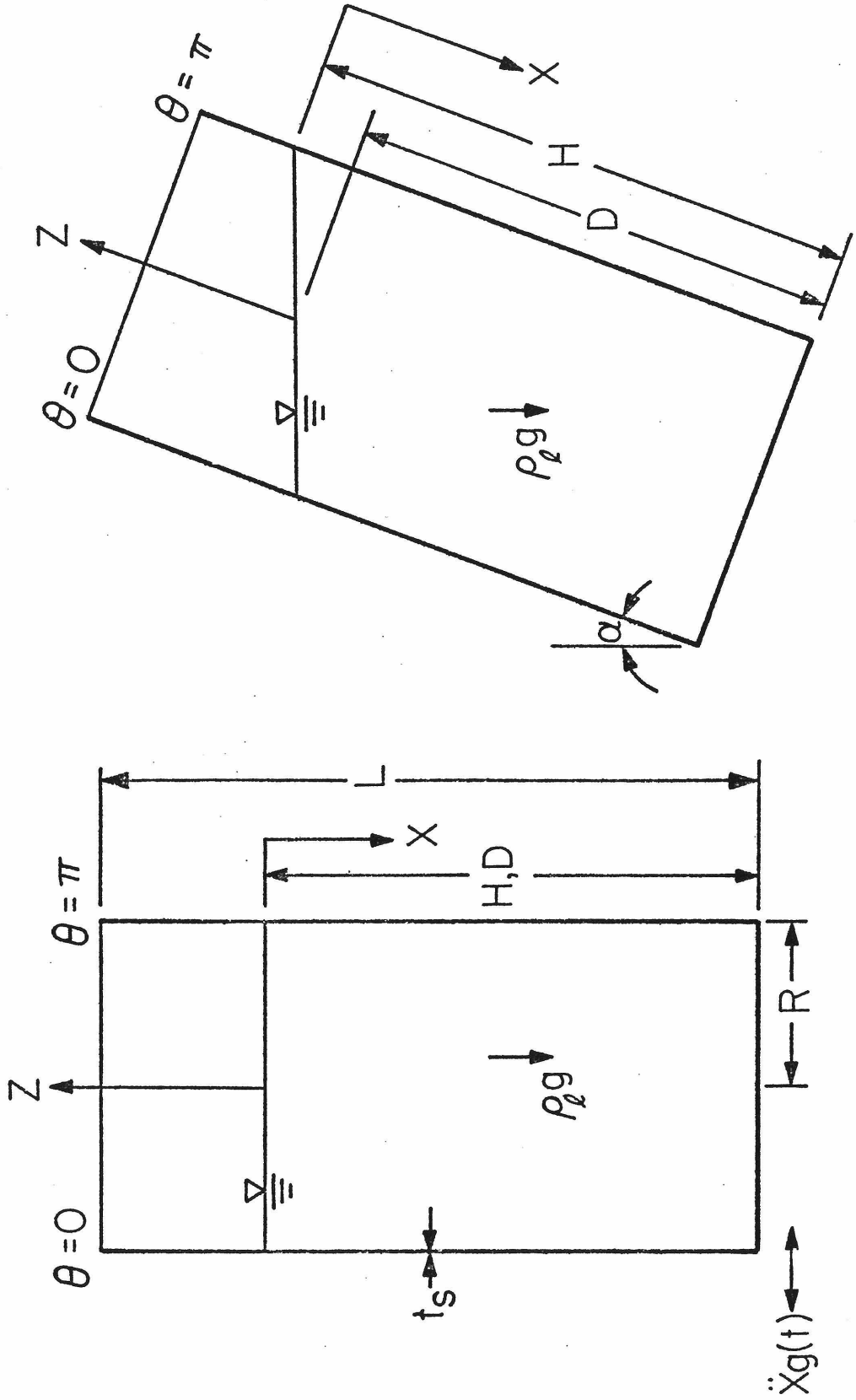

Fig. 4.1 Loading Condition and Nomenclature

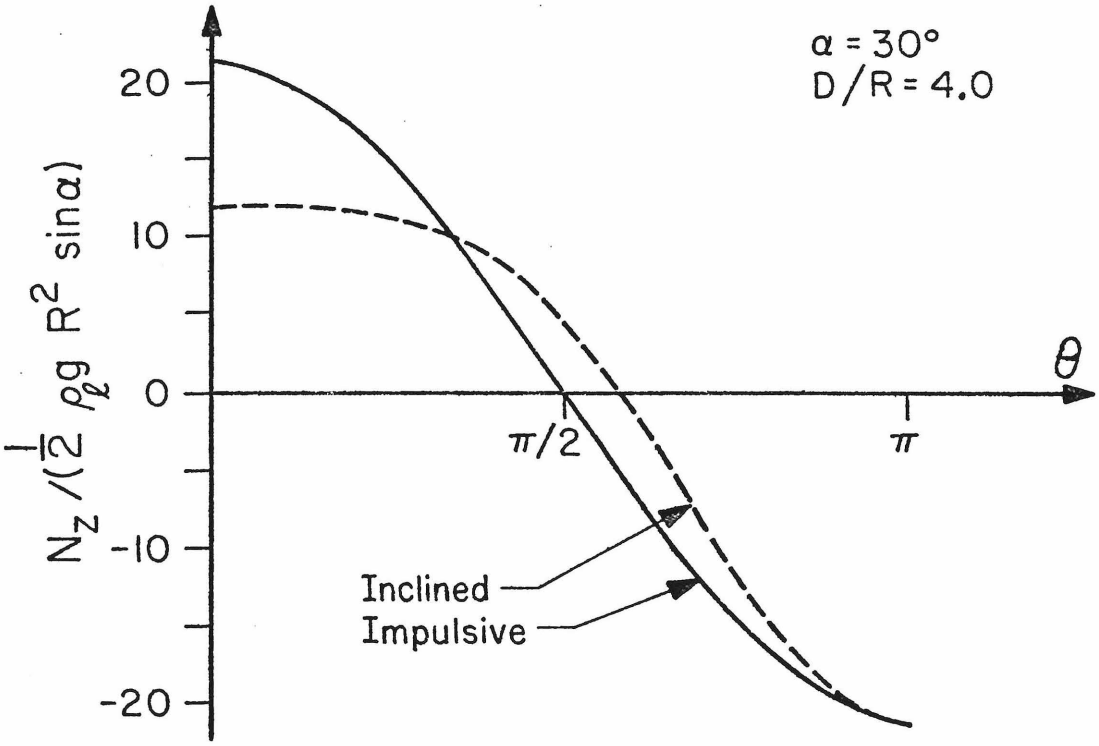

Fig.4.2a Axial Membrane Stress vs θ

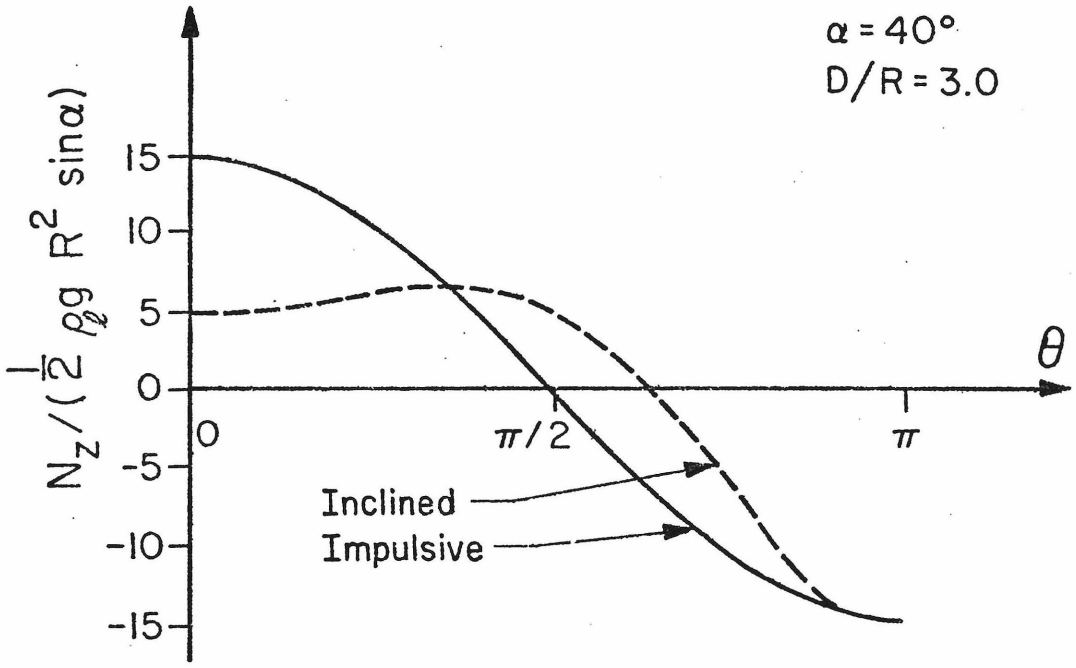

Fig. 4.2 b Axial, Membrane Stress vs θ

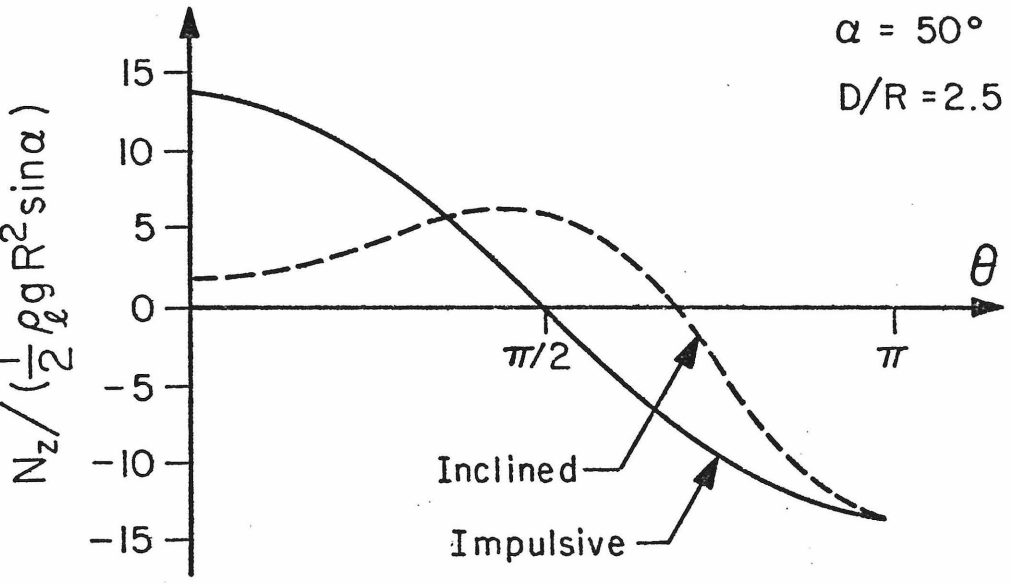

Fig. 4.2 c Axial Membrane Stress vs θ

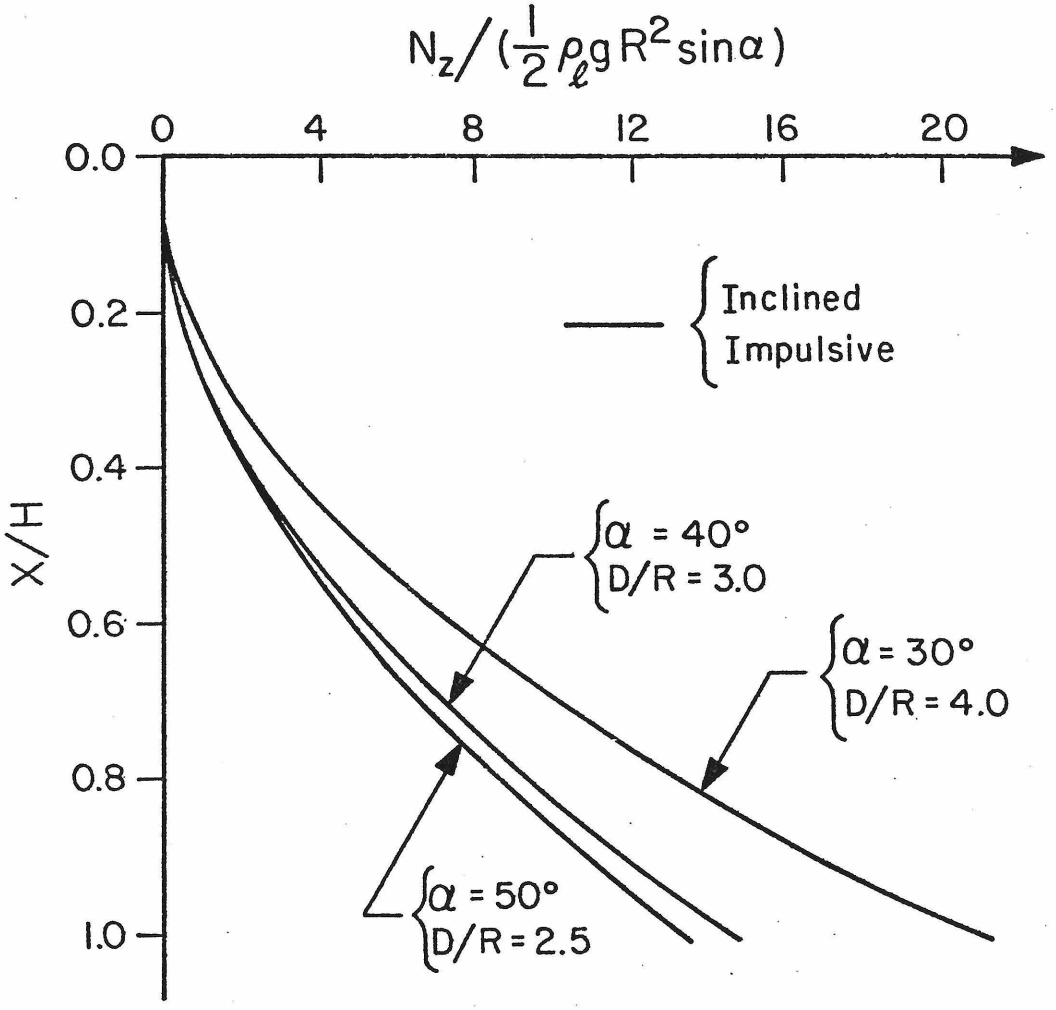

Fig.4.3 Axial Membrane Stress vs X

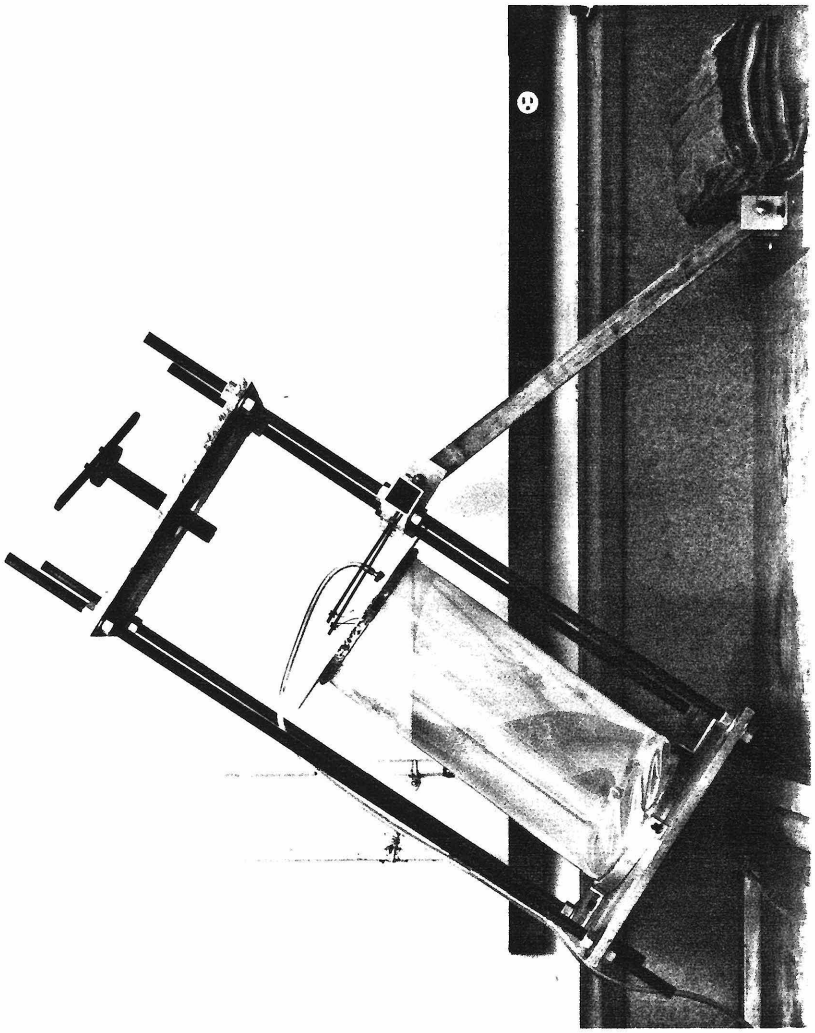

FIG. 4.4 STATIC BUCKLING TEST ON AN ANCHORED TANK

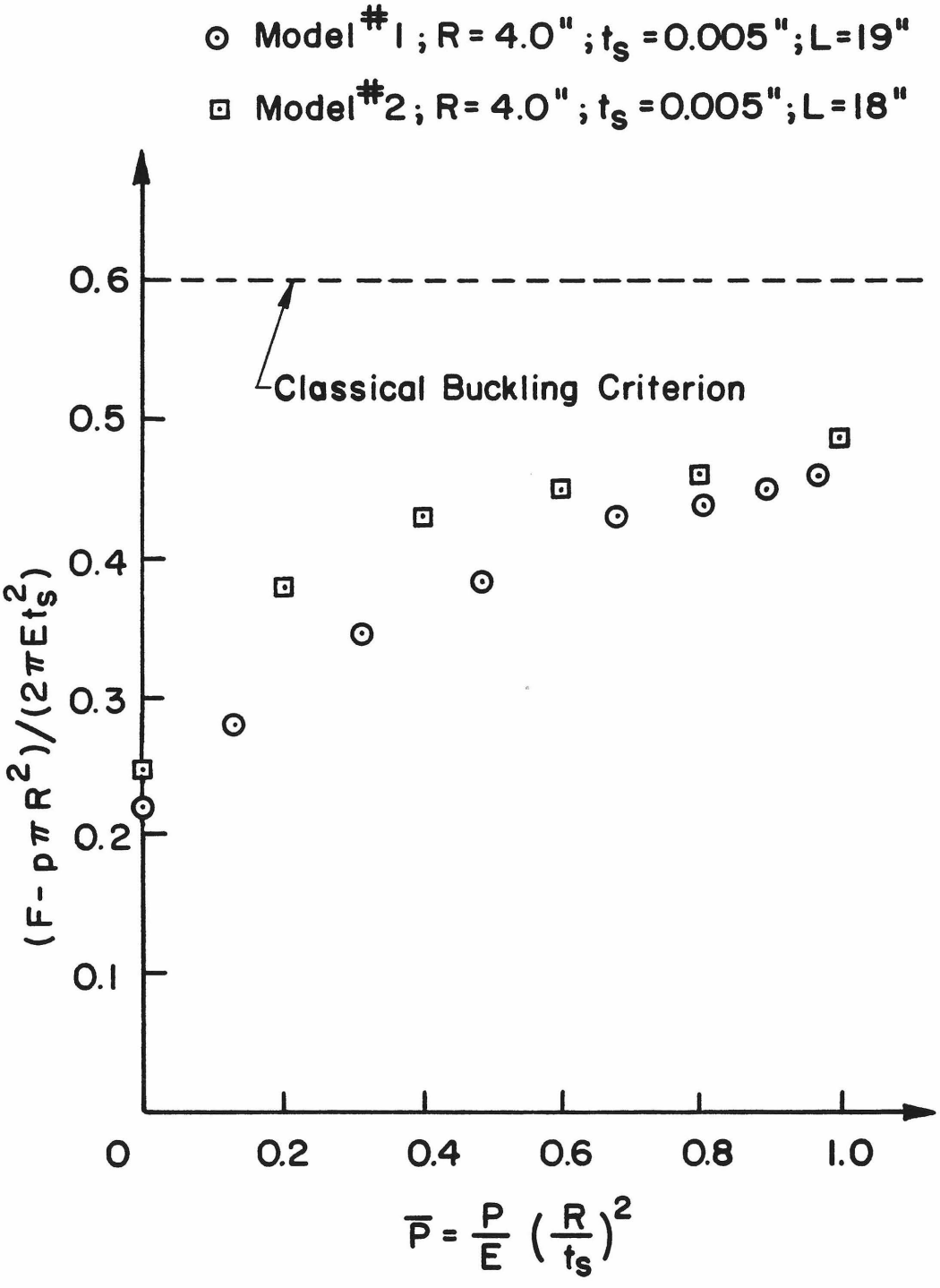

FIG. 4.5 UNIFORM LOADING TEST RESULTS

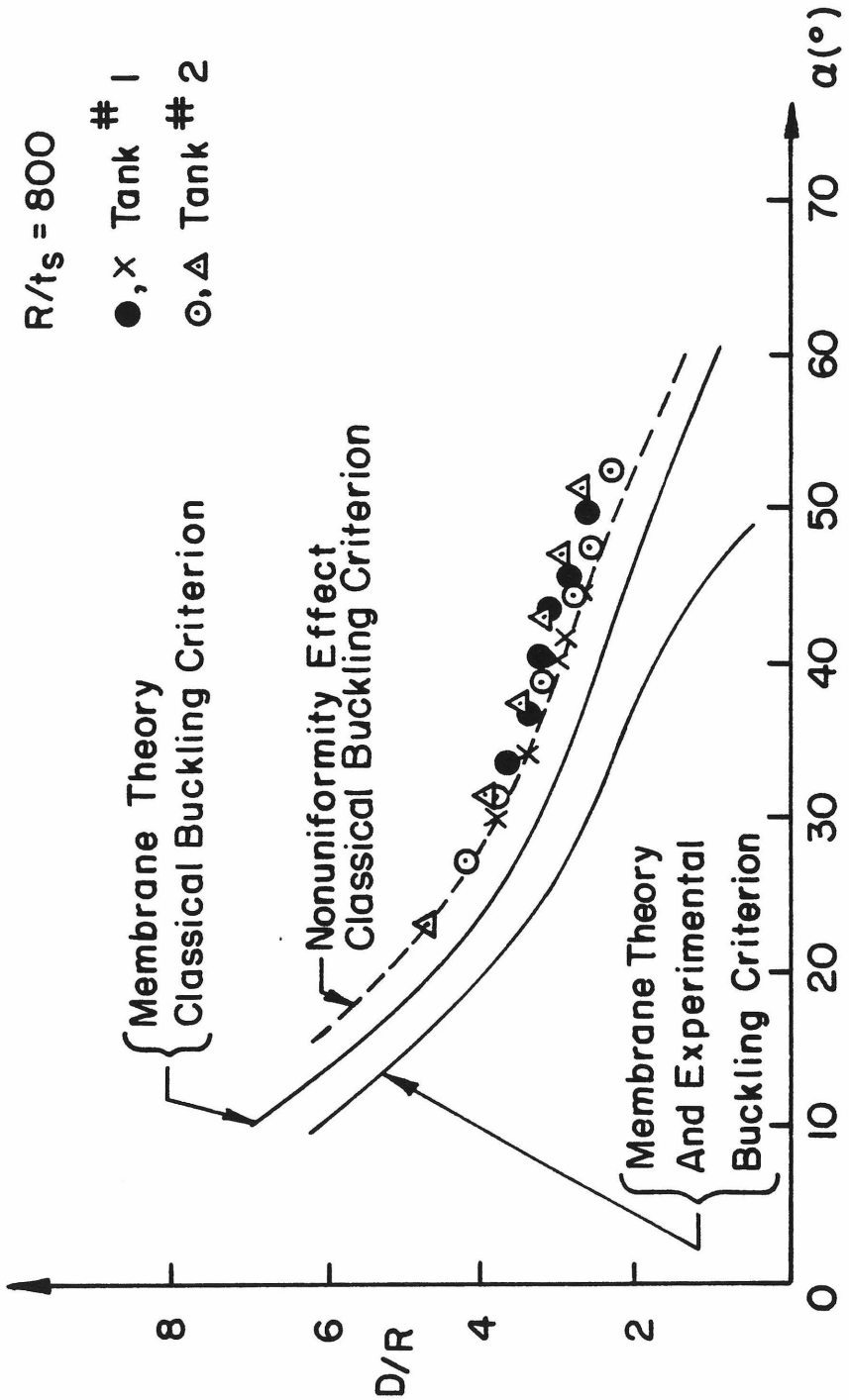

FIG. 4.6 CRITICAL WATER DEPTH VS. INCLINED ANGLE

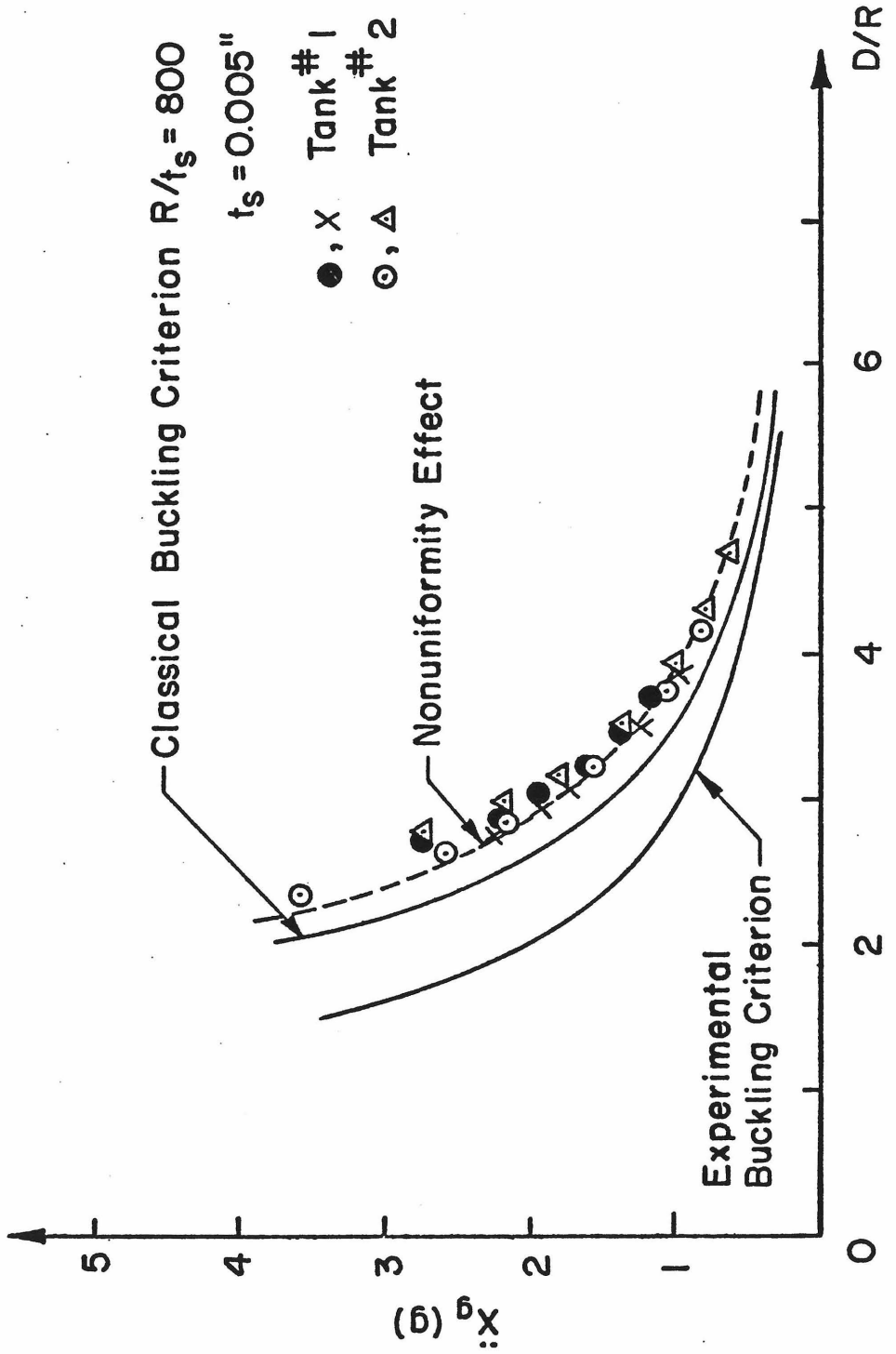

FIG. 4.7 CRITICAL BASE ACCELERATION VS. WATER DEPTH

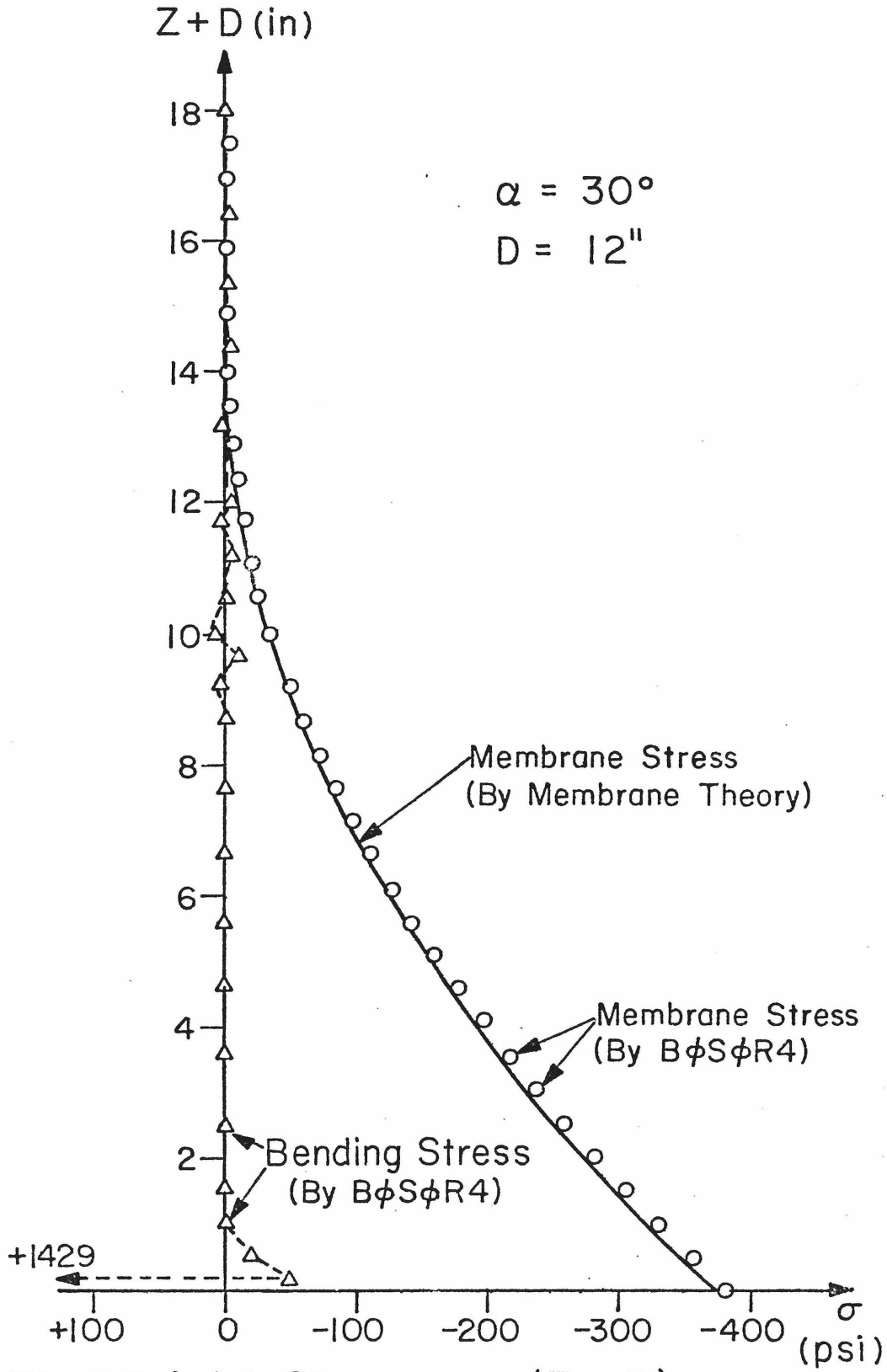

Fig. 4.8 Axial Stress vs. (Z + D)

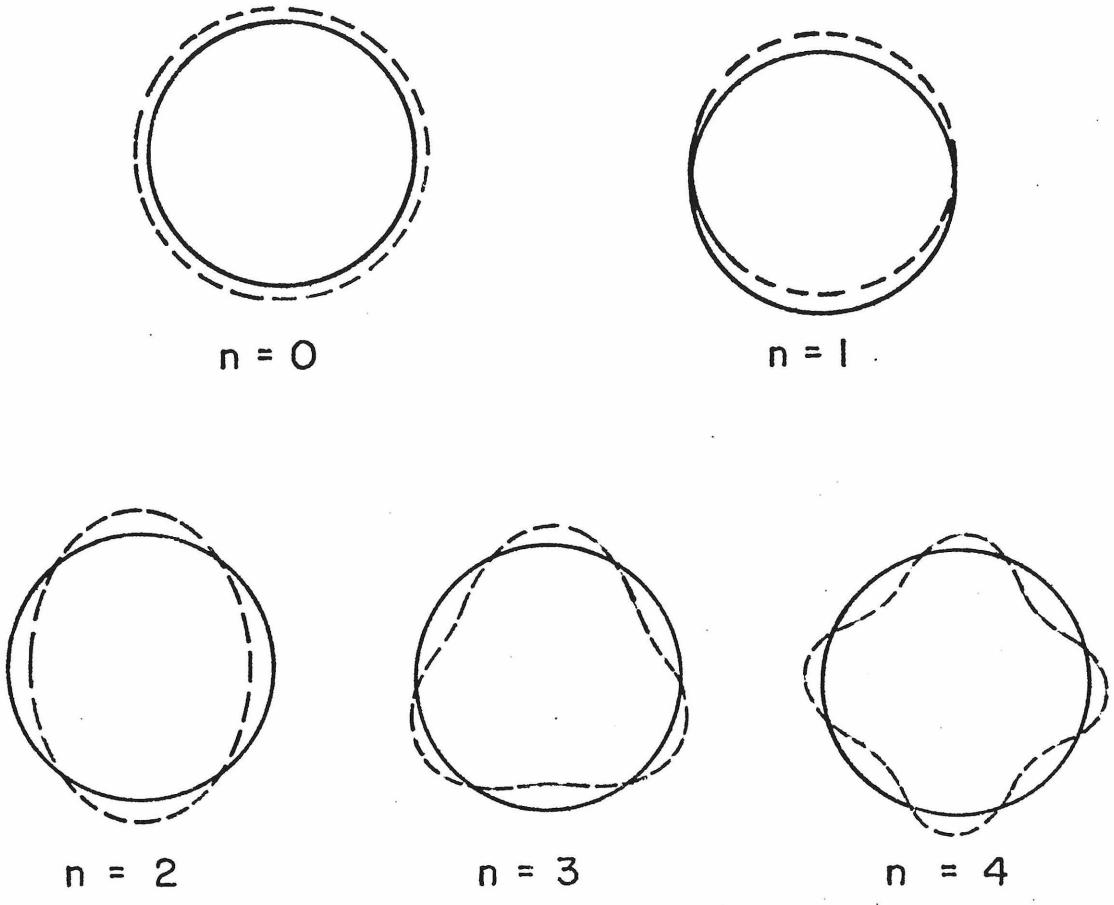

(a) Circumferential Modes

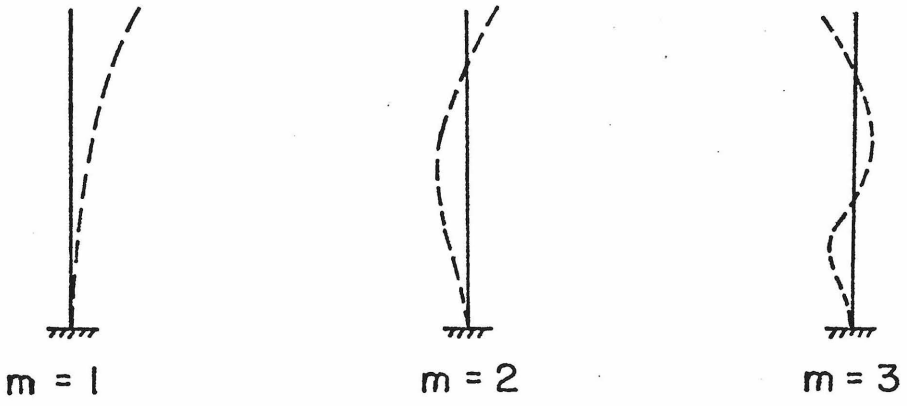

(b) Axial Modes

FIG. 4.9 VIBRATIONAL MODES OF CANTILEVER SHELLS

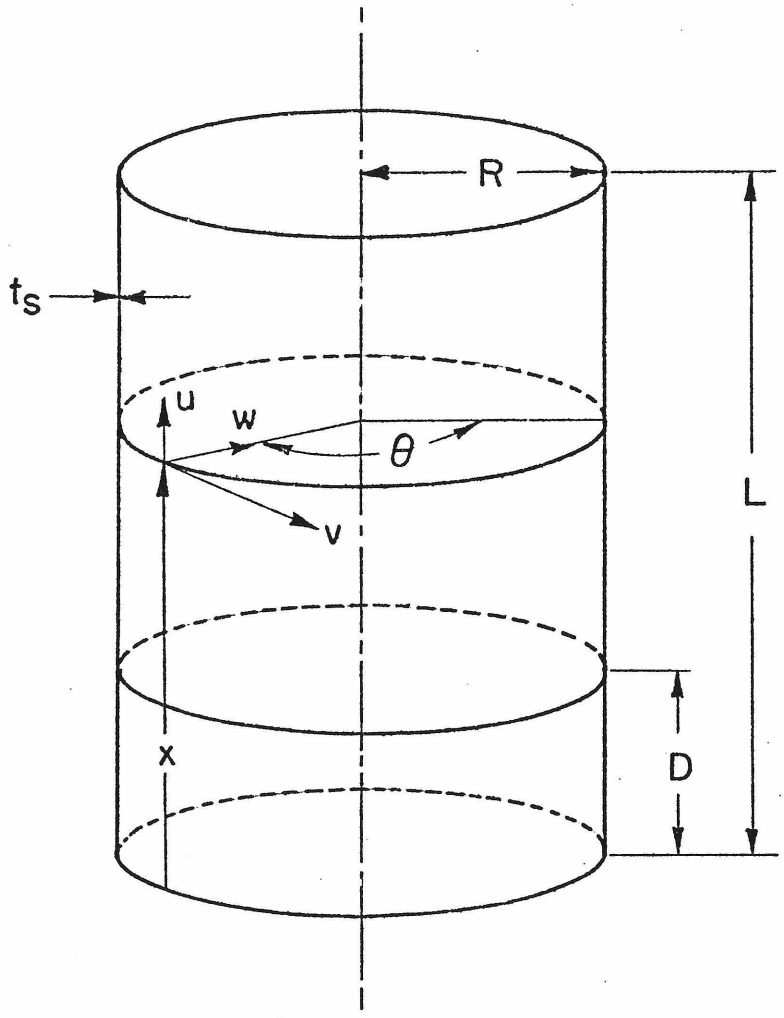

FIG. 4.10 COORDINATE SYSTEM OF A CYLINDER

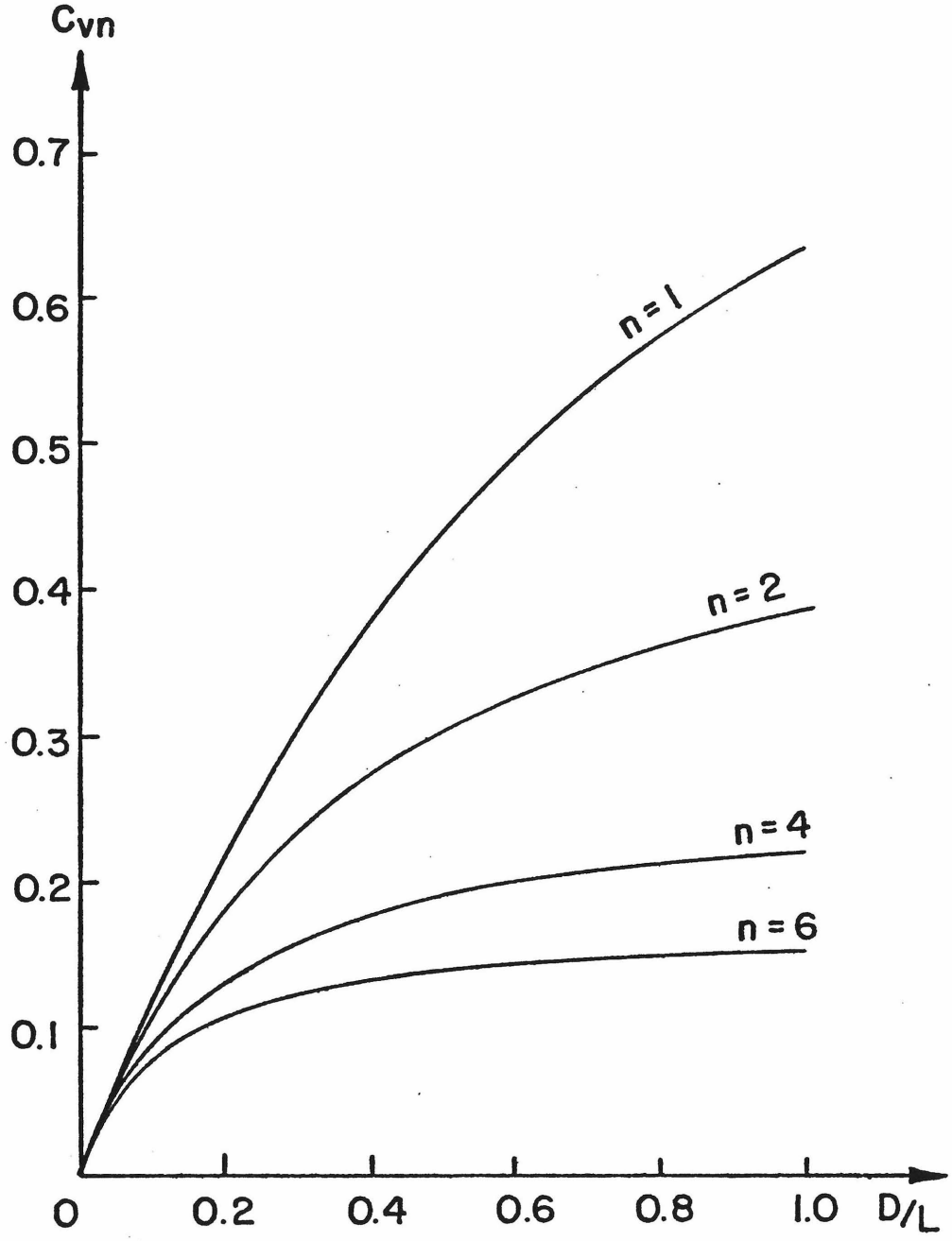

FIG.4.11 VIRTUAL MASS COEFFICIENT–WATER DEPTH / TANK LENGTH

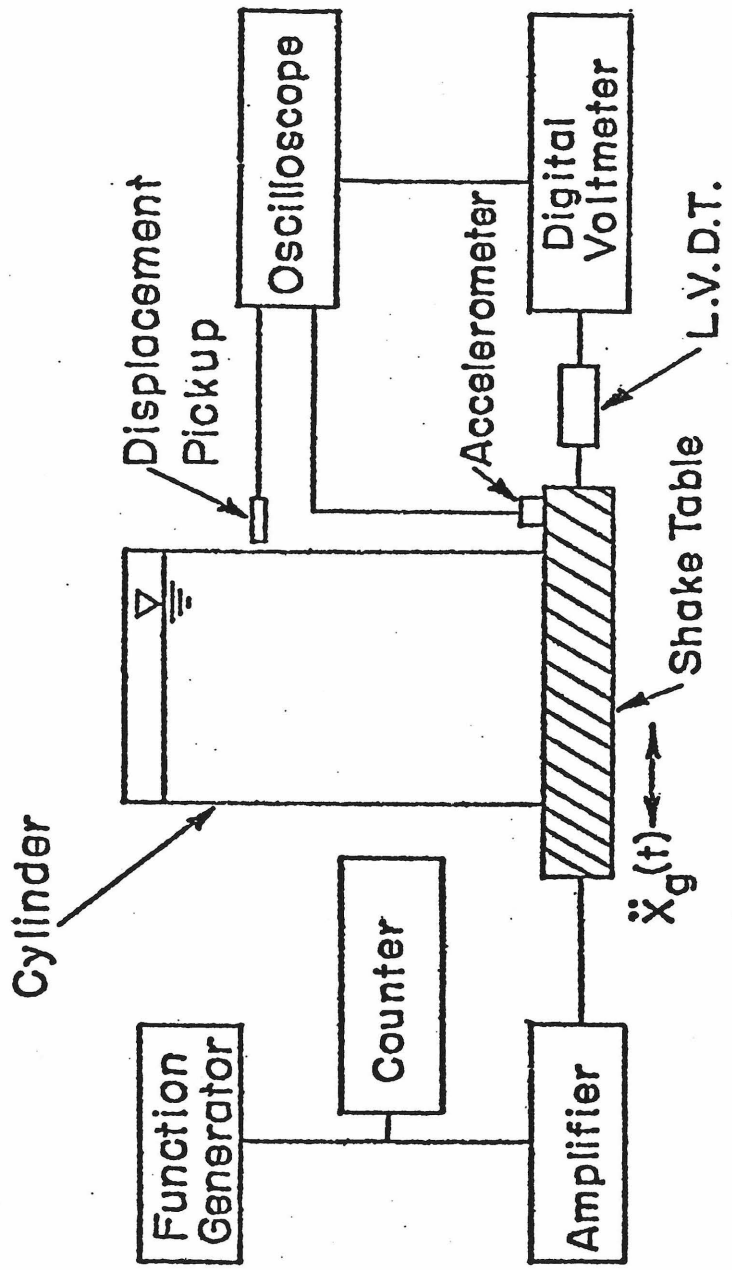

FIG. 4.12 EXPERIMENTAL SET UP FOR HARMONIC INPUT

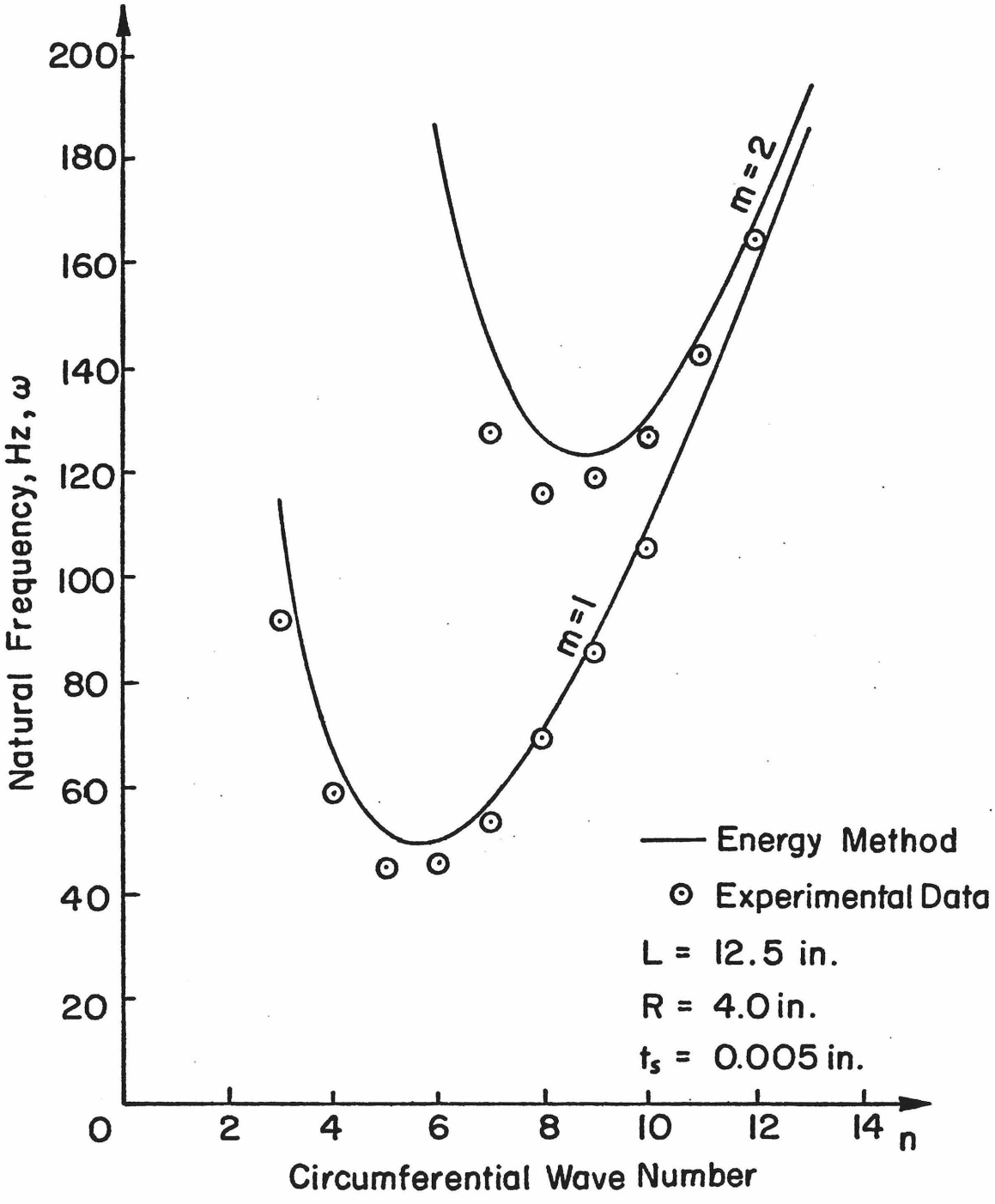

FIG.4.13 NATURAL FREQUENCY OF EMPTY CYLINDRICAL TANK

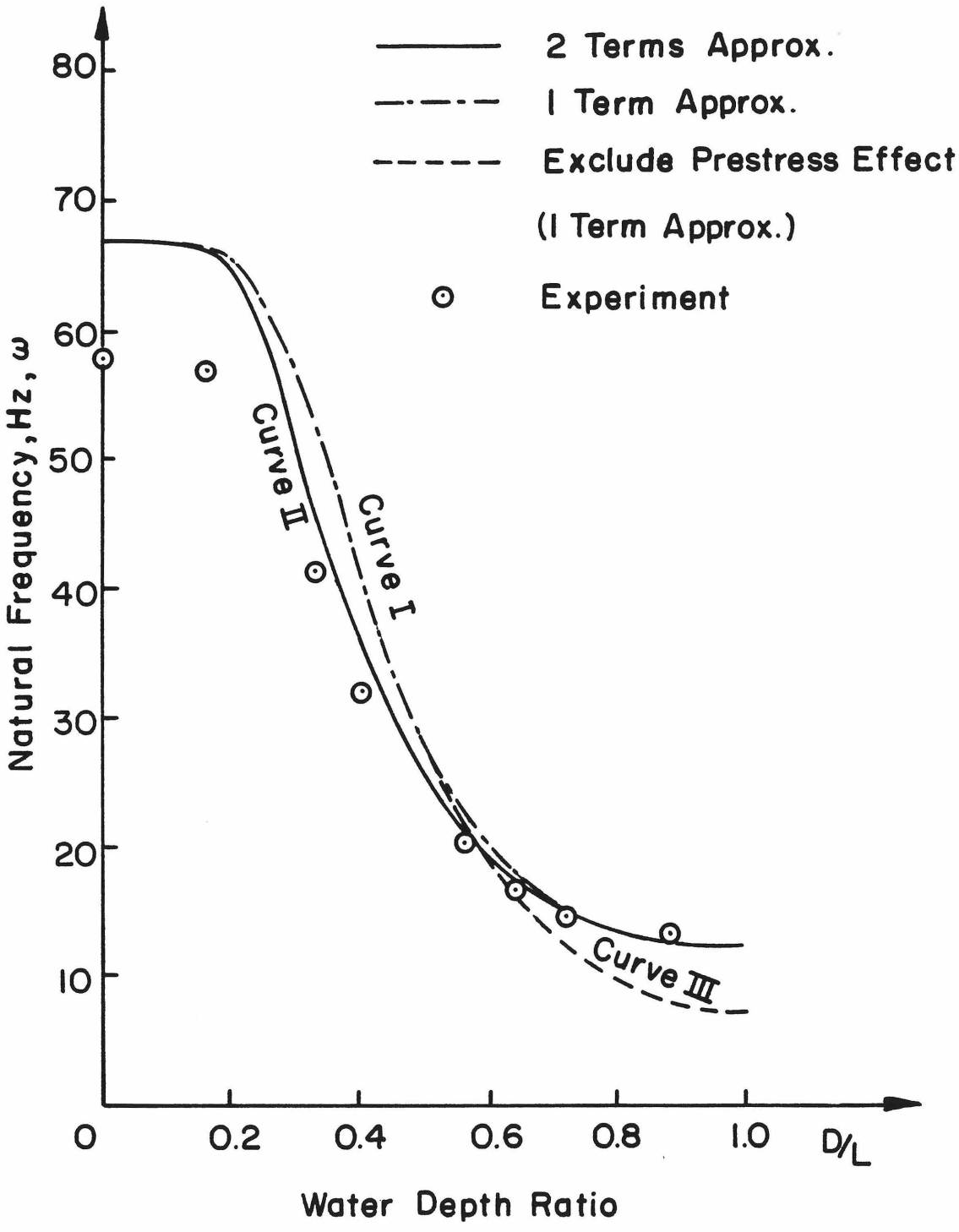

FIG.4.14 NATURAL FREQUENCY VS. WATER DEPTH RATIO

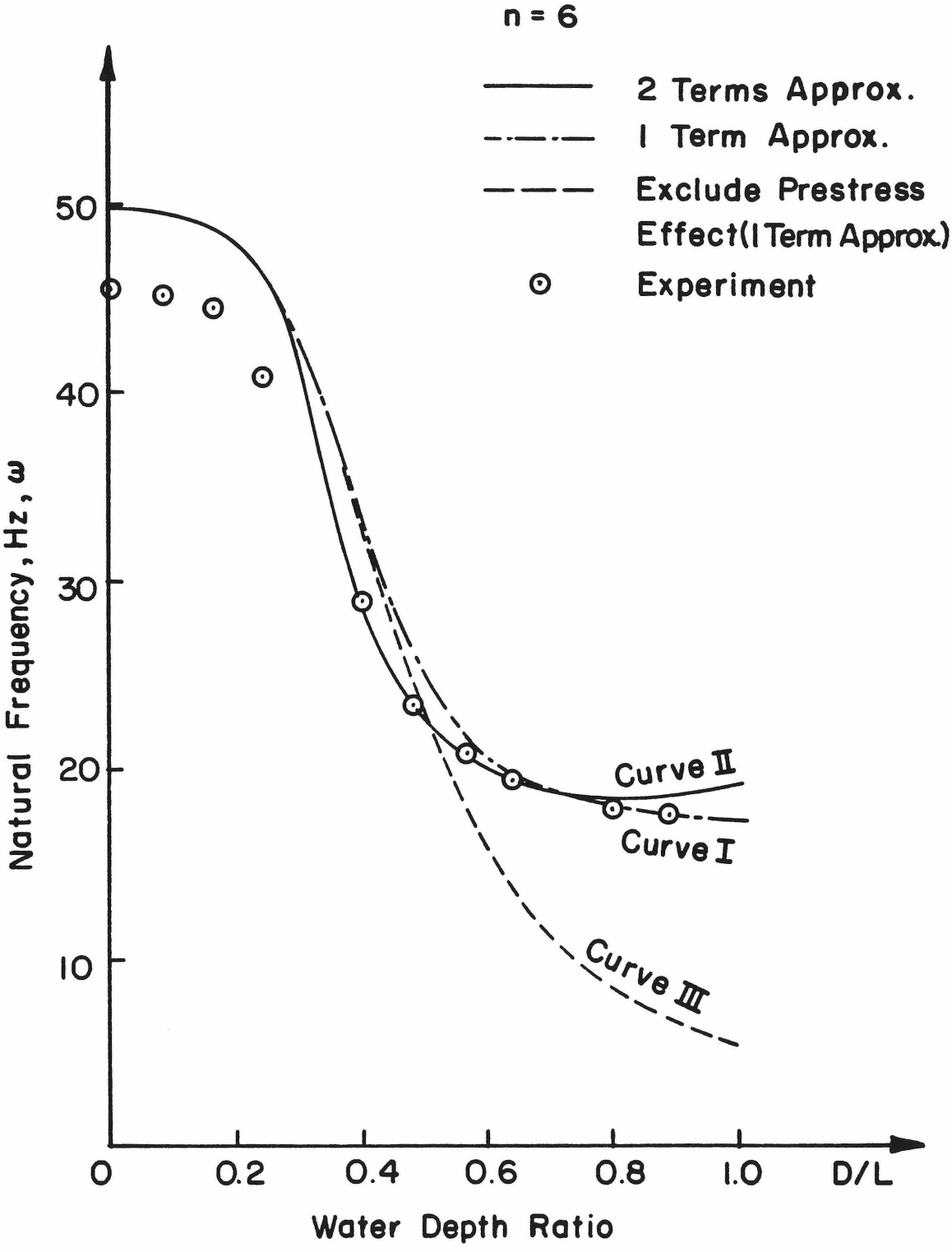

FIG. 4.15 NATURAL FREQUENCY VS. WATER DEPTH RATIO

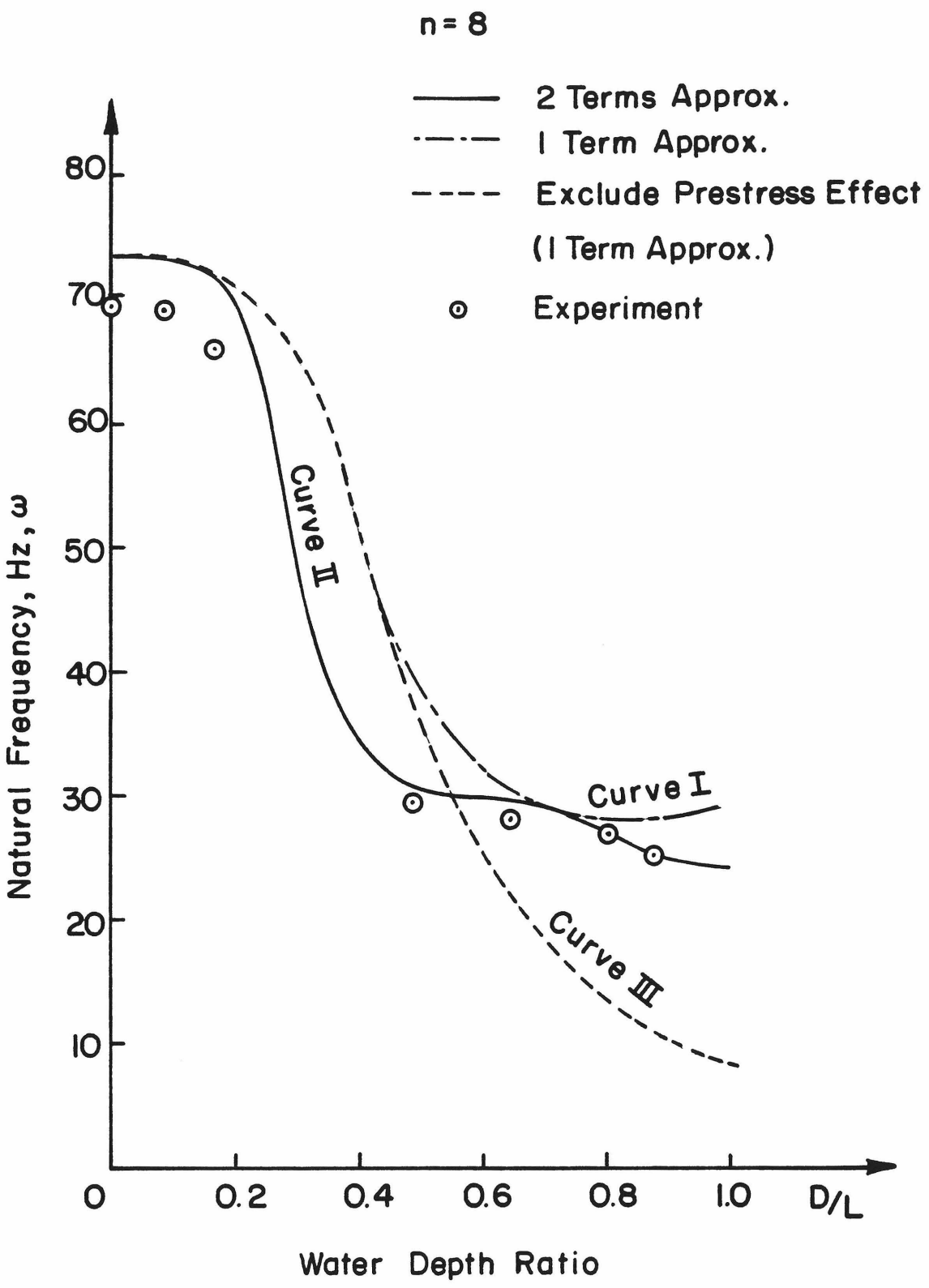

FIG.4.16 NATURAL FREQUENCY VS. WATER DEPTH RATIO

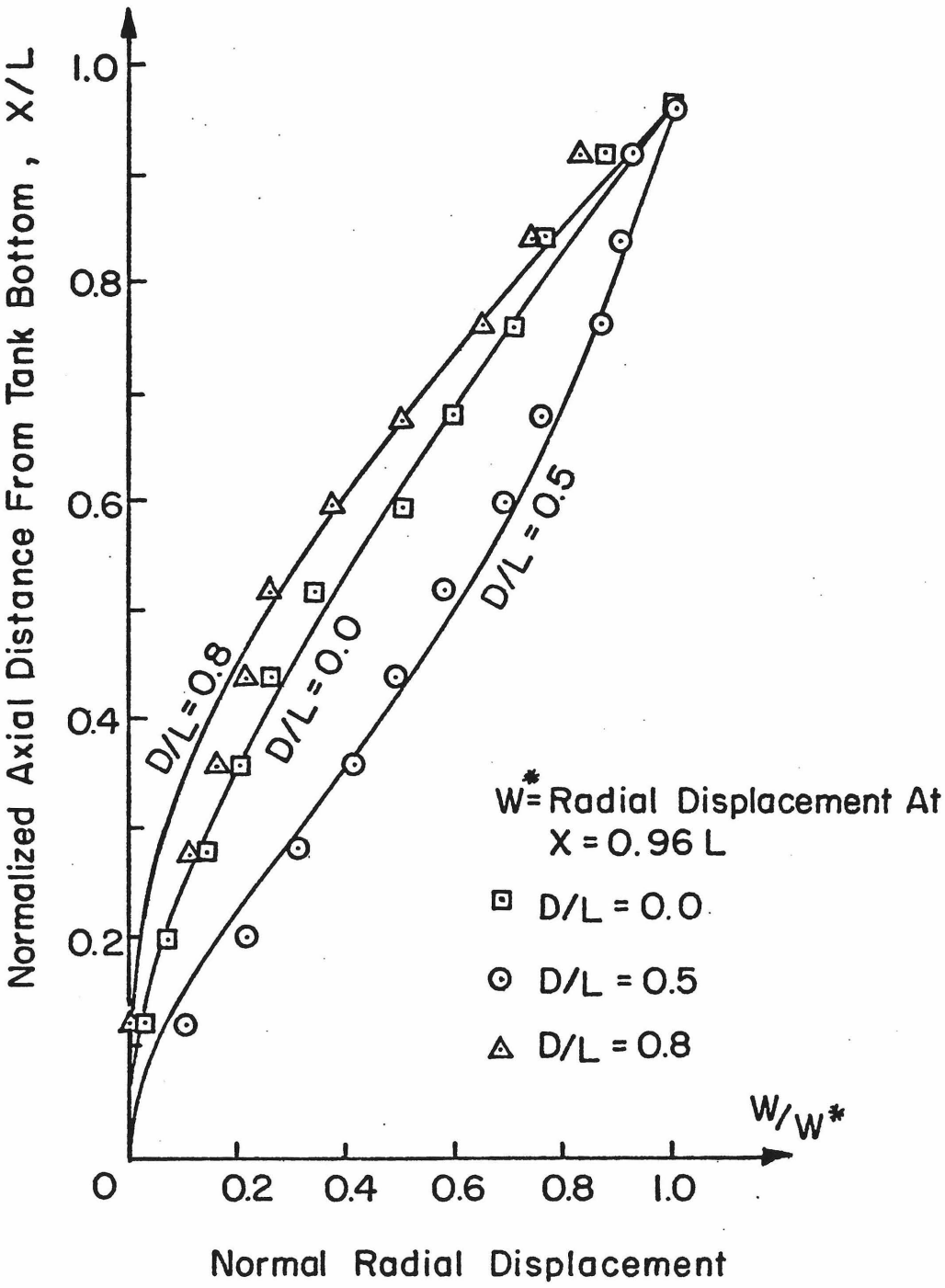

FIG. 4.17 AXIAL MODE SHAPES

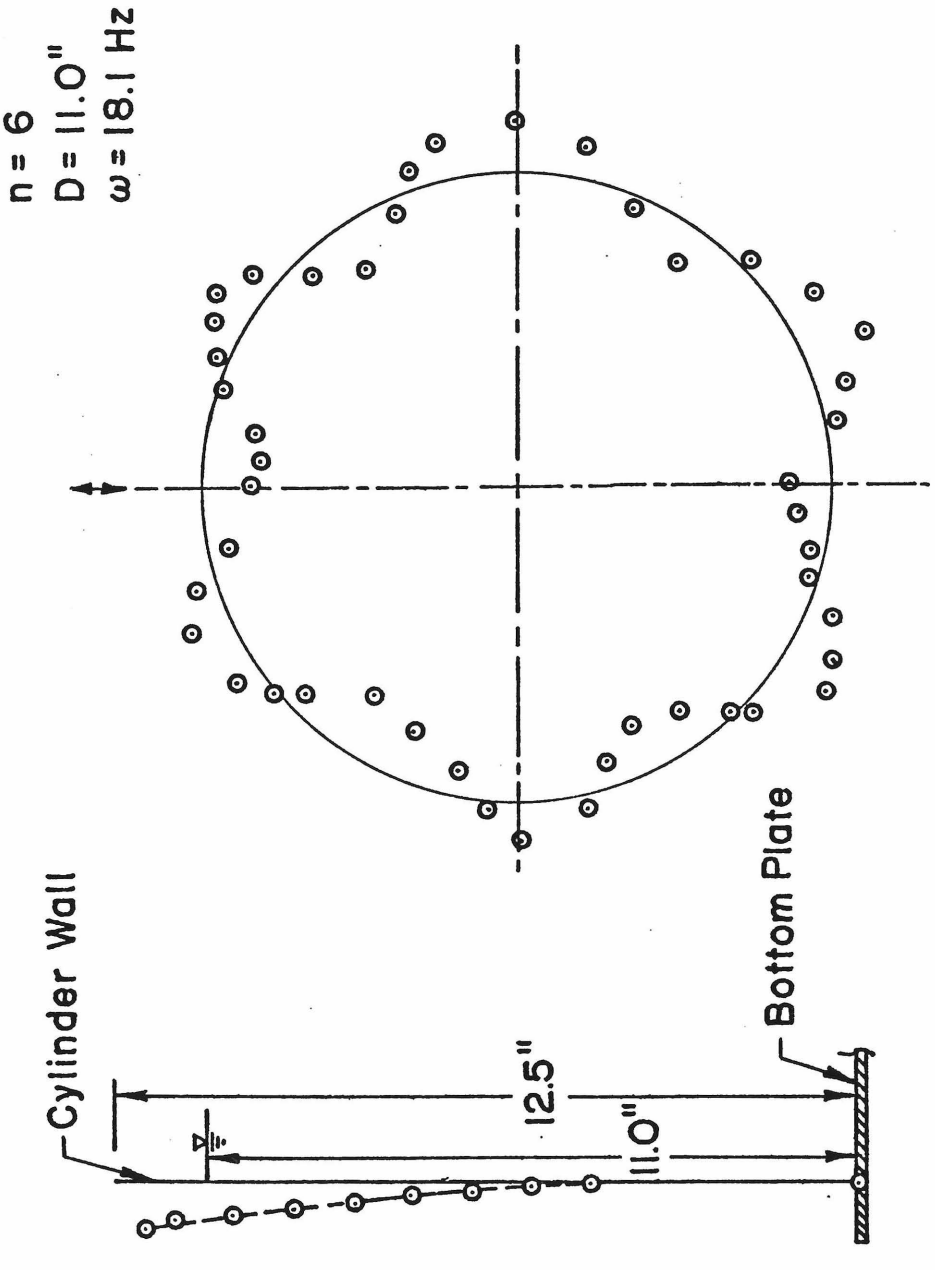

FIG.4.18 EXPERIMENTAL VIBRATION MODES

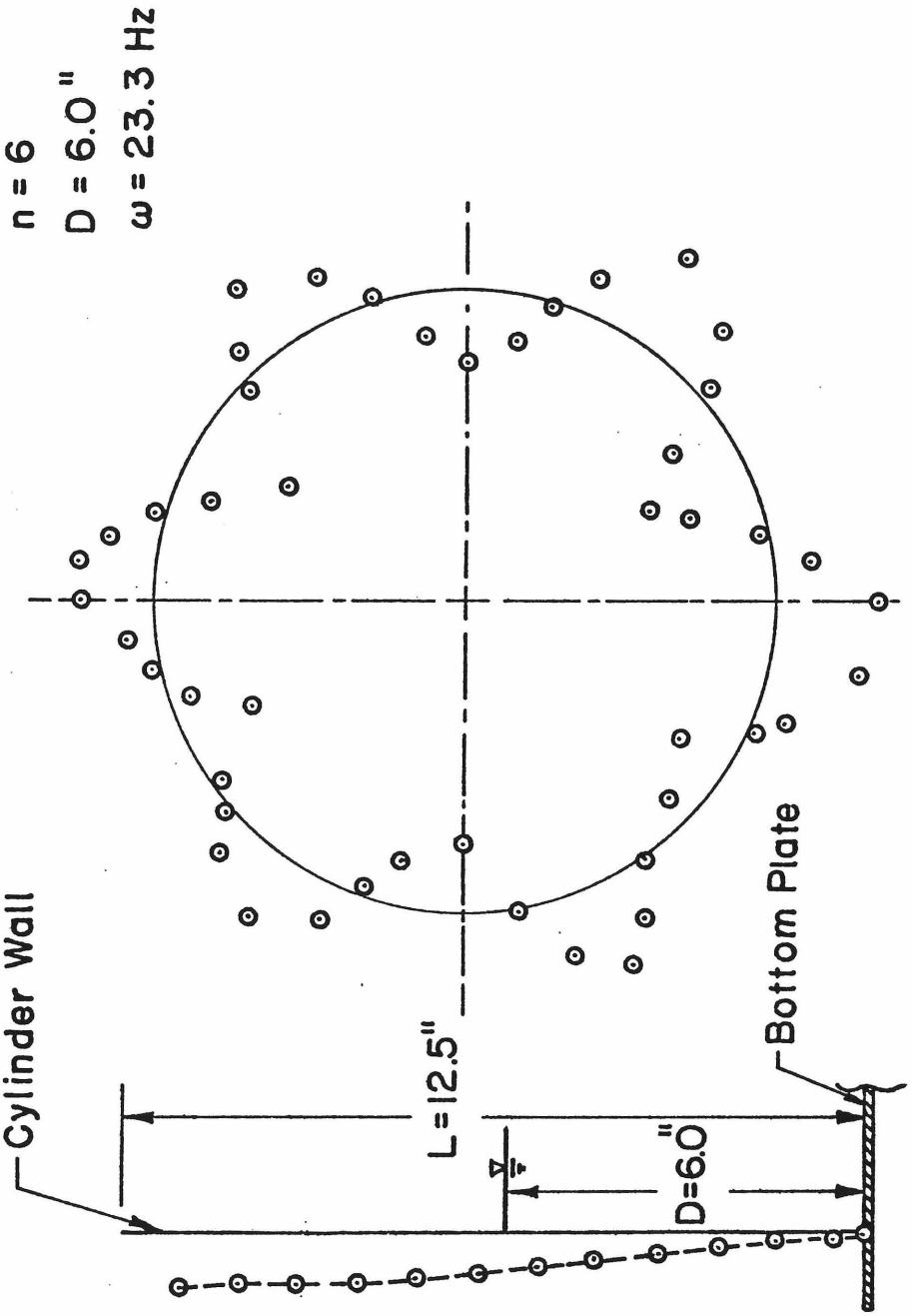

FIG4.19 EXPERIMENTAL VIBRATION MODES

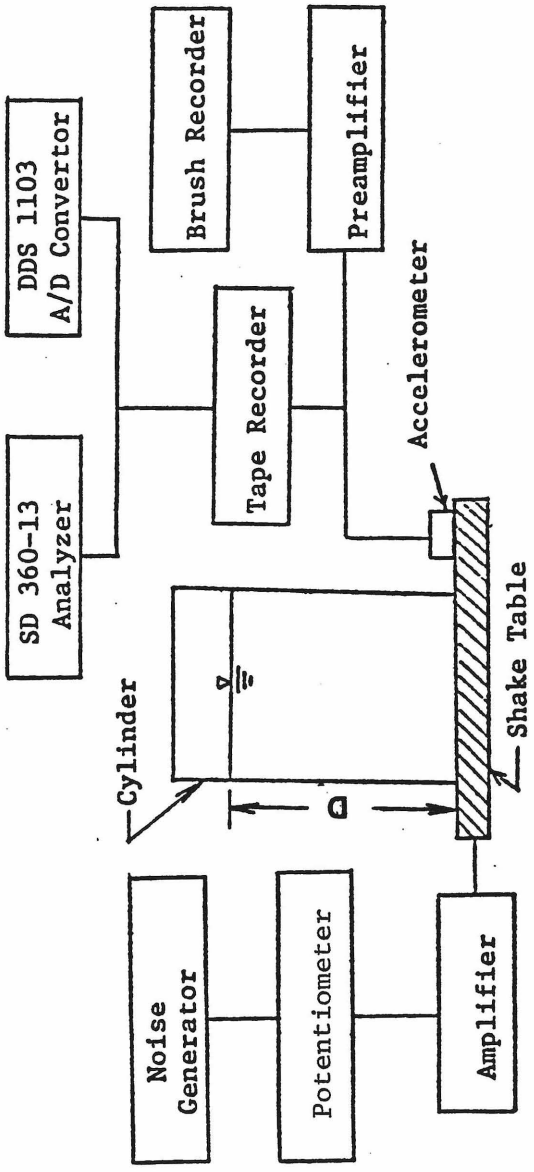

Fig. 4.20 Experimental Set Up for Transient Buckling Test

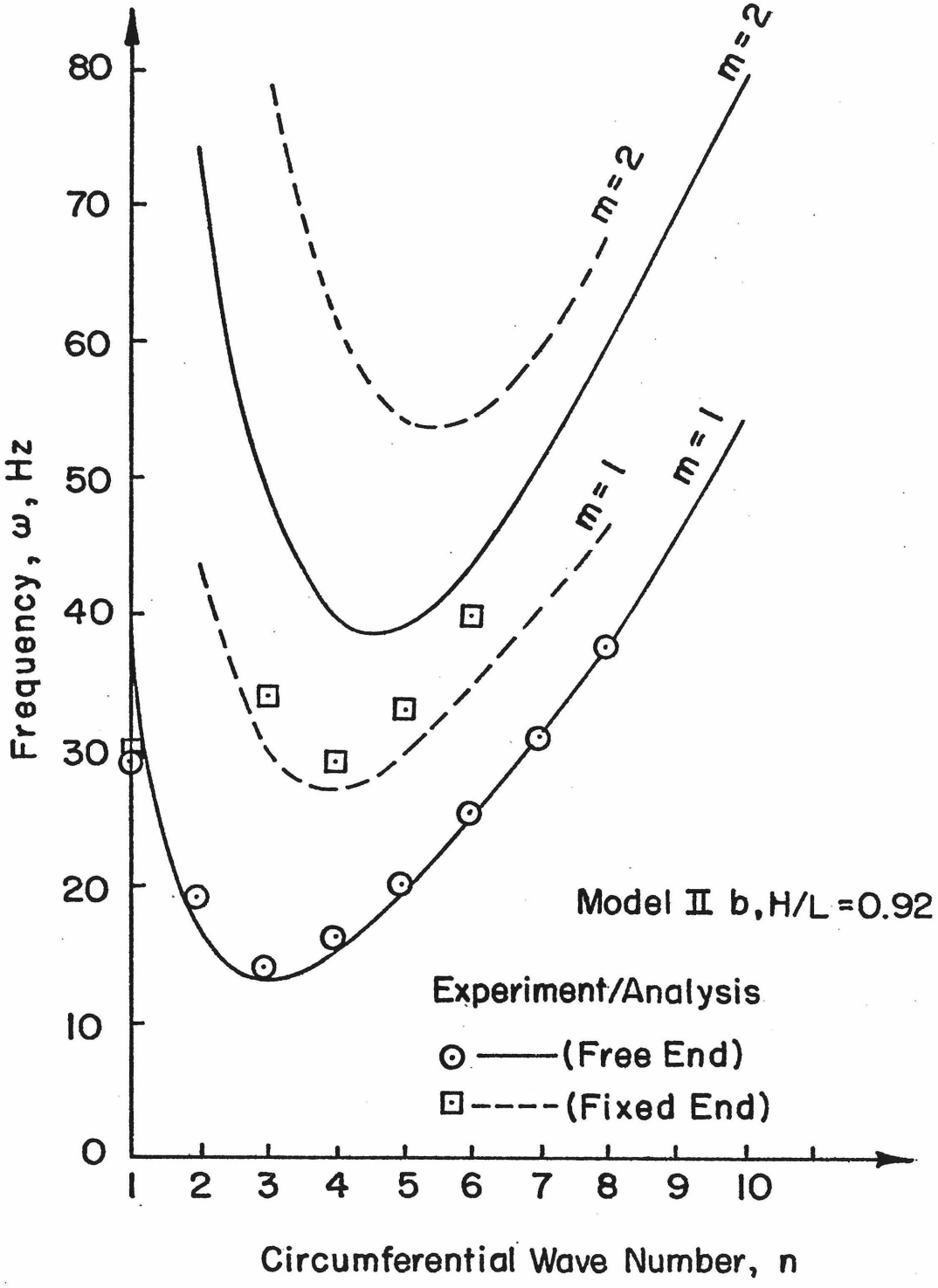

FIG4.21 EXPERIMENTAL/ANALYSIS RESULTS FOR NATURAL FREQUENCY

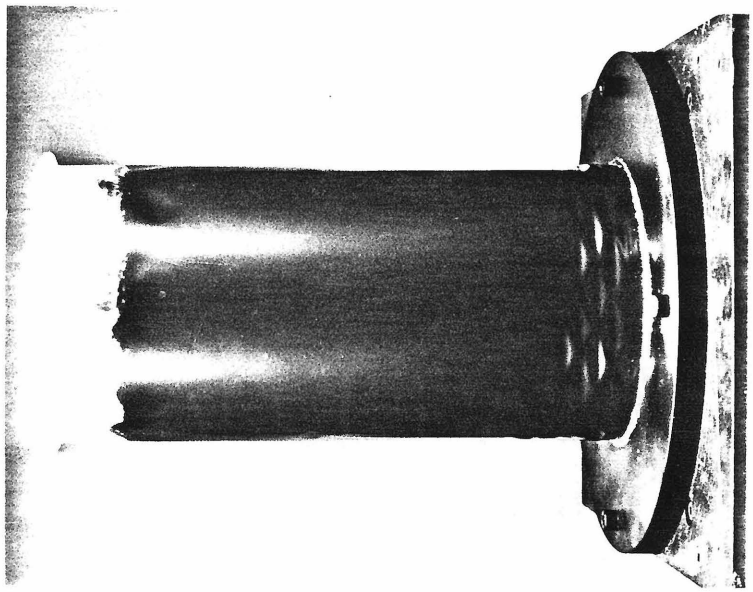

FIG. 4.22 b

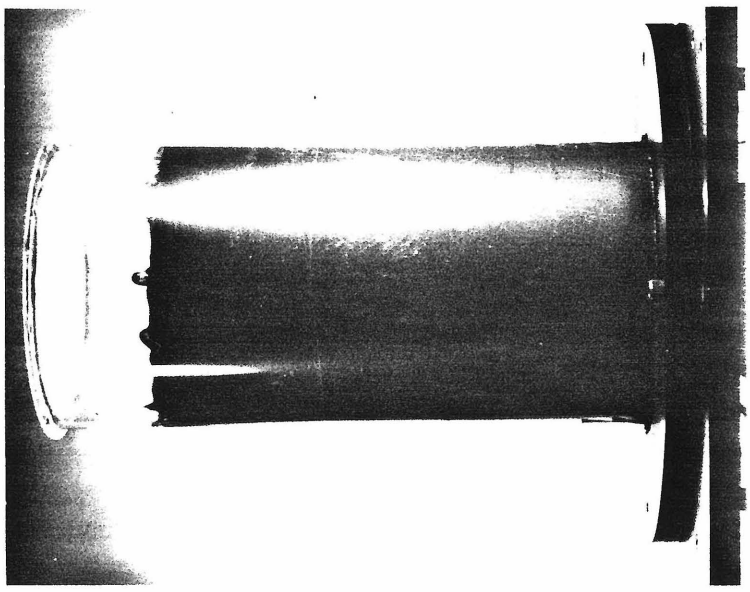

FIG. 4.22 a

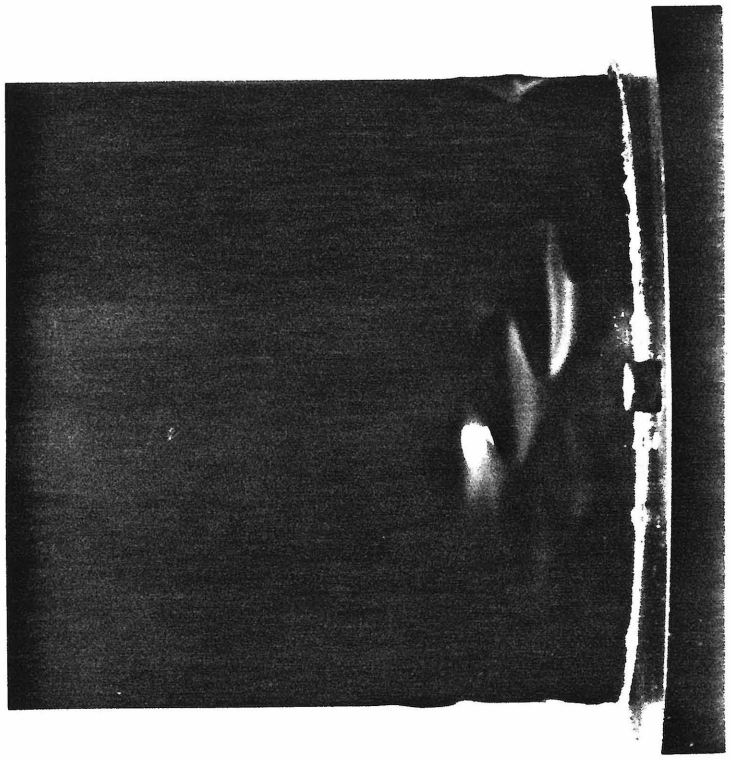

FIG. 4.23

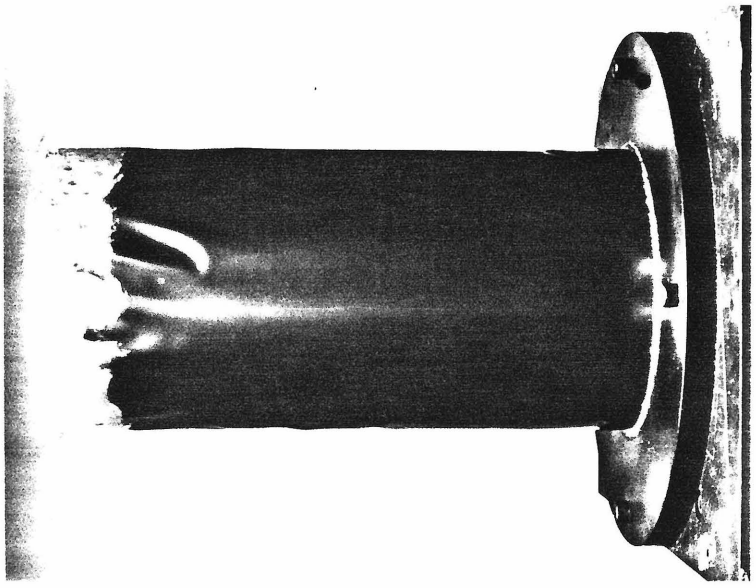

FIG. 4.22 c

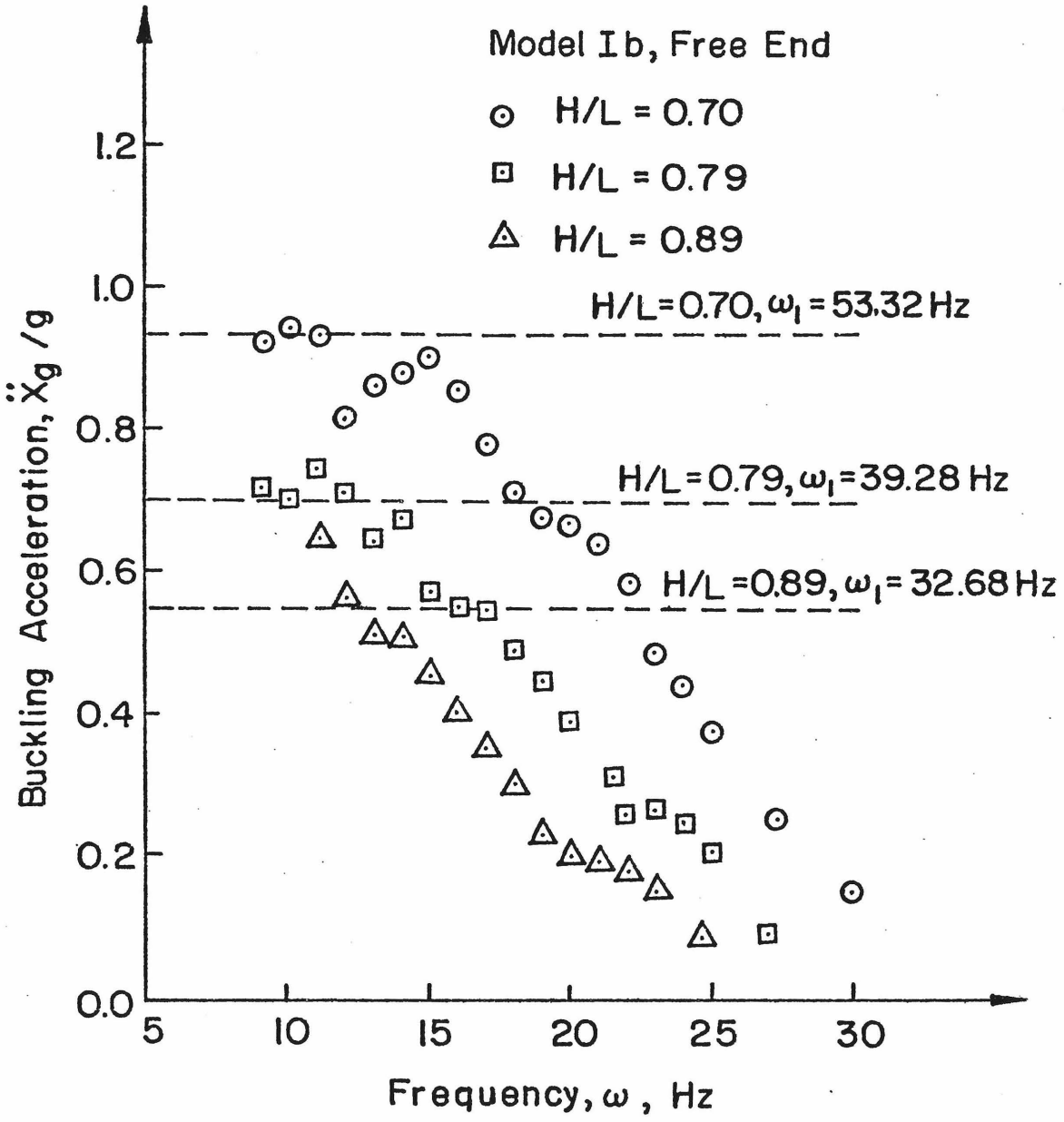

FIG.4.24 LIQUID DEPTH EFFECT ON BUCKLING ACCELERATION

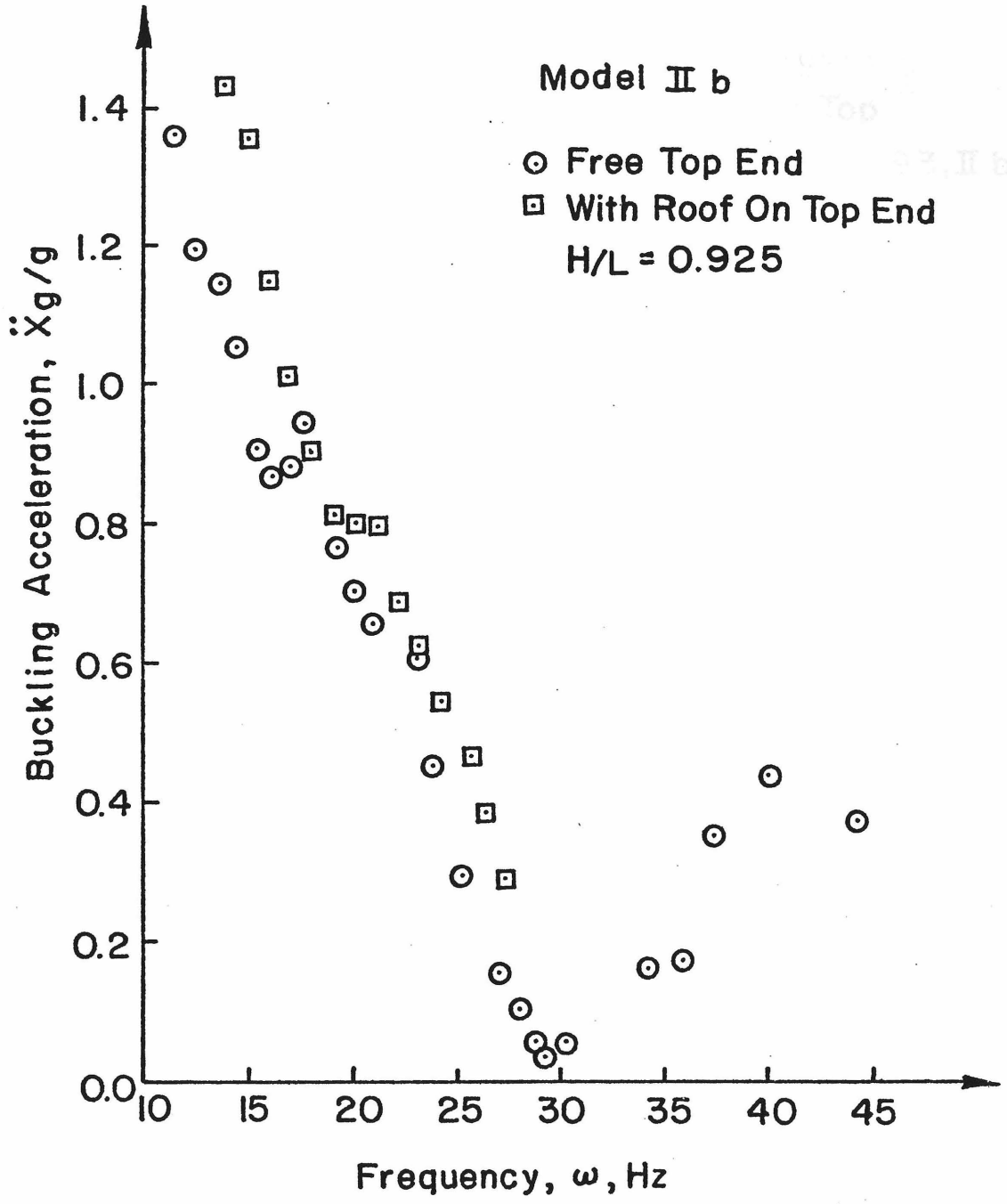

FIG. 4.25 ROOF EFFECT ON BUCKLING ACCELERATION

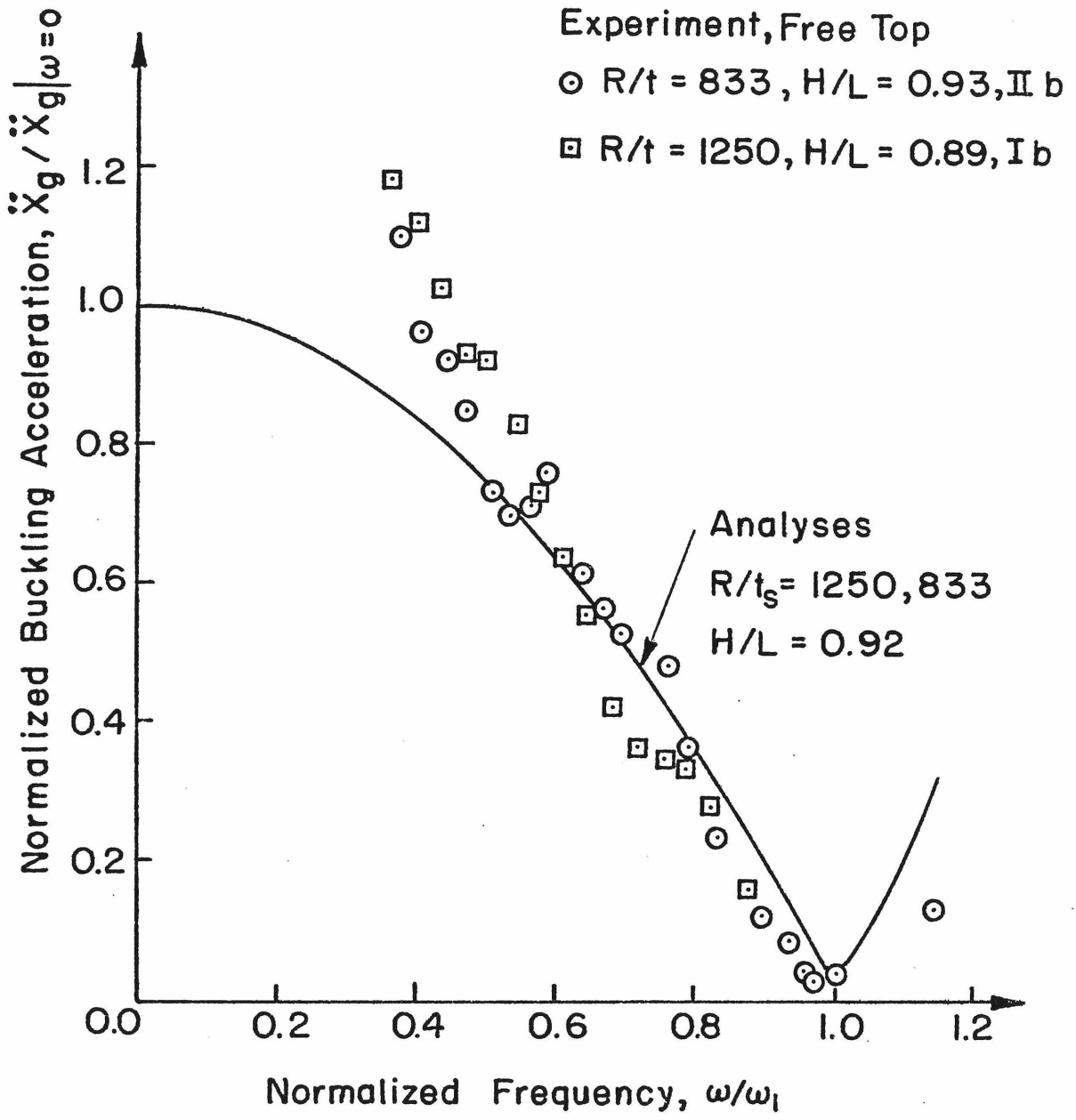

FIG.4.26 COMPARISON OF ANALYSIS/EXPERIMENTAL RESULTS

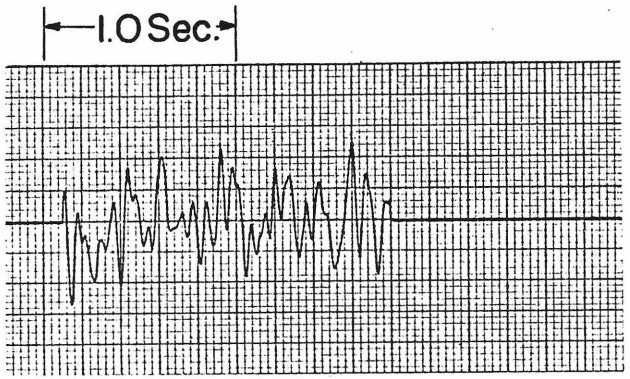

Fig. 4.27a A-Type Noise Pattern

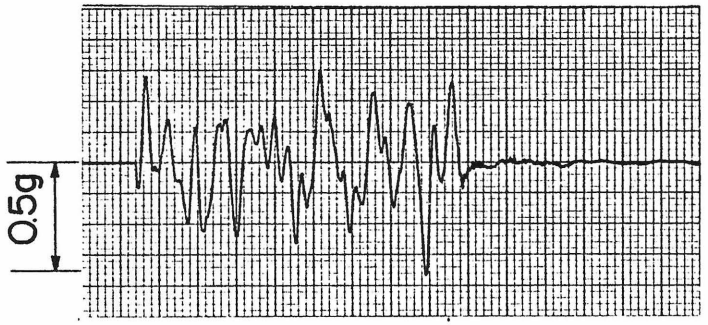

Fig. 4.27b A-Type Base Acceleration

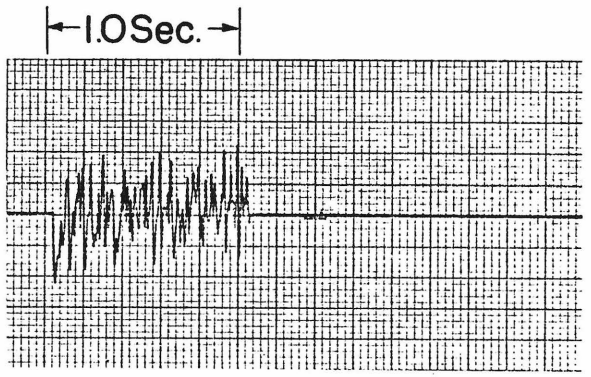

Fif. 4.28a B-Type Noise Pattern

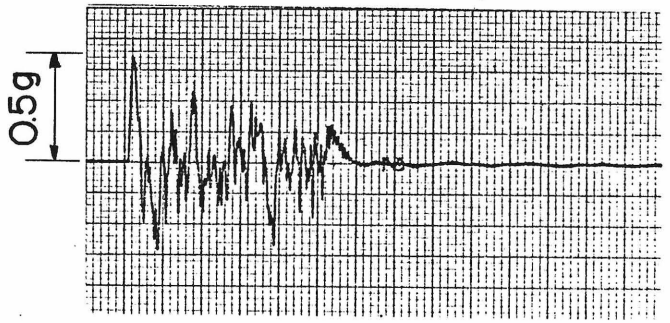

Fig. 4.28b B-Type Base Acceleration

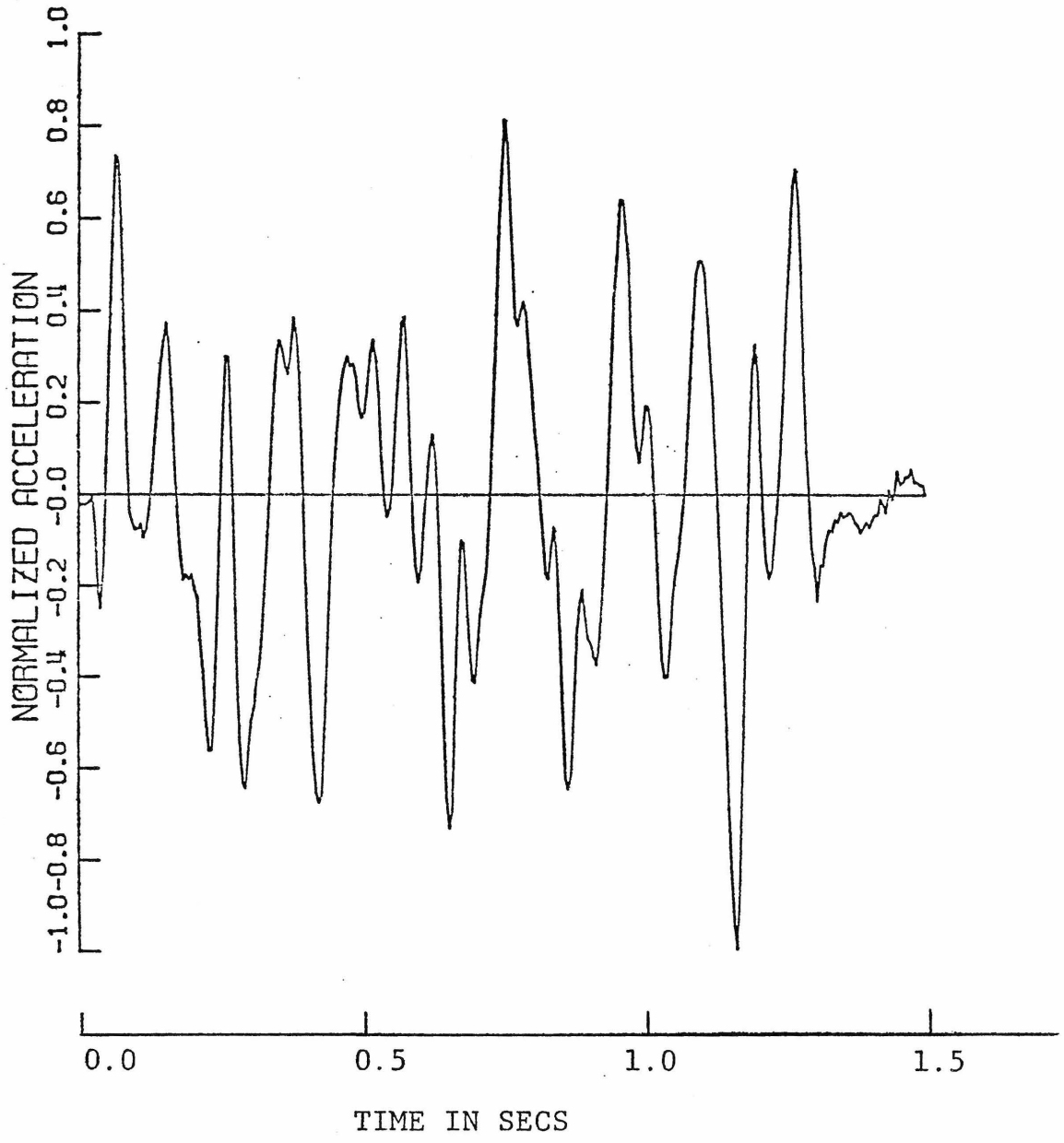

Fig. 4.27c A-Type Base Acceleration for Theoretical Analysis

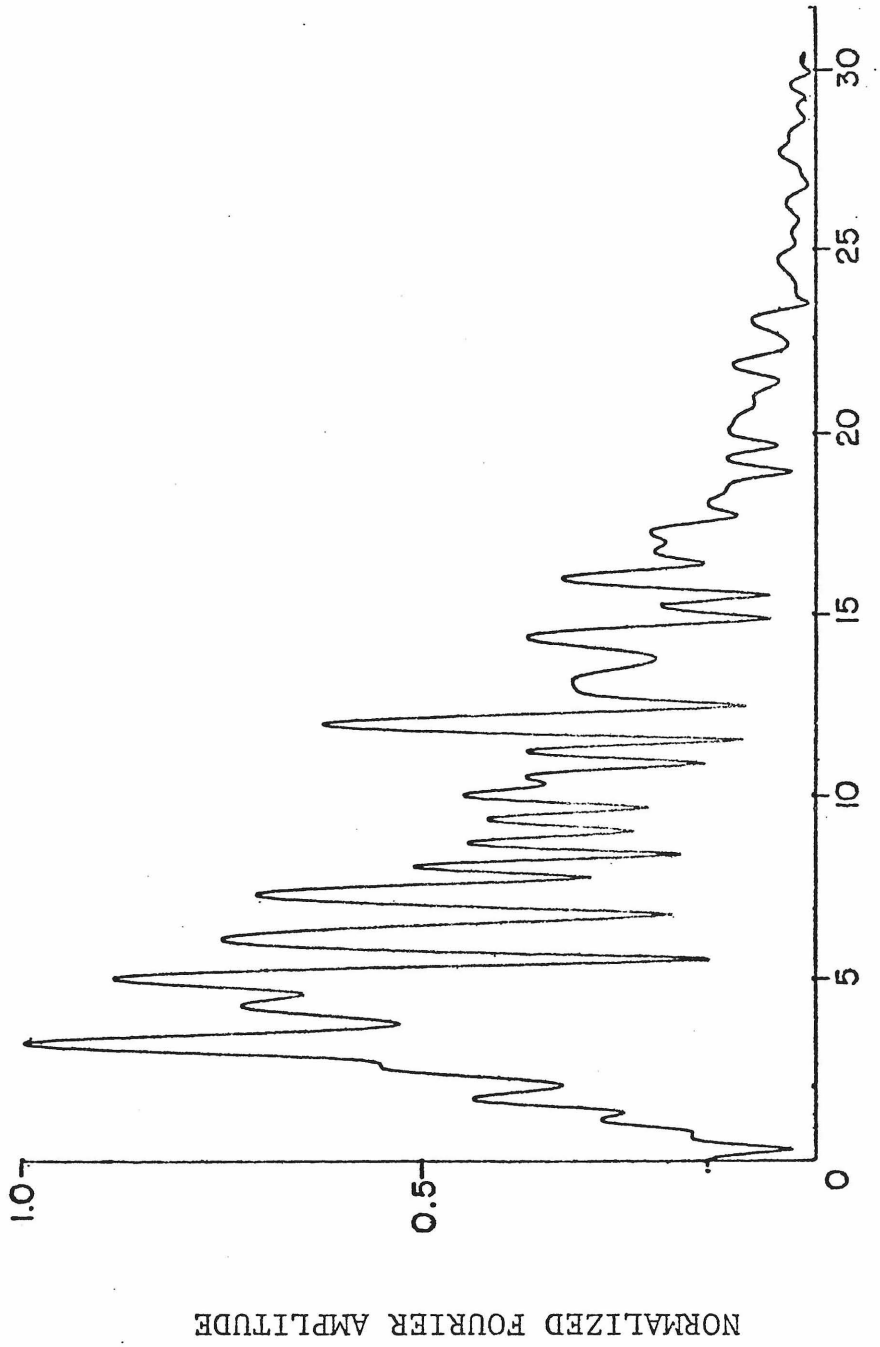

Fig. 4.27d Fourier Amplitude of A-Type Base Acceleration

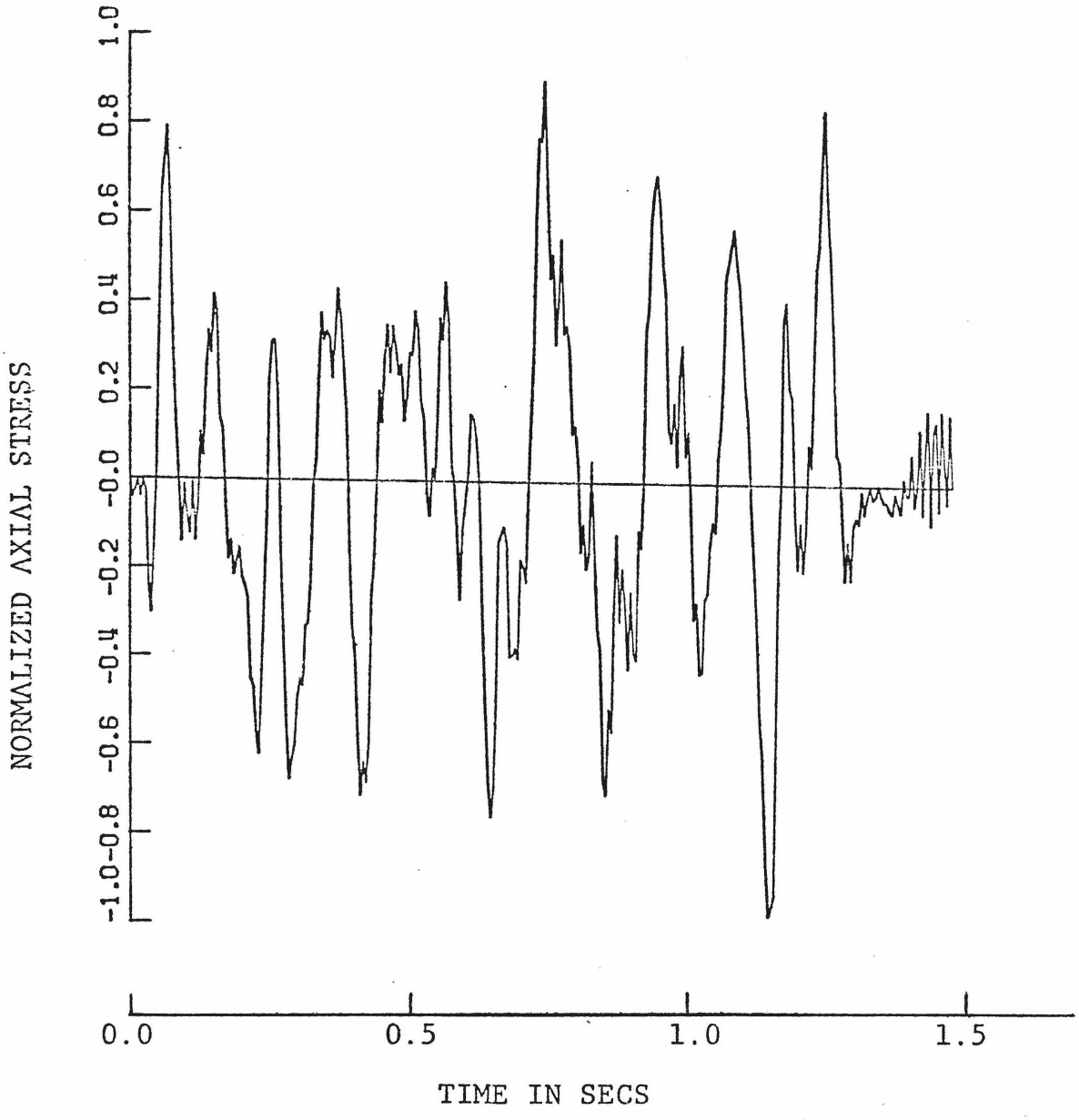

Fig. 4.27e Axial Membrane Stress on the Shell Wall of the Tank Subjected to A-Type Base Excitation

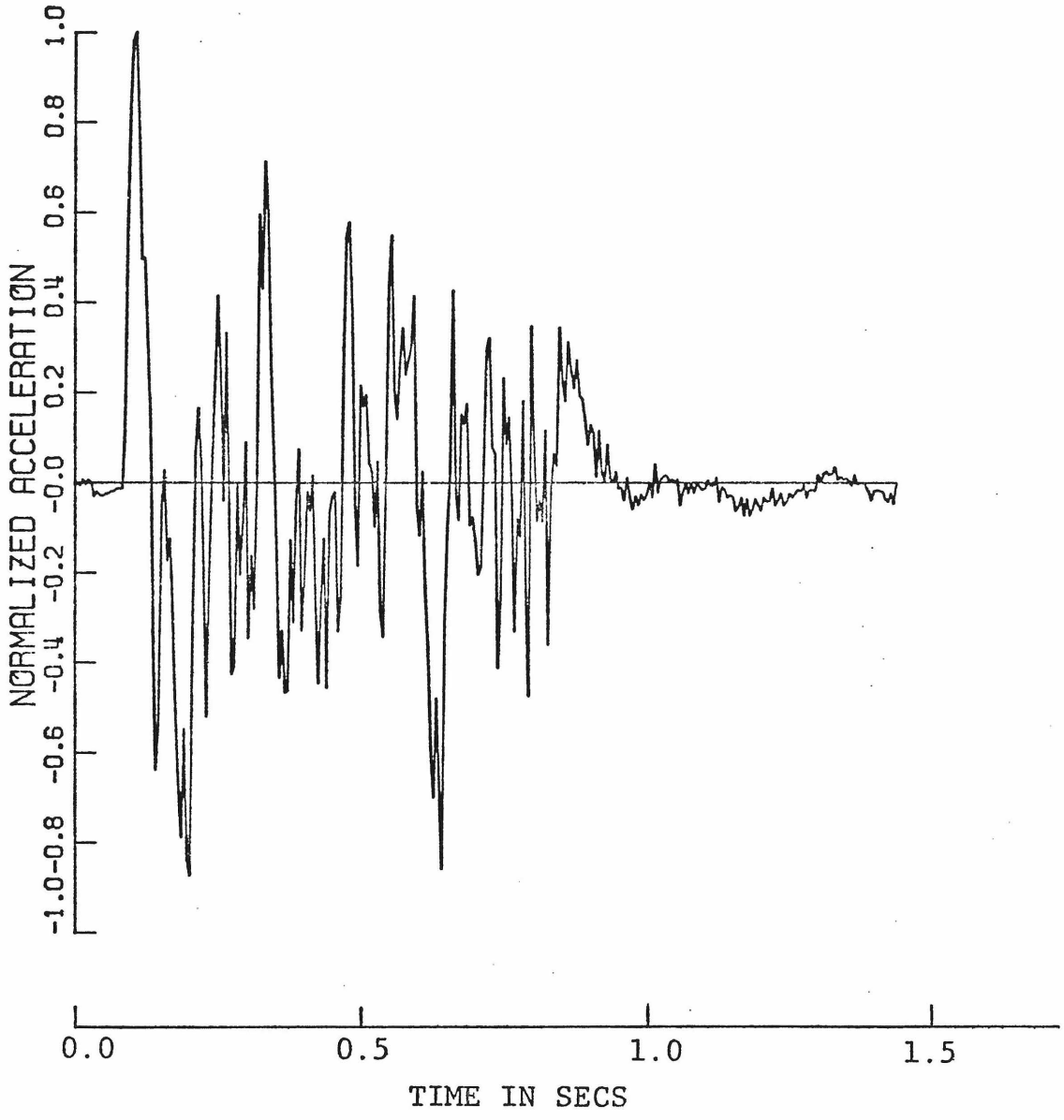

Fig. 4. 28c B-Type Base Acceleration for Theoretical Analysis

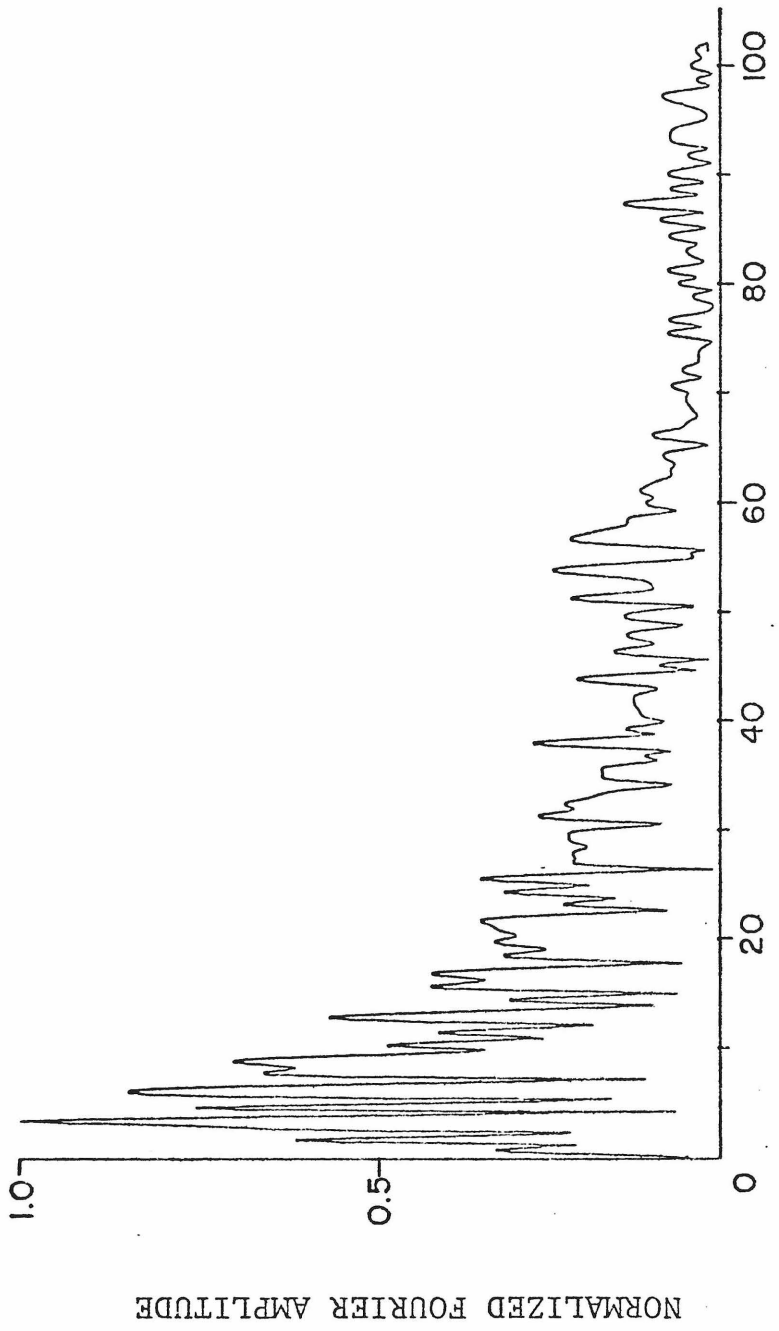

Fig. 4.28d Fourier Amplitude of B-Type Base Acceleration

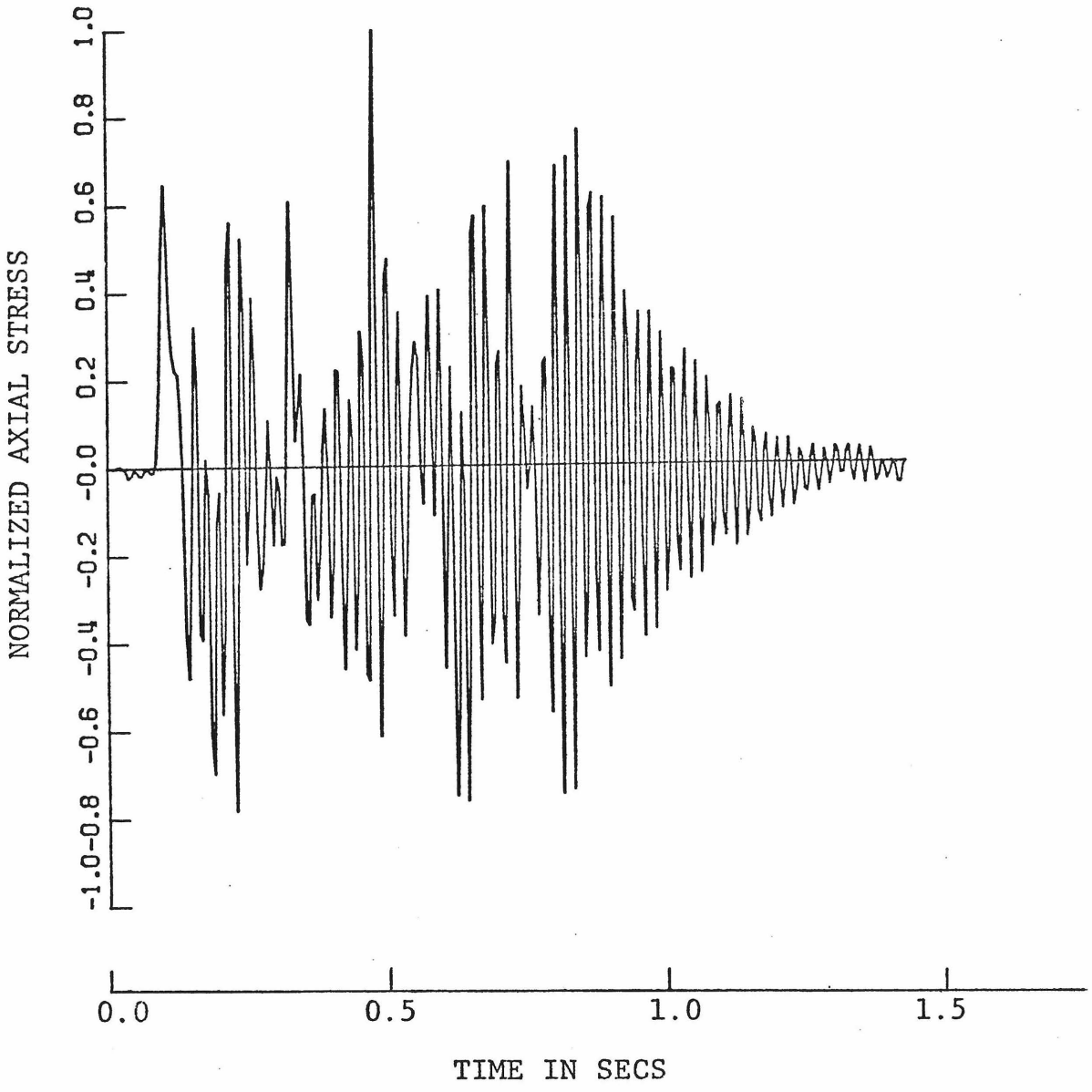

Fig. 4.28e Axial Membrane Stress on the Shell Wall of the Tank Subjected to B-Type Base Excitation

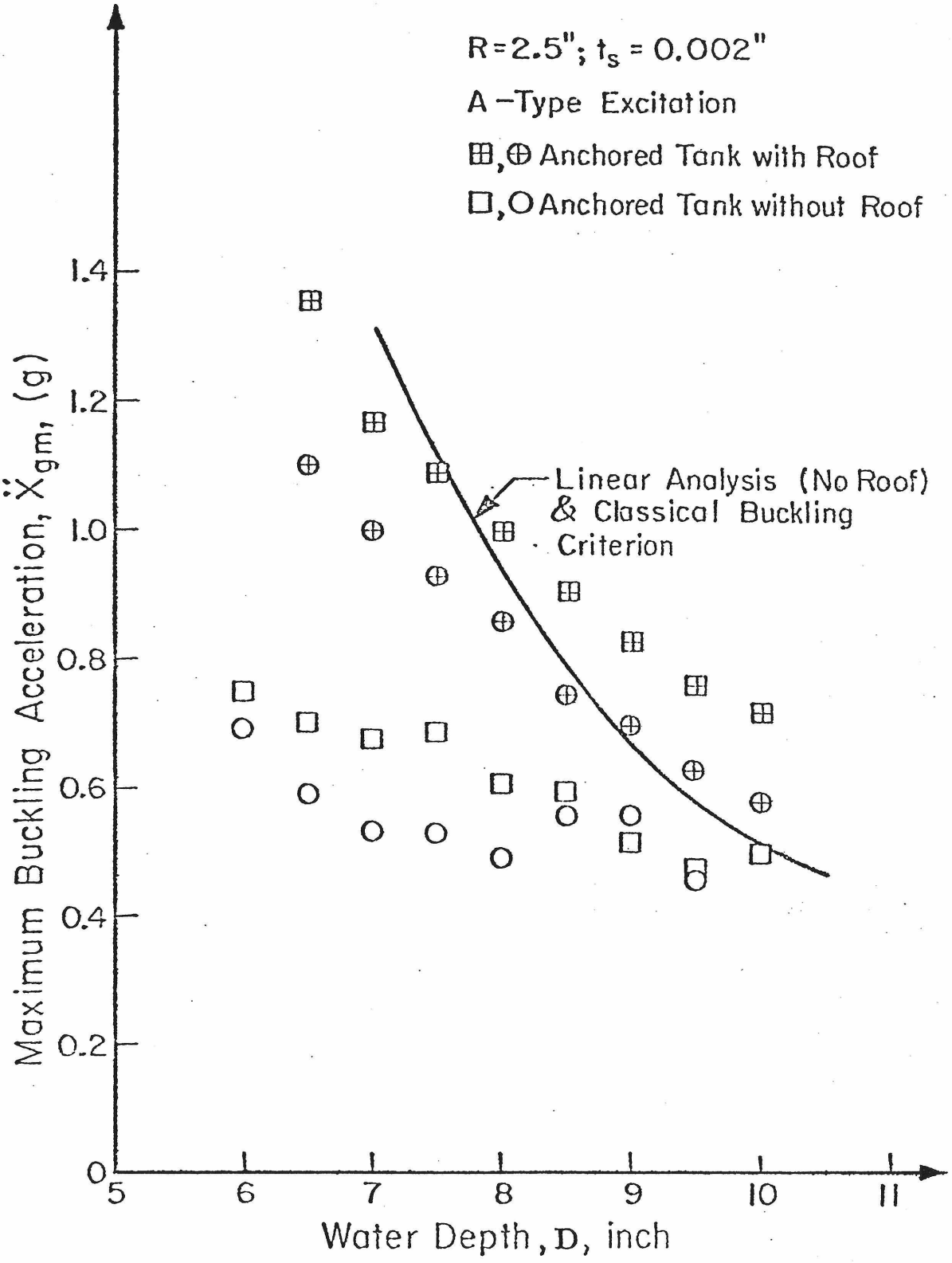

Fig. 4.29 Transient Buckling Test Results of an Anchored Tank

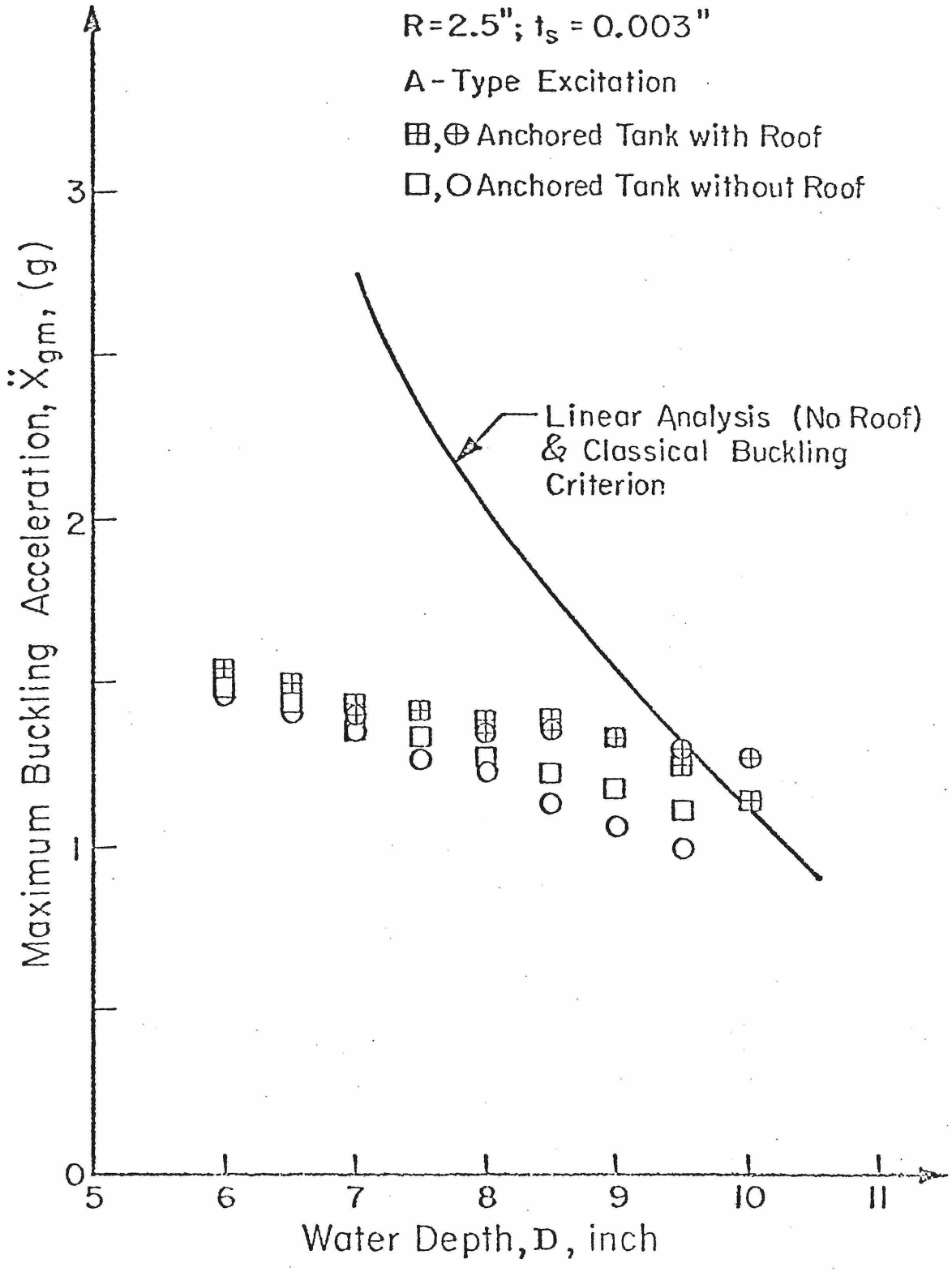

Fig. 4.30 Transient Buckling Test Results of an Anchored Tank

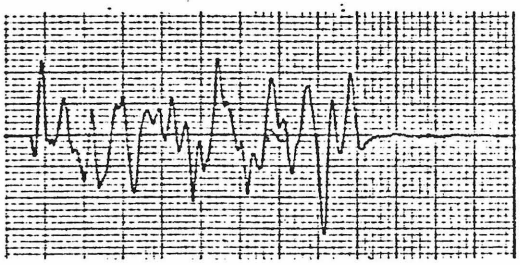

D = 6.0 in. Buckle

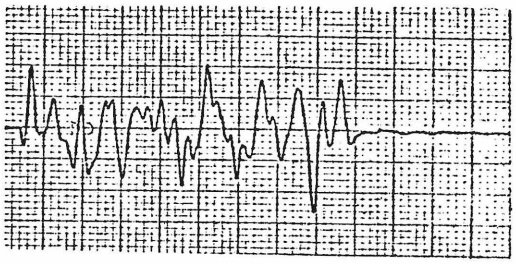

D = 6.0 in. No Buckle

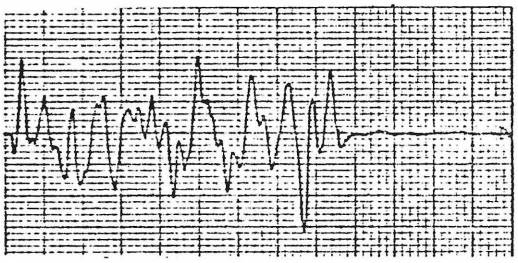

D = 7.0 in. Buckle

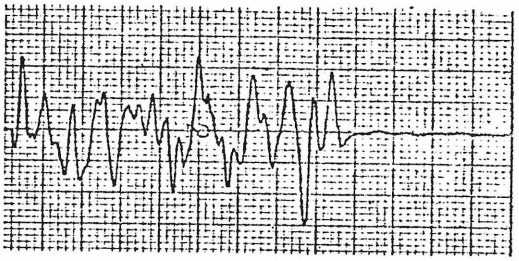

D = 7.0 in. Small Buckle

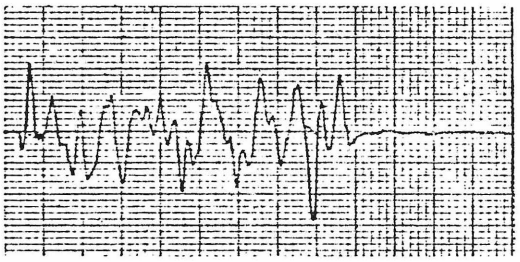

D = 8.0 in. Buckle

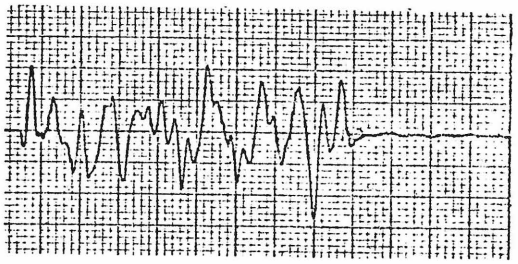

D = 8.0 in. Small Buckle

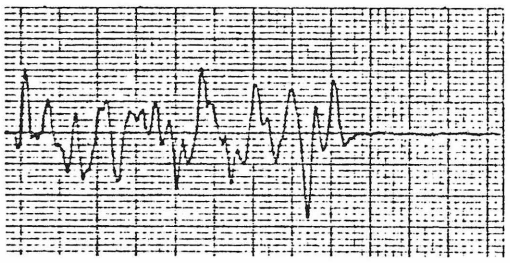

D = 9.0 in. Buckle

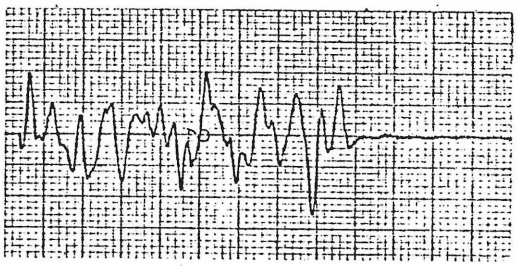

D = 9.0 in. Small Buckle

R = 2.5 inch; t_s = 0.003 inch; Free Top End

Fig. 4.31 A-Type Base Excitation Patterns for Different Water Depth Cases

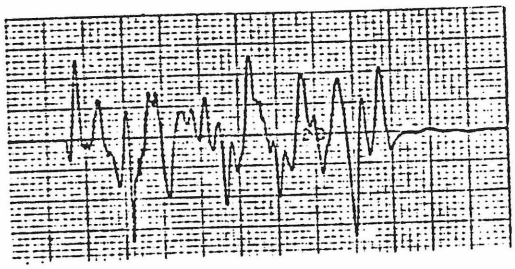

D = 6.0 in. Buckle

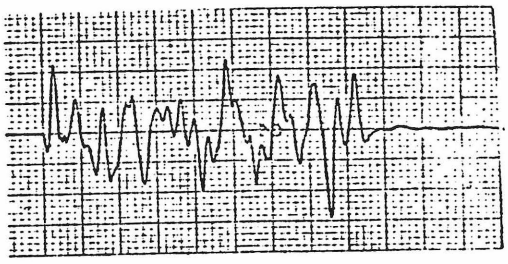

D = 6.0 in. No Buckle

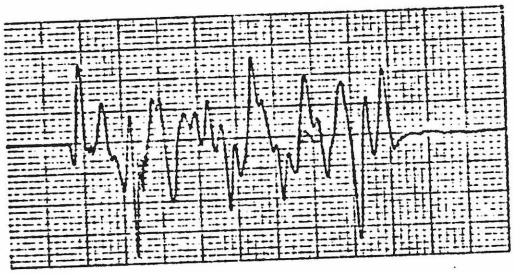

D = 7.0 in. Buckle

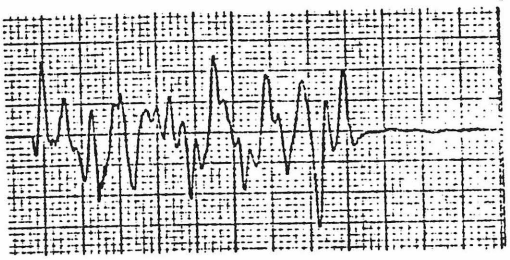

D = 7.0 in. Small Buckle

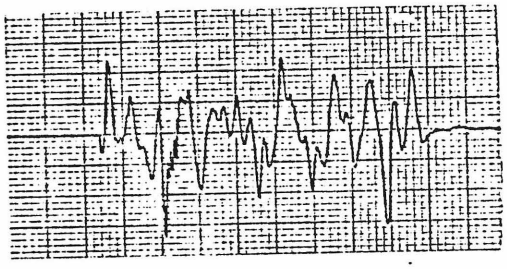

D = 8.0 in. Buckle

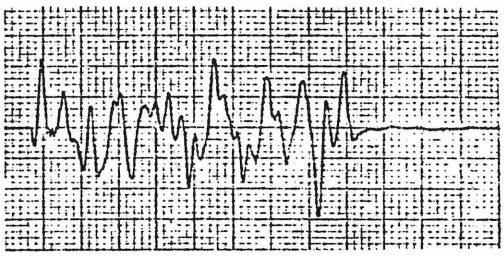

D = 8.0 in. No Buckle

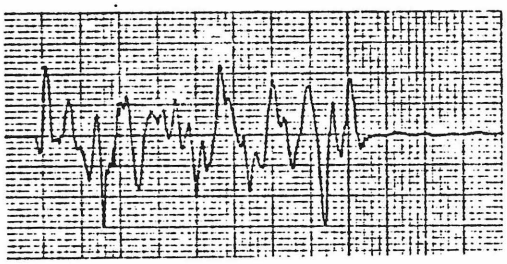

D = 9.0 in. Buckle

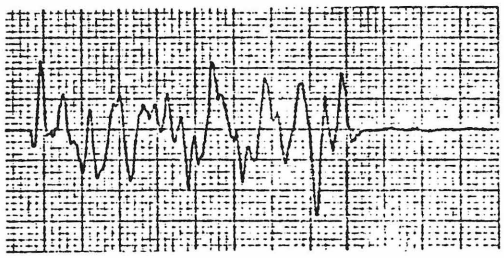

D = 9.0 in. No Buckle

R = 2.5 inch; t_s = 0.003 inch; Roof on Top End.

Fig. 4.32 A-Type Base Excitation Patterns for Different Water Depth Cases

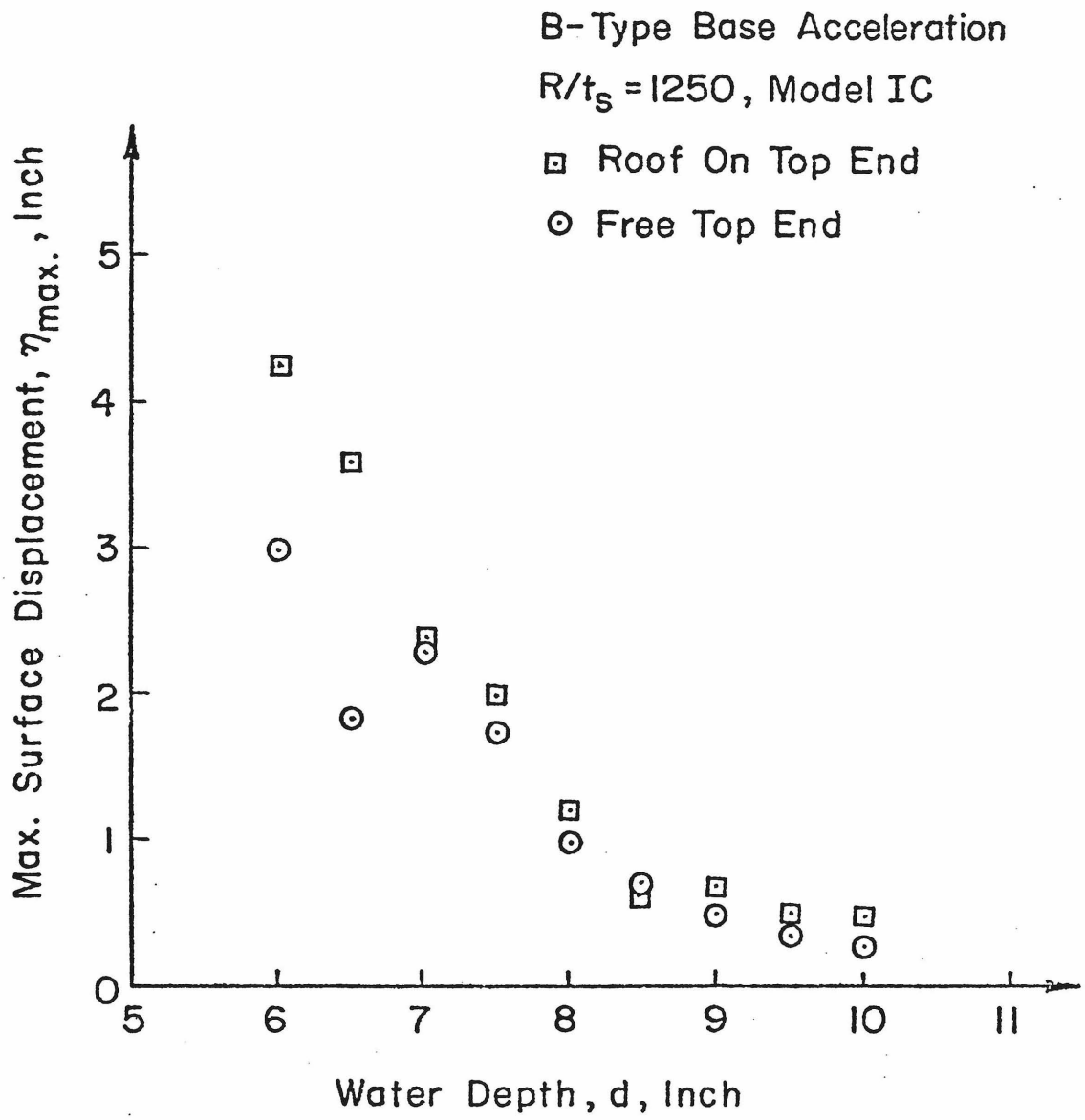

Fig. 4.33 Maximum Surface Displacement, vs. Water Depth

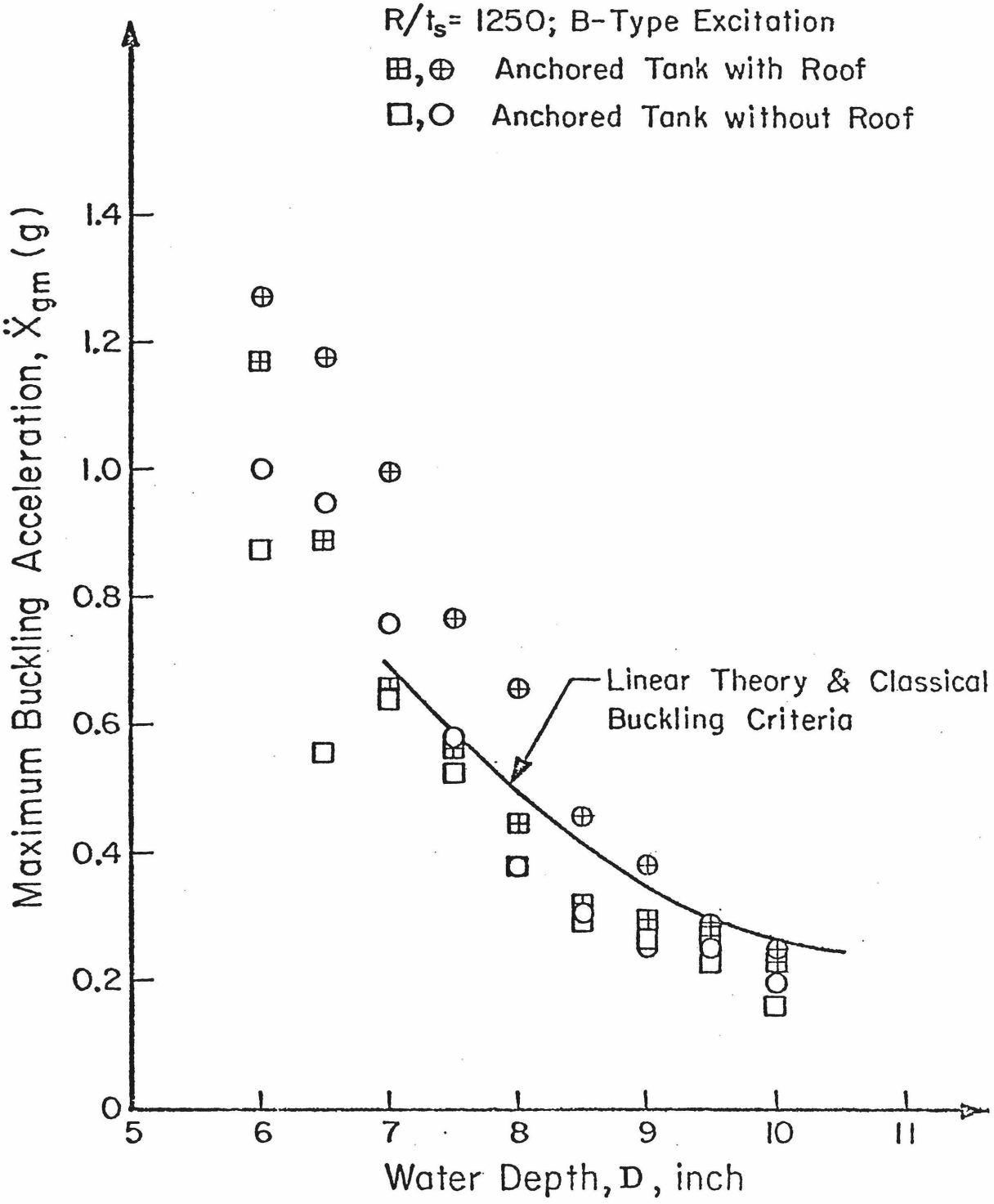

Fig. 4.34 Transient Buckling Test Results of an Anchored Tank

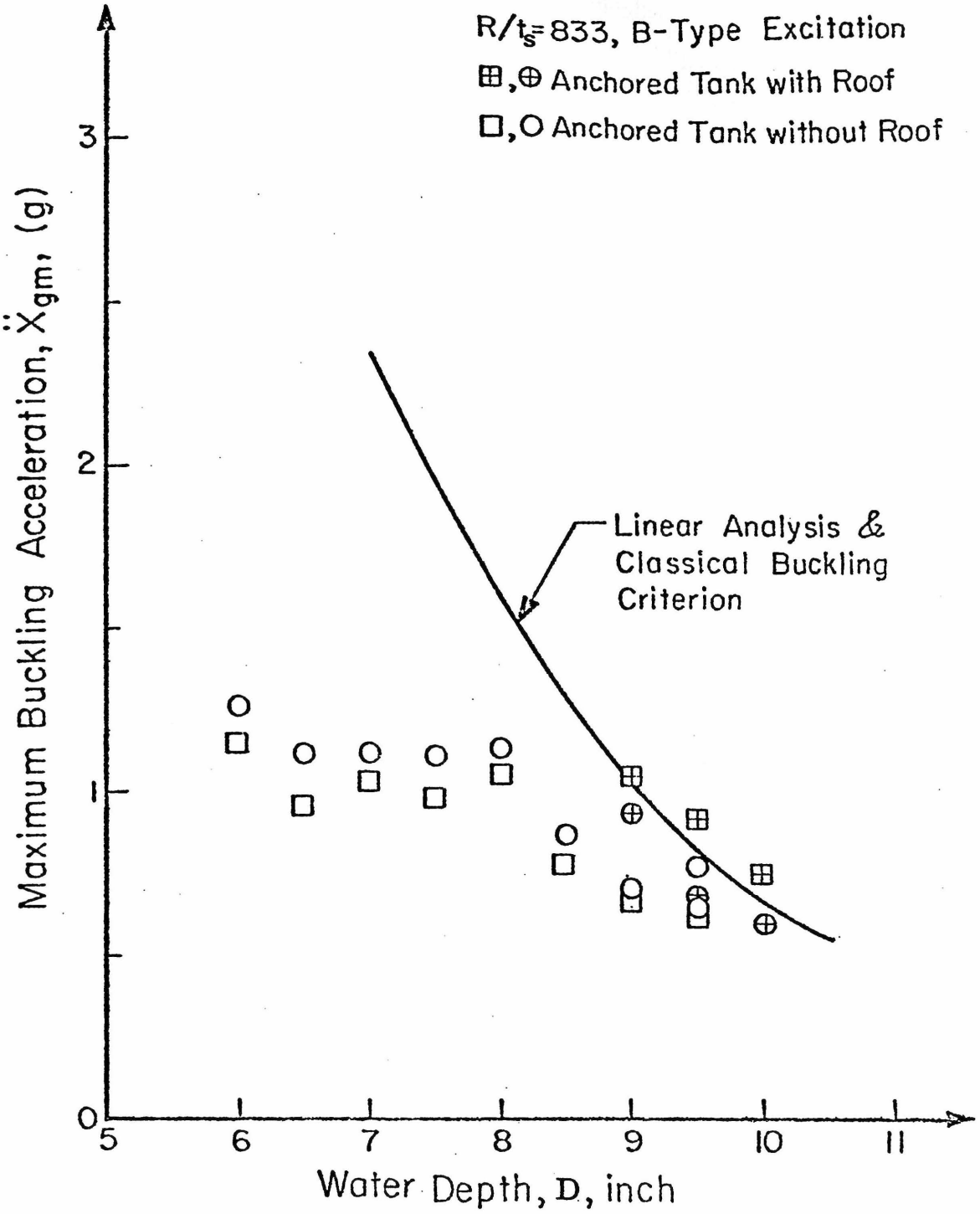

Fig. 4.35 Transient Buckling Test Results of an Anchored Tank

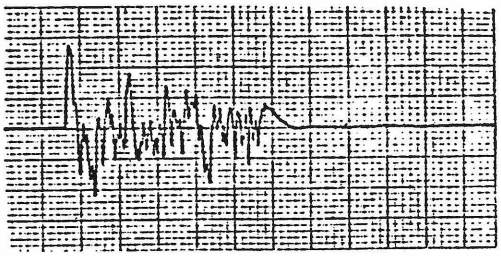

D = 6.0 in. Buckle

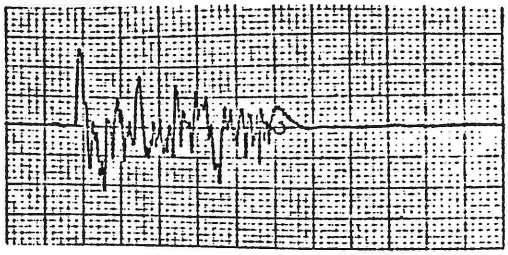

D = 6.0 in. No Buckle

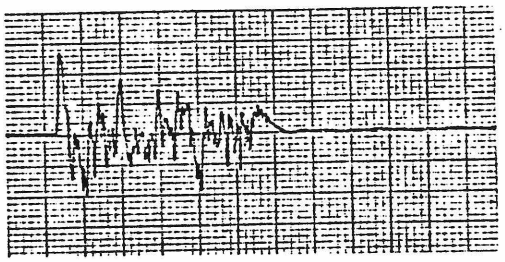

D = 7.0 in. Buckle

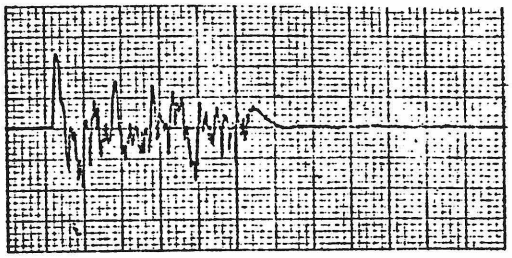

D = 7.0 in. No Buckle

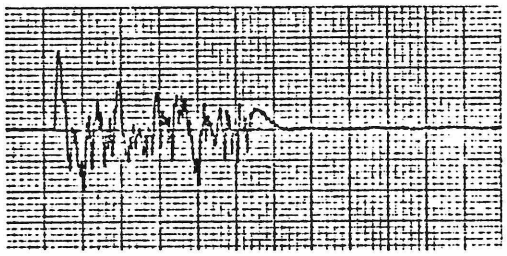

D = 8.0 in. Buckle

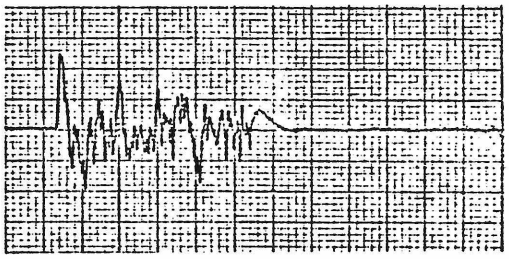

D = 8.0 in. No Buckle

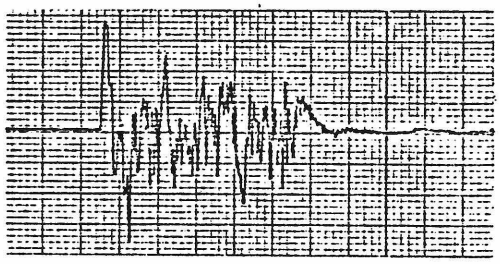

D = 9.0 in. Buckle

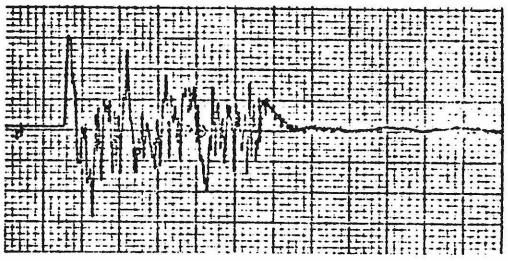

D = 9.0 in. No Buckle

R = 2.5 inch; t_s = 0.003 inch; Free Top End.

Fig. 4.36 B-Type Base Excitation Patterns for Different Water Depth

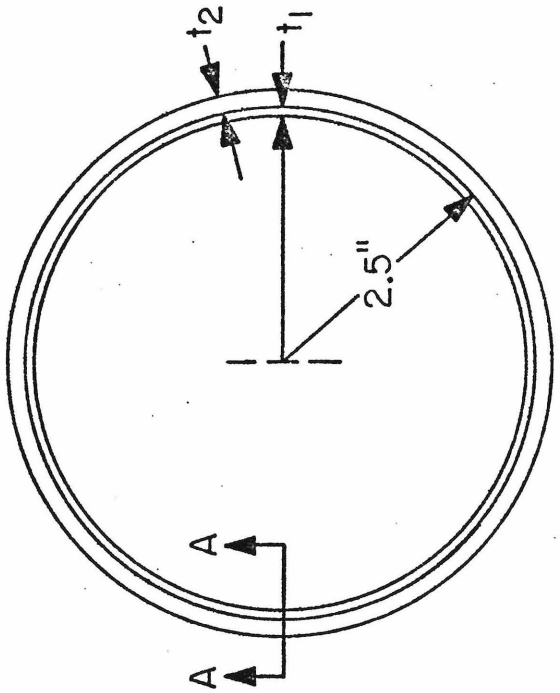

Lucite Thickness	Ring No. 1	Ring No. 2
t_1	1/16"	1/32"
t_2	1/8"	1/16"
t_3	1/4"	1/4"
t_4	1/16"	1/32"

Figure 5.1 THE DIMENSIONS OF BOTTOM REINFORCING RING

Fig. 5.3 EXPERIMENTAL BUCKLING TEST

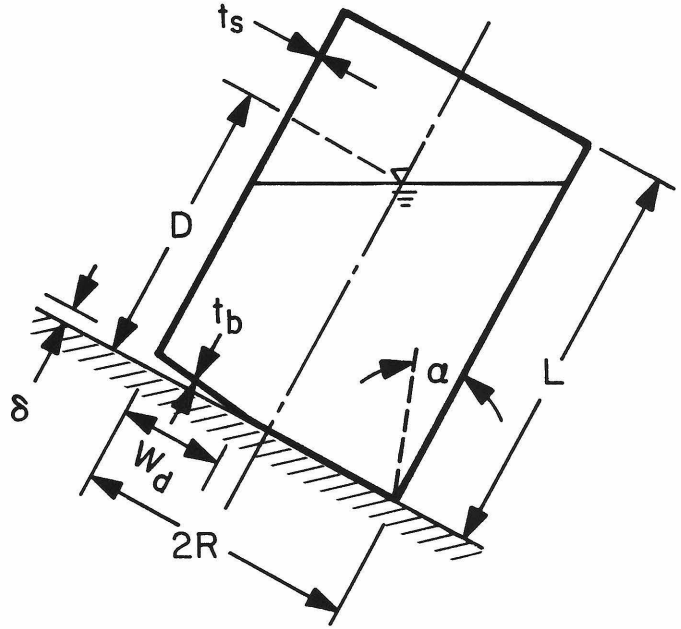

Fig. 5.2 LOADING CONDITION AND NOMENCLATURE

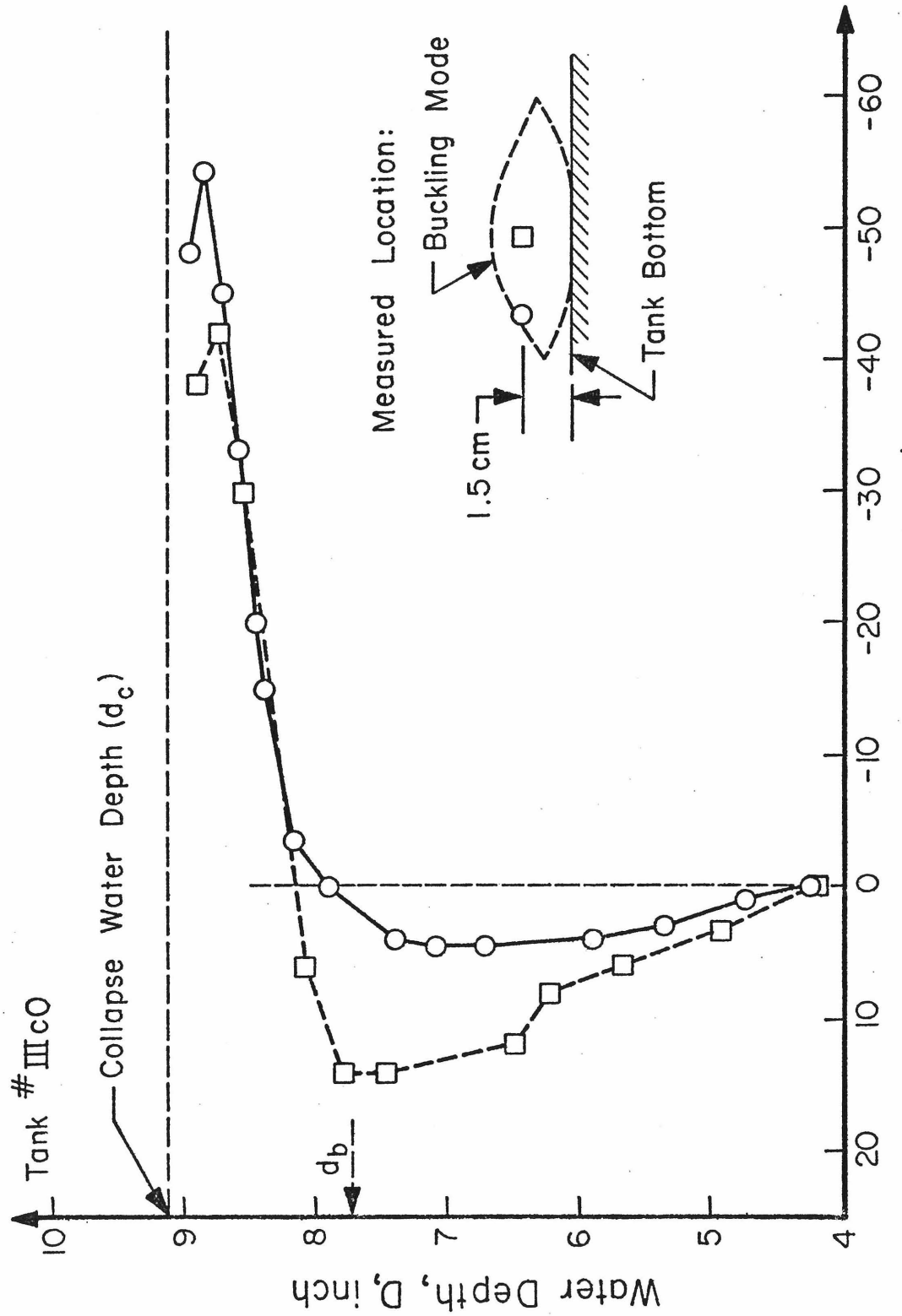

Fig. 5.4 RADIAL DISPLACEMENT VS. WATER DEPTH

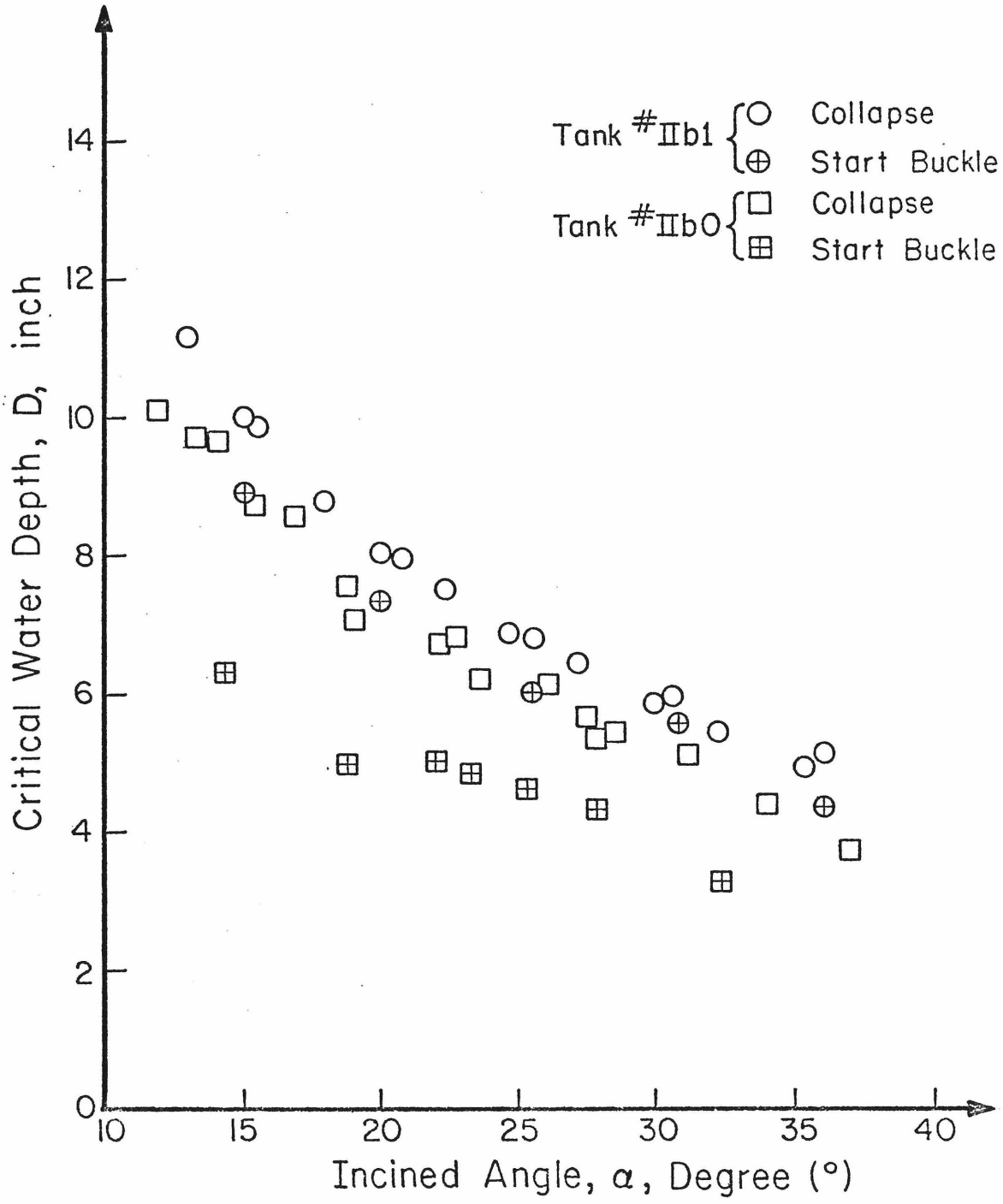

Fig. 5.5 THE COMPARISON BETWEEN CRITICAL BUCKLING WATER DEPTH AND COLLAPSE WATER DEPTH

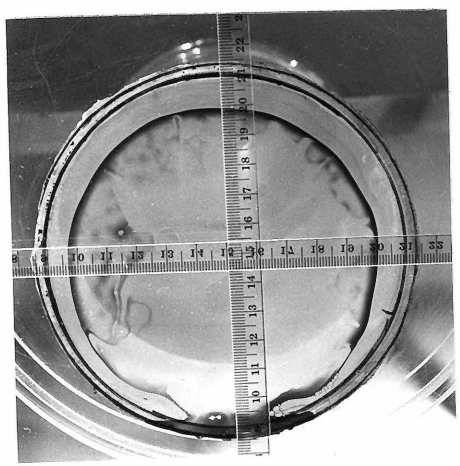

(a) **D** = 4.64 in.
α = 19.6°
Tank# IIb2

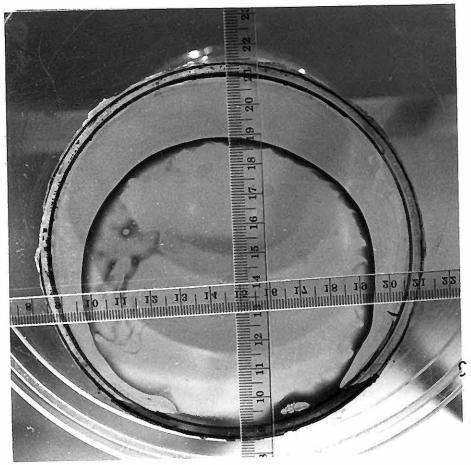

(b) **D** = 5.84 in.
α = 19.6°
Tank# IIb2

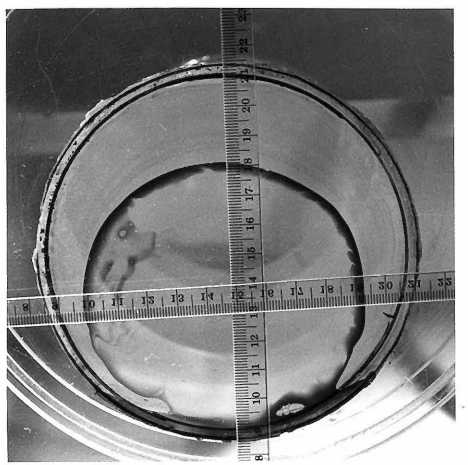

(c) **D** = 7.09 in.
α = 19.6°
Tank# IIb2

Figure 5.6 Bottom Uplifting Area of Unanchored Tank

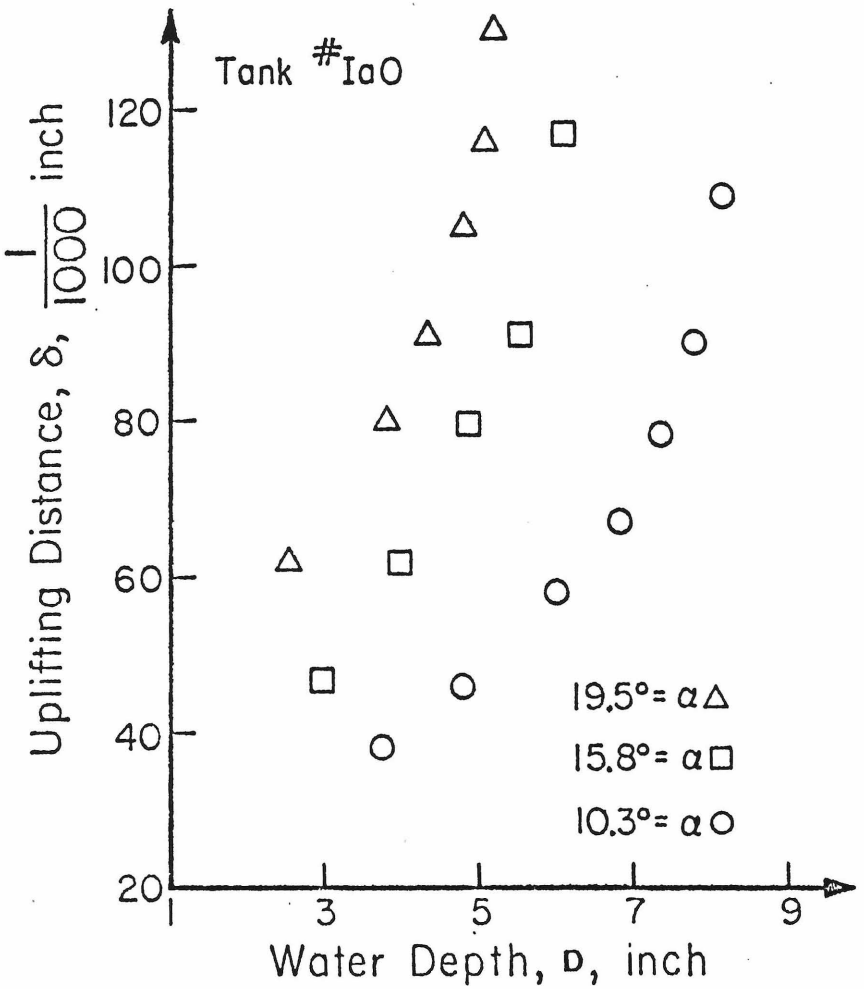

Fig.5.7a Uplifting Distance vs. Water Depth

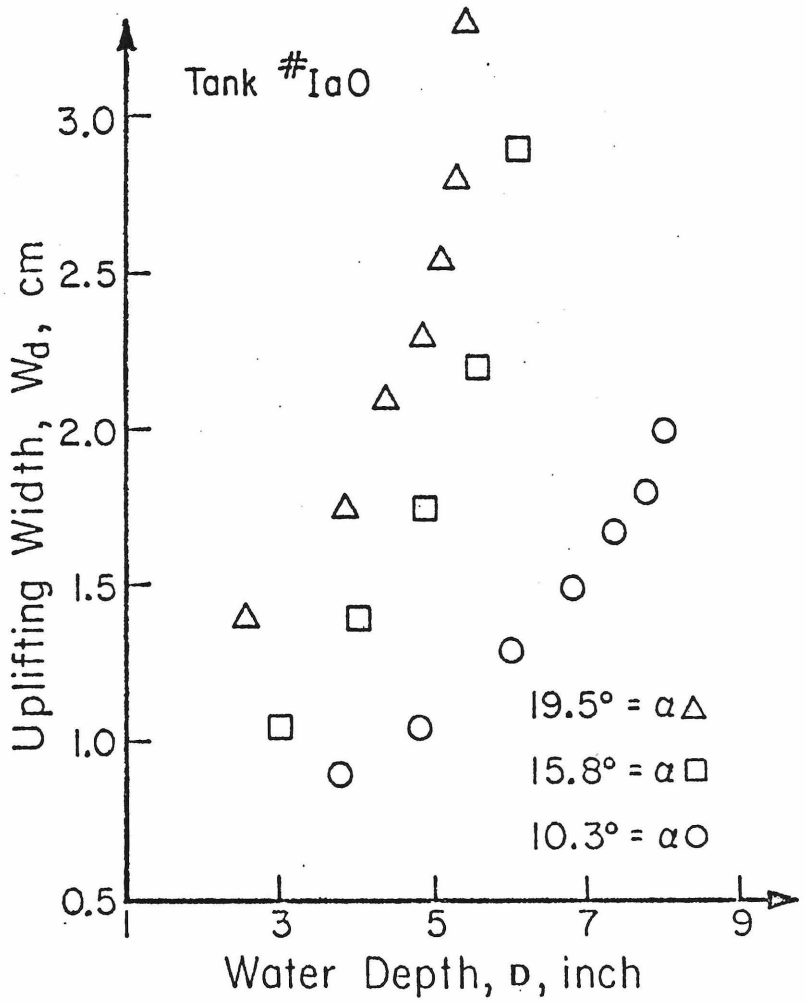

Fig.5.7b Uplifting Width vs. Water Depth.

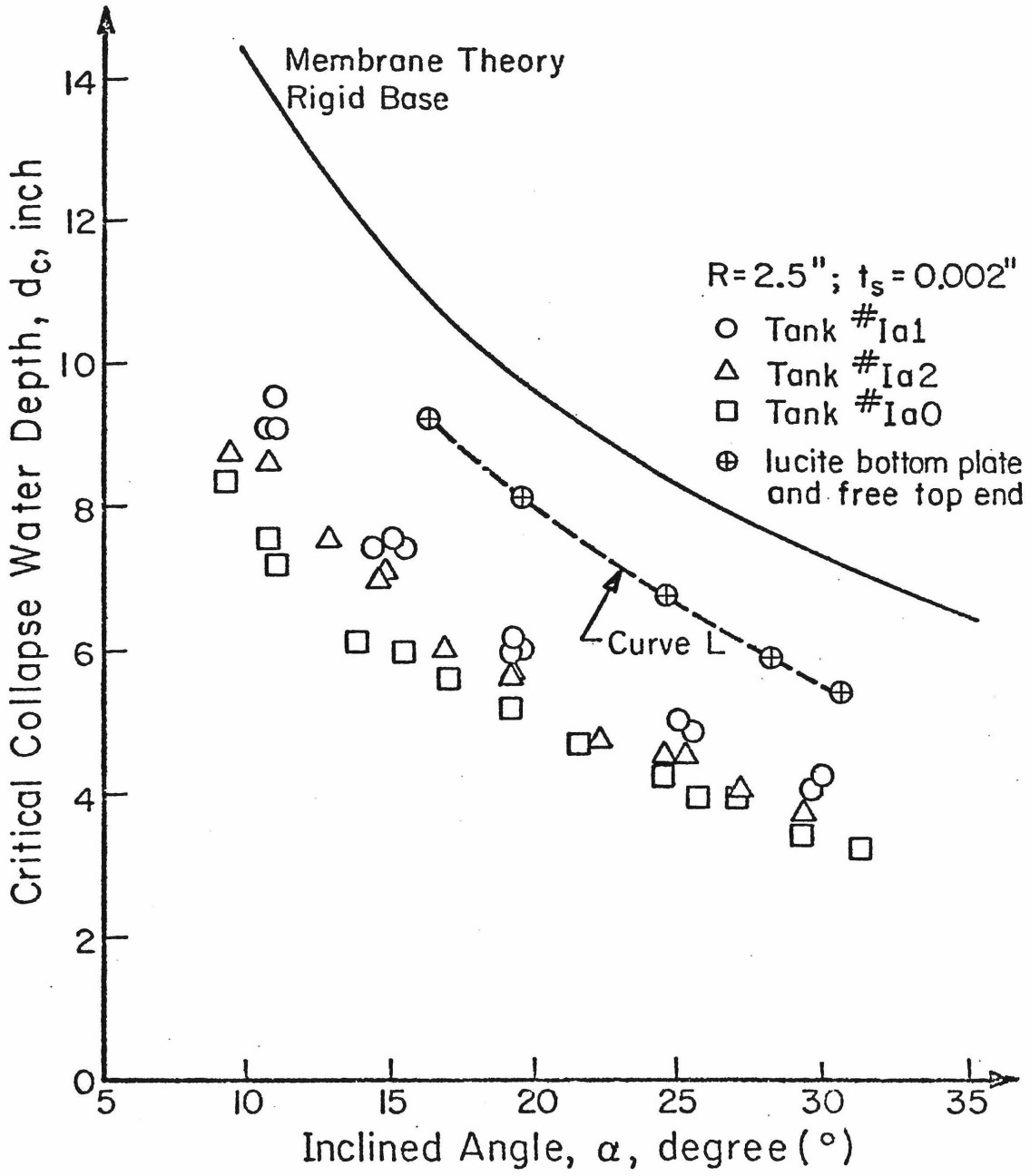

Fig.5.8a Collapse Water Depth vs. Inclined Angle

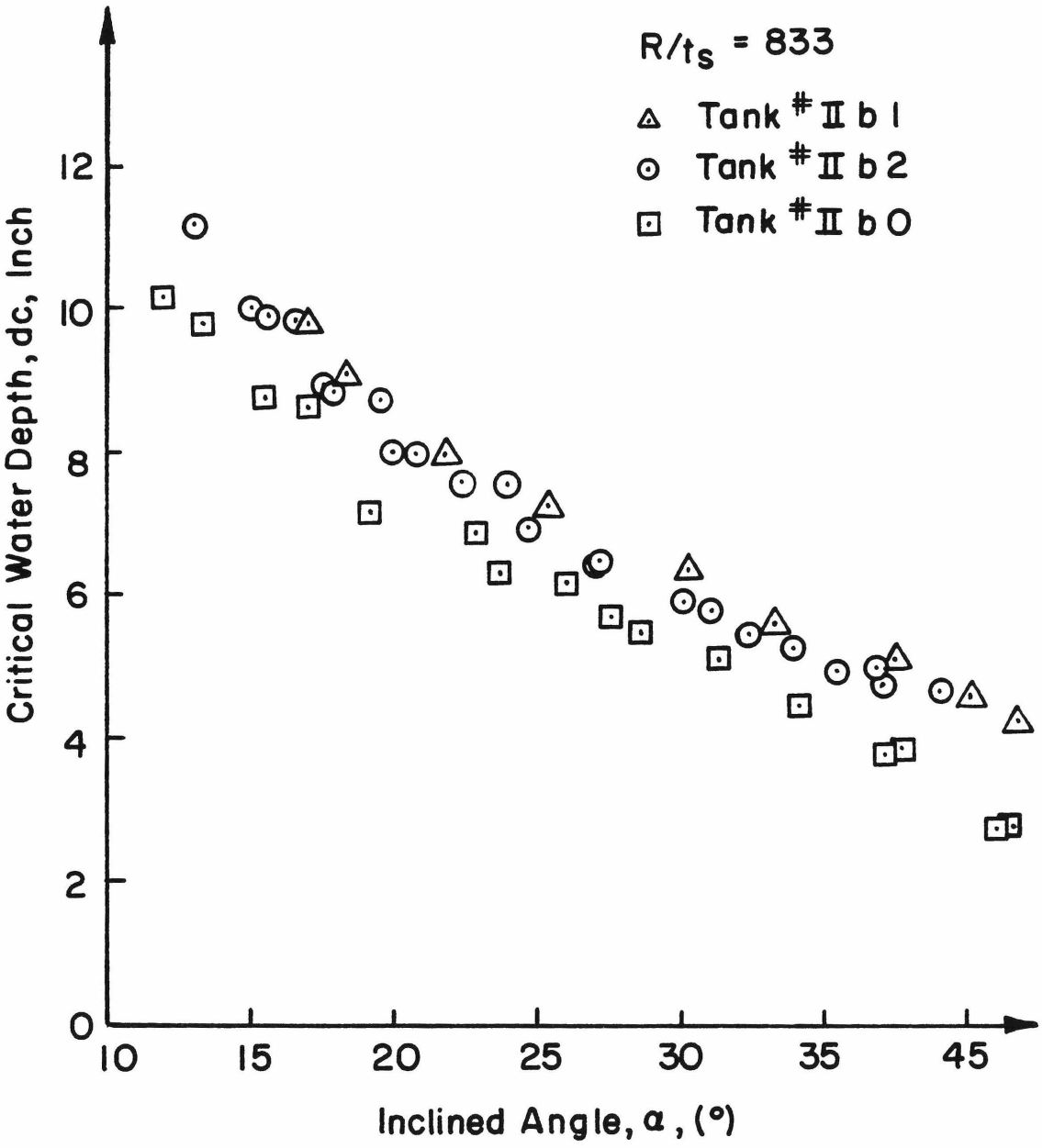

FIG. 5.8 b CRITICAL COLLAPSE WATER DEPTH VS. INCLINED ANGLE

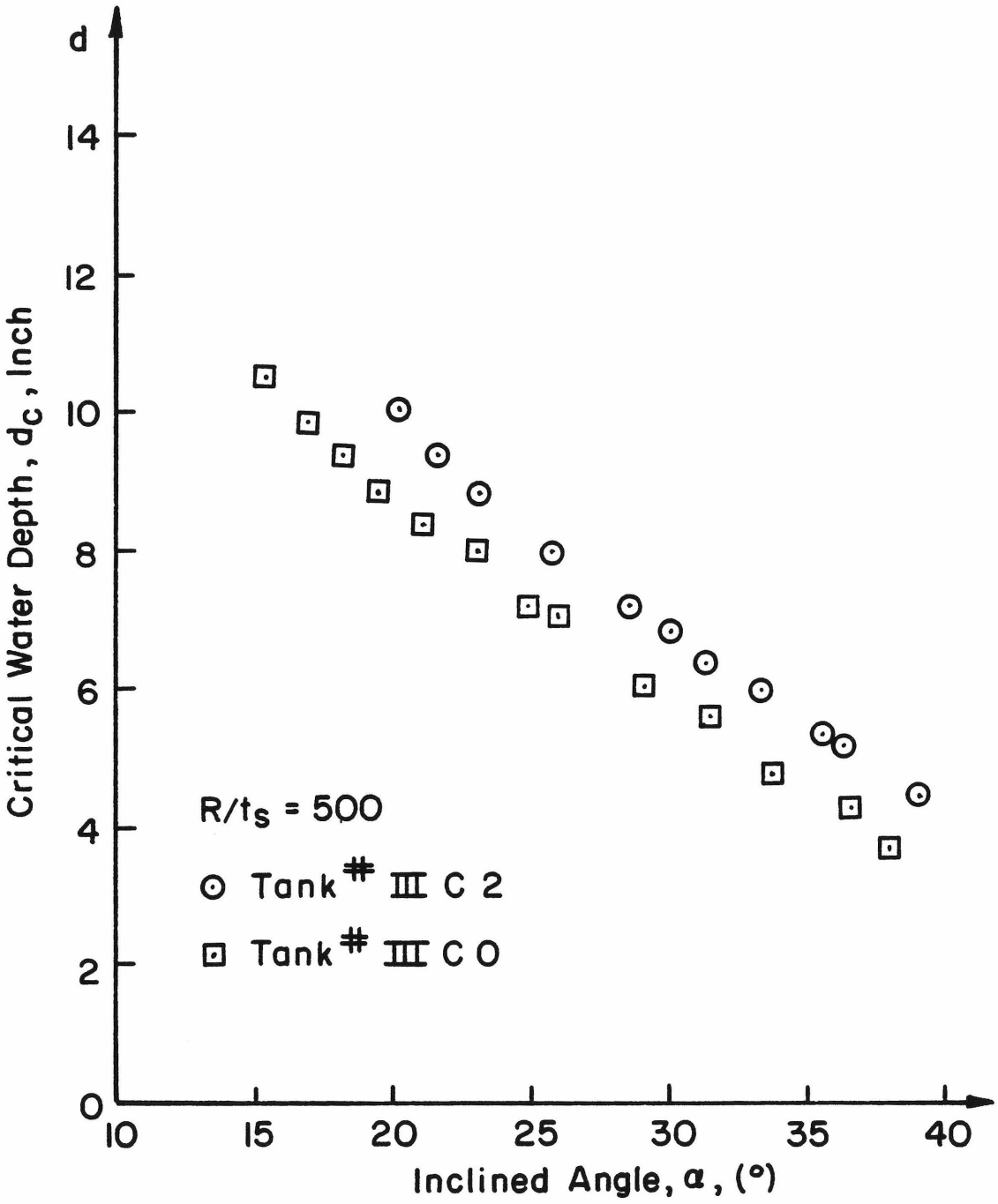

FIG.5.8c CRITICAL COLLAPSE WATER DEPTH VS. INCLINED ANGLE

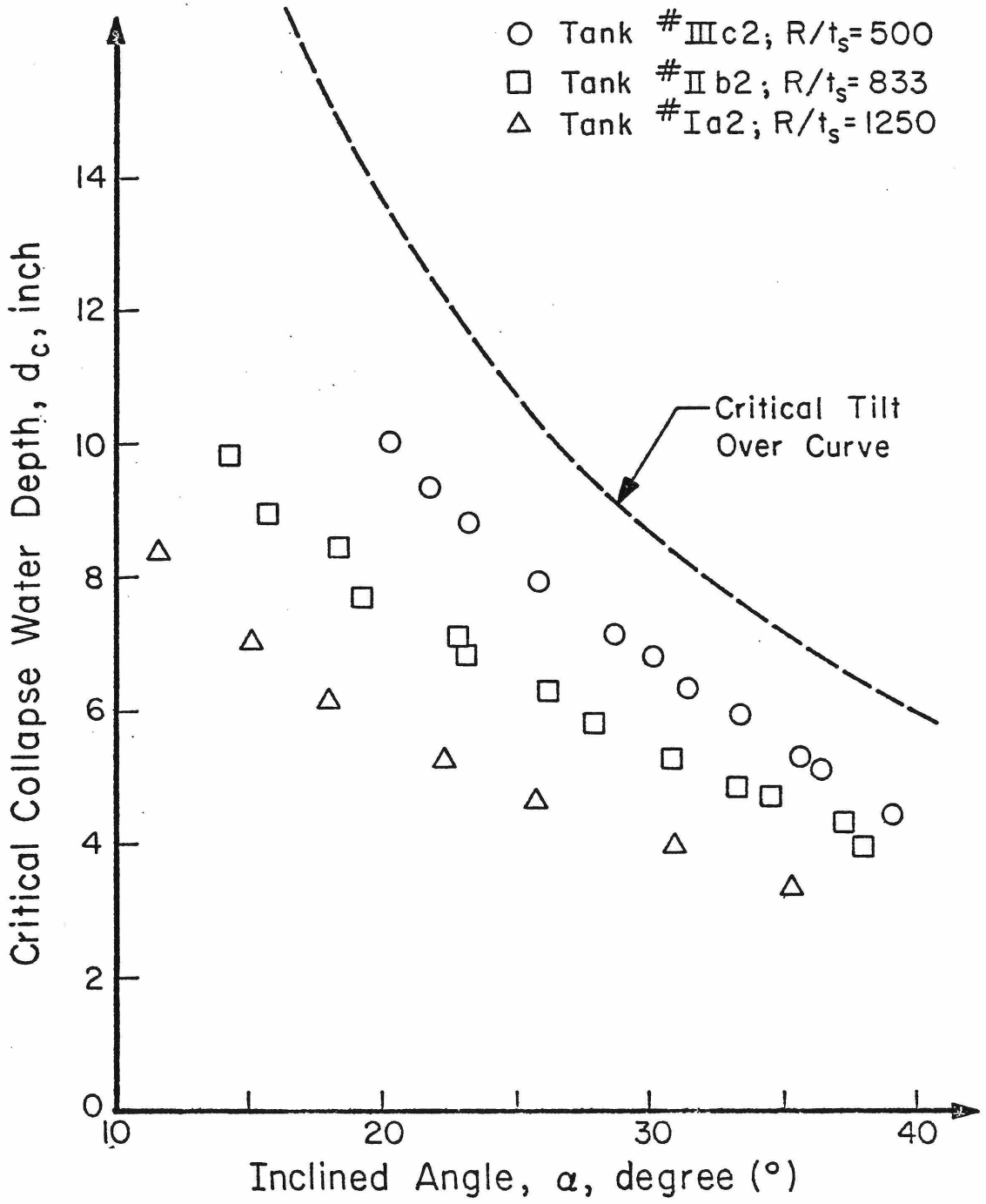

Fig. 5.9 R/t_s RATIO EFFECT ON THE COLLAPSE WATER DEPTH

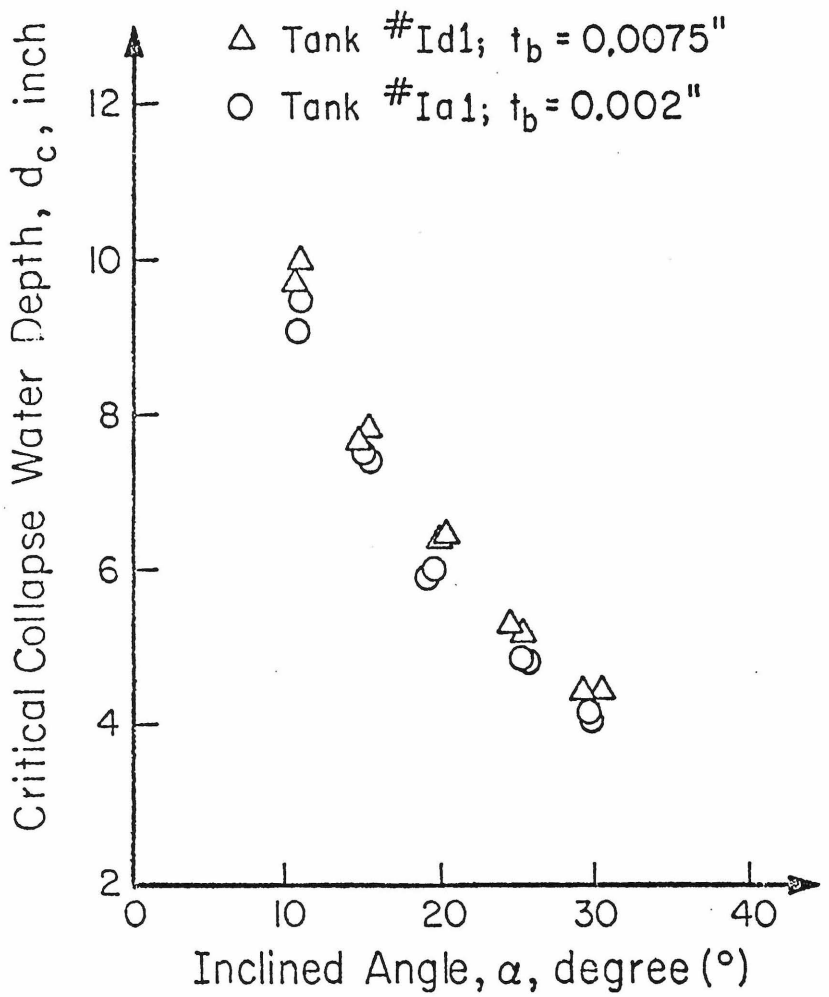

Fig.5.10a Bottom Plate Thickness Effect on Collapse Water Depth

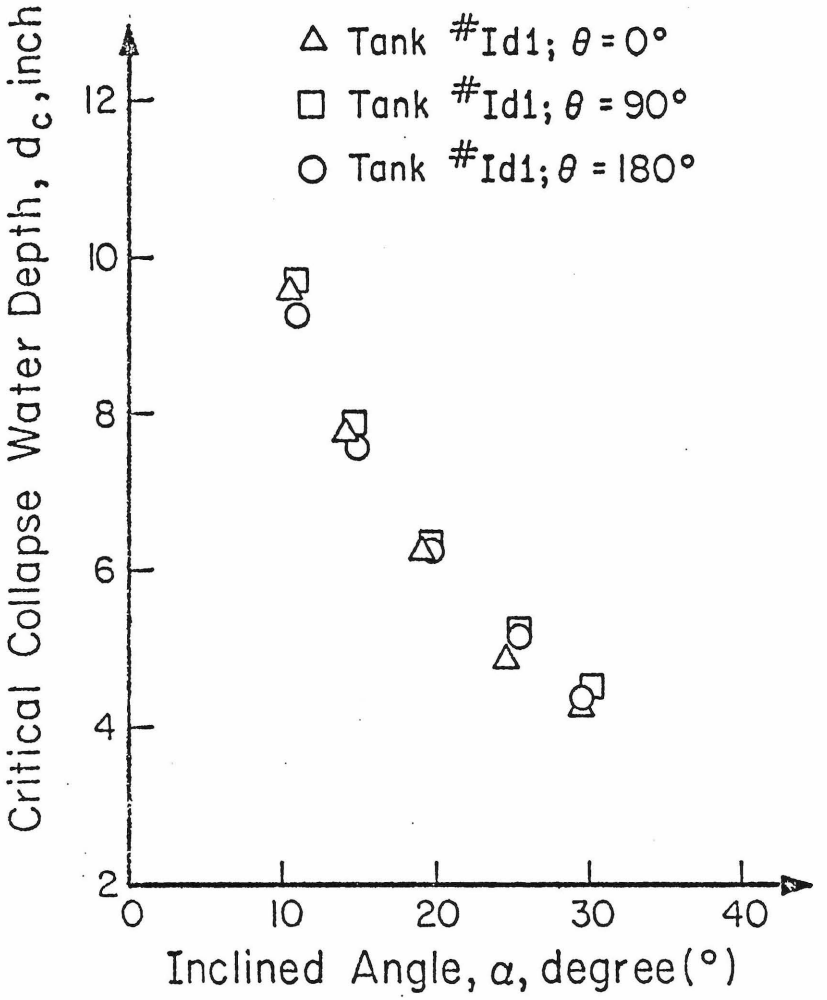

Fig.5.10b Initial Imperfection Effect on Collapse Water Depth

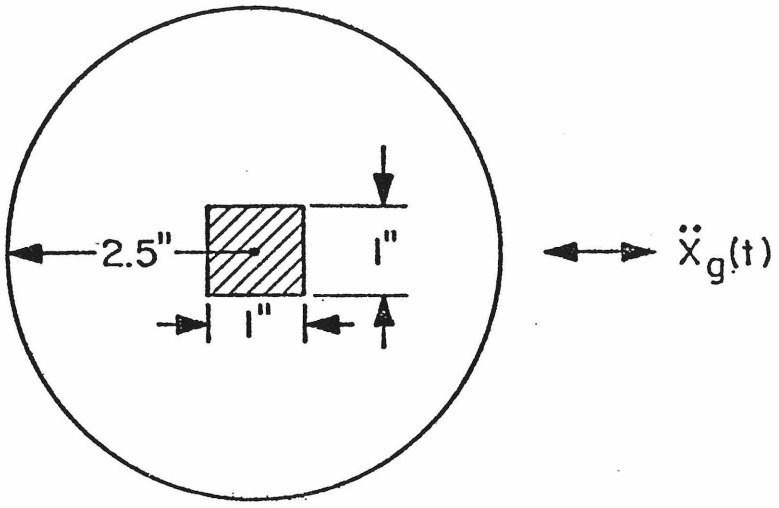

Fig. 5.11 Adhesive Area of Bottom Plate

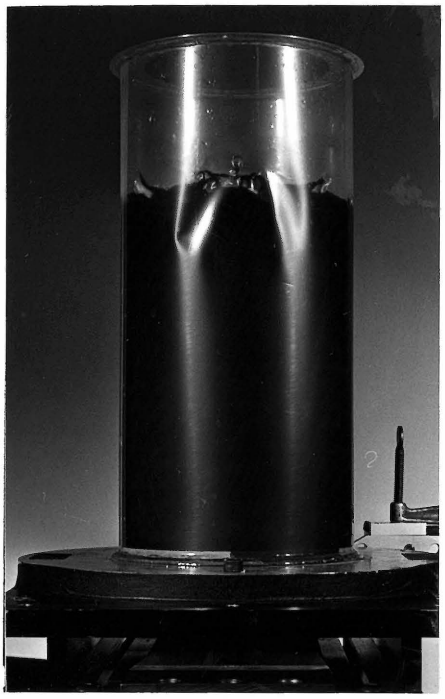

Figure 5.12a

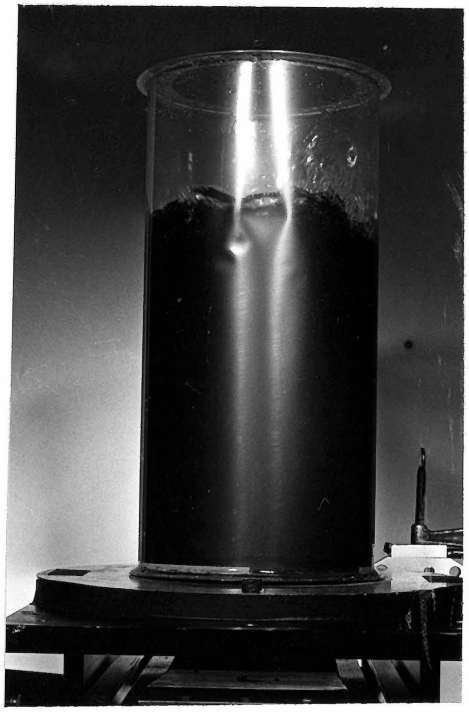

Figure 5.12b

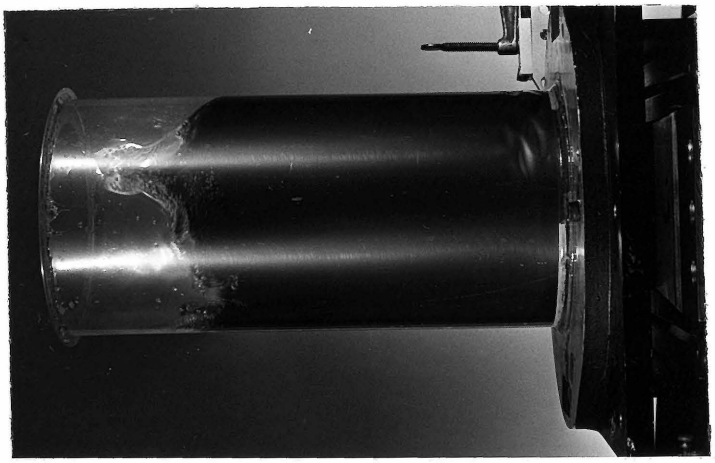

Figure 5.12e

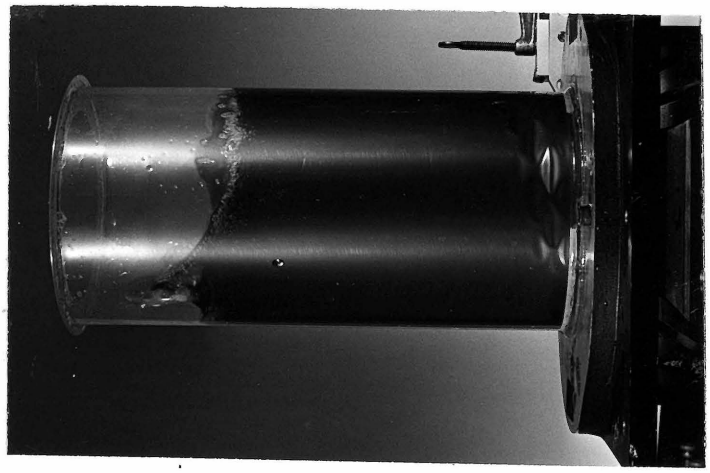

Figure 5.12d

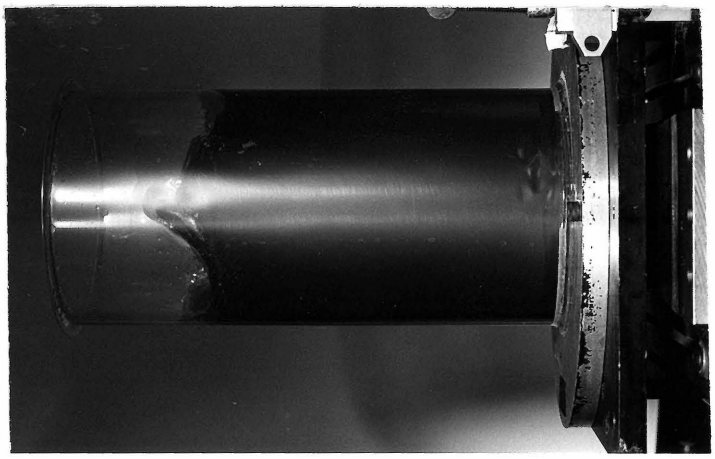

Figure 5.12c

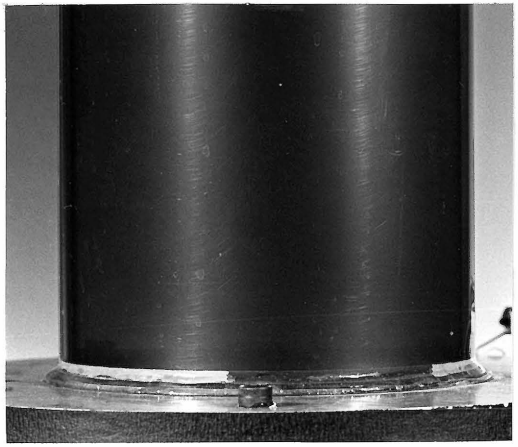

ω = 0 Hz

A = 0.0 g

Tank Bottom End

Figure 5.13a

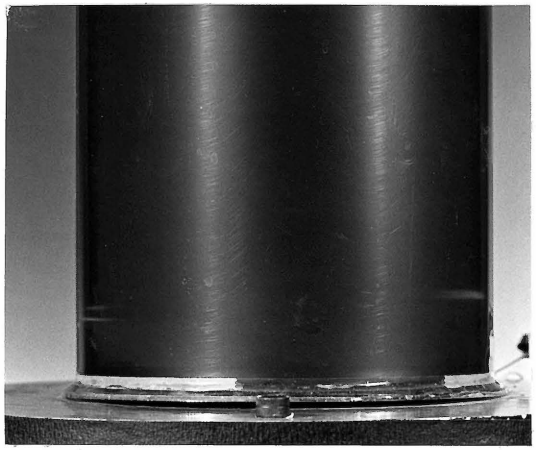

ω = 8 Hz

A = 0.2 g

Uplifting

Figure 5.13b

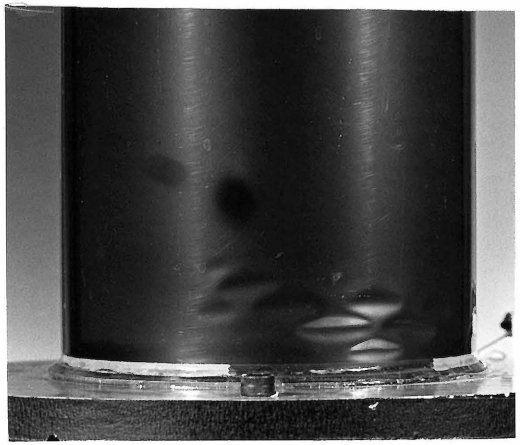

ω = 8 Hz

A = 0.2 g

Buckling

Figure 5.13c

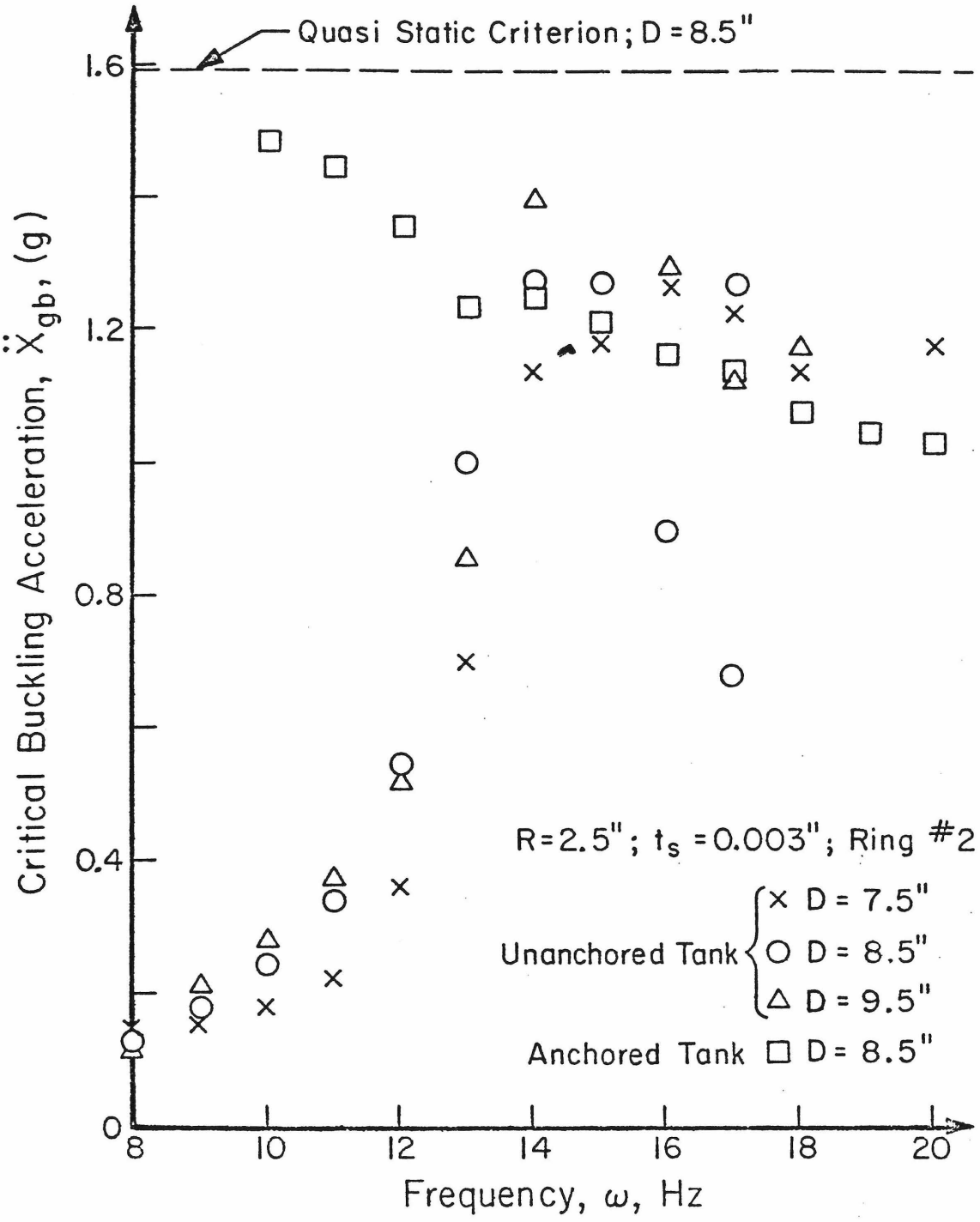

Fig. 5.14 Critical Buckling Acceleration vs. Frequency

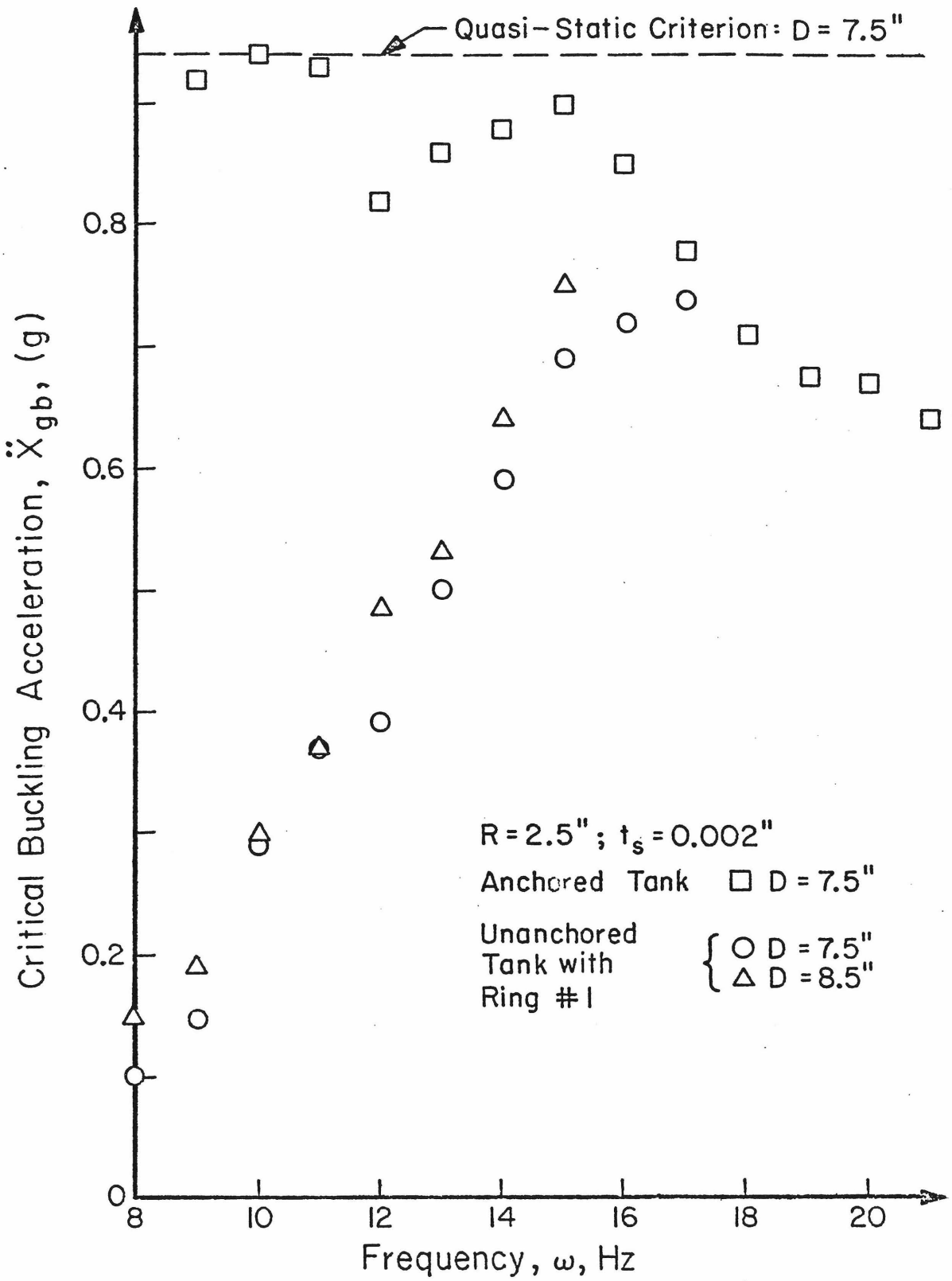

Fig. 5.15 Critical Buckling Acceleration vs. Frequency

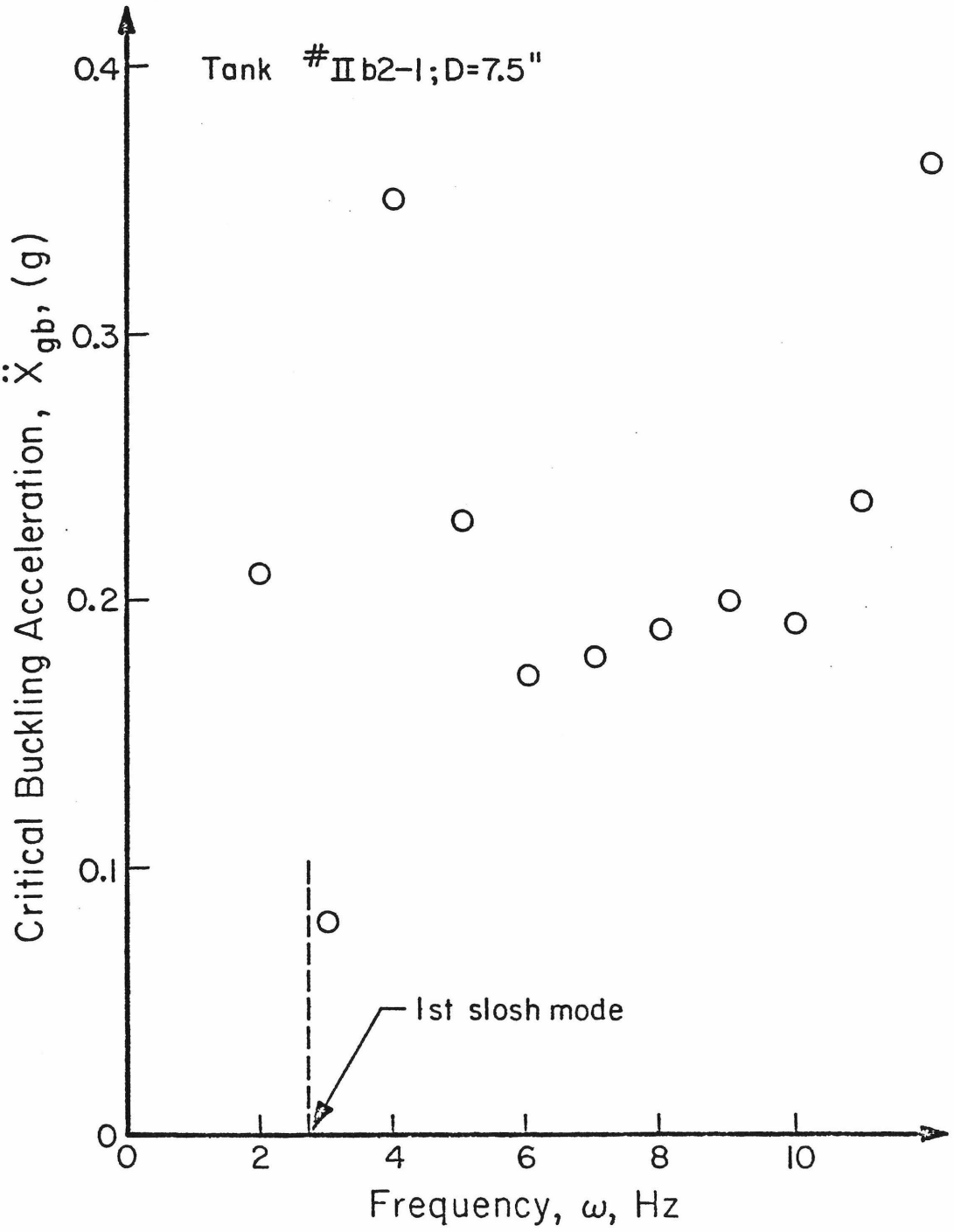

Fig. 5.16 Critical Buckling Acceleration vs. Frequency

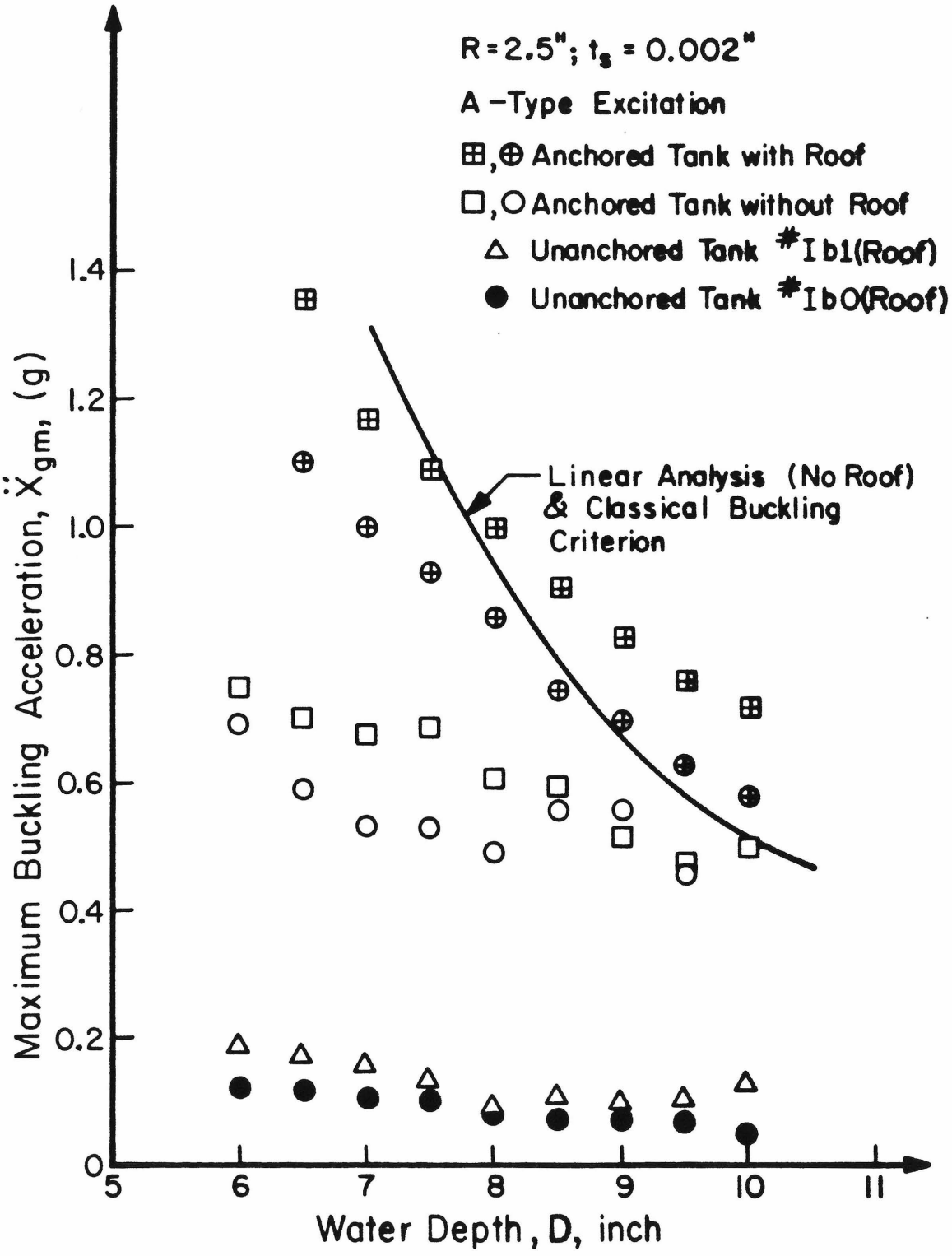

Fig. 5.17a Transient Buckling Test Results
(A-Type Excitation)

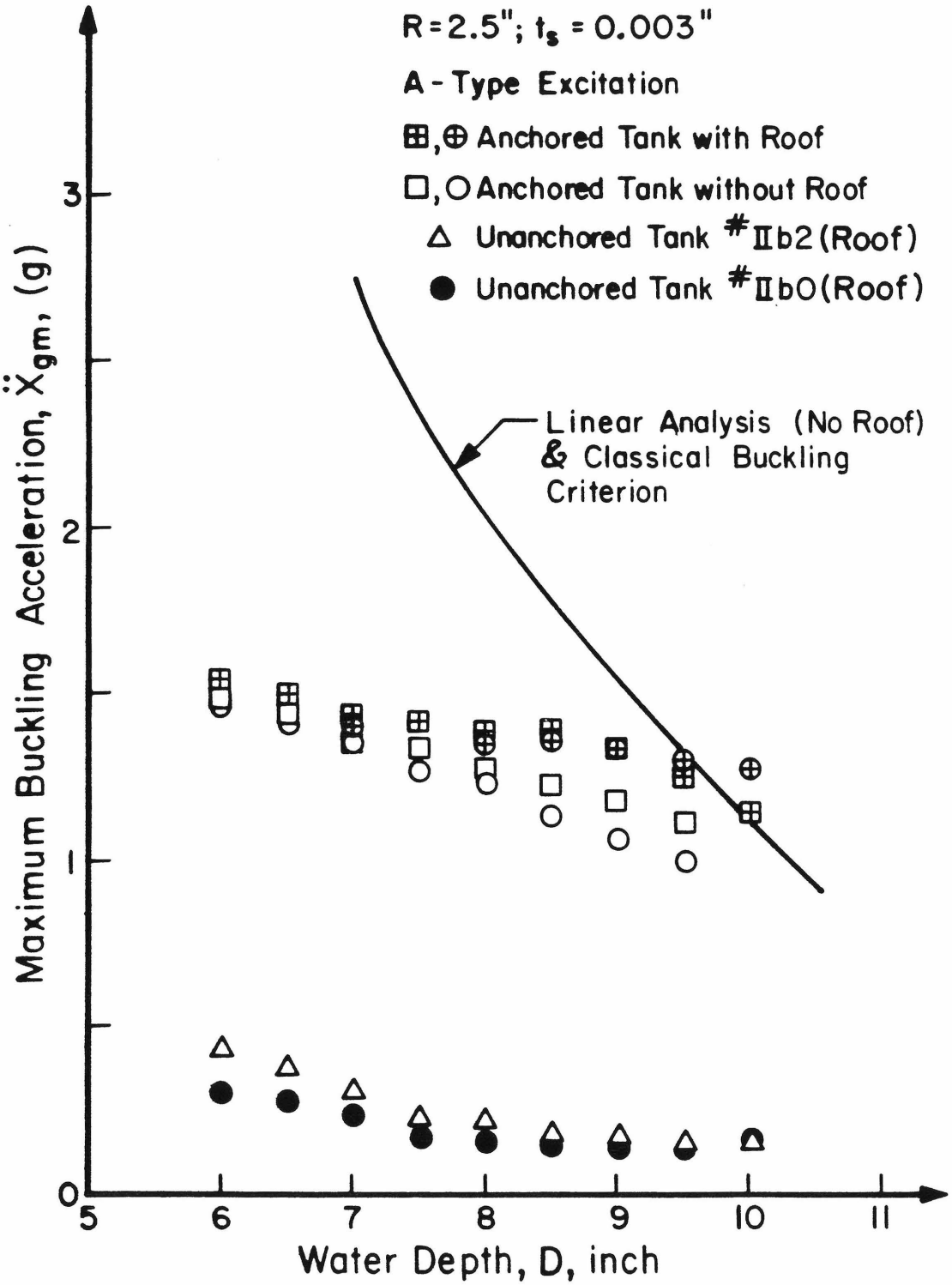

Fig. 5.17b Transient Buckling Test Results
(A-Type Excitation)

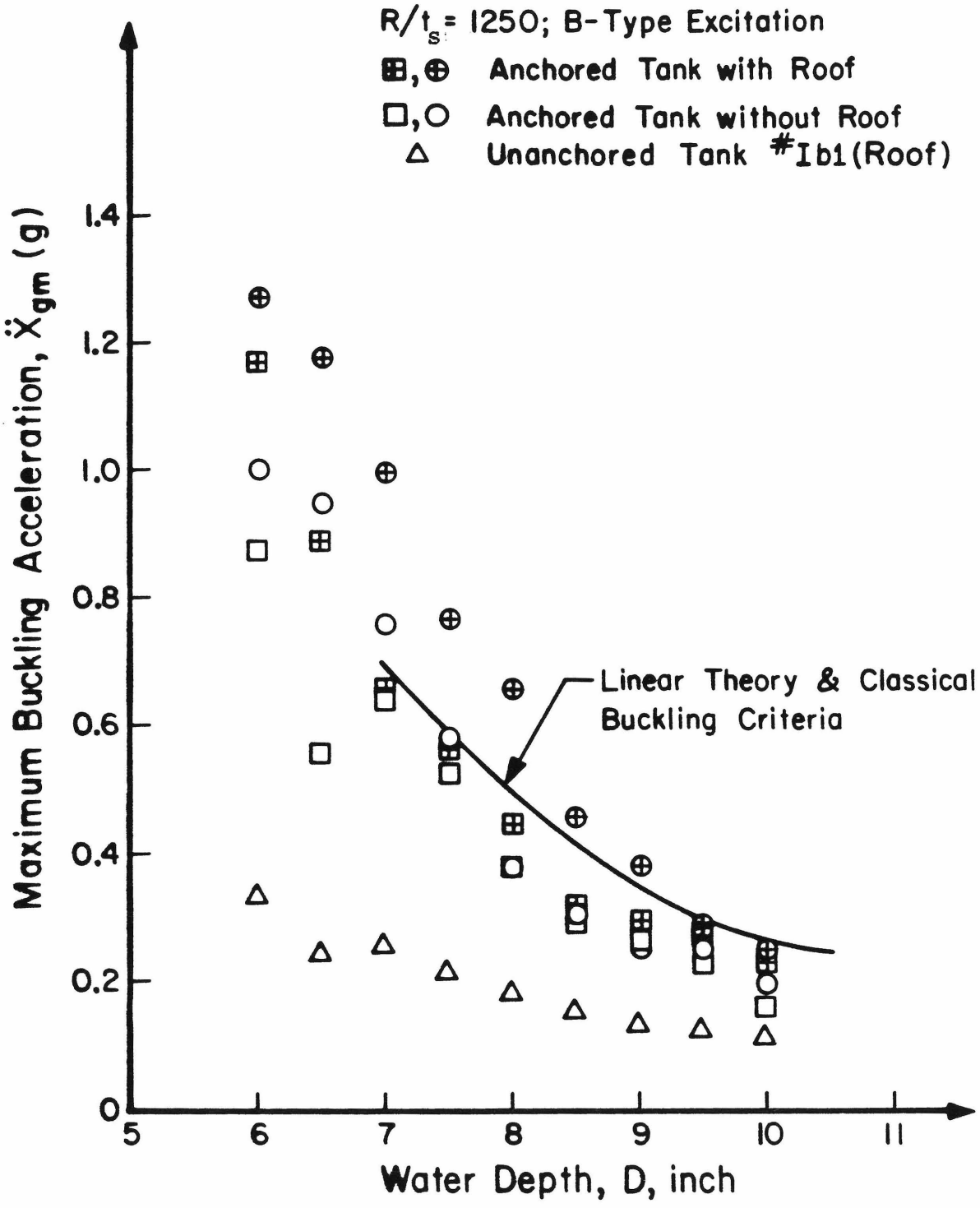

Fig. 5.18a Transient Buckling Test Results (B-Type Excitation)

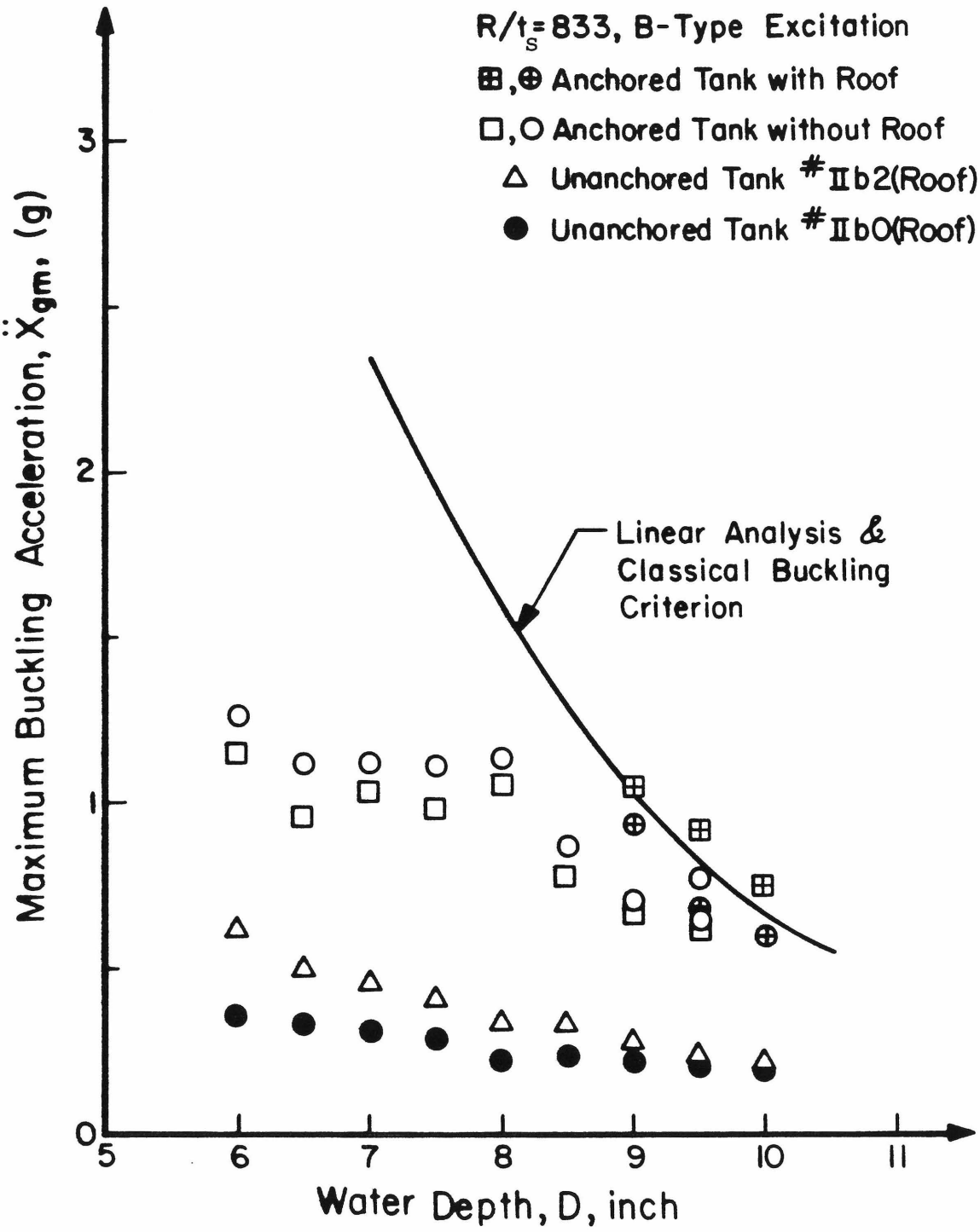

Fig. 5.18b Transient Buckling Test Results
(B-Type Excitation)

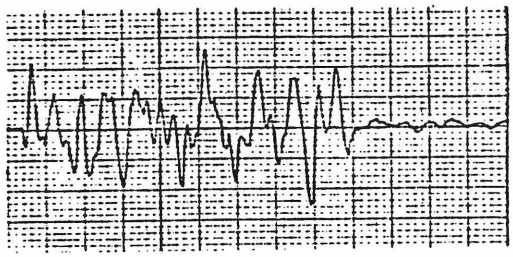

D = 6.0 in. Buckle

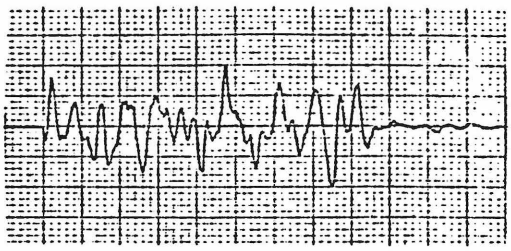

D = 6.0 in. No Buckle

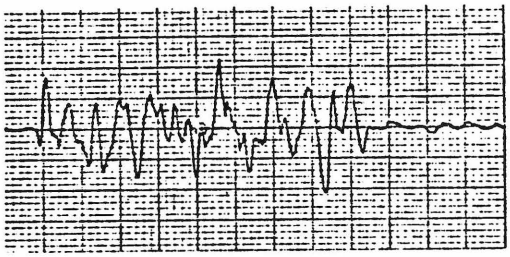

D = 7.0 in. Buckle

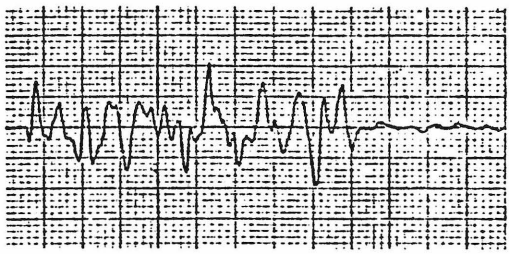

D = 7.0 in. No Buckle

D = 8.0 in. Buckle

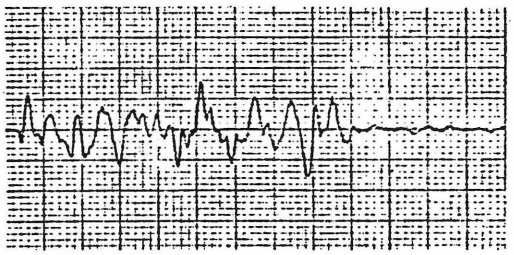

D = 8.0 in. No Buckle

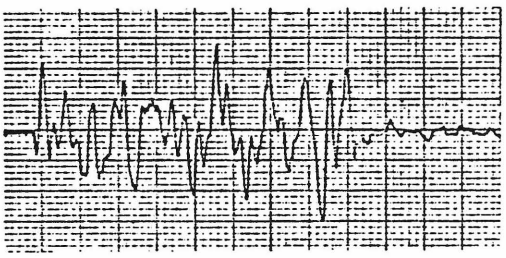

D = 9.0 in. Buckle

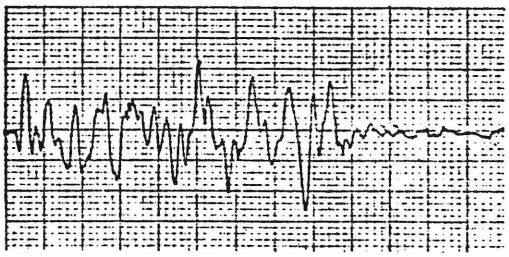

D = 9.0 in. No Buckle

R = 2.5 in.; t_s = 0.002 in.: t_b = 0.002 in.

No Bottom Reinforcing Ring; Roof on Top End.

Fig. 5.19 A-Type Base Excitation Patterns for an Unanchored Tank

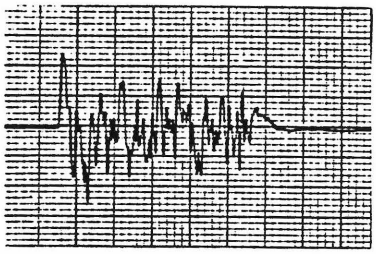

D = 6.0 in. Buckle

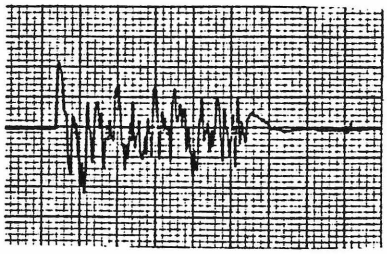

D = 6.0 in. No Buckle

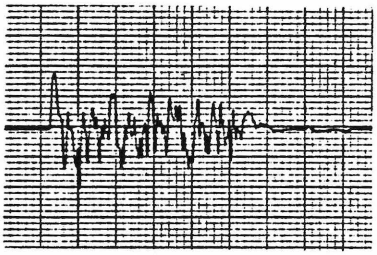

D = 7.0 in. Buckle

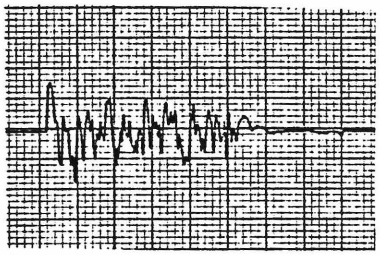

D = 7.0 in. No Buckle

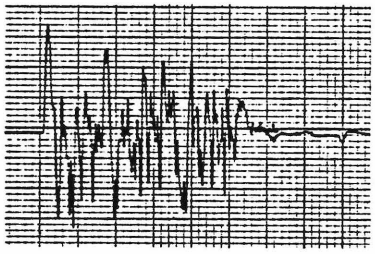

D = 8.0 in. Buckle

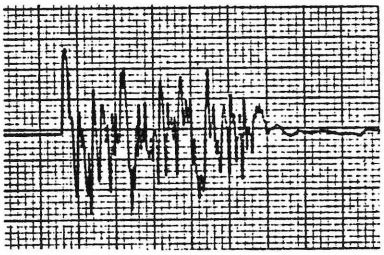

D = 8.0 in. No Buckle

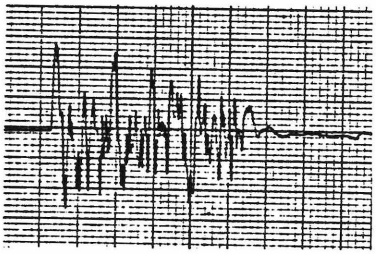

D = 9.0 in. Buckle

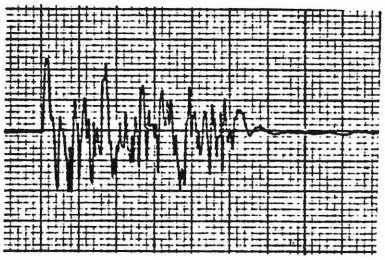

D = 9.0 in. No Buckle

R = 2.5 in.; t_s = 0.003 in.; t_b = 0.003 in.

Bottom Ring #2; Roof on Top End.

Fig. 5.20 B-Type Base Excitation Patterns for an Unanchored Tank

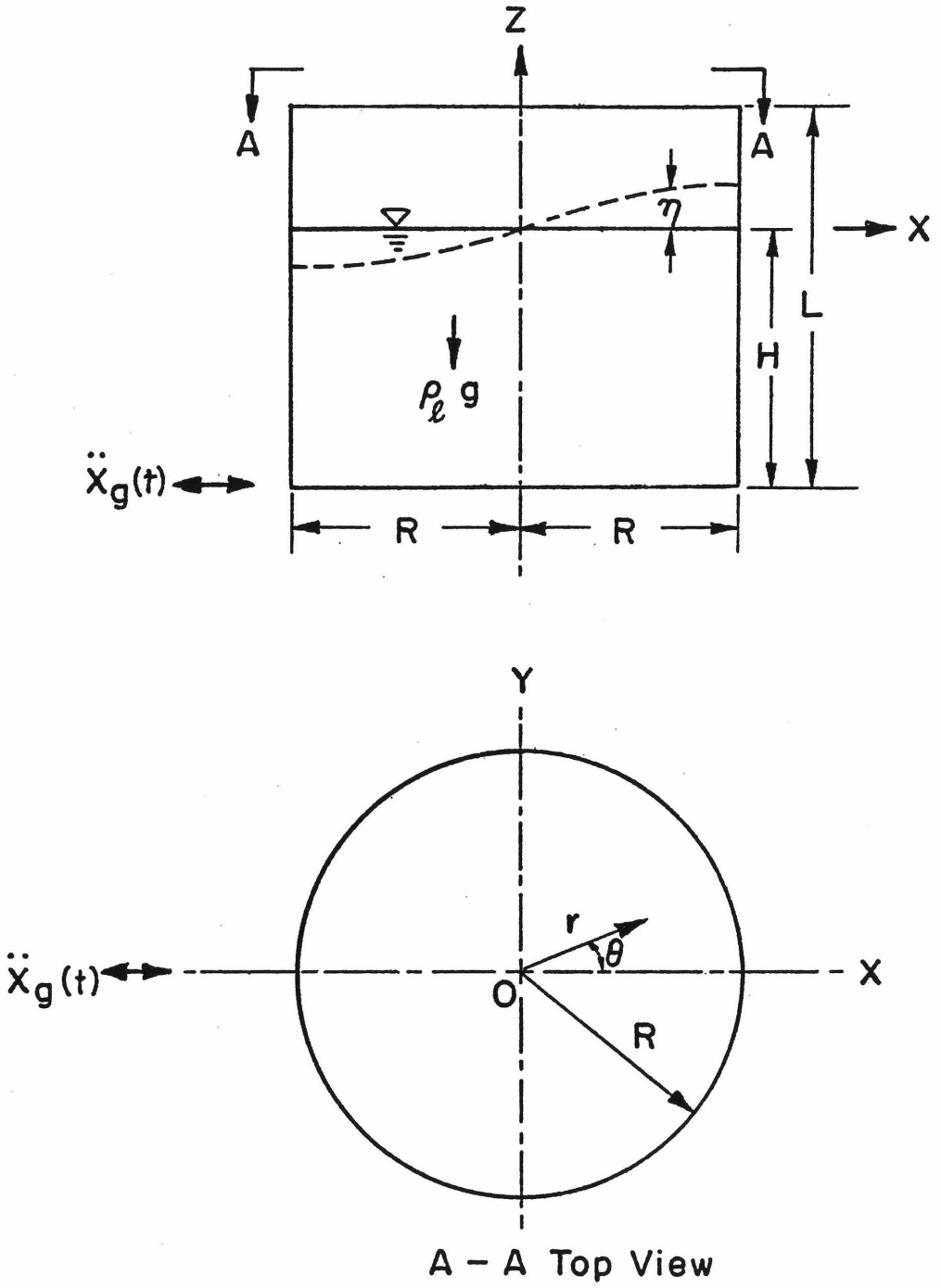

FIG. A.1 CYLINDRICAL TANK AND COORDINATE SYSTEM

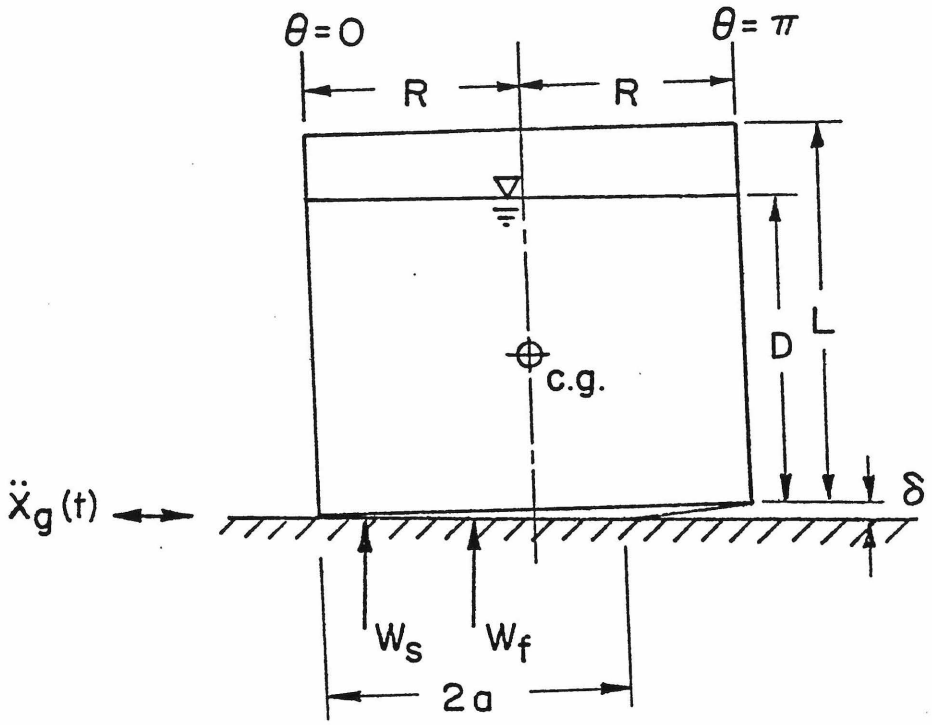

FIG. D.1 THE UNANCHORED TANK SUBJECTED TO GROUND MOTION

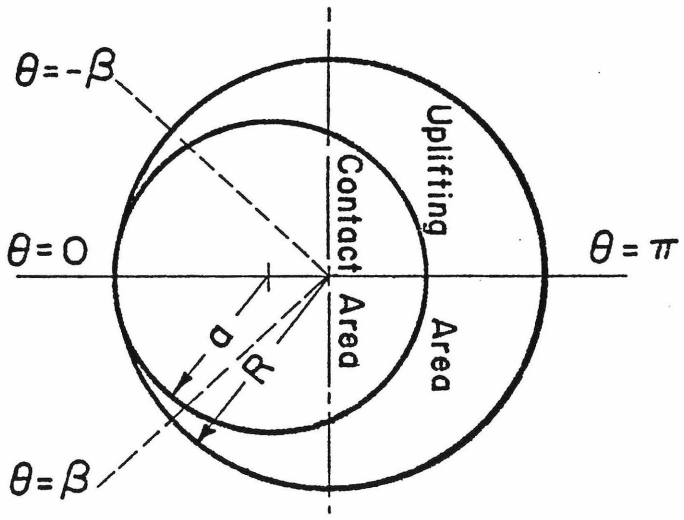

FIG. D.2 BOTTOM PLATE OF UNANCHORED TANK

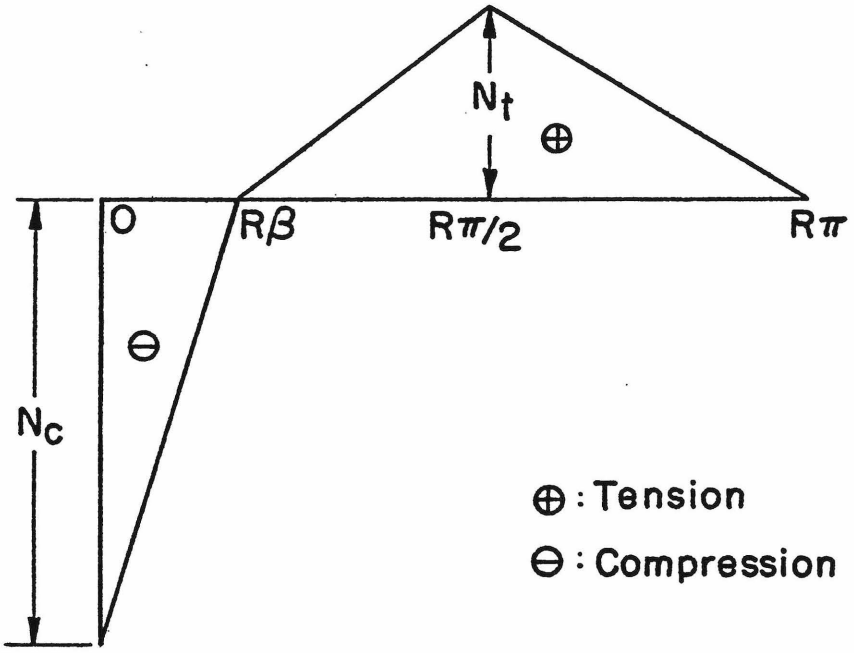

FIG. D.3 SHEAR FORCE DISTRIBUTION ALONG THE CIRCUMFERENCE OF TANK BOTTOM

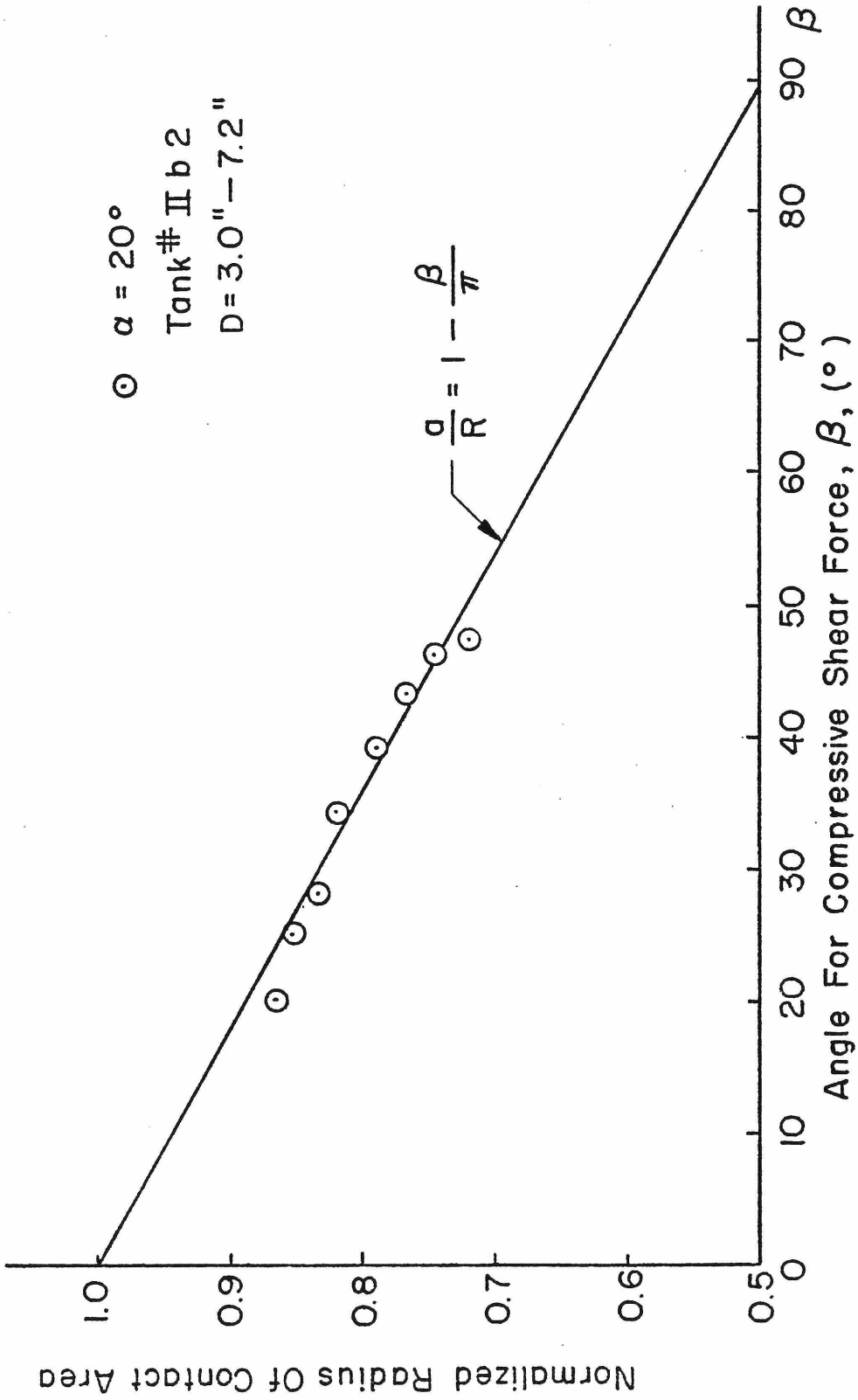

FIG. D.4 RADIUS OF CONTACT AREA VS. ANGLE FOR COMPRESSIVE SHEAR FORCE

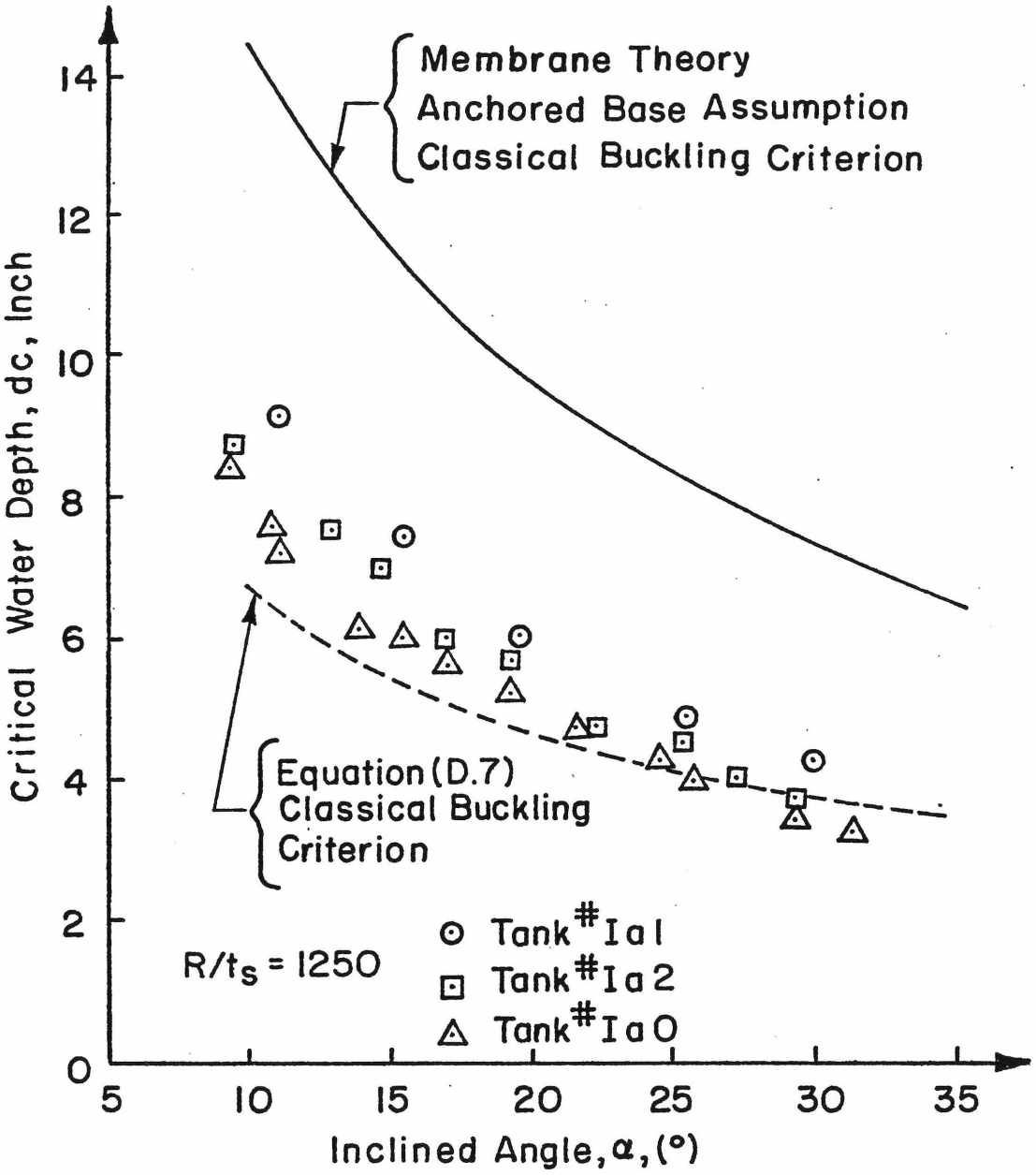

FIG. D.5a CRITICAL WATER DEPTH VS. INCLINED ANGLE

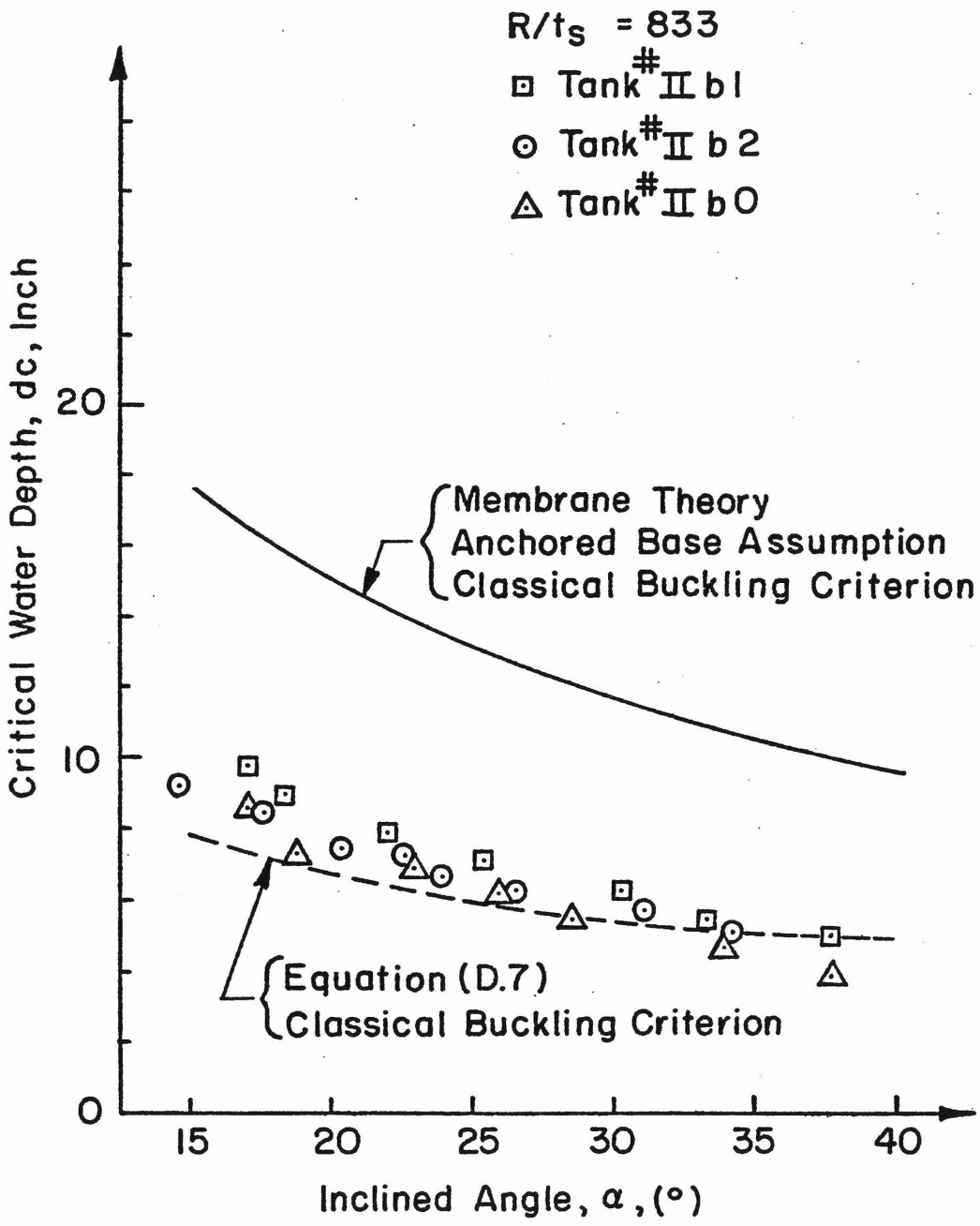

FIG. D.5b CRITICAL WATER DEPTH VS. INCLINED ANGLE

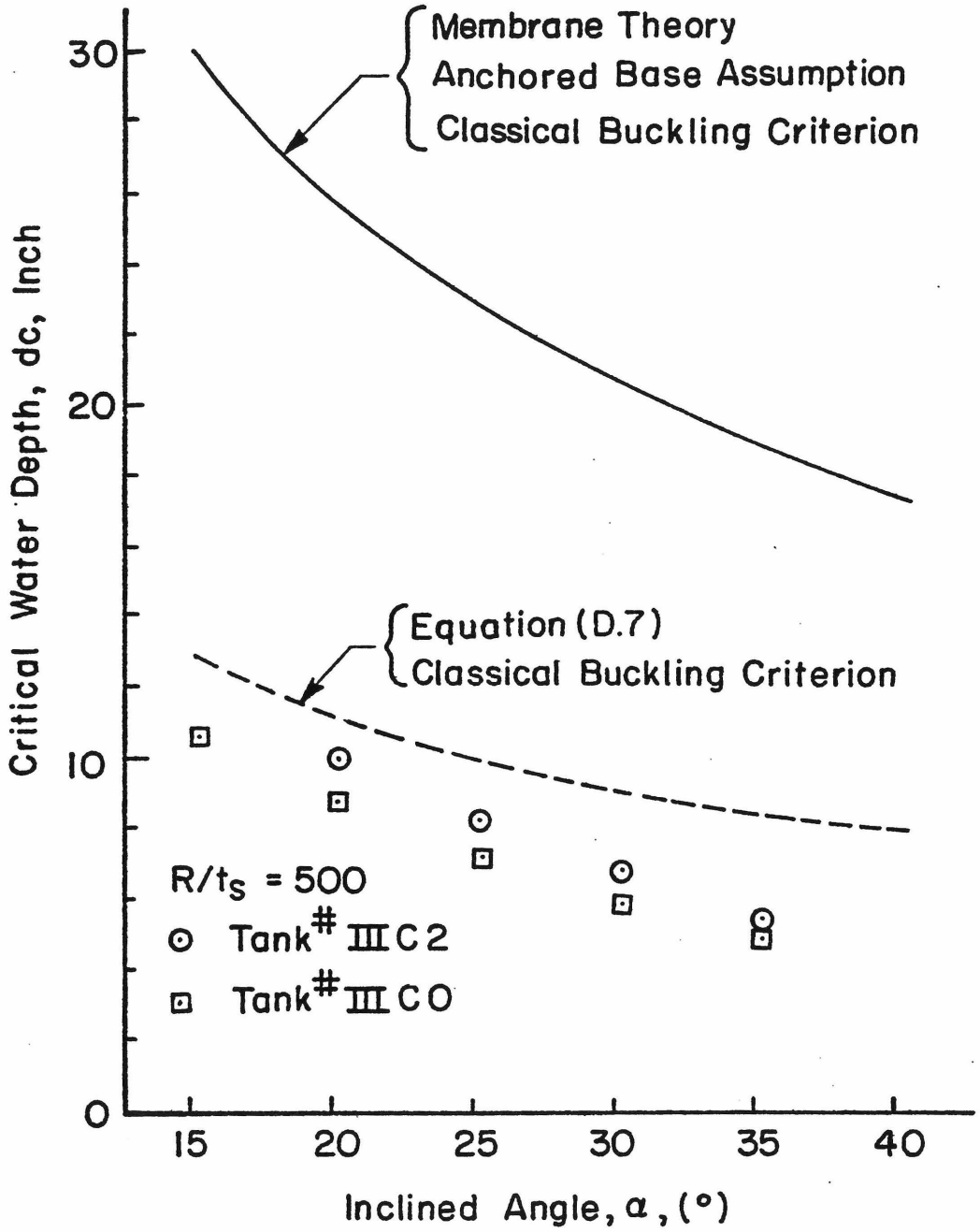

FIG. D.5C CRITICAL WATER DEPTH VS. INCLINED ANGLE